

New fibre-reinforced polymer box beam: investigation of static behaviour

by

Mario Springolo
BE (Civil) (Hons I)

A dissertation submitted for the award of
DOCTOR OF PHILOSOPHY

Faculty of Engineering and Surveying
University of Southern Queensland

Abstract

This thesis discusses the development of a new type of fibre-reinforced polymer (FRP) beam for use in civil engineering systems. After a detailed evaluation of the advantages and disadvantages of current FRP beam technology, a different approach is proposed which combines traditional laminates with a novel casting technique.

To pre-dimension the beam, the classical beam theory is adapted to allow for FRP materials. The resulting formulae were used to determine critical parameters, such as laminate thickness and location in the cross-section, and core dimensions, and to identify failure modes. Based on the results of this analytical study, a detailed testing program was developed. In addition to classical tests, such as bending, shear, and lateral torsion, the performance of the beam was also examined under particular loading regimes specifically designed to induce local failure modes, such as buckling of the web and bearing failure of the section under concentrated loads. The experimental results revealed very good agreement with the analytical predictions. These results were corroborated by a detailed non-linear finite-element analysis, including core cracking and laminate damage. This analysis, in particular, highlighted the synergy between bending and shear behaviour of the beam.

This study has revealed that this new type of FRP beam behaves in a predictable manner. Furthermore, the experimental results verified that the cross-section, which combines traditional laminates with cast polymer concrete, did not suffer from many of the disadvantages identified in current FRP beams. The cracking of the polymer concrete under shear, however, does cause the beam to fail prior to the laminates reaching their ultimate shear stress.

Certification of Dissertation

I certify that the ideas, experimental work, results, analysis and conclusions reported in this dissertation are entirely my own effort, except where otherwise acknowledged. I also certify that the work is original and has not been previously submitted for any other award, except where otherwise acknowledged.

/ /

Signature of Candidate

Date

Endorsed:

/ /

Signature of Supervisor

Date

Acknowledgements

Prof. Gerard Van Erp – my supervisor, for recognising the potential within myself and encouraging me to do this work

Dr. Amar Kehanne – my co-supervisor, for the support, encouragement, and critical review of this thesis and, for spending hours at a time working through this thesis with me.

USQ workshop and technical staff – for providing practical help with experimental test jigs and running experiments.

The Fibre composites design and development team (FCDD) – for providing the space and tools to produce the test specimens

Karen – my wife, for her constant and unwavering support while having to put up with my late nights at the Uni and in the study.

God – Without whom, nothing is possible.

Contents

Chapter 1 Introduction	1
1.1 Introduction	1
1.2 Background	1
1.3 Application of FRP in civil engineering systems	2
1.4 Objective of the study.....	5
1.4.1 Aim	5
1.4.2 Scope.....	5
1.5 Layout of the Thesis	6
References	7
Chapter 2 Overview of fibre-reinforced polymer materials and their manufacture	10
2.1 Introduction	10
2.2 Background	10
2.3 Constituents of fibre-reinforced polymers.....	11
2.3.1 Matrix.....	12
2.3.1.1 General.....	12
2.3.1.2 Thermosetting.....	12
Unsaturated polyesters.....	13
Epoxydes.....	14
Vinyl-ester	14
Other thermosetting resins.....	14
2.3.1.3 Thermoplastics.....	15
2.3.2 Fibres	15
2.3.2.1 General.....	15
2.3.2.2 Inorganic	16
2.3.2.3 Organic	17
Carbon.....	17
Aramid	17
Other fibres	17
2.3.2.4 Fibre forms for use in FRP	18
Chopped strand (CSM) and Continuous strand (CCSM) mats.....	18
Unidirectional mat (UD).....	18
Woven roving mat (WR)	19
Bi-axial (BA) and Double-bias (DB) mats	19

2.3.2.5	Sizing	19
	Yarn Sizes	20
	Roving Sizes	20
2.3.3	Filler materials	20
2.4	Laminated fibre-reinforced polymers and their properties	20
	Considerations for Laminate Lay-up	23
	Laminate terminology	24
2.5	Manufacturing techniques	25
2.5.1	Pultrusion	25
2.5.2	Filament-winding	26
2.5.3	Injection moulding	27
2.5.4	Hand and machine laminating	28
2.5.5	Consolidation techniques	28
	Vacuum bagging	28
	Autoclave consolidation	29
2.6	Conclusion	29
	References	30
Chapter 3 Existing FRP beams: advantages and limitations		32
3.1	Introduction	32
3.2	Description and behaviour of FRP beams developed for civil engineering applications.....	33
3.2.1	Commercially Available beams	33
3.2.1.1	Pultruded beams.....	33
	Delamination due to radial stresses and associated flange buckling	34
	Web buckling.....	34
	Connecting pultruded beams	35
	Limitations of the pultrusion process.....	35
3.2.1.2	Recent improvement in pultruded section design.....	35
3.2.1.3	Filament-wound beams.....	37
3.2.2	Custom designed beams.....	37
3.2.2.1	I beam with optimum fibre orientations	38
3.2.2.2	Concept combining concrete and an FRP box beam	38
3.2.2.3	Concrete-filled tubes.....	39
3.2.2.4	Concept combining a polymer core material and an FRP box beam.....	40
3.3	Conclusion.....	42
	References	42

Chapter 4 State of the art in FRP beam analysis and design methodologies.....	46
4.1 Introduction	46
4.2 Analysis techniques for FRP beams	47
4.2.1 From micro to macro mechanics.....	47
4.2.2 Three dimensional analysis.....	49
4.2.3 Two-dimensional analysis	52
4.2.4 One-dimensional analysis	54
4.2.4.1 Flexure	54
Stress versus strain.....	54
Beam theory.....	55
Determination of engineering constants	56
Combination of material and section constants into one term.....	58
4.2.4.2 Buckling.....	58
4.2.4.3 Lateral torsional buckling	59
4.2.5 Time effects	61
4.3 Shortcomings of current methodologies used to determine FRP beam section size.....	63
4.3.1 General.....	63
4.3.2 Moment and shear.....	64
4.3.3 Combined moment and shear.....	64
4.3.4 Lateral torsional buckling	65
4.3.5 Bearing capacity.....	66
4.3.6 Creep and creep rupture	67
4.3.7 Ductility	69
4.4 Conclusion.....	70
References	72
Chapter 5 Conception of a new hybrid composite beam	77
5.1 Introduction	77
General.....	77
Proposed solution to flange buckling and associated delamination at the web-flange interface	77
Control of web buckling	78
Proposed solution to compressive failure under vertical loads.....	78
Fibre orientation.....	79
5.2 Description of the new beam.....	79
5.2.1 Section Design	79

5.2.2	Determination of section size of test beams.....	81
5.2.2.1	Span	81
5.2.2.2	Selection of test beam depth	82
5.2.2.3	Width	83
5.2.2.4	Flange and web core dimensions	84
5.2.2.5	Final beam dimensions	84
5.3	Materials.....	85
5.3.1	E-Glass.....	85
5.3.2	Laminate properties	86
5.3.3	Core properties.....	88
5.4	Production processes	90
5.4.1	Material Use.....	90
5.4.2	Production.....	91
5.5	Summary	92
	References	92
Chapter 6 Analytical modelling of the FRP beam behaviour.....		94
6.1	Introduction	94
6.2	Pure bending.....	94
6.2.1	Moment curvature behaviour	94
6.2.2	Un-cracked beam behaviour	95
6.2.3	Effects of cracking of the PFR material on the behaviour of the beam	97
	Effective stiffness of the beam.....	99
6.2.4	Primary failure modes.....	101
6.2.4.1	General.....	101
6.2.4.2	Critical components.....	101
6.2.4.3	Tensile failure of the bottom unidirectional laminate.....	102
6.2.4.4	Compressive failure of the unidirectional laminate.....	102
6.2.4.5	Predominant primary failure mode	103
6.2.5	Secondary failure modes.....	103
6.2.5.1	General.....	103
6.2.5.2	Moment buckling of the webs	104
6.2.5.3	Compression buckling of the top flange	106
6.2.5.4	Web failures (a), (b) and (c).....	108
	Compression buckling capacity of the webs (a).....	111
	Crushing or tearing of the web (b) and (c).....	112
6.2.5.5	RHS laminate failure within the flanges (d)	113

6.2.5.6	Longitudinal cracking of the core in the flanges (e) and (f)	114
6.2.5.7	Other failure modes	115
6.3	Pure shear	115
6.3.1	Shear-deformation behaviour.....	115
6.3.2	Shear stress distribution	116
6.3.3	Shear-induced failure modes.....	119
6.3.3.1	Cracking of the core.....	119
6.3.3.2	Shear failure of the webs	120
6.3.3.3	Shear buckling of the webs.....	120
6.3.3.4	Flange failure	122
6.4	Moment-shear interaction.....	123
6.4.1	Deformation behaviour	123
6.4.2	Shear-moment capacity.....	124
6.4.2.1	General.....	124
6.4.2.2	Principal stress determination (Mohr's circle).....	125
6.4.2.3	Empirical models	126
Linear relationship (Eurocomp).....	126	
Elliptical relationship (General).....	126	
6.4.2.4	Comparison of models.....	127
6.5	Lateral torsional resistance of the beam	128
6.5.1	General.....	128
6.5.2	Determination of the torsion constant.....	128
6.5.3	Simplified analysis of lateral torsional buckling.....	131
6.5.3.1	Analytical formulation of lateral torsional buckling behaviour.....	131
6.5.3.2	Critical buckling moment formulae.....	133
Generalised approach.....	133	
FRP beam.....	134	
6.6	Determination of the bearing stress distribution angle.....	135
6.7	Key parameters.....	136
6.8	Conclusions	139
	References	140
Chapter 7 Experimental characterisation of the beam behaviour.....		142
7.1	Introduction	142
7.2	Strain distribution throughout the section	142
7.3	Bending	143
7.3.1	General.....	143

7.3.2	Beam tests	145
	Tensile failure of the unidirectional laminate	146
	Compressive failure of the unidirectional laminate	150
	Compression buckling of the top flange	150
	Longitudinal cracking of the core in the flanges	151
7.3.3	Moment buckling of the webs.....	152
7.3.4	Compression buckling of the webs	155
7.3.5	Characterisation of the local bearing capacity	156
7.4	Shear.....	157
7.4.1	General.....	157
7.4.2	Beam shear capacity	158
	7.4.2.1 Estimation of beam shear capacity by testing under combined moment and shear loading	158
	7.4.2.2 Determination of beam shear capacity by testing web specimens.....	163
	7.4.2.3 Comparison of results and the analytical solution for the pure shear capacity of the beam	168
7.4.3	Shear buckling capacity of the webs.....	169
7.5	Combined moment and shear	171
7.6	Lateral torsional buckling.....	174
	7.6.1 Torsion constant.....	174
	7.6.2 Lateral torsional buckling behaviour	176
7.7	Bearing stresses distribution angle	178
7.8	Creep	180
7.9	General Discussion.....	183
7.10	Conclusions	186
	References	188

Chapter 8 Non-linear finite element modelling of the FRP beam behaviour..... 189

8.1	Introduction	189
8.2	Modelling the complex behaviour of the FRP beam.....	189
	8.2.1 Limitations of standard FE software.....	189
	8.2.2 Description of the FE models.....	190
	8.2.2.1 Modelling the FRP beam using Strand7	190
	8.2.2.2 Modelling the FRP beam using ABAQUS	193
8.3	Models under specific loading regimes	197
	8.3.1 General.....	197
	8.3.2 Moment buckling of the webs.....	197

8.3.3	Compression buckling of webs.....	198
8.3.4	Longitudinal cracking of the core in the flanges.....	199
8.3.5	Shear	201
8.3.5.1	Web shear strength	201
8.3.5.2	Shear buckling of the webs.....	202
8.3.5.3	Overall beam performance.....	203
8.3.6	Combined moment and shear.....	204
8.3.7	Lateral torsional buckling	205
8.3.7.1	Torsion constant.....	205
8.3.7.2	Lateral torsional buckling	206
8.4	Conclusions	208
	References	209
Chapter 9 Conclusions and recommendations		210
9.1	Review of research	210
9.2	Main findings	211
9.3	Recommendations for further research.....	212
Appendices		214
Appendix A. Classical Laminate Theory		214
References		218
Appendix B. Production Process.....		219
	Preparation of unidirectional laminates.....	219
	Laying of the inner RHS laminates	219
	Provision of spacers	220
	Assembling the mould.....	220
	Pumping of PFR.....	221
	Laying the outer RHS laminates	222
	Curing the beams.....	223
Appendix C. Theory		224
C.1	Transformed section	224
C.2	Poisson ratio of the FRP beam web.....	228
C.3	Derivation of F_w	229
C.4	Flow chart of analytical program for pure bending	232
C.5	Calculation of shear deformation	233
C.6	Flow chart of analytical program for pure shear	235
C.7	Flow chart of analytical program for combined shear and moment.....	236
C.8	Analytical formulation of lateral torsional buckling behaviour	237

C.9	Flow chart of analytical program for torsion.....	241
C.10	Flow chart of analytical program for lateral torsional buckling	242
Appendix D.	Experimentation.....	243
D.1	Web buckling	243
Appendix E.	Results	244
E.1	Beams in pure bending	244
B4	(ms03-b4)	244
B5	(ms03-b5)	244
B6	(ms03-b6)	244
B7	(ms03-b7)	245
B8	(ms03-b8)	246
B9	(ms03-b9)	247
E.2	Web compression buckling	247
E.3	Beam crushing	248
E.4	Web shear capacity.....	248
S1	(ms04-1).....	248
S2	(ms04-2).....	249
E.5	Beams under combined loading of moment and shear.....	252
S1	(ms04-b-1).....	252
S2	(ms04-b-2).....	253
S3	(ms04-b-3).....	254
S4	(ms04-b-4).....	255
S5	(ms04-b-5).....	256
S6	(ms04-b-6).....	257
E.6	Beams under torsion loading	258
Beams T-b1 and T-b2.....		258
E.7	Distribution angle	260
E.8	Time effects: Short-term failure load and deflection of the beams	260
B1	(ms03-b1)	260
Appendix F.	FEA	262
F.1	Fortran program for damage analysis and material properties used by ABAQUS	262
F.2	Damage and failure of a laminated composite plate.....	265
References	270

Figures

Figure 1.1 FRP pedestrian cable stay bridge across the River Tay in Aberfeldy, Scotland (Barbero 1998).....	3
Figure 1.2 Pedestrian bridge (Ashland Chemical Company 1997).....	4
Figure 1.3 Parson’s Bridge, Ceredigion mid-Wales (Strongwell Ltd. 2002).....	4
Figure 1.4 Vehicular bridge in the City of Hamilton, Butler County, Ohio (iCivil).....	4
Figure 1.5 Ten metre vehicular bridge undergoing testing in Toowoomba, Queensland.....	4
Figure 2.1 Reinforcement – matrix interface.....	10
Figure 2.2 Forms of reinforcement (not to scale).....	11
Figure 2.3 Unidirectional mat.....	19
Figure 2.4 Woven roving mat.....	19
Figure 2.5 Bi-axial mat.....	19
Figure 2.6 Double-bias mat.....	19
Figure 2.7 Layers of plies that form a laminate.....	21
Figure 2.8 Laminate designation [45/0/45/90/90/30].....	24
Figure 2.9 The pultrusion process (Fibreforce Composites Limited 2002).....	26
Figure 2.10 Filament-winding technique (Saint-Gobain Vetrotex America International 2001).....	27
Figure 2.11 Injection moulding (Michigan State University 1999).....	27
Figure 2.12 Typical vacuum bagging.....	29
Figure 3.1 Sea Life Park bridges, Hawaii (Strongwell Ltd. 2002).....	33
Figure 3.2 DURAGRID® Phenolic Grating on an offshore platform (Strongwell Ltd. 2002).....	33
Figure 3.3 Delamination around curved regions.....	34
Figure 3.4 Strongwell 36-inch hybrid double web beam (Strongwell Ltd. 2002).....	36
Figure 3.5 Lee beam.....	37
Figure 3.6 Drummond beam.....	38

Figure 3.7 Deskovic beam.....	39
Figure 3.8 Zhao beam.....	40
Figure 3.9 Van Erp beam.....	41
Figure 4.1 Stress relations of a ply under a uniform strain.....	48
Figure 4.2 Anisotropic state of stress	49
Figure 4.3 Strain and stress distributions throughout a beam in bending.....	55
Figure 4.4 Published moment-shear interaction for steel, concrete and composites.....	65
Figure 4.5 Bearing distribution angle.....	66
Figure 4.6 Indicative creep modulus versus time (American Society of Civil Engineers 1984, p. 210).....	67
Figure 4.7 Indicative creep modulus versus time (Clarke 1996, p. 127).....	68
Figure 4.8 Tensile stress rupture of polyester composites (Clarke 1996, p. 128)	68
Figure 4.9 General stress – strain relationships of steel and FRP	70
Figure 5.1 Progression of FRP beam designs to alleviate flange buckling	78
Figure 5.2 Placement of core between web laminates.....	78
Figure 5.3 Rectangular void to reduce stress concentrations under compressive loading	79
Figure 5.4 Exploded view of the beam.....	80
Figure 5.5 Beam dimensions and designations	81
Figure 5.6 Avery Universal Testing Machine	82
Figure 5.7 Number of unidirectional laminates versus cross-sectional area for the FRP beam.....	84
Figure 5.8 MTS 810 Material Test System Machine	86
Figure 5.9 Non-linear stress strain behaviour of the PFR in compression.....	89
Figure 5.10 Non-linear stress strain behaviour of the PFR in tension.....	90
Figure 5.11 Form and pour beam production	92
Figure 6.1 FRP beam: load deformation behaviour.....	95
Figure 6.2 Transformed section of the un-cracked FRP beam	96

Figure 6.3 Comparison between the use of a constant and variable stiffness of the un-cracked FRP beam	97
Figure 6.4 Close-up of cracking with associated de-bonding.....	98
Figure 6.5 Transformed section of cracked FRP beam	98
Figure 6.6 Moment-curvature of the FRP beam.....	99
Figure 6.7 Moment-curvature of the FRP beam, and the Branson model.....	100
Figure 6.8 Moment-curvature of the FRP beam and the bilinear model.....	100
Figure 6.9 Some secondary failure modes in bearing.....	104
Figure 6.10 Stresses upon the web	104
Figure 6.11 Moment buckling of web specimen	105
Figure 6.12 Stresses upon the flange	106
Figure 6.13 Compression buckling of the flange	107
Figure 6.14 Top flange of curved beam: vertical force component.....	108
Figure 6.15 Secondary forces in flanges and webs	108
Figure 6.16 Standard determination of web dimensions for bearing capacity prediction ...	109
Figure 6.17 Deformed shape of beam due to the vertical force F_w	110
Figure 6.18 Moment diagrams throughout beam section; due to beam curvature (a) and bearing load (b).....	110
Figure 6.19 Bearing plate loading	111
Figure 6.20 FEA model cross-section of the FRP beam under bearing load	112
Figure 6.21 FRP beam; shear load deformation behaviour	116
Figure 6.22 Shear stresses throughout the beam cross-section.....	117
Figure 6.23 Shear correction values throughout the beam	118
Figure 6.24 Exaggerated localised shear dislocation caused by cracking of the PFR.....	120
Figure 6.25 Principal stresses on the webs.....	121
Figure 6.26 Shear buckling of web specimen.....	121
Figure 6.27 Beam in 4-point bending.....	124
Figure 6.28 Principal strains of the transformed FRP beam.....	126

Figure 6.29 Moment-shear interaction diagrams.....	128
Figure 6.30 Torsional rotation of the beam.....	130
Figure 6.31 Lateral buckling behaviour of the FRP beam.....	131
Figure 6.32 Deflections of a beam undergoing lateral torsional buckling.....	132
Figure 6.33 Comparison of methods to determine the critical buckling moment of the FRP beam.....	134
Figure 6.34 Comparison of FEA and analytical solution of the in-plane stresses at centre depth of a beam subject to 3-point bending.....	135
Figure 6.35 Stress factor ($D/2b$) as a function of beam depth for an orthotropic beam....	136
Figure 6.36 Effect on capacity by varying top flange core thickness.....	137
Figure 6.37 Effect on capacity by varying bottom flange core thickness.....	138
Figure 6.38 Effect on shear and moment capacities by varying web thickness.....	138
Figure 7.1 B6 strain gauge locations.....	142
Figure 7.2 Moment-strain relationship of beam B6.....	143
Figure 7.3 Beam geometries.....	144
Figure 7.4 Loading arrangement of beams.....	145
Figure 7.5 Loading plates for beam tests.....	146
Figure 7.6 Typical moment-strain relationship of the test beams.....	147
Figure 7.7 Moment-curvature relationship of the test beams.....	147
Figure 7.8 Moment-strain relationship of beam series B7.....	148
Figure 7.9 Moment-strain relationship of beam series B5.....	149
Figure 7.10 Moment-strain relationship of beam series B8.....	150
Figure 7.11 Moment-strain relationship of beam series B9.....	151
Figure 7.12 Moment-strain relationship of beam series B4.....	152
Figure 7.13 Extra reinforcement on web specimen.....	153
Figure 7.14 Web specimen testing.....	153
Figure 7.15 Testing web buckling specimen.....	154

Figure 7.16 Failure of web	155
Figure 7.17 Buckling loads of web test strips	156
Figure 7.18 Comparison of beam crushing capacity and analytical solution	157
Figure 7.19 Moment-shear testing set-up	159
Figure 7.20 Strain gauge rosette arrangement	160
Figure 7.21 Shear loading versus shear strain (normalised based upon maximum values from each series)	162
Figure 7.22 Normalized shear loading versus deflection	163
Figure 7.23 Section geometry of web shear specimens.....	163
Figure 7.24 Web specimen failure.....	164
Figure 7.25 Shear stress-strain behaviour of web specimens (inclusive of core).....	165
Figure 7.26 Failure of webs in shear and ISO 14129 prediction	165
Figure 7.27 Free body diagrams of the initial and final fibre orientation at a crack in the core.....	167
Figure 7.28 Failure of webs in shear and analytical prediction.....	168
Figure 7.29 Comparison of ultimate shear capacities and predictions	169
Figure 7.30 Extra reinforcement on web specimen.....	170
Figure 7.31 Shear buckling of test specimen.....	170
Figure 7.32 Load versus deformation of shear buckling specimen	171
Figure 7.33 Total deformations of beams.....	172
Figure 7.34 Moment versus shear	173
Figure 7.35 Torsion testing arrangement.....	174
Figure 7.36 Beam undergoing torsion testing	175
Figure 7.37 Torsion versus rotation angle	176
Figure 7.38 Test set-up for lateral torsional buckling.....	176
Figure 7.39 Cantilever beam, lateral torsional buckling.....	177
Figure 7.40 z-axis rotation of cantilever beam.....	178
Figure 7.41 Failure loads for beams versus model predictions	179

Figure 7.42 Failure load and bearing distance of fully-supported series.....	180
Figure 7.43 Test regime for long-term loading of the beams	181
Figure 7.44 Beams undergoing sustained loading.....	181
Figure 7.45 Time versus deflection for the three beams tested	182
Figure 7.46 Time versus factor of initial deflection	183
Figure 7.47 Compression flange core thickness versus failure load	184
Figure 7.48 Tension flange core thickness versus failure load.....	185
Figure 7.49 Web core thickness versus failure load.....	185
Figure 8.1 Use of thick shell elements results in inaccurate models due to overlapping materials.....	190
Figure 8.2 Model with orthotropic bricks for flange laminates.....	190
Figure 8.3 Finite element model of the core with brick elements removed to simulate cracking of a beam in bending	192
Figure 8.4 Comparison of Strand7, analytical solution, and experimental results	193
Figure 8.5 Flow chart of Python script.....	194
Figure 8.6 FE model versus analytical and experimental results	196
Figure 8.7 FE model versus analytical and experimental results for changing flange core thickness.....	197
Figure 8.8 Moment buckling of the web specimen	198
Figure 8.9 Modified beam to force punching shear dominant.....	199
Figure 8.10 Uniformly distributed load on symmetric beam	200
Figure 8.11 FEA results, longitudinal cracking of the core material.....	201
Figure 8.12 Shear buckling of web specimen.....	202
Figure 8.13 FEA results, shear stress throughout beam	203
Figure 8.14 Comparison of FE model deflections of the beam under shear loads.....	204
Figure 8.15 Models of 4-point bending.....	204
Figure 8.16 Comparison of combined loading models.....	205
Figure 8.17 Comparison between torsion models showing a linear response	206

Figure 8.18 Finite element results for first positive eigenvalue	207
Figure 8.19 Comparison of LTB predictions.....	208
Figure A.1 Measurement of ply in a laminate. (Swanson 1997).....	216
Figure B.1 Unidirectional laminate lay-up sequence	219
Figure B.2 RHS laminate lay-up	220
Figure B.3 Mandrels and laminates in mould.....	220
Figure B.4 Pump operation.....	221
Figure B.5 Injection moulding	222
Figure B.6 Curing cycle	223
Figure C.1 Curvature of beam undergoing pure moment.....	228
Figure C.2 Laminate orientation.....	229
Figure C.3 Curved beam, top flange only	230
Figure C.4 Section of top laminate.....	230
Figure C.5 Flow chart for predicting pure moment behaviour.....	232
Figure C.6 Shear deformation of a beam segment	233
Figure C.7 Analytical flow chart for shear behaviour.....	235
Figure C.8 Analytical flow chart for combined shear and moment behaviour (Mohr's circle)	236
Figure C.9 Deflections of a beam undergoing lateral torsional buckling.....	237
Figure C.10 Force P transformed into the x' and y' component forces	238
Figure C.11 Flow chart of torsion numerical analysis.....	241
Figure C.12 Flow chart of lateral torsional buckling analysis.....	242
Figure E.1 Experimental shear strains series 1 (Experimental results line up with FE ABAQUS).....	252
Figure E.2 Experimental shear strains series 2.....	253
Figure E.3 Experimental shear strains series 3.....	254
Figure E.4 Experimental shear strains series 4.....	255

Figure E.5 Experimental shear strains series 5.....	256
Figure E.6 Experimental shear strains series 6.....	257
Figure E.7 ms03-b1	261

Tables

Table 2.1 Typical Properties of Cast Thermosets (at 23 °C) compiled from Fibre Composite Design and Development Group 1997; Hull & Clyne 1996.....	13
Table 2.2 Typical properties of cast thermoplastics at 23°C (t=tensile, y=yield)	15
Table 2.3 Properties of typical fibres (Bishop 1989; Hanson 1987)	16
Table 2.4 The properties of FRP laminates, steel, concrete and timber (E. I. duPont de Nemours. 1980; Fiber Science Division of EDO Corp. 1995; Pagano & Hahn 1997; Swanson 1997; Tsai 1986).....	22
Table 2.5 Properties of E-Glass / West system epoxy (Fibre Composite Design and Development Group 1997)	23
Table 5.1 Nominal beam dimensions	85
Table 5.2 E-Glass mat properties	86
Table 5.3 Laminate properties	87
Table 5.4 The properties of PFR	90
Table 7.1 Beam dimensions	144
Table 7.2 Shear test beam dimensions.....	160
Table 7.3 Shear testing beam spans.....	161
Table 8.1 Material properties for failure modelling	195
Table 8.2 Moment buckling predictions.....	198
Table 8.3 FE model indicates that true boundary condition of web is between simply-supported and fixed-ends restraints.....	199
Table 8.4 Predictions of punching capacity in modified beam	200
Table 8.5 Predictions of PFR failure within the flanges.....	200

Table 8.6 Comparison between web shear models.....	202
Table 8.7 Shear buckling predictions	202
Table D.1 Buckling specimens.....	243
Table E.1 ms03-b4 results	244
Table E.2 ms03-b5 results	244
Table E.3 ms03-b6 results	245
Table E.4 ms03-b7 results	246
Table E.5 ms03-b8 results	247
Table E.6 ms03-b9 results	247
Table E.7 Web buckling results, series 1.....	247
Table E.8 Web buckling results, series 2.....	247
Table E.9 Beam crushing results	248
Table E.10 ms04-1 tab results	249
Table E.11 ms04-2 tab results	249
Table E.12 Web shear testing results taking area as total area of specimen.....	250
Table E.13 Web shear results taking only laminate area into account	251
Table E.14 Web shear specimens including glass stresses.....	251
Table E.15 ms04-b-1 beam results	253
Table E.16 ms04-b-2 beam results	253
Table E.17 ms04-b-3 beam results	255
Table E.18 ms04-b-4 beam results	256
Table E.19 ms04-b-5 beam results	257
Table E.20 ms04-b-6 beam results	258
Table E.21 Torsion test results	259
Table E.22 Bearing distribution results	260
Table E.23 ms03-b1 results	261

Nomenclature

a	Bearing distribution angle (Radians)
g	Absolute shear strain (Radians)
g_i	Failure shear strain in the laminate i (Radians)
g	Shear strain in the laminate i (Radians)
D_M	Deformation due to moment loading. (mm)
D_m	Moment deflection of the beam (mm)
D_S	Deformation due to shear loading (mm)
D_s	Shear deflection of the beam (mm)
D_t	Total deflection of the beam (mm)
e_c	Compression strain to outer face of beam (mm/mm)
$e_{cb.c}$	Compressive compression buckling strain (mm/mm)
$e_{cb.t}$	Tensile compressive buckling strain (mm/mm)
e_{ci}	Average compressive strain in laminate i (mm/mm)
e_{fci}	Compressive failure strain of laminate i (mm/mm)
e_{fji}	Tensile failure strain of laminate i (mm/mm)
e_{ij}	Strain on face i in direction j (mm/mm)
e_{mb}	Moment buckling strain (mm/mm)
$e_{mb.cr}$	Critical moment buckling strain (mm/mm)
e_t	Tensile strain to outer face of beam (mm/mm)
e_{ti}	Average tensile strain in laminate i (mm/mm)
q_x	x direction plate rotation component relative to the middle plane ($radians$)
q_y	y direction plate rotation component relative to the middle plane ($radians$)
k	Curvature of a beam ($1/mm$)
n	Poisson ratio
n_i	Poisson ratio of laminate i
n_f	Poisson ratio of the flange.
n_w	Poisson ratio of web
p	Pi
s_{cb}	Compressive stress in outer face of column due to buckling.
s_f	Failure stress of fibres (MPa)
s_{fci}	Compressive failure stress of laminate i (MPa)
s_{fji}	Tensile failure stress of laminate i (Mpa)
s_{ij}	Stress on face i in direction j (Mpa)
s_m	Failure stress of matrix (MPa)
s_{mb}	Moment buckling stress (MPa)
$s_{mb.cr}$	Critical stress for moment buckling (MPa)
s_p	Failure stress of ply (MPa)
s_x	Normal stress in the x direction (Mpa)
t_{fi}	Failure shear strain of laminate i

t_{fw}	Shear failure stress of the web (<i>Mpa</i>)
t_{fxyi}	Failure shear stress of laminate i. (<i>MPa</i>)
t_{xy}	Shear stress in the x-y plane (<i>Mpa</i>)
t_{xyi}	Shear stress of laminate i (<i>MPa</i>)
f	Angle of torsional rotation (<i>radians</i>)
f_f	Fibre volume fraction (mm^3/mm^3)
f_{fi}	Fibre volume fraction for laminate i
f_m	Matrix volume fraction (mm^3/mm^3)
A	Cross-sectional area of section (mm^2)
A_i	Area of laminate i (mm^2)
A_q	Quadratic equation coefficient
A_s	Shear area of beam (mm^2)
A_t	Area of transformed section (mm^2)
B	Quadratic equation coefficient
C	Quadratic equation coefficient
c	Distance from outer tensile face of beam to neutral axis in x direction (<i>mm</i>)
c_c	Distance from outer tensile face of beam to neutral axis in x direction in cracked section (<i>mm</i>)
c_f	Distance from outer tensile face of flange to neutral axis of flange in z direction (<i>mm</i>)
CFRP	Carbon fibre-reinforced polymer
C_{ta}	Equation constant for core tensile modulus
C_{tb}	Linear equation coefficient for core tensile modulus
c_u	Distance from outer tensile face of beam to neutral axis in x direction in uncracked section (<i>mm</i>)
c_y	Distance from outer tensile face of beam to neutral axis in y direction (<i>mm</i>)
D	Overall depth of beam (<i>mm</i>)
d	$D-t_f$ (<i>mm</i>)
d_b	$D-2t_f$ (<i>mm</i>)
d_c	$D-c$. (<i>mm</i>)
D_y	Single term for EI
E	Tensile modulus (<i>MPa</i>)
E_{cc}	Compression modulus of core material (<i>MPa</i>)
E_{ci}	Longitudinal compressive modulus of laminate i. (<i>MPa</i>)
E_{ct}	Tensile modulus of core material (<i>MPa</i>)
E_f	Modulus of fibres (<i>MPa</i>)
E_f	Young's modulus of the flange (<i>MPa</i>)
E_m	Modulus of matrix (<i>MPa</i>)
E_p	Modulus of ply (<i>MPa</i>)
E_{tci}	Transverse compressive modulus of the laminate i. (<i>MPa</i>)
E_{ti}	Longitudinal tensile modulus of laminate i (<i>MPa</i>)
E_{titi}	Transverse tensile modulus of the laminate i. (<i>MPa</i>)
E_w	Young's modulus of Web
F	Longitudinal force in flange (<i>N</i>)

FE	Finite Element
FEA	Finite Element Analysis
F_i	Longitudinal force in laminate i. (N)
FRP	Fibre-Reinforced Polymer
F_w	Transverse compressive force in web (N)
F_{wc}	Compressive crushing capacity in webs (N)
F_{wc}	Transverse compressive capacity of web (N)
G	Shear modulus (MPa)
GFRP	Glass fibre-reinforced polymer
G_i	Shear modulus of laminate i (MPa)
I	Second moment of area about x axis (mm^4)
I_c	Second moment of area about x axis in cracked section (mm^4)
I_f	Second moment of area of flange about the z axis
I_u	Second moment of area about x axis in un-cracked section (mm^4)
I_w	Second moment of area of web about the z axis
I_{warp}	Warping constant of the beam
I_y	Second moment of area about y axis (mm^4)
J	Torsion Constant
k	Timoshenko shear adjustment factor
k_1	Compression buckling factor
k_2	Plate buckling factor
k_3	Shear correction factor
L	Span of beam specimen (mm)
L_{ef}	Effective buckling length (mm)
L_i	Laminate i.
M	Bending Moment ($N.mm$)
M_f	Bending Moment at failure ($N.mm$)
n_i	Number of plies in laminate i.
P	Buckling load (N)
P_{cr}	Critical buckling load (N)
R	Radius of curvature (mm)
RC	Reinforced Concrete
RHS	Rectangular Hollow Section
S	Ratio of fibres within a laminate aligned in the direction of force applied
t_f	Overall thickness of flange. (mm)
t_i	Thickness of laminate i. (mm)
t_{pi}	Thickness of ply in laminate i (mm)
t_{ti}	Transformed thickness of laminate i for y-axis properties.
t_w	Overall width of web (mm)
u	x-axis displacement of a plate (mm)
v	y-axis displacement of a plate (mm)
V^*	Shear force on beam (N)
W	Overall width of beam (mm)
w	z-axis displacement of a plate (mm)

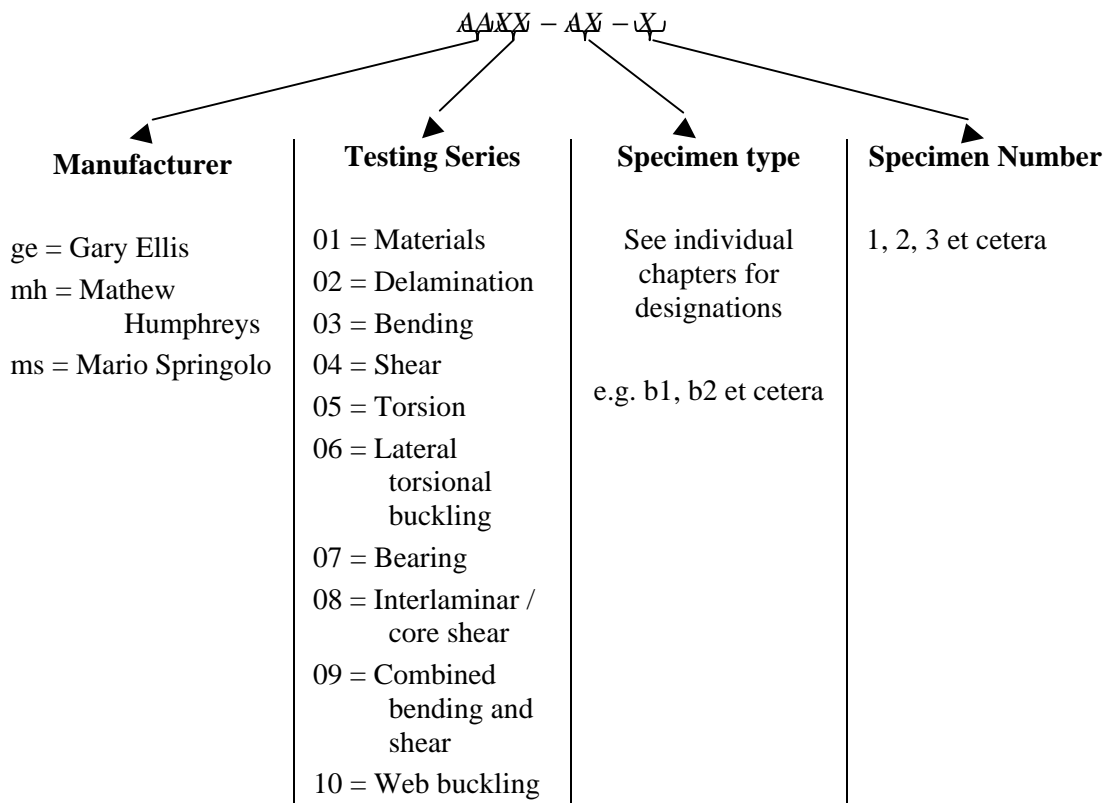
- w_c $W-c_y$ (mm)
- w_i Width of laminate i. (mm)
- w_{ii} Transformed width for laminate i for x-axis properties.
- Z Section modulus (mm^3)

Units

- ° Degrees Celsius ($^{\circ}C$)
- mm** Micrometer
- GPa** Giga Pascals
- kg** Kilograms
- mm** Millimetres
- MPa** Mega Pascals
- N** Newtons
- Pa** Pascals

Specimen designation

The testing specimens used for this study were designated as follows:



1.1 Introduction

As structural elements, beams are widely used in civil infrastructure. For fibre-reinforced polymer (FRP) beams to gain wide acceptance in this field, they must display satisfactory and predictable performance under load. However, according to the current state of the art, criteria for such performance are yet to be achieved. Indeed, as will be detailed in subsequent chapters, current FRP beam designs are known to suffer from second-order failures such as flange and web buckling, and delamination of laminates. Therefore, the focus of this study is to develop and test a fibre-reinforced beam that is less sensitive to these second-order failures. The project is a logical progression of work undertaken by the Fibre Composites Design and Development centre (FCDD) at the University of Southern Queensland, involving FRP use in Civil infrastructure.

1.2 Background

It was not until the 1940's that major developments were made in resin and fibre technology; these developments made the materials feasible for wide-scale manufacture and use. Unlike more traditional materials, such as timber, steel, and concrete, fibre-reinforced polymers (often referred to as fibre-composite materials) combine good tailorable mechanical properties with increased fatigue performance, resistance to chemical attack, high strength-to-weight ratio, and electromagnetic transparency. This wide range of advantages has made FRPs attractive for use in a number of industries. The largest user of FRP materials is the recreational boat-building industry. The invention of cheap, easily-cured resins and glass fibre mats replaced timber, which suffers from biological attack. Subsequently, maintenance costs associated with owning and running an FRP-constructed boat are substantially lower than those of a timber boat. Moreover, major technology improvements in FRP quality and performance have been facilitated by military developments (Ballinger 1992). The high strength-to-weight ratio, fatigue resistance, and electromagnetic transparency of FRPs make them extremely attractive for use in aircraft, missiles and rockets. FRPs can be considered as 'smart materials' (Gandhi & Thompson 1992), since they can be tailored for a specific application and have the ability to change overall shape under loadings if designed and manufactured to do so. Unsymmetrical laminates that change their profile when loaded are of great benefit for use – with aircraft, in particular – on control surfaces such as wings. Most of the military applications were developed by private aviation companies to meet military objectives. According to

Milkovich (1994), the military and space industries demand for composites technology is insufficient to support an adequate composite industry. Therefore, current suppliers need to develop substantial markets in non-military and space areas. For this to occur, the civilian areas of applications must provide a large market, and this can only be fulfilled through the incorporation of FRPs into civil engineering systems.

1.3 Application of FRP in civil engineering systems

The use of FRPs within civil engineering systems has been discussed in articles by Chambers (1991), Bank, Mosallam & McCoy (1994), Van Erp (1999a) and Karbhari (2000). These authors have highlighted two fields of application of FRPs: the repair of existing structures and the construction of new structures incorporating FRPs as part of the primary structural system. Added to these applications is renewed interest in integrated 'Intelligent' systems, which alludes to the potential of FRP materials and systems for use in civil engineering structures (Anon, *Journal of Intelligent Material Systems and Structures* 1995; Gandhi & Thompson 1992; Lee, Lee & Yun 1995).

In the field of rehabilitation and strengthening of existing structures, including repair to damage caused by seismic vibrations, FRPs have an immense potential (Karbhari 2000). FRPs can be bonded to the surfaces of structural members, bridging cracks in concrete to provide extra load-carrying material and thereby restoring or increasing the structural members' capacity to withstand loadings. Columns can be wrapped with FRP to provide total constraint of the concrete, thereby increasing the capacity of the column to withstand static and dynamic loadings. This added material, whilst increasing the capacity of the structure, adds little extra dead-loading or volume to the existing structure. Minimisation of extra dead-loading is of vital importance to avoid the necessity of strengthening other parts of a structure to compensate for the extra dead-weight added (Darby 1999). A notable application is in the strengthening of bridges. The application of externally-bonded plates to an existing bridge can increase the allowable vehicle weights and traffic volume (Oehlers 2000; Taljsten 2001). The repair and maintenance of existing infrastructure is of particular relevance, worldwide, since there is a significantly large number of structures that are reaching the end of their original design life and are in need of replacement or repair (Dunker, Klaiber & Sanders 1987; IEAust 2000; Yates & Jackson 2001).

The second field of application of FRP is in innovative structural systems, mainly in bridge design and construction. There are many advantages in this form of bridge construction because of the reduced weight, which results in savings on materials and costs

of abutment and foundation works, as well as reductions in transportation and crane costs. The bridges also have the advantages of being resistant to environmental and biological attack, which results in reduced life-cycle costs (Karbhari et al. 2000). Furthermore, composite bridges possess good vibrational dampening characteristics. A number of innovative bridges using FRP have already been constructed. For example, Figure 1.1 shows a pedestrian cable stay bridge. The use of FRP cables in long span cable-stay bridges was shown by Meier (2000) to be not only structurally advantageous, due to the FRPs lower mass, but also economically competitive when compared to conventional steel cable systems.



Figure 1.1 FRP pedestrian cable stay bridge across the River Tay in Aberfeldy, Scotland (Barbero 1998)

The use of FRP in bridges is not limited to cables, Figure 1.2 shows an 18 m pedestrian I-girder bridge that was designed and manufactured by Harik et al. (Ashland Chemical Company 1997; Harik et al. 1996). This bridge was made of beams consisting of glass and carbon fibres designed in accordance with the official requirements of the American Association of State Highway and Transportation. Figure 1.3 shows Parson's Bridge, Ceredigion mid-Wales. FRP vehicular bridges have also been built throughout the world. For example, pictured in Figure 1.4 is a bridge in the state of Ohio USA. Figure 1.5 shows

the first FRP vehicular bridge in Australia, being tested by the University of Southern Queensland. It is hoped that this innovative bridge concept will be the answer to the replacement of around 500 timber bridges in Queensland (Fenwick 2002). Based on this successful design, a second bridge will be constructed for the Road and Traffic Authority and located in northern NSW. Further examples of FRP bridges could be found in (Meier 1991).



Figure 1.2 Pedestrian bridge
(Ashland Chemical Company 1997)



Figure 1.4 Vehicular bridge in the
City of Hamilton, Butler County, Ohio
(iCivil)

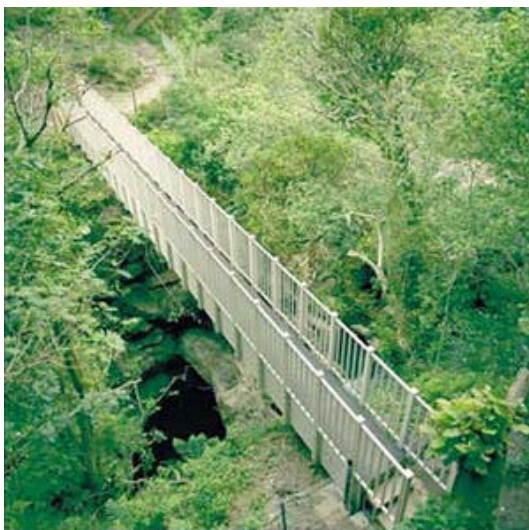


Figure 1.3 Parson's Bridge,
Ceredigion mid-Wales (Strongwell Ltd.
2002)



Figure 1.5 Ten metre vehicular
bridge undergoing testing in Toowoomba,
Queensland

Most of the existing bridges, including the previously mentioned bridges, use beams as the major component of the structural system. Initial designs of FRP beams resemble existing steel sections (Kabir & Sherbourne 1998). However, these beams suffered premature failures due to delamination of laminates around corners, and flange and web buckling. New concepts were developed, such as hybrid FRP-concrete beams (Deskovic, Triantafillou & Meier 1995). Albeit the likelihood of flange buckling was reduced, these

new concepts caused other structural integrity problems such as interfacial bond failure between the FRP and concrete. Concrete was replaced by polymer concrete in a new beam design (Van Erp 1999b). Interfacial bond delamination did not precipitate bending failure with this new concept. However other issues became apparent such as under-reinforcing and delamination of the web laminates under compressive loads. As a possible remedy to these above-mentioned problems, a new design incorporating a polymer based core material is proposed. It is envisaged that this concept will contribute to improving the design of the composite beam.

1.4 Objective of the study

1.4.1 Aim

The objective of this study is to contribute to the development of an FRP beam for use in civil engineering systems. A new beam is proposed and its behaviour is studied to gain a fundamental understanding of its response under load.

1.4.2 Scope

During the course of the study, particular attention will be given to the following:

- review of currently available FRP beam designs;
- review of current analysis methods in use for FRP beam analysis;
- development of a new FRP beam design aimed at overcoming the limitations in existing concepts;
- first and second-order analyses, using analytical methods based on classical beam theory, combined with the use of a transformed section in order to develop a rigorous testing regime;
- formulation of an integrated numerical analysis of the beam behaviour using non-linear finite element analysis;
- manufacturing beams for testing;
- testing of beams to observe their behaviour and failure modes;
- discussions of observed behaviours; and
- comparisons between models and experimental results,

to achieve the following outcomes:

- contribute to overcoming the limitations inherent in existing designs for a simply-supported beam in bending;
- provide a fundamental understanding of the structural behaviour of the new beam through experimental testing and identification of the failure modes;
- develop computationally efficient, simplified methods to model the behaviour of the new beam; and
- determine whether the behaviour of the new beam conforms to the underlying principles of classical beam theory and the use of a transformed section, by comparing experimental results with model predictions.

Of course, the first step in assessing the viability of the newly proposed beam involves observing its behaviour as a single-span simply-supported beam. Such an arrangement induces a number of loading types throughout the beam. These loading types were identified as pure bending, shear, the combination of bending and shear, lateral torsional buckling, bearing, and the application of sustained loads. As these constitute a broad area of investigation, the investigations into each area were conducted to a limited detail. All these areas could, in themselves, constitute entire doctoral studies. However, this broader approach was taken in order to ascertain the validity of the new beam so that the fundamentals of the beam behaviour could be established, providing a base from which further research could continue. As a result of this adopted broad approach, the following issues are beyond the scope of this study:

- material properties and characterisation, short and long-term;
- dynamic effects and responses;
- cyclic loading and their effects upon the beam responses;
- durability and environmental effects;
- effect of changes to end conditions and number of spans; and
- size and geometry effects.

1.5 Layout of the Thesis

The dissertation consists of nine Chapters. Chapter 1 introduces the subject, discusses current usage of FRP, identifies their potential in infrastructure applications, and presents the objectives of the thesis. Chapter 2 provides an overview of FRP materials and manufacturing techniques. It is not intended as a detailed literature review of this continually improving area, but rather as a summary of commonly used materials and manufacturing techniques. In Chapter 3 currently available FRP beam cross-sections are

presented along with the latest developments. The advantages and limitations of these developments are also discussed. The present understanding of FRP beam behaviour is reviewed in Chapter 4. In particular, the contradictions and limitations of existing analysis and design methods are identified.

The main body of the dissertation lies within Chapter 5 through to Chapter 8. The generic form of the FRP beams investigated in this study is introduced in Chapter 5. Based on the identified limitations of FRP beam designs discussed in the literature review, a new design for a beam is presented. The design includes the development of the shape, the determination of the overall dimensions, selection of materials and manufacturing techniques. Chapter 6 through to Chapter 8 respectively discuss the theoretical analysis, experimental program, and the finite-element analysis (FEA). Results from the experiments are respectively compared against the theoretical and FEA in Chapter 7 and Chapter 8. In Chapter 6 the behaviour of the beam in bending, shear, combined loadings, lateral torsional buckling, bearing, and long-term loading is investigated. In the author's opinion, such an arrangement within each chapter is justified by the fact that failure modes under these loading arrangements are equally important for a successful design. Furthermore, it is customary in codes of practice to write guidelines separately for bending, shear, combined loadings, lateral torsional buckling, bearing and creep.

Finally, in Chapter 9 the summary of the concluding remarks is given together with recommendations for extending the work carried out in this thesis.

References

- Anon, *Journal of Intelligent Material Systems and Structures* 1995, 'Rebuilding and enhancing the nation's infrastructure: A role for intelligent systems and structures', vol. 6, no. 1, pp. 4 - 12
- Ashland Chemical Company 1997, *Hybrid composite beams used in park bridge*, Available: [<http://www.ashchem.com/comm/WI97/one.asp>] (Winter 1997).
- Ballinger, C. A. 1992, 'Advanced composites in the construction industry', in *37th International SAMPE symposium and exhibition*, SAMPE, Anaheim, CA, USA, pp. 1 - 14.
- Bank, L. C., Mosallam, A. S. & McCoy, G. T. 1994, 'Design and performance of connections for pultruded frame structures', *Journal of Reinforced Plastics and Composites*, vol. 13, pp. 199-212.

- Barbero, E. J. 1998, 'Construction', in *Handbook of Composites*, ed. S. T. Peters, Chapman & Hall, London, pp. 982-1003.
- Chambers, R. E. 1991, '21st Century composites require ASCE standards and SDS', *Workshop on Advanced Composites for Offshore Structures*, vol. October 30-31, pp. 56-72.
- Darby, J. J. 1999, 'Role of bonded fibre-reinforced composites in strengthening of structures', in *Strengthening of Reinforced Concrete Structures*, eds. L. C. Hollaway & M. B. Leeming, Woodhead Publishing Ltd, CRC Press LLC, Cornwall, England, pp. 1-10.
- Deskovic, N., Triantafillou, T. C. & Meier, U. 1995, 'Innovative design of FRP combined with concrete: Short-term behavior', *Journal of Structural Engineering*, vol. July, pp. 1069 - 1077.
- Dunker, K. F., Klaiber, F. W. & Sanders, W. W. 1987, *Bridge strengthening needs in the United States*, Iowa State University, Iowa.
- Fenwick, J. 2002, *Managing the Bridge Network in Queensland*, Available: [<http://www.eng.nus.edu.sg/civil/whatsnew/announcement/seminar/02112002.html>].
- Gandhi, M. V. & Thompson, B. S. 1992, *Smart materials and structures*, Chapman & Hall, London.
- Harik, I. E., Szak, P. J., Robson, B. N., Hopwood, T. H., Witcher, D. & Brailsford, B. 1996, 'Hybrid Composite I-girder pedestrian bridge', in *28th International SAMPE Technical Conference*.
- iCivil, *Tech21 Composite bridge installation*, Available: [<http://www.engr.udayton.edu/faculty/dfarhey/t222.jpg>].
- IEAust 2000, *A report card on the nation's infrastructure*, Institution of Engineers, Australia, Barton ACT.
- Kabir, M. Z. & Sherbourne, A. N. 1998, 'Lateral-Torsional Buckling of Post-Local Buckled Fibrous Composite Beams', *Journal of Engineering Mechanics*, vol. 124, no. 7, pp. 754 - 764.
- Karbhari, V. M. 2000, 'FRP Composites for Infrastructure Renewal - Status and Challenges for the 21st Century', in *ACUN-2*, eds. S. Bandyopadhyay et al., University of New South Wales, Sydney, Australia, pp. 51-60.
- Karbhari, V. M., Seible, F., Bugueno, R., Davol, A., Wernli, M. & Zhao, L. 2000, 'Structural Characterization of fibre-reinforced composite short- and medium-span bridge systems', *Applied Composite Materials*, vol. 7, no. 2, pp. 151-182.
- Lee, D. C., Lee, J. J. & Yun, S. J. 1995, 'Mechanical characteristics of smart structures with embedded optical fiber sensors', *Composite Structures*, vol. 32, no. 1-4, pp. 39 - 50.
- Meier, U. 1991, *Case histories: Advanced composite materials with application to bridges*, CSCE, Switzerland.

- Meier, U. 2000, 'Composite Materials in Bridge Repair', *Applied Composite Materials*, vol. 7, pp. 75-94.
- Milkovich, S. 1994, *Infrastructure Applications of Composite Materials*, Available: [<http://iti.acns.nwu.edu/projects/milk.html>].
- Oehlers, D. J. 2000, 'Development of Design Rules for Retrofitting by Adhesive Bonding or Bolting either FRP or Steel Plates to RC Beams in Bridges and Buildings.' in *Composites in the Transportation Industry*, eds. S. Bandyopadhyay et al., University of New South Wales, Sydney, Australia, pp. 110 - 119.
- Strongwell Ltd. 2002, *Special market products*, Available: [<http://www.strongwell.com/Special/bridges.htm>].
- Taljsten, B. 2001, 'Full Scale Test of Structures Strengthen with CFRP Strengthening of a Railroad Bridge', in *ACUN-3*, eds. S. Bandyopadhyay, N. Gowripalan & N. Drayton, University of New South Wales, Sydney, Australia, pp. 54-65.
- Van Erp, G. M. 1999a, 'Design and Analysis of Fibre Composite Beams for Civil Engineering Applications.' in *Composites: Innovations and Structural Applications*, eds. S. Bandyopadhyay et al., University of New South Wales, Sydney, Australia, pp. 229 - 238.
- Van Erp, G. M. 1999b, 'A New Fibre Composite Beam for Civil Engineering Applications', *Composites Fabrication Journal*, vol. July, pp. 30 - 33.
- Yates, A. & Jackson, R. 2001, 'Crumbling infrastructure needs urgent funding', In *Engineers Australia*, 73 Vol., Institution of Engineers, Australia, pp. 26 - 29.

Chapter 2 Overview of fibre-reinforced polymer materials and their manufacture

2.1 Introduction

Many books have been published describing fibre-reinforced polymers (FRP) and their manufacture (Gibson 1994; Hancox 1981; Harper 2000; Jones 1975; Mallick 1993; Nielson & Landel 1994; Norwood 1994; Potter 1997; Powell 1994; Schwartz 1992; Strong 2000; Swanson 1997). Each of these authors presents the subject giving terminology and definitions from their own perspective. A great variety in terminology and definitions abounds. In order to avoid confusion, the materials, terminology and manufacturing techniques used throughout this thesis are described in this Chapter.

2.2 Background

Fibre-reinforced polymers are specific to the group of materials referred to as composite materials. A composite material is one that consists of two or more distinct constituents - which differ in form and / or material composition - that are essentially insoluble in (and complementing) each other. Usually one plays the role of the reinforcement, thus conferring to the composite the desired mechanical and / or thermal properties, and the other, the body constituent (matrix), serves to enclose the composite and give it its bulk form. The performance of the composite material is higher than those of the constituents taken separately. Sometimes a third material is needed to serve as a bonding agent between the matrix and the reinforcement. This arrangement is schematically represented in Figure 2.1.

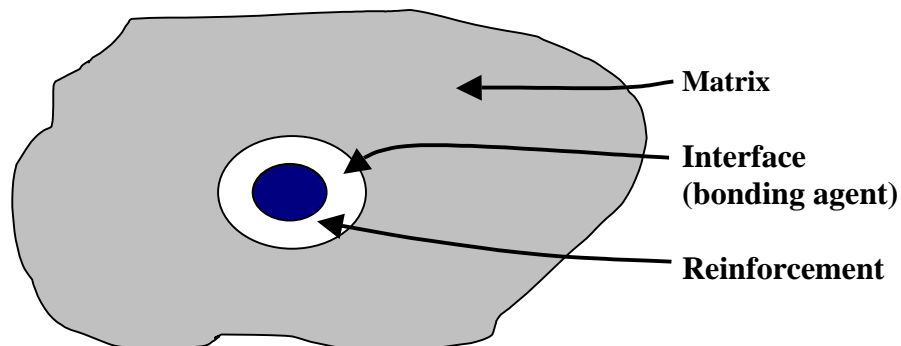


Figure 2.1 Reinforcement – matrix interface

Depending on the sought-after properties, there is an endless combination of matrix–reinforcement. Most of the time the matrix is of organic nature, made out of some polymer (plastic) material. However, these are not suitable for high temperature performances. In this case an inorganic matrix made out of metal or ceramics is mostly used. Like the matrix, the reinforcement can be organic or inorganic in nature and usually comes in the form of flakes, particles, or fibres, Figure 2.2.

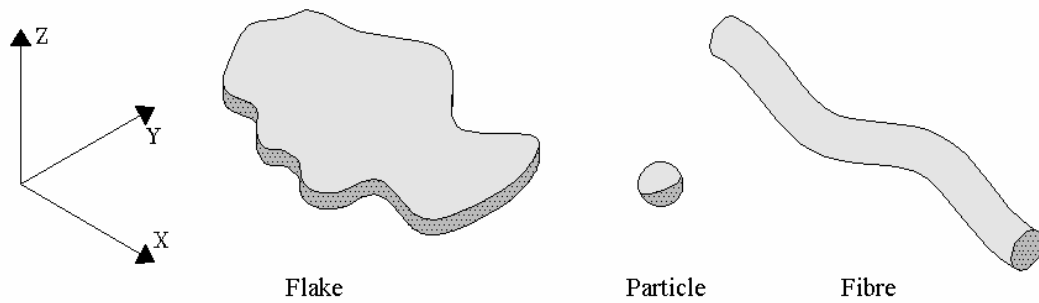


Figure 2.2 Forms of reinforcement (not to scale)

The composite material may be manufactured in a bulk or laminar form with any combination of reinforcement types. However, from a structural point of view, the use of fibre reinforcement provides the best mechanical properties. Fibre composite materials also occur in nature and can be produced from natural materials. For example, timber is a fibrous composite consisting of cellulose fibres and lignin. However, this study will concentrate upon synthetic fibre composites that are referred to as fibre-reinforced polymers.

2.3 Constituents of fibre-reinforced polymers

The manufacture of resins and fibres developed independently until the 1940's. The first resins, patented in 1899, were synthetic polymers that required heat and pressure to cure. These materials were found to have low tensile strength and exhibited a brittle failure mode. It was discovered that the inclusion of reinforcing materials such as cloth, wood pulp, and asbestos fibres significantly enhanced the mechanical properties. The first mass produced product from these new materials was an electrical insulating product called Bakelite (phenol-formaldehyde resin with linen fibre). More widespread use of fibre composites did not occur until after the first ambient cure resin was patented in 1936 (polyester resin). The first well-known epoxy resin (Araldite) was patented in 1938.

The early fibres were derivations of those used in the textile industry and their mechanical properties were poor. The first major breakthrough in reinforcements came in

1932 with the production of high quality glass fibres. Initially these fibres were manufactured for insulation purposes. Adaptation of textile weaving machinery led to the development of glass fibre mats. In 1941 a surface treatment technology was developed that allowed for the mechanical bonding of the resins to the glass fibres. This significantly improved the performance of FRP (Owens Corning 1998).

With the development of an ambient cure resin, the production of high quality fibres, and the introduction of bonding agents, a new generation of structural materials was created. Subsequent to World War II, with the introduction of the jet engine requiring even lighter materials, a large variety of resin formulations and fibre types were introduced. For instance, the last fifty years have seen the introduction of resins such as polyether ether ketone (1982) and fibres manufactured from boron (early 1960), carbon, and aramid (late 1960's) (Owens Corning 1998).

The following sections will describe the matrix and fibre constituents.

2.3.1 Matrix

2.3.1.1 General

While reinforcing fibres have high modulus and strength in the direction of their longitudinal axis, they have no effective compressive or shear capacity unless confined. Matrix materials confine the fibres to provide the bulk form of an FRP. The matrix distributes loads between fibres and greatly influences the shear, chemical resistance, durability, and flammability characteristics of the FRP. Matrix materials are often referred to as resins. Inorganic matrices provide high temperature and high abrasion performances, but they are very expensive. Organic matrices, conversely, are cheaper, possess good chemical properties and excellent specific mechanical characteristics. They are generally capable of withstanding temperatures up to 150 degrees to a maximum of 300 °C (Hull & Clyne 1996). Organic resins are therefore of more interest for civil engineering applications. These resins are often classified into two types: thermosetting or thermoplastic resins.

2.3.1.2 Thermosetting

Thermosetting resins are the most widely used matrices. They come in the form of polymer strands in suspension in a solution, to avoid cross-linking between the pre-polymerised macromolecules. The principal kinds are unsaturated polyesters, epoxydes, vinyl-esters, polyimides, phenolics and furanes. Of these matrices, polyester, epoxyde and

vinyl-ester are the three most common resins used in civil engineering systems and their respective properties are shown in Table 2.1.

Table 2.1 Typical Properties of Cast Thermosets (at 23 °C) compiled from Fibre Composite Design and Development Group 1997; Hull & Clyne 1996

	Unsaturated polyesters	Epoxydes	Vinyl-ester
<i>Density (kg/m³)</i>	1100 - 1400	1200 - 1300	1120 - 1320
<i>Tensile strength (MPa)</i>	34.5 – 103.5	55 - 130	73 - 81
<i>Tensile modulus (GPa)</i>	2.1 - 3.45	2.75 - 4.1	3 - 3.5
<i>Poisson's ratio</i>	0.2 - 0.3	0.2 - 0.33	0.2 - 0.3
<i>Elongation (%)</i>	1 - 5	4 - 8	3.5 - 5.5
<i>Coefficient of thermal expansion (10⁻⁶ m/m/°C)</i>	30.9 - 60	50 - 80	52.6 - 64.8
<i>Heat Distortion Temperature (°C)</i>	60 - 205	50 - 300	93 - 135
<i>Cure shrinkage (%)</i>	8 - 12	0.5 - 2	5.4 - 10
<i>Approximate Cost (\$/kg)</i>	3 - 4	10 - 12	6 - 8

Unsaturated polyesters

Unsaturated polyesters are widely used in the manufacture of composite materials. Their popularity is due to their low cost as well as an easily automated production process (Berthelot 1992). They offer other advantages such as good dimensional stability, good wetting and penetrating ability of the fibres, and good chemical resistance to hydrocarbons. However, they have low resistance to shocks and a high cure-shrinkage (about 8 to 12 %). They are degraded by ultra-violet light and attacked by water vapour with a high risk of hydrolysis. They burn easily and require fire retardation or external protection when used in fire-prone areas.

The typical polyester consists of an unsaturated polyester resin, which is dissolved with a monomer in a substance such as styrene. The polyester matrix is formed by the chemical reaction of the polyester resin and the monomer, via the use of a catalyst. Curing time is dependent upon the decomposition rate of the catalyst. Temperature plays an important part in this process. However, increasing the temperature above the recommended optimum temperature can cause wasteful side-reactions to occur. Styrene is the most commonly-used solvent for polyester resins and, when used, the liquid polyester presents a

fire risk and is a suspected carcinogenic. Therefore, appropriate safety procedures should be implemented when using polyester resins.

Epoxydes

After unsaturated polyesters, epoxyde resins are the most widely used. They have a relatively high working temperature of up to 300 °C, and very good mechanical properties. They possess: excellent chemical resistance, environmental stability, low shrinkage (0.5 to 2 %), a good wetting and penetrating ability of the fibres and an excellent adherence to metallic materials. Indeed, due to good bonding characteristics, epoxy resins are the most commonly used matrix for carbon fibre composites (Rebouillat et al. 1998, p. 478). However, a long cure time, a high cost and a low resistance to shocks also characterise them.

Epoxydes resins come in two parts - the resin and a hardener. The hardener forms part of the chemical reaction to form the matrix. Therefore, the choice of, and the amount of, hardener used affect the characteristics of the matrix. The chemical reaction is exothermic and can be accelerated by heating.

Vinyl-ester

Vinyl-ester resins are obtained by the addition of an epoxide to acrylic acid. They are similar to polyester in that a catalyst initiates the chemical reaction. The difference is in the unsaturated vinyl-ester resin, which contains fewer double bonds. The reduction in the amount of double bonds results in a matrix material that is more flexible and has higher impact toughness than polyester. Another difference is that the presence of hydroxyl groups along the molecule's length makes vinyl-ester resins bond well to glass. They have a low absorption of moisture and exhibit a resistance to alkali environment better than that of polyesters. However, vinyl-ester resins have relatively high cure shrinkage and are marginally dearer than polyester resins.

Other thermosetting resins

A large number of matrix materials has been, and continue to be, formulated for specific applications (Harper 2000). These applications are primarily in the aerospace industry where particular performances are desired. For example, the polyamides are a range of specialist thermosets for use in high temperature applications. As such, they are expensive and do not offer significant advantages over the existing thermosetting resins currently used in civil engineering applications.

2.3.1.3 Thermoplastics

Thermoplastics include a wide range of polymers. Some of them, such as polyethylene, polypropylene, polysulphone, polyacetal, polyethersulphone, polymethylmethacrylate and polystyrene, have been used as matrix materials. They are easy to manufacture and the raw materials are readily available. However, their high viscosity at low temperatures renders composite manufacture extremely difficult because of poor infiltration and wetting of the fibres (Hancox 1983). Compared to thermosetting resins, they have low mechanical and thermo-mechanical properties (Berthelot 1992). These resins are initially in solid form, usually in beads. They are melted and introduced to the fibres under high pressure. The resin can be re-melted. This characteristic makes thermal moulding possible. Thermal-moulding techniques are used for the mass production of vehicle body panels, manufacture of chemical containers, and for aerospace components. Due to their poor properties, the use of these resins is limited to non-structural applications within the civil engineering field. Table 2.2 lists the properties of common thermoplastics.

Table 2.2 Typical properties of cast thermoplastics at 23°C (t=tensile, y=yield)

	PEEK	PPS	PSUL	PEI	PMR-15
<i>Density (kg/m³)</i>	1300–1320	1360	1240	1270	1400
<i>Tensile strength (MPa)</i>	100y	82.7t	70.3y	105y	185.5t
<i>Tensile modulus (GPa)</i>	3.24	3.3	2.48	3	3.03
<i>Poisson's ratio</i>	0.4	0.36	0.37	0.37	0.36
<i>Elongation at fail (%)</i>	50	4	75	60	12
<i>Coefficient of thermal expansion (10⁻⁶ m/m/°C)</i>	47	49	56	56	36
<i>Heat Distortion Temperature (°C)</i>	160	135	174	200	274

2.3.2 Fibres

2.3.2.1 General

Fibres are thin long cylinders of material, which are similar in appearance to human hair. The diameter of fibres used in FRP is typically between 5 – 14 *mm*. The mechanical properties of fibres differ from the bulk material from which the fibres are manufactured. Alignment of their molecules is better and surface flaws are reduced, subsequently fibres have a higher tensile strength and elastic modulus than the bulk material. Fibres, like resins,

can be inorganic or organic. Table 2.3 lists the properties of a number of fibre types used in composites industries. Glass, carbon and aramid fibres are the most widely used fibres for civil engineering applications.

Table 2.3 Properties of typical fibres (Bishop 1989; Hanson 1987)

<i>Fibre</i>		<i>Diameter (mm)</i>	<i>Density (kg/m³)</i>	<i>Tensile Strength (GPa)</i>	<i>Tensile Modulus (GPa)</i>	
Inorganic	Glass	E-Glass	8 - 14	2540	3.45	72.4
		S-Glass	8 - 14	2490	4.58	86.2
	Silicon Carbide (ceramic)		100 - 150	3190	1.52	483
Organic	Carbon	HS Carbon, T300	7	1760	3.53	230
		AS4 Carbon	7	1800	4	228
		IM7 Carbon	5	1800	5.41	276
		GY80 Carbon	8.4	1960	1.86	572
	Aramid (Kevlar 49[®])		12	1440	3.62	130
	Boron		20 - 50	2600	3.44	407
	Polyethylene		10 - 12	970	2.7	87

2.3.2.2 Inorganic

The choice of materials for inorganic fibres is wide. It includes glass, metals, ceramics and refractory material. However, the most widely-used inorganic fibre is glass; it is also the cheapest of all man-made fibres. Glass fibres are manufactured in four categories: S-Glass (high strength); E-Glass (electrical); ECR-Glass (chemical resistant); and C-Glass (chemical resistant). E-Glass is the weakest of the four. However, it is the most popular because of its affordability. At approximately \$10/kg, it is three to four times cheaper than S-Glass, which is the next cheapest grade. When compared with carbon and aramid, glass fibres have the lowest tensile strength and modulus. Glass fibres are used in recreational boating, insulation bats, car body parts, radar cones for aircraft and submarines, helicopter blades and many other applications. One major disadvantage of glass fibres is their susceptibility to a reduction in strength under long-term static loading, known as creep rupture. The fibres fail because stress corrosion starts at minute imperfections in the fibres. The imperfections are largely attributed to the manufacturing process.

2.3.2.3 Organic

Organic fibres are characterised by a low specific gravity and they are usually used in weight-critical applications. Two types of fibres are usually employed in structural applications: carbon (graphite) and aramid.

Carbon

Although graphite exists naturally, the one used in manufacturing composite materials is artificially made. There are two methods of production: one is from organic precursor fibres such as rayon, PAN (polyacrylonitrile) and pitch, the other is from gas growth (also known as vapour growth) (Bahl et al. 1998). Carbon fibres are supplied in various grades. Unlike most organic materials, carbon fibres perform well at elevated temperature. They have good property retention up to 1500 °C. However, if unprotected, they oxidise in air at 427 °C. They possess high tensile modulus, strength, and fatigue performance, all combined with a lower density than that of glass fibres. Carbon fibres are not susceptible to creep rupture. However they are expensive (approximately \$50/kg for the least expensive types) when compared with glass. This has limited their use to specialised applications and critical placement. The different grades available vary in properties, with the variation depending upon the manufacturing process and the purity of the fibres. Carbon fibres are widely used in the aerospace industry, racing vehicles and sporting goods.

Aramid

Aramid fibres are produced from an aromatic polyamide and they are characterised by their high specific strength. Five varieties of aramid fibres are currently produced commercially. These are sold under the trade names Kevlar[®], Twaron[®] and Technora[®]. They have similar strengths but different elastic moduli. Aramid fibres also have exceptional energy absorption characteristics and a non-linear compressive behaviour. However, they are made up of numerous microfilaments, which cause the compressive and transverse strengths to be poor. Furthermore, the fibres have a tendency to absorb moisture, degrade under ultraviolet light, and have a higher creep rate than glass fibres. The bonding of the fibres to matrix materials is not as good as that of glass or carbon. The fibres are often used in place of glass for an increase in short-term strength and stiffness. They are also used for protective clothing, such as bulletproof vests and military helmets.

Other fibres

Boron fibres were the original fibres used in the aerospace industry. Their continued high cost compared to carbon fibre has reduced the use of boron to that of specialised applications. A further example is polyethylene. It combines high strength with low weight

(lighter than water). However, adhesion to matrix materials is poor and has limited the applications for these fibres to within the textile industry primarily. Further developments in fibre technology have resulted in the production of new ranges of fibres to increase the choice and adaptability of FRP.

2.3.2.4 Fibre forms for use in FRP

After manufacture, fibres are stored on spools in strands of a number of fibres. The individual strand is termed a 'tow' or 'roving'. A tow is classified by the weight in grams per length in kilometres. The strands used in FRP materials are similar in dimension to the threads used in the textile industry and therefore textile-knitting techniques are readily transferable to composite fibres. Certain applications use the tows of fibres to manufacture end products. However further processing of the tows into weaves facilitates use for many other applications. Woven mats come in a variety of forms, which gives the engineer flexibility in design. Each type of mat is available in a variety of masses per square meter. Mats can be manufactured in two and three-dimensional fibre orientations. The main types of two-dimensional mats used in civil applications are discussed below.

Chopped strand (CSM) and Continuous strand (CCSM) mats

A chopped strand mat consists of randomly arranged short thick fibres. The fibres are adhered together with a thinly-applied glue to hold the fibres as a mat until incorporated with resin. Often, the glue has been designed to dissolve when in contact with styrene-based resins, so that it plays no structural role in the completed FRP. Continuous strand mats are similar except that the fibres are continuous. These mats have low tensile strength and modulus due to the random orientation of the fibres. Subsequently, their use is limited to non-critical components and protective layers.

Unidirectional mat (UD)

As the name suggests, these mats have tows running parallel in one direction. There may be minor tows running at 90° to hold the mat together. Figure 2.3 depicts a unidirectional mat. When positioned into a laminate, the mat can be placed in the principal stress direction to take advantage of the fibre properties. These mats are particularly well-suited to pure tension and compression applications.

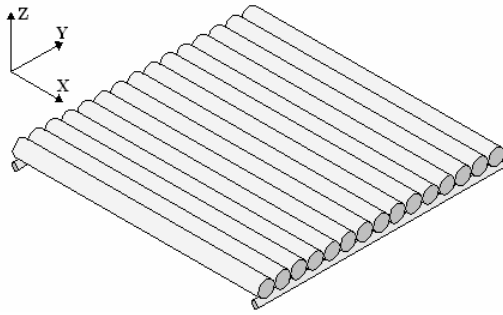


Figure 2.3 Unidirectional mat

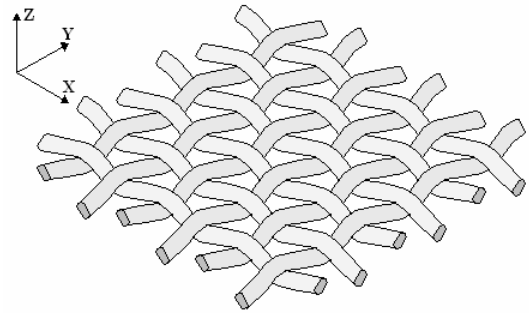


Figure 2.4 Woven roving mat

Woven roving mat (WR)

A woven roving mat has equal numbers of tows perpendicular to each other. These tows are woven over and under the tows in the other direction. Figure 2.4 depicts a woven roving mat. A mat of woven roving is weaker than two layers of UD of the same total weight because the fibres in woven roving are not straight. In compression, these fibres are pre-buckled and in tension, they try to straighten out causing transverse (z-axis on Figure 2.4) stresses at contacts with the perpendicular fibres.

Bi-axial (BA) and Double-bias (DB) mats

Bi-axial and double-bias mats consist of two layers of UD perpendicular to each other. These two layers are fixed together via stitching or glue. Figure 2.5 and Figure 2.6 depict the bi-axial and double-bias mats respectively. Double-bias mat is a bi-axial mat at a 45° orientation.

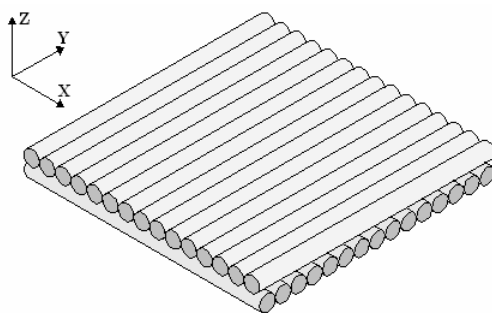


Figure 2.5 Bi-axial mat

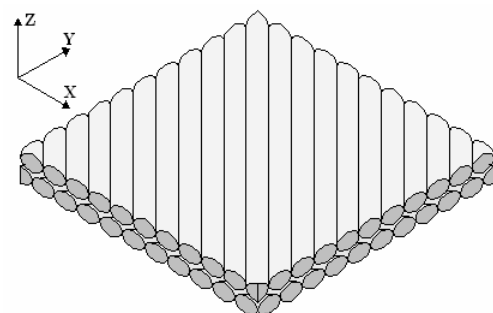


Figure 2.6 Double-bias mat

2.3.2.5 Sizing

Damage of the fibres may result due to manipulation throughout the manufacturing process. A surface coating that protects and lubricates is added to minimise damage.

Furthermore, some matrix materials do not adhere well to particular fibres and therefore, coupling agents are required to ensure a bond. 'Sizing' is the name given to these surface treatments. There are two types of sizes: yarn sizes, which are used in the manufacture of weaves, and roving sizes, which ensure bonding between the fibre and matrix.

Yarn Sizes

The manufacturing processes require the fibres to be rapidly moved through machinery. A sizing is applied to fibres to protect them from damage and make them more workable. Once the mats are made, the sizing is removed by being washed off with a solvent or by heat treatment.

Roving Sizes

Roving size act as a coupling agent between the fibre and the matrix material. Not all fibres require sizing; for example, carbon fibres and epoxy resin are compatible, as both are organic (although the application of a surface treatment to the carbon fibre is recommended because it increases shear strength of the bond (Peng et al. 1998)). However, glass fibres, which are inorganic, require sizing to ensure bonding with the matrix. The type of sizing required will depend upon the fibre, resin, and the intended application. Sizing is applied at the end of the manufacturing process and is usually manufacturer specific. Therefore, consultation with the manufacturer is essential to ensure that the bond required is achieved. Roving sizes are also referred to as 'finishes'.

2.3.3 Filler materials

Filler materials are incorporated into FRPs to provide a cheap and light bulking agent, either to create a core material or within the FRP itself. Some fillers are also added to resin formulations to alter viscosity. The type and amount of filler added will affect the mechanical properties of the FRP. Typical filler materials that have been used with FRP are cotton, wood pulp, talcum powder, sand, glass microspheres, and flyash microspheres. Of these, the last three are considered as suitable for use in civil and structural applications.

2.4 Laminated fibre-reinforced polymers and their properties

When it comes to producing composite components with load-carrying abilities, such as the ones used in civil engineering applications, the most suitable fabrication processes are those based on a layer-by-layer concept. Components produced in this manner use continuous fibres with fibre lengths that are comparable to the overall length of the component itself. They are also the most efficient in terms of stiffness and strength.

A lamina or a ply is a plane or layer of unidirectional fibres or mat in a matrix. The lamina is an orthotropic material with the principal material axis in the direction of the fibres. A laminate is made of two or more laminae or plies stacked together at various orientations. The plies can be of different thicknesses and can consist of different materials. A three-ply laminate is depicted in Figure 2.7. When the laminate is relatively thin, laminate analysis using in-plane properties is appropriate and the cross ply (z-axis in Figure 2.7) properties are usually ignored. Table 2.4 lists the properties of different fibre laminates and Table 2.5 lists the properties of a number of ply types.

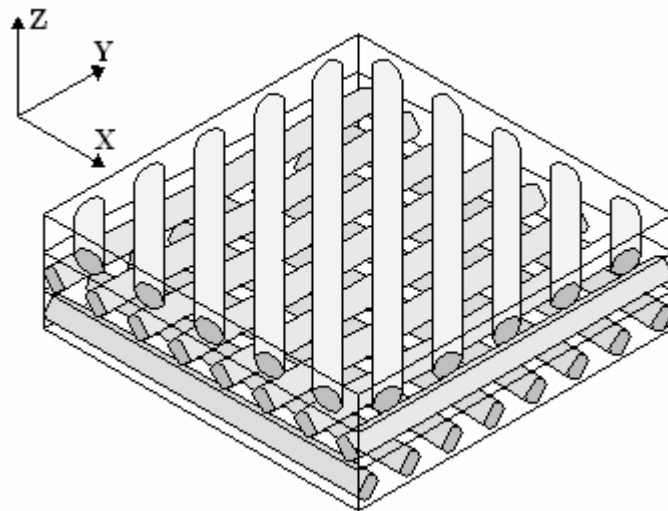


Figure 2.7 Layers of plies that form a laminate

Table 2.4 The properties of FRP laminates, steel, concrete and timber (E. I. duPont de Nemours. 1980; Fiber Science Division of EDO Corp. 1995; Pagano & Hahn 1997; Swanson 1997; Tsai 1986)

<i>Material</i>	Carbon/epoxy AS4/3501-6	Carbon/epoxy T300/5208	Carbon/epoxy G30-500/2431	Boron/epoxy	Kevlar 49/epoxy	E-Glass/epoxy	Steel (for steel sections)	Concrete	Timber (for timber beams)
<i>Modulus E_{11} (GPa)</i>	131	153	129	204	76	38.6	200	25	12
<i>Modulus E_{22} (GPa)</i>	11.2	11.2	8.6	18.5	5.5	8.27	200	25	8
<i>Poisson Ratio ν_{12}</i>	0.28	0.33	0.31	0.23	0.34	0.26	0.27	0.2	0.2-0.4
<i>Shear modulus G_{12} (GPa)</i>	6.55	7.1	4.1	5.59	2.3	4.41	79	10.4	0.61
<i>Tensile strength (MPa)</i>	2280	1524	1210	1490	1380	750	300	2	14
<i>Density (kg/m^3)</i>	1550	1550	1570	1850	1380	1740	7860	2320	900
<i>Specific modulus (MNm/kg)</i>	84.5	98.7	82.2	110	55.1	22.2	25.5	10.8	7.8
<i>Specific strength (kNm/kg)</i>	1470	983	771	805	1000	431	38	1	8.4
<i>Cost* (\$1000/$\text{m}^3$)</i>	100	100	80	277.2	36	20	10	0.125	1
<i>Cost* (\$/kg)</i>	64.51	64.51	50.96	149.84	26.09	11.50	1.27	0.05	1.11
<i>Specific modulus cost* (\$/GNm)</i>	763.50	653.65	619.89	1362.16	473.4	517.75	49.89	4.98	140
<i>Specific strength cost* (\$/MNm)</i>	43.88	65.63	66.11	186.13	26.1	26.66	33.48	53.87	132.27

* Approximates (Fibre Composite Design and Development Group 2002, pers. comm.).

Table 2.5 Properties of E-Glass / West system epoxy (Fibre Composite Design and Development Group 1997)

<i>Allowable Material Properties</i>						
<i>Orientation</i>		UD	WR	DB*	CSM	UD(C)
0°	<i>UTS</i>	588	187	65	98	900
	<i>UCS</i>	372	339	150	150	472
	<i>E</i>	26800	13700	9482	8200	79800
90°	<i>UTS</i>	40	166	65	98	81
	<i>UCS</i>	372	420	150	150	114
	<i>E</i>	10000	12177	9482	8200	4900
-	<i>USS</i>	50	80	146	69	88
	<i>G</i>	4500	3200	8168	2800	4500
	<i>t</i>	0.68	1.35	0.58	0.67	0.51
	<i>Density</i>	1740	1510	1630	1380	1340
	<i>v</i>	0.3	0.1	0.52	0.3	0.1
Where: UD Unidirectional 62.5% glass by weight WR Woven Roving 45% glass by weight DB Double-bias 55% glass by weight CSM Chopped Strand Mat 32% glass by weight, 300g mat UD(C) Unidirectional carbon fibres						
<i>UTS</i> Ultimate tensile strength (<i>MPa</i>) <i>UCS</i> Ultimate compressive strength (<i>MPa</i>) <i>E</i> Modulus of elasticity (<i>MPa</i>) <i>USS</i> Ultimate shear strength (<i>MPa</i>) <i>G</i> Shear modulus (<i>MPa</i>) <i>t</i> Thickness (<i>mm</i>) <i>Density</i> Density (<i>kg/ m³</i>) <i>v</i> Poisson's ratio						

* From (Ellis 2001 pers. comm.)

Considerations for Laminate Lay-up

The consolidation and architecture of a laminate influence the performance of that laminate. Fibres provide the primary resistance to the imposed loads. Higher fibre fractions

result in higher capacity and stiffer sections (for the same cross-sectional area). Fibre fractions up to 60% are still achievable with full adhesion of the fibres and matrix. Additionally, the matrix shrinks when a laminate is laid-up and cured. This shrinkage adds stresses to the laminate and can cause curvature of the plate, if the laminate is not symmetric about its centreline. Other effects on non-symmetric laminates include heat distortion and stress distortion. For these reasons, it is usually best to design laminates to be symmetric - unless distortion effects are desirable.

Laminate terminology

The standard method used to describe the lay-up of laminates is as follows.

- the lay-up is written between square brackets;
- symbols for the different mat types are used. The 'UD' is omitted for unidirectional mats, and the angle in degrees from the global axis is used instead;
- successive plies are separated by a slash '/' if their angle is different
- if the laminate is symmetric, half of the lay-up is written in the brackets and the subscript 'S' is written after the brackets.

The following is an example for designating laminates.

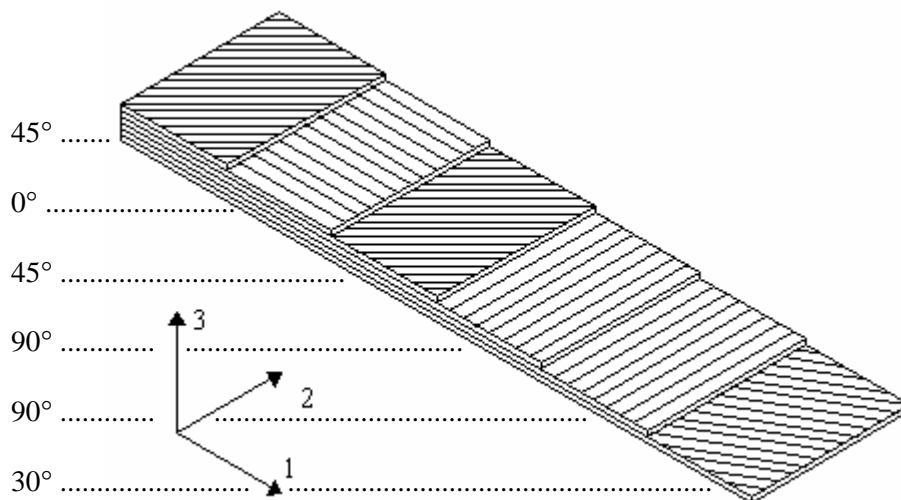


Figure 2.8 Laminate designation [45/0/45/90/90/30]

A further example, where the dash above the 0 represents a single ply, is:

90°

DB

DB

0° = $[90/DB_2/\overset{-}{0}]_s$

DB

DB

90°

2.5 Manufacturing techniques

There are various methods available to produce a completed FRP component. Common manufacturing techniques used in the production of beams include: pultrusion, filament-winding, injection moulding, and laminating by hand or machine lay-up. Laminating and filament-winding may also involve techniques to increase compaction, such as vacuum bagging and autoclave consolidation. These methods are described below.

2.5.1 Pultrusion

Pultrusion is a continuous process for making lightweight linear profiles, with constant sections and highly reinforced in the principal direction. The reinforcements, - in the form of rovings, continuous filament mats or fabrics - pass through a resin bath where they are impregnated before entering a heated die that gives it its cross-sectional shape. After the die, the profile is cooled by air or water and cut into desired lengths. The process is depicted in Figure 2.9.

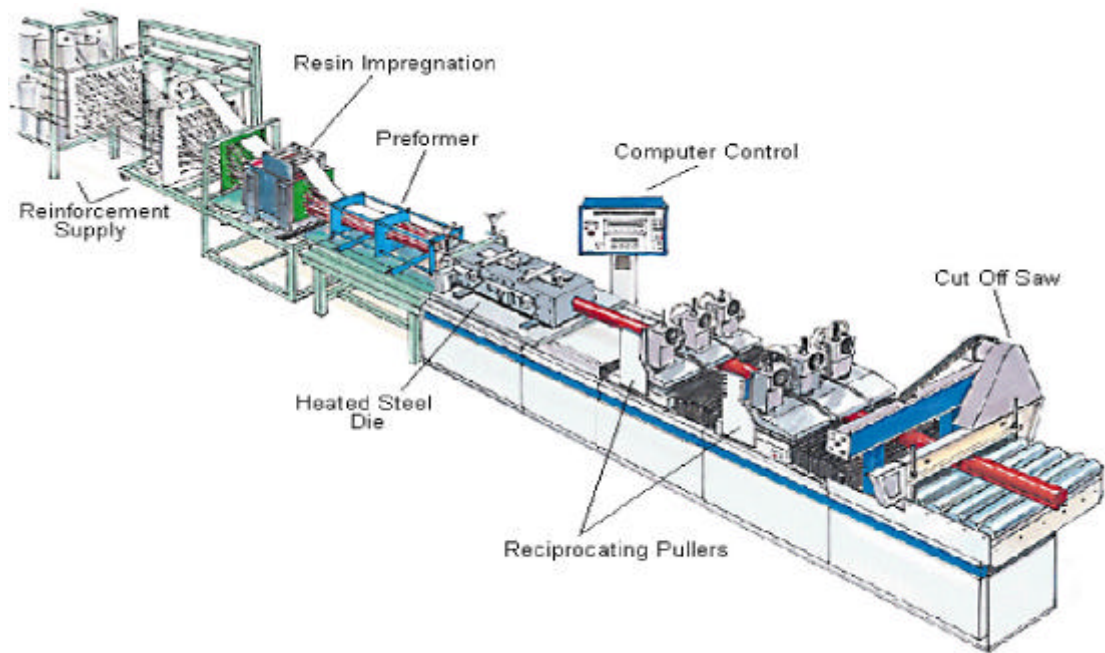


Figure 2.9 The pultrusion process (Fibreforce Composites Limited 2002)

The pultrusion process is best suited to the continuous production of a single section, as any new section requires dies to be made. The cost of the die can only be justified when large quantities of a section are produced so that the capital cost can be spread over a large volume of product. Moreover, the fitting of dies, setting up of tows, and the calibration of the pultrusion machine for any die is time-consuming and adds to the initial costs. As a result, manufacturers prefer to produce large quantities of a limited number of profiles. Specific issues relating to pultruded beams are discussed in Chapter 3

2.5.2 Filament-winding

In this process the reinforcement, in the form of a roving or continuous filament, passes through a resin bath where it is impregnated before being wound around a suitable mandrel until the required thickness is achieved. The mandrel gives the shape of the final item. This process is best suited for the fabrication of hollow items like tubes, pipes, elbows, tanks, vessels with a typical 70%-30% fibre-resin weight ratio. Figure 2.10 gives a schematic of the process.

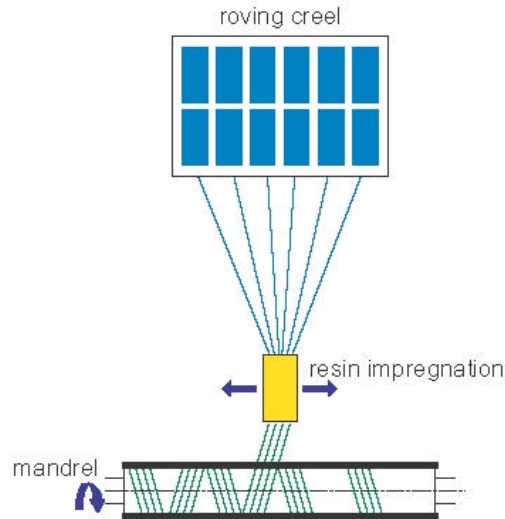


Figure 2.10 Filament-winding technique (Saint-Gobain Vetrotex America International 2001)

2.5.3 Injection moulding

Resin is injected at high pressure to impregnate a reinforcement placed inside a two-sided closed metal mould. A helical screw and ram apparatus can be used to inject the polymer into the mould, as shown in the schematic of Figure 2.11. After the part cools and solidifies, the mould is opened and the part is ejected. The injection is easy to automate and this process is best suited to the production of parts with fine details and complex geometry. It also offers high quality and repeatability as well as a good surface finish. However, if the matrix contains hollow fillers, the helical screw can damage these and an alternate pumping method is required.

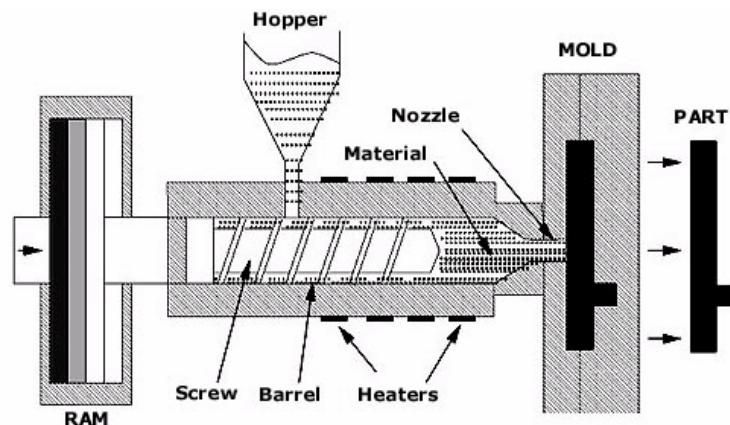


Figure 2.11 Injection moulding (Michigan State University 1999)

2.5.4 Hand and machine laminating

Hand lay-up is probably the earliest form of manufacturing composite components. It is well-suited to small or medium size components with complex lay-up patterns, complex geometry, and / or difficult access. A combination of reinforcements, including woven or knitted fabric, is laid into an open mould and impregnated with resin, layer by layer. This method suffers from the following disadvantages: the resin to fibre ratio is difficult to control; compaction is uneven and uncontrolled; the operation is messy; the resin and fibres are exposed continuously to impurities; there is a physical limit to the number of layers of plies that can be laid up in one session due to resin drain, compaction, and workability; and fibres can be lifted up off the component, especially around corners. In general, quality control is a major concern. Subsequently, the material properties of hand lay-up laminates have a high degree of variation.

In machine lay-up, usually the constituents (resin and fibres) are supplied in the form of a pre-preg (short for pre-impregnated material). Pre-pregs come in different forms including tape, sheets, and woven cloths for use as plies. The plies are laid to the required number, thickness, and orientations. The finished product is cured by exposure to heat and pressure to allow the removal of any air pockets and to produce a consistent part.

2.5.5 Consolidation techniques

The consolidation of FRP components increases the fibre to resin ratio, holds fibres against the mould and helps to expel entrapped air, thereby reducing voids in a laminate. Two common methods of consolidation are vacuum bagging and autoclave consolidation.

Vacuum bagging

Vacuum bagging is a method of applying pressure to an FRP while it cures. A cross-section of vacuum bagging is depicted in Figure 2.12. This process can be applied to laminated or filament-wound FRP. The component is laid-up and a layer of perforated plastic is placed over the laminated component. This plastic allows air and resin to escape and ensures that the breather cloth does not stick to the laminated component. Breather cloth is placed over the perforated plastic. The role of the breather cloth is to form a conduit for the air and resin to travel towards the vacuum port. A flexible plastic membrane is then laid over the breather cloth and sealed airtight. A vacuum is applied once the vacuum port is inserted and sealed to the outer plastic membrane.

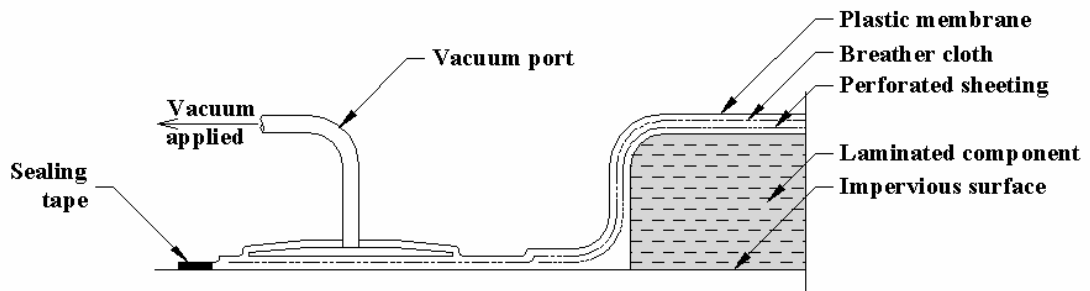


Figure 2.12 Typical vacuum bagging

The main advantages of vacuum bagging are that: it is considerably cheaper than autoclave consolidation, it is portable, and it works well on unusual shapes. However, the use of a vacuum can cause some resins to ‘out gas’ resulting in: boiling of the resin, voids in the laminate, and changes to the mechanical and adhesion properties of the resin. Furthermore, for the process to be effective it must be performed before the resin starts to set.

Autoclave consolidation

Autoclave consolidation involves placing the completed component, before curing, into a pressure chamber. Autoclaves can use steam, high capacity compressors or nitrogen to build up pressure. The increase in pressure is associated with temperature increase therefore autoclave consolidation also provides heated curing of the component. If steam is used, the environment within the chamber is under high pressure, hot and wet. In this case, the FRP component is sealed within an impervious membrane to protect it from the ingress of water.

2.6 Conclusion

The history of fibre-reinforced polymers is relatively short, with most developments having taken place over the last 65 years. Development of new reinforcement materials, matrix formulations, and production techniques continue at a fast rate. This Chapter introduced this very vast topic, and as such, was not intended as a detailed investigation or literature review, but rather as an overview of FRP materials and production systems suitable for infrastructure applications.

References

- Bahl, O. P., Shen, Z., Lavin, J. G. & Ross, R. A. 1998, 'Manufacture of carbon fibres', in *Carbon fibers*, 3rd , rev. and expand edn, eds. J. B. Donnet et al., Marcel Dekker, New York, pp. 1-83.
- Berthelot, J. M. 1992, *Matériaux composites- Comportement mécanique et analyse des structures*, Masson, Paris.
- Bishop, W. 1989, 'High performance fibers in advanced composites', K. Partridge, London: Elsevier, pp. 111-144.
- E. I. duPont de Nemours. 1980, *Data Manual*, E. I. duPont de Nemours, Wilmington DE.
- Fiber Science Division of EDO Corp. 1995, *Properties of fibre composites*, Fiber Science Division of EDO Corp. (Salt Lake City 1995).
- Fibre Composite Design and Development Group 1997, *Allowable material properties*, University of Southern Queensland, Toowoomba.
- Fibreforce Composites Limited 2002, *Pultrusion process*, Available: [<http://www.fibreforce.co.uk/>].
- Gibson, R. F. 1994, *Principles of composite material mechanics*, McGraw-Hill, Singapore.
- Hancox, N. L. 1981, *Fibre Composite Hybrid Materials*, Applied Science Publishers Ltd., London.
- Hancox, N. L. 1983, 'High Performance Composites with Resin Matrices in Fabrication of Composites', in *Handbook of Composites*, vol. 4, eds. A. Kelly & S. T. Mileiko, Elsevier Science, The Netherlands.
- Hanson, N. W. 1987, 'Carbon fibers in engineered materials handbook', in *ASM International*, Metals Park, OH, pp. 49-53.
- Harper, C. A. 2000, *Modern plastics handbook*, McGraw-Hill, New York.
- Hull, D. & Clyne, T. W. 1996, *An introduction to composite materials*, 2nd edn, Cambridge University Press, Cambridge ; New York.
- Jones, R. M. 1975, *Mechanics of Composite Materials*, McGraw-Hill, New York.
- Mallik, P. K. 1993, *Fiber-Reinforced Composites Materials Manufacturing and Design*, 2nd edn, Marcel Dekker Inc., New York.
- Michigan State University 1999, *What is injection molding?*, Available: [http://islnotes.cps.msu.edu/trp/inj/int_what.html].
- Nielson, L. E. & Landel, R. F. 1994, *Mechanical Properties of Polymers and Composites*, 2nd edn, Marcel Dekker Inc., New York.
- Norwood, L. S. 1994, 'Handbook of Polymer Composites for Engineers', in *Handbook of Polymer Composites for Engineers*, Woodhead Publishing Ltd., Cambridge, England, pp. 9, 19.

- Owens Corning 1998, *A history of innovation-historical background*, Available: [<http://www.owenscorning.com/acquainted/about/history/index.asp>].
- Pagano, N. J. & Hahn, H. T. 1997, 'Evaluation of Composite Curing Stresses in Composite Materials: Testing and Design', in *Testing and Design (4th conf.) ASTM STP 617*, Philadelphia: American Society for Testing and Materials, pp. 317-329.
- Peng, J. C. M., Donnet, J. B., Wang, T. K. & Rebouillat, S. 1998, 'Surface treatment of carbon fibers', in *Carbon fibers*, 3rd , rev. and expand edn, eds. J. B. Donnet et al., Marcel Dekker, New York, pp. 161-229.
- Potter, K. 1997, *An introduction to composite products*, Chapman & Hall, London.
- Powell, P. C. 1994, *Engineering with fibre-polymer laminates*, Chapman & Hall, London.
- Rebouillat, S., Peng, M. C., Donnet, J. B. & Ryu, S. K. 1998, 'Carbon fiber applications', in *Carbon fibers*, 3rd , rev. and expand edn, eds. J. B. Donnet et al., Marcel Dekker, New York, pp. 463-541.
- Saint-Gobain Vetrotex America International 2001, *Filament Winding*, Available: [http://www.sgva.com/fabrication_processes/rna_filwind.html].
- Schwartz, M. M. 1992, *Composite materials handbook*, 2nd edn, McGraw-Hill, New York.
- Strong, A. B. 2000, *Plastics materials and processing*, 2nd edn, Prentice-Hall, New Jersey.
- Swanson, S. R. 1997, *Introduction to Design and Analysis with Advanced Composite Materials*, Prentice-Hall Inc., USA.
- Tsai, S. W. 1986, *Composites Design*, Dayton OH.

Chapter 3

Existing FRP beams: advantages and limitations

3.1 Introduction

Civil engineering progress is often profoundly influenced by the development and introduction of new materials. Indeed, materials in common use today, such as reinforced concrete (RC), were considered revolutionary in the late 18th century (Warner, Rangan & Hall 1989, p. 6). Advancement of new materials into civil engineering has often concentrated upon a common element, the beam. Beams constitute the predominant structural element since they transfer loads to abutments or supporting columns. Examples of their use can be found in structures such as bridges, wharves, high-rise buildings, factories and domestic housing. It is therefore not surprising that manufacturers, and researchers alike, have concentrated upon developing beams when trying to introduce a new material into the civil engineering market. Naturally, for any new beam to become successful it must provide advantages over the traditional alternatives.

Traditionally, beams have been made from timber, steel and RC. In Australia, beams produced from timber were predominantly used in infrastructure well into the 20th century. Unfortunately, timber suffers from biological attack, requiring maintenance and replacement at regular intervals. Furthermore, hardwood timbers, used in infrastructure, are no longer readily available. Steel gradually replaced timber as the predominant beam material. However, steel beams also have disadvantages; they readily corrode if unprotected and are costly. The innovation of combining steel and concrete, to form reinforced concrete, provided an alternative beam construction. RC beams offer better corrosion resistance than steel, but they are not totally immune to corrosion. Indeed, once concrete cracks, the reinforcing steel is exposed to atmospheric agents. Further disadvantages of RC beams are that the concrete is susceptible to chemical attack, they may require in-situ manufacture, and the beams are larger than the steel alternative.

With the invention of FRP a new material became available for beam construction. Not surprisingly, the potential for FRP use as a beam material has been recognised by industry, with pultruded and filament-wound beams commercially available. Research groups (Bank 1989; Bank, Nadipelli & Gentry 1994; Barbero 1991; Barbero & Sonti 1991; Davalos et al. 1996; Haj-Ali & Kilic 2002; Kabir & Sherbourne 1998; Kabir & Sherbourne 1999; Mosallam & Bank 1991; Mottram 1991; Nagaraj & Gangarao 1997; Roberts 2001)

have been studying their behaviour and have identified limitations with these FRP designs. Subsequently, different designs have been proposed, prototyped, and tested (Deskovic, Triantafillou & Meier 1995; Drummond & Chan 1999; Fam & Rizkalla 2000a; Lee et al. 1995; Van Erp 1999; Zhao, Karbhari & Seible 2001), each design with advantages and limitations. The following sections review the different designs and discuss the developments.

3.2 Description and behaviour of FRP beams developed for civil engineering applications

3.2.1 Commercially Available beams

3.2.1.1 Pultruded beams

Currently the majority of FRP beams used in civil engineering applications are produced using the pultrusion process, discussed in Section 2.5.1. Pultrusion offers high volume output, a variety of sections, good surface finish, and external dimension control. Examples of applications where pultruded beams have been used are pedestrian bridges (Figure 3.1), vehicular bridges, off-shore structures (Figure 3.2), and highway safety structures (Dutta 1998).



Figure 3.1 Sea Life Park bridges, Hawaii (Strongwell Ltd. 2002)

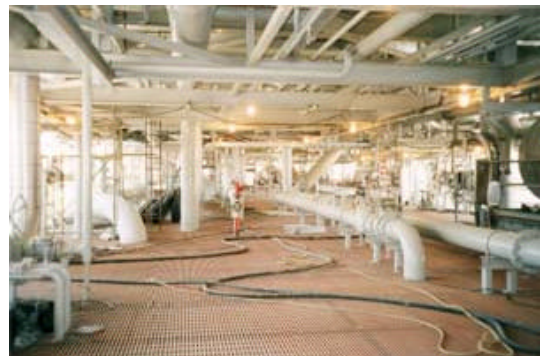


Figure 3.2 DURAGRID® Phenolic Grating on an offshore platform (Strongwell Ltd. 2002)

Pultruded beams are typically produced into section profiles that resemble steel beams. The cross-sectional shapes of steel beams have evolved over many years, based upon economic, structural, and practical considerations. The performance and load carrying mechanisms of these sections is well-known. The direct transfer of these shapes to FRP materials however, has highlighted serious inefficiency in the designs, resulting in premature

failures of most pultruded beams due to second-order effects (Gilchrist et al. 1996). Typical problems encountered include: the inability to transmit radial stresses, compression flange buckling, and web buckling. In addition, pultruded beams are difficult to connect and the pultrusion process itself requires sacrifices in structural efficiency.

Delamination due to radial stresses and associated flange buckling

When pultruded beams are subject to bending moments, radial stresses are induced in the sections around curved regions (Kedward, Wilson & McLean 1989). Kedward et al. showed that the radial stresses around the internal corners lead to delamination of the laminates and subsequent premature failure of the beams due to compression flange buckling. The affected area is shown on Figure 3.3. Kedward et al. also noted that the effect was most pronounced for Z, C, and I sections that have a singular web to restrain the compression flange. Gilchrist et al. (1996) also found that failures were usually premature due to flange buckling, when they investigated second-order failure modes in pultruded I-beams. Kabir & Sherbourne (1998) and Barbero & Sonti (1991) also confirmed Kedward et al.'s findings that Z, C, and I sections were particularly prone to flange buckling failure, when investigating the flange buckling of pultruded FRP beams.

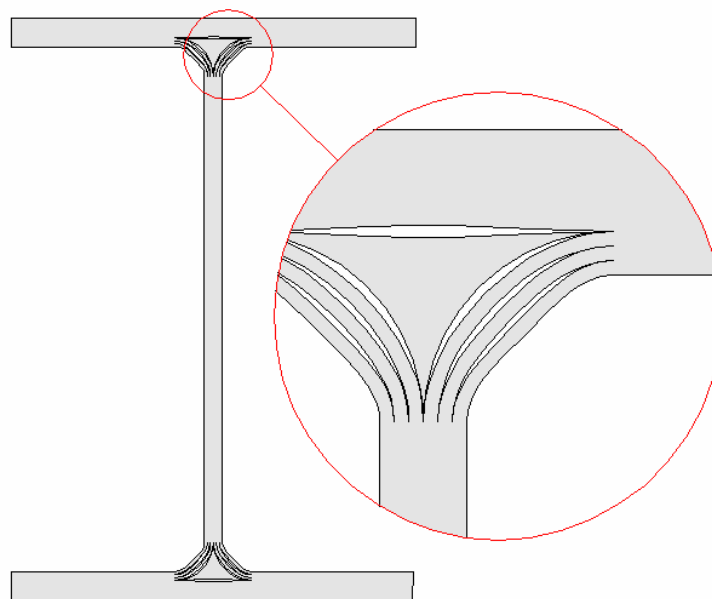


Figure 3.3 Delamination around curved regions

Web buckling

Buckling of the webs of the pultruded beams due to bending, shear and bearing loads can also occur. Investigations have shown that pultruded beams have a limited capacity to

bearing loadings with the failures being due to second-order effects. Experiments conducted by Mottram (1991) have shown that primary compression crushing failure is generally preceded by longitudinal cracking at the web-flange interface, web buckling, or a combination of web buckling and shear cracking at the web-flange interface. The longitudinal cracking is due to the orientation of the fibres in the webs not being at the optimum ± 45 degrees to the longitudinal axis.

Connecting pultruded beams

In addition, joining of pultruded beams is an area of concern. Most methods mimic bolted connection methods common in steel construction, where the ductile property of steel forms an integral part in the jointing method. Composites do not yield, and as such are subject to different types of failure modes, which require careful consideration when designing these jointing systems. The plates and angles used in bolted connections are generally produced or cut from pultruded sections. Hence, these connection members suffer from the same limitations as the beams, fibre orientation is not at an optimum, angle brackets delaminate around their corners and bearing failures around bolt holes are common (Bank, Mosallam & McCoy 1994; Mosallam 1993; Mottram & Zheng 1999; Zheng & Mottram 1996). Furthermore, connections with full or partial moment fixity require a large number of cleating plates to be bolted to the respective sections of the connection. The bolt holes reduce the load carrying material of the sections, which results in stress concentrations around the holes.

Limitations of the pultrusion process

The pultrusion process can produce large volumes and a variety of sections. However this process is accompanied by quality sacrifices such as, relatively low fibre volume fraction, of the order of 28 to 40% (Nagaraj & Gangarao 1997) due to the addition of fillers. Furthermore, fibre orientation is predominantly aligned with the longitudinal axis of the beam. The result is a section that has little strength in the directions perpendicular to the fibres. In addition, the pultruded box beams are usually manufactured with uniform wall architecture and geometry, taking no account of ideal fibre placement for bending and shear.

3.2.1.2 Recent improvement in pultruded section design

The large number of premature failures associated with pultruded beams has prompted researchers, and manufacturers alike, to investigate the causes and improve the designs of these beams. For example, Strongwell Ltd. (2002) has developed a hybrid beam for a government-sponsored research and development program. The beam is pictured in Figure 3.4. In an attempt to avoid web buckling, and to increase the shear stiffness of the section, the beam has two webs that are connected at third points along the beam height. The

double web arrangement also increases torsional rigidity when compared to a standard pultruded I beam. The flanges are provided with layers of carbon fibres orientated along the length of the beam. The carbon layers provide increased moment capacity and stiffness to the section. The unrestrained distance of the flange has been decreased, compared to a standard pultruded I beam, thus reducing the possibility of flange buckling. This prototype beam has been used as a bridge girder in Virginia, USA (Waldron 2001).

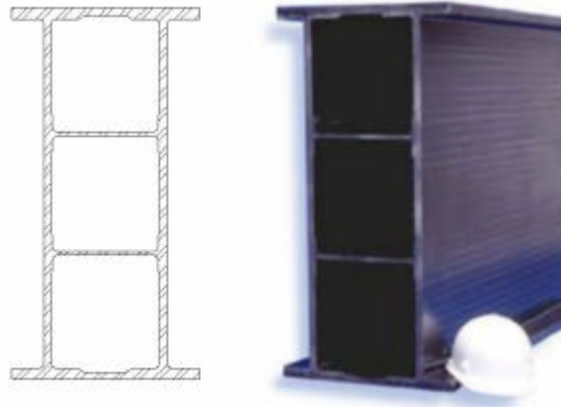


Figure 3.4 Strongwell 36-inch hybrid double web beam (Strongwell Ltd. 2002)

Despite the improvements in the Strongwell's design, a number of the limitations of pultruded beams still remain: the orientation of fibres in the webs are not optimised for shear loadings, fibre fractions are still rather low, the web-flange interface is weak, and methods of connection remain the same as for single web pultruded beams - with the added complication of access to voids for bolting. Tests by Waldron (2001) showed that the beams no longer failed due to overall web or flange buckling, but, rather, by compression buckling of the carbon-fibre laminate in the top flange, which is still a second-order failure.

Other attempts to address some of the problems associated with pultruded beams include the use of small stable pultruded components, which are then assembled into larger beams. One example of this approach is the pultruded plank system utilised by Lee et al. (1995) to construct a cellular box beam. The beam was made from pultruded planks that were connected using three-way pultruded connectors together with 'dog bone' inserts and steel shear pins as shown on Figure 3.5. The concept provides flexibility in design with the use of only three pultruded elements. Testing has shown that this concept has significant advantages over standard pultruded beams.

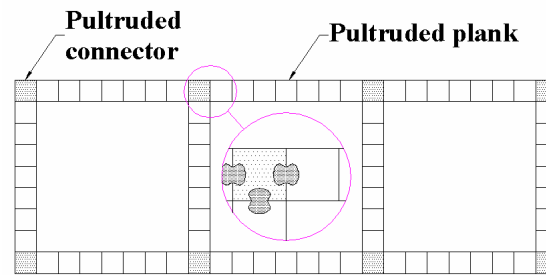


Figure 3.5 Lee beam

Unfortunately, the thin-walled members failed under the loading points when tested in 4-point bending. The failure was a local crushing of the pultruded section webs. The compression and tension flanges in the beam are identical in construction, so it was not surprising that compression buckling would be the primary failure mode for the beam. Furthermore, the beam deflected to a greater degree than expected. Lee et al. attributed the extra deflection upon creep during testing; however, the assumption requires experimentation for verification.

3.2.1.3 Filament-wound beams

A very limited number of beams have been produced using the filament-winding process. This is because of the geometric limitations of the process, which requires the use of a mandrel and it is only suitable for sections of revolution. This technique is most commonly used in the production of pipes or rectangular sections. The sections have uniform wall cross-sections with the fibres typically orientated from 15 to 90 degrees to the longitudinal axis. The technique does not allow for automated placement of fibres in line with the longitudinal axis and as such is not ideally suited to beams. The fibre orientation can be optimal for shear and torsion - but not for bending, where fibres in line with the longitudinal axis are the best for stiffness and strength. Unlike the pultrusion process, filament-winding does allow for the manual placement of laminates within layers of winding, but this is very time-consuming and hence not often used. The sections produced have higher fibre volume fraction than pultruded beams. Connections are awkward with the same problems arising as for the pultruded beams.

3.2.2 Custom designed beams

In order to overcome the aforementioned problems inherent to the pultruded and filament-wound beams, researchers have resorted to prototyping custom designs. These new concepts are discussed in the following sections.

3.2.2.1 I beam with optimum fibre orientations

To address the poor fibre orientation of pultruded beam webs, Drummond & Chan (1999) designed and tested custom-made GFRP (Glass FRP) I-beams. The lay-up is shown on Figure 3.6. Unidirectional laminates were provided in the flanges and double bias in the webs. To ensure that no coupling effects took place, an extra layer of double bias was placed on the flanges to provide symmetric laminates throughout the beam. Vee section laminates were provided where the web laminates curved onto the flanges to provide for the curve of the laminate and reduce air voids at the critical section. During testing, the beams were found to fail prematurely due to the buckling of the flange in compression; thereby further demonstrating the insufficient compression flange restraint provided by single web FRP profiles.

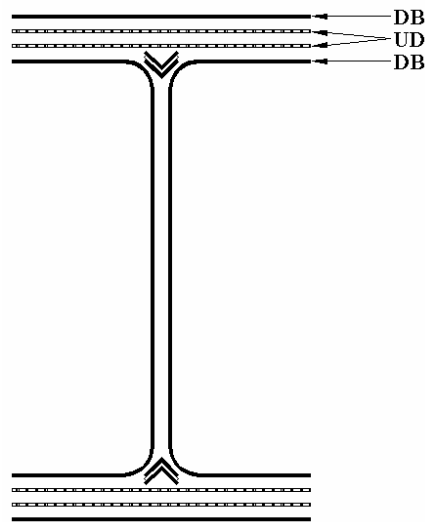


Figure 3.6 Drummond beam

3.2.2.2 Concept combining concrete and an FRP box beam

As highlighted previously, many problems in pultruded beams are associated with the poor compression behaviour of the thin composite laminate. Deskovic (1993) tried to address this issue by combining a GFRP box beam with concrete on the compression flange. The concrete placement was to allow for the lower compressive strength of the FRP materials and to overcome compression buckling of the flange. Furthermore, the use of concrete was seen as an inexpensive solution when compared to thickening the flange with GFRP. Deskovic initially intended to apply this innovative approach to a pultruded section, however the capital costs associated with production of a pultrusion pre-former and die were restrictive. Therefore, the beam was manufactured using filament winding. To provide

sufficient shear capacity, extra laminates were manually incorporated within the webs, with a fibre orientation of ± 45 degrees to the longitudinal axis. In addition, Deskovic bonded an extra CFRP (Carbon FRP) laminate to the tension flange in an attempt to create a pseudo-ductile failure. The concept is schematically represented on Figure 3.7.

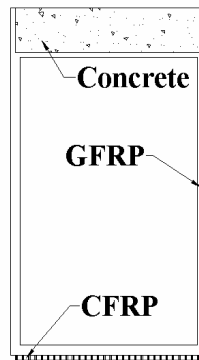


Figure 3.7 Deskovic beam

Deskovic investigated short and long-term behaviour with encouraging outcomes. Particular problems were encountered with the bonding of the concrete to the FRP; delamination at the interface caused premature failure of two of the beams tested. To overcome this problem, shear connectors were added through the FRP flange and concrete. The beam was developed with bending moment as the major design criterion and exhibits a major improvement in this area. However, like pultruded beams, the beam suffers from buckling of the webs due to second-order effects. Furthermore, the quantity of glass reinforcement used in the flanges was excessive due to the poor orientation that the filament winding process affords. Deskovic concluded that the beam was pseudo-ductile. This conclusion may have been premature as testing was conducted under deformation control only. Hence, the influence of dynamic effects on the beam behaviour when the CFRP fails has not been investigated.

Due to the encouraging outcomes that Deskovic's concept displayed, it was used in conjunction with Lee et. al's approach to manufacture the first composite bridge in Australia. Square pultruded sections were glued together to form box beams, these then had pre-cast concrete slabs adhered to the top flange.

3.2.2.3 Concrete-filled tubes

The combination of a concrete core and GFRP tubes was used by Fam & Rizkalla (2000a; 2000b). The concrete provided restraint to the tubes to avoid buckling and a medium for connections. Many geometric and concrete strength combinations were

investigated ranging from fully-filled to hollow-core. Experiments showed that the hoop stresses played an important role in the overall performance of the tubes in bending. The direction of the fibres in the tubes had a significant contribution to the performance of the beams. Fam & Rizkalla showed that filament-wound tubes performed better than the pultruded variety, due to a more varied fibre orientation. However, the use of tubes as beams is uneconomic, due to the poor overall placement of fibres throughout the cross-section. Only a small number of fibres at the top and bottom of the tube are fully utilised in bending. Albeit, the tube philosophy has been used in a bridge concept by Zhao, Karbhari & Seible (2001) as the bottom section of a beam-and-slab combination for bridges. This arrangement is shown on Figure 3.8. In such applications, the tube is primarily in tension, while the slab, or deck, is in compression. However, with a significant number close to the neutral axis, the fibres are under-utilised. Furthermore, Zhao et al. found that mechanical interlock between the FRP and concrete was required, so only filament-wound tubes with internal ribs could be used in such a system.

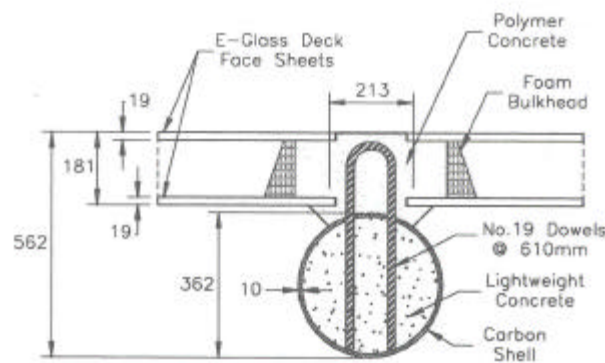


Figure 3.8 Zhao beam

3.2.2.4 Concept combining a polymer core material and an FRP box beam

A different approach to addressing the problems inherent with pultruded beams was developed by Van Erp (1999). Van Erp used an in-house developmental polymer concrete, named particulate-filled resin (PFR), for inclusion in a box beam. PFR is a combination of polymer resin and fly-ash micro-sphere filler. To alleviate buckling of the flanges and webs, the PFR was provided as a core to the beam. Circular voids were introduced in the core to reduce material use. The fibres surrounding this core were orientated for optimum performance. To provide protection to the laminates, an overlaying skin of PFR is incorporated into the design. The use of a polymer based core alleviated the adhesion problems prevalent with the combined concrete-FRP systems as well as reduced the dead weight, as the PFR is lighter than concrete. Furthermore, the PFR inclusion allowed for the

distribution of concentrated loadings and the provision of a medium to support screws and bolts. Figure 3.9 shows a photograph of the beam.

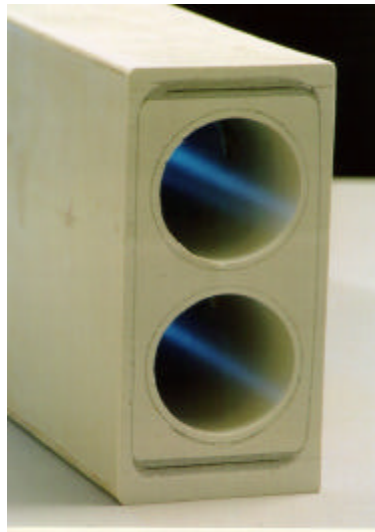


Figure 3.9 Van Erp beam

Three of these beams were manufactured and tested. Initial investigations into the beam behaviour yielded favourable outcomes with all the beams failing in a primary failure mode. This finding is significant, as it is the first beam investigated herein that did not fail due to a second-order effect. The information gained from the experimentation also highlighted areas to note where the PFR and cross-sectional design affected the beam's performance. The PFR in the beam has a lower tensile failure strain than that of the glass and carbon unidirectional laminates that constitute the flanges. Cracks in the core and associated delamination at the core-laminate interface occurred when tensile strains exceeded the PFR's capacity. When the cracking occurred, surrounding laminates, if capable, absorbed the energy released. In the first beam tested, the laminates were incapable of absorbing the released energy and the beam failed without the addition of further loads. Subsequent beams were designed so that the energy released during the cracking of the PFR was supported safely by the tensile reinforcement. Testing provided favourable outcomes.

Problems were experienced with localised failure under high compression loads. The core material shrunk during cure and introduced stresses within the section, in particular, in the webs where the amount of core material was not uniform (Davey 1999). Subsequently, when the beam was subjected to vertical compressive loads, the circular voids caused premature failure of the webs. Due to arch action, the outward bulge in the beam was pronounced compared to the Poisson action at the flange and the centre of the beam, where

the PFR extends throughout the width of the section. This variation in deformations added to the shrinkage effects, and induced tensile stresses in-between the web laminates and the core material. The tensile stresses caused delamination of the web laminates to occur, resulting in the web laminates becoming non-restrained. The unrestrained web laminates then buckled, so that the subsequent contribution to resisting the compressive load applied was greatly reduced. Finite element analysis (Ryan 2000) has shown that beams with rectangular voids are less likely to suffer from this problem.

3.3 Conclusion

This chapter has reviewed the state of FRP beam development for civil engineering structures. From the review, it appears that limited engineering has been used in the development of commercial FRP beams. This is particularly noticeable for the pultruded beams where the advantage of mass production overshadows quality. Pultruded beams are characterised by a large number of premature failures such as delamination at internal corners, compression flange buckling, and web buckling. In addition, pultruded beams are difficult to connect, have low fibre-volume fractions and fibre orientation is not optimum. Based on the conglomerate of problems associated with pultruded sections, it is not surprising that Ballinger (1994) classifies pultruded beams as a 'pseudo-structural general purpose product'. The other commercial process used to produce FRP beams is filament-winding. Because of inherent geometric limitations this process is not well-suited for the manufacture of beams. Sections must be uniform, fibre orientation is restricted, with the optimum zero degree in the flanges being unobtainable, and the shape of the beam can have no reverse curvature.

To address these shortcomings custom designed beams have been proposed with mixed success. The most successful are those that combine FRP with a core material, such as concrete. These concrete-filled beams appear to have solved many problems. However, bonding of the concrete to the FRP has emerged as a major deficiency of this concept. Replacement of cementitious concrete with polymer concrete appears to be a solution. This replacement has been trailed with initial success. However, the trial highlighted that improvement in the design is possible, and warrants further investigation.

References

- Ballinger, C. A. 1994, 'Specification needs for FRP composite products', in *3rd Materials engineering conference*, ed. A. S. o. C. Engineers, American Society of Civil Engineers, San Diego, CA, USA, pp. 56 - 63.

- Bank, L. C. 1989, 'Flexural and shear moduli of full-section fiber reinforced plastic (FRP) pultruded beams', *Journal of Testing and Evaluation*, vol. 17, no. 1, pp. 40 - 45.
- Bank, L. C., Mosallam, A. S. & McCoy, G. T. 1994, 'Design and performance of connections for pultruded frame structures', *Journal of Reinforced Plastics and Composites*, vol. 13, pp. 199-212.
- Bank, L. C., Nadipelli, M. & Gentry, T. R. 1994, 'Local buckling and failure of pultruded fiber-reinforced plastic beams', *Journal of Engineering Materials and Technology*, vol. 116, no. 2, pp. 233 - 237.
- Barbero, E. J. 1991, 'Pultruded structural shapes: Stress analysis and failure prediction.' in *Conference on Advanced Composites in Civil Engineering Structures*, ed. ASCE, ASCE, New York, pp. 194 - 204.
- Barbero, E. J. & Sonti, S. 1991, 'Micro-mechanical modelling for pultruded composite beams', in *32nd Structural dynamics conference*, American Institute of Aeronautics and Astronautics, Baltimore, Md.
- Davalos, J. F., Salim, P., Qiao, R., Lopez-Anido, R. & Barbero, E. J. 1996, 'Analysis and design of pultruded FRP shapes under bending', *Composites Part B: engineering*, vol. 27, no. 3/4, pp. 295 - 306.
- Davey, S. 1999, *The fabrication of a fibre composite floor slab*, Fibre composite design and development, University of Southern Queensland, Toowoomba, Australia.
- Deskovic, N. 1993, *Innovative design of FRP composite members combined with concrete*, PhD, Massachusetts Institute of Technology.
- Deskovic, N., Triantafillou, T. C. & Meier, U. 1995, 'Innovative design of FRP combined with concrete: Short-term behavior', *Journal of Structural Engineering*, vol. July, pp. 1069 - 1077.
- Drummond, J. A. & Chan, W. S. 1999, 'Fabrication, analysis, and experimentation of a practically constructed laminated composite I-beam under pure bending', *Journal of Thermoplastic Composite Materials*, vol. 12, no. May, pp. 177 - 187.
- Dutta, P. K. 1998, 'Investigations of plastic composite materials for highway safety structures', *CRREL Report*, vol. 98, no. 7, p. 1.
- Fam, A. & Rizkalla, S. 2000a, 'Hybrid FRP/concrete structural members', in *Composites in the Transportation Industry*, eds. S. Bandyopadhyay et al., University of New South Wales, Sydney, Australia, pp. 191 - 197.
- Fam, A. Z. & Rizkalla, S. H. 2000b, 'Concrete-filled FRP tubes for flexural and axial compression members', in *Advanced Composite Materials in Bridges and Structures*, eds. J. Humar & A. G. Razaqpur, Canadian Society for Civil Engineering, Ottawa, Ontario, Canada, pp. 315 - 322.

- Gilchrist, M. D., Kinloch, A. J., Matthews, F. L. & Osiyemi, S. O. 1996, 'Mechanical performance of carbon-fibre- and glass-fibre-reinforced epoxy I-beams: I. Mechanical behaviour', *Composites Science and Technology*, vol. 56, no. 1, pp. 37-53.
- Haj-Ali, R. & Kilic, H. 2002, 'Nonlinear behavior of pultruded FPR composites', *Composites Part B: engineering*, vol. 33, pp. 173 - 191.
- Kabir, M. Z. & Sherbourne, A. N. 1998, 'Lateral-Torsional Buckling of Post-Local Buckled Fibrous Composite Beams', *Journal of Engineering Mechanics*, vol. 124, no. 7, pp. 754 - 764.
- Kabir, M. Z. & Sherbourne, A. N. 1999, 'Local Buckling of Thin-Walled Fibre Composite Beams Under Transverse Loading', *Canadian Journal of Civil Engineering*, vol. 26, no. 1, pp. 107 - 118.
- Kedward, K. T., Wilson, R. S. & McLean, S. K. 1989, 'Flexure of Simply Curved Composite Shapes', *Composites*, vol. 20, no. 6, pp. 527-536.
- Lee, J., Hollaway, L., Thorn, A. & Head, P. 1995, 'The structural characteristic of a polymer composite cellular box beam in bending', *Construction and building materials*, vol. 9, no. 6, pp. 333 - 340.
- Mosallam, A. S. 1993, 'Stiffness and Strength Characteristics of PFRP UC/Beam-to-Column Connections.' *Composite Material Technology*, vol. 53, pp. 275-283.
- Mosallam, A. S. & Bank, L. C. 1991, 'Creep and recovery of a pultruded FRP frame', in *Advanced composites materials in civil engineering structures*, eds. S. L. Iyer & R. Sen, American Society of Civil Engineers, Las Vegas, Nevada, pp. 24 - 35.
- Mottram, J. T. 1991, 'Evaluation of Design Analysis for Pultruded Fibre-Reinforced Polymeric Box Beams', *The Structural Engineer*, vol. 69, no. 11, pp. 211 - 220.
- Mottram, J. T. & Zheng, Y. 1999, 'Further Tests on Beam-to-Column Connections for Pultruded Frames: Web-Cleated', *Journal of Composites for Construction*, vol. 3, no. 1, pp. 3-11.
- Nagaraj, V. & Gangarao, H. V. S. 1997, 'Static Behavior of Pultruded GFRP Beams', *Journal of Composites for Construction*, vol. 3, pp. 120-129.
- Roberts, T. M. 2001, 'Mechanical properties and buckling of pultruded FRP profiles', in *International conference on FRP composites in civil engineering*, ed. J. G. Teng, Elsevier Science Ltd., Hong Kong, China, pp. 1435 - 1442.
- Ryan, H. 2000, *Investigation of the compressive behaviour and the optimum cross-section of a fibre composite girder-web*, Undergraduate Thesis, Faculty of Engineering and Surveying, University of Southern Queensland.
- Strongwell Ltd. 2002, *Special market products*, Available: [<http://www.strongwell.com/Special/bridges.htm>].

- Van Erp, G. M. 1999, 'A New Fibre Composite Beam for Civil Engineering Applications', *Composites Fabrication Journal*, vol. July, pp. 30 - 33.
- Waldron, J. 2001, *Determination of the design parameters for the rout 601 bridge*, Master of Science in Civil Engineering, Virginia Polytechnic Institute and State University.
- Warner, R. F., Rangan, B. V. & Hall, A. S. 1989, *Reinforced concrete*, 3rd edn, Longman Australia Pty Ltd.
- Zhao, L., Karbhari, V. M. & Seible, F. 2001, 'Development and implementation of the carbon shell system for the Kings stormwater channel bridge', in *International conference on FRP composites in civil engineering*, ed. J. G. Teng, Elsevier Science Ltd., Hong Kong, China, pp. 1299 - 1306.
- Zheng, Y. & Mottram, J. T. 1996, 'Analysis of Pultruded Frames With Semi-Rigid Connections', *Advanced Composite Materials in Bridges and Structures*, pp. 919-926.

Chapter 4 State of the art in FRP beam analysis and design methodologies

4.1 Introduction

Critical to the success of any new civil engineering technology is the ability to predict behaviour with reasonable accuracy. To this end, FRP beams have been studied, and models to predict their behaviour have been formulated (Bank 1990; Bank, Nadipelli & Gentry 1994; Barbero 1991; Barbero & DeVivo 1999; Barbero, Fu & Raftoyiannis 1991; Barbero, Lopez-Anido & Davalos 1993; Davalos, Qiao & Salim 1997; Lee & Kim 2002; Loughlan & Ata 1998; Nagaraj & Gangarao 1997; Patel, Tripathy & Pang 1993). These models are typically used to predict the behaviour of a beam when the size, material, and material orientation are known. However, if composite structures are to become commercially viable in the building industry - and therefore to compete with steel and reinforced concrete - then design methods which determine dimensions and constitution are required.

Current FRP design methods in aeronautics have used analytical formulations in conjunction with computer modelling, and testing of prototypes. The cost of such approaches cannot be justified for most civil applications. Therefore, in order for FRP beams to gain wide acceptability, design methods appropriate to the industry are required (Ballinger 1994). Consequently, analysis techniques have been altered so that simplified design methodologies can be formulated. In particular, numerous methods have been presented for various loading configurations and failure modes. However, a complete, coherent design method has yet to be established.

In this chapter, a review of the current state of the art of FRP beam analysis techniques and design methodologies for use by the civil engineering industry is presented. Due to the two different foci of analysis and design - the former determining behaviour, given dimensions and constitution, and the latter determining dimensions and constitution, given performance criteria - the two subjects are discussed separately. The chapter begins by presenting analysis techniques in order to identify their applicability, limitations and accuracy. The latter part of the chapter is devoted to identifying the shortcomings within current FRP beam design methods in the context of the civil engineering industry.

4.2 Analysis techniques for FRP beams

4.2.1 From micro to macro mechanics

Figure 4.1(a) depicts a single ply composed of fibres and matrix; the properties of such a ply vary from point to point. If the ply undergoes a uniform strain in the x-direction as depicted on Figure 4.1(b), the resulting stress distribution is not uniform across the cross-section (Figure 4.1(c)). Abu-Farsakh, Numayr & Hamad (1997), Ivanov & Tabiei (2001), Nikkel & Christensen (1990), and Yang, Gokhale & Shan (2000) studied individual fibre behaviour and interaction phenomena between matrix materials and developed models. The main purpose of these models is to gain an understanding into damage accumulation in FRP. However, their use at larger scales is prohibited due to their computationally-intensive nature. Albeit, a model based upon this micro-mechanical behaviour has been used, in a limited way, by Davalos et al. (1996) in a software program, FRPBEAM (Qiao, Davalos & Barbero 1994), to determine optimum fibre orientation in pultruded beams. The considerable number and variability of placement of individual fibres within a ply, let alone a complete fibre-composite component, make analysis at this micro-mechanical level extremely involved and impractical, so a simplification has been adopted universally. The simplification involves describing the heterogeneous ply on a macro-mechanical level. On this level the stress, strain, and properties are expressed in terms of average stresses (Figure 4.1(d)), strains and effective properties of an equivalent homogeneous material, where the constituent material interactions are no longer considered.

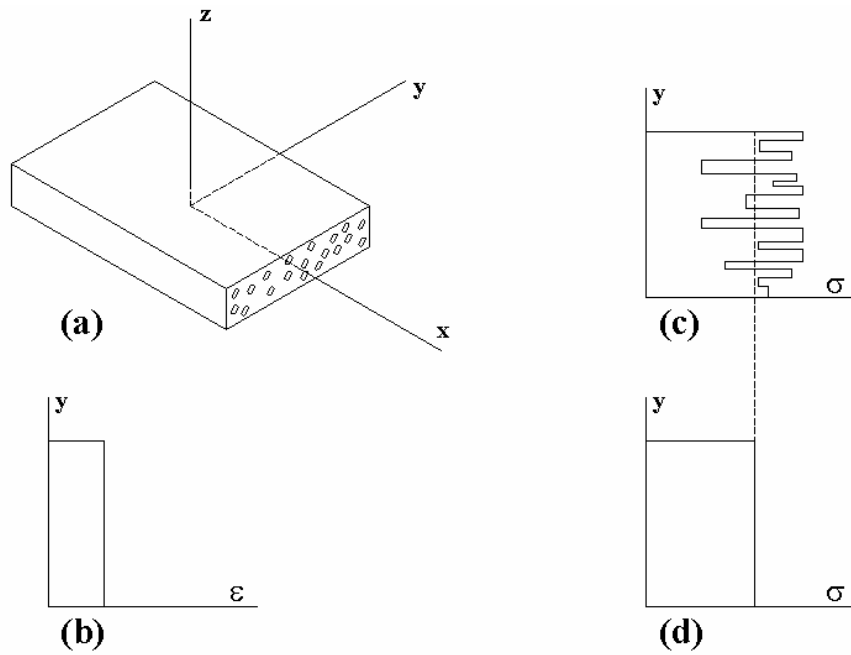


Figure 4.1 Stress relations of a ply under a uniform strain

These equivalent ply properties, in the direction of the fibres, may be estimated from the constituent proportions and properties using the following rule of mixtures (Jones 1975):

$$\begin{aligned}
 \mathbf{s}_p &= \mathbf{s}_{fi} \mathbf{f}_{fi} + \mathbf{s}_m \mathbf{f}_m \\
 E_p &= E_{fi} \mathbf{f}_{fi} + E_m \mathbf{f}_m \dots\dots\dots (4.1)
 \end{aligned}$$

where:

$$\mathbf{f}_{fi} + \mathbf{f}_m = 1;$$

\mathbf{s} = tensile strength;

\mathbf{f} = volume fraction (ratio of volume to total ply volume); and

E = tensile modulus, and

the subscripts denote:

fi = fibres;

m = matrix; and

p = ply.

However, the rule of mixtures assumes a perfect bond between the fibres and matrix - which is a gross simplification of the fibre-matrix interface behaviour particularly at high load levels. Consequently, experimental testing of fibre-matrix plies is used to ascertain the properties for specific fibre-matrix combinations.

4.2.2 Three dimensional analysis

Describing the stress-strain relationship of a ply on a macro-mechanical level allows a unidirectional ply to be considered one of the basic building blocks of a fibre-composite component. The ply properties are anisotropic. That is, the properties associated with an axis passing through a point in the material generally depend on the orientation of the axis. For anisotropic materials, there are nine stress components, denoted \mathbf{s}_{ij} on Figure 4.2 using conventional subscript notation. Corresponding to each of the stress components, there is a strain component \mathbf{e}_{ij} describing the deformation at that point.

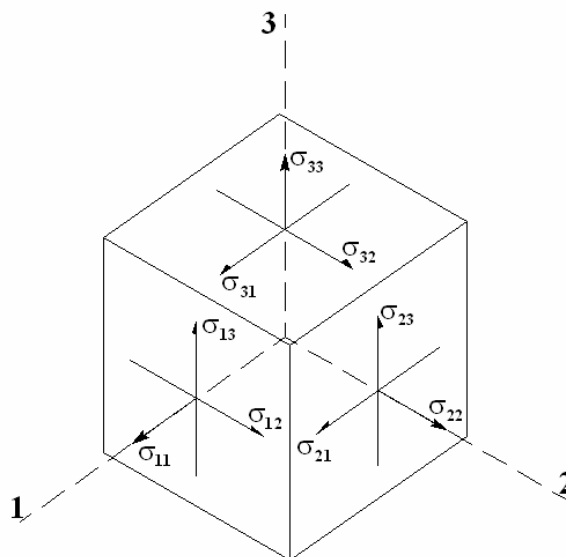


Figure 4.2 Anisotropic state of stress

Hooke's law gives the relationship between the stresses and strains as:

$$\{\mathbf{s}\} = [\mathbf{C}]\{\mathbf{e}\} \dots\dots\dots (4.2)$$

where $[\mathbf{C}]$ is a full 9×9 matrix of elastic constants for the ply. Fortunately, the shear stresses and strains are symmetric, ($\mathbf{s}_{ij} = \mathbf{s}_{ji}$ and $\mathbf{e}_{ij} = \mathbf{e}_{ji}$) so that there are only six independent components of $\{\sigma\}$ and $\{\epsilon\}$. Subsequently the elastic constants in $[\mathbf{C}]$ are also symmetric

($C_{ij} = C_{ji}$) and the matrix can be reduced to a 6×6 matrix where there are 21 independent elastic constants.

$$[C] = \begin{bmatrix} C_{11} & C_{12} & C_{13} & C_{14} & C_{15} & C_{16} \\ & C_{22} & C_{23} & C_{24} & C_{25} & C_{26} \\ & & C_{33} & C_{34} & C_{35} & C_{36} \\ & & & C_{44} & C_{45} & C_{46} \\ \text{Symmetric} & & & & C_{55} & C_{56} \\ & & & & & C_{66} \end{bmatrix} \dots\dots\dots (4.3)$$

A further simplification can be made because the unidirectional ply is orthotropic, that is, it has three mutually-orthogonal planes of material property symmetry. The corresponding stiffness matrix is then specific to these principal material coordinates. When this symmetry is incorporated into [C], the matrix has only nine independent elastic constants as follows:

$$[C] = \begin{bmatrix} C_{11} & C_{12} & C_{13} & 0 & 0 & 0 \\ & C_{22} & C_{23} & 0 & 0 & 0 \\ & & C_{33} & 0 & 0 & 0 \\ & & & C_{44} & 0 & 0 \\ \text{Symmetric} & & & & C_{55} & 0 \\ & & & & & C_{66} \end{bmatrix} \dots\dots\dots (4.4)$$

By noting that, for the unidirectional ply, the material properties in the y-and z-axis directions are identical (Figure 4.1 (a)), a final simplification can be made. It becomes apparent that the ply is transversely isotropic, so that the stiffness matrix becomes:

$$[C] = \begin{bmatrix} C_{11} & C_{12} & C_{12} & 0 & 0 & 0 \\ & C_{22} & C_{23} & 0 & 0 & 0 \\ & & C_{22} & 0 & 0 & 0 \\ & & & (C_{22} - C_{23})/2 & 0 & 0 \\ \text{Symmetric} & & & & C_{66} & 0 \\ & & & & & C_{66} \end{bmatrix} \dots\dots\dots (4.5)$$

which now has only five independent constants. The constants are determined from the effective engineering properties.

For engineering problems, often the stresses are known and the strains are to be determined, so the equation (4.2) is rearranged as follows:

$$\{\mathbf{e}\} = [\mathbf{C}^{-1}]\{\mathbf{s}\} \dots\dots\dots (4.6)$$

It is common practice to designate $[\mathbf{C}^{-1}] = [\mathbf{S}]$ so equation (4.6) becomes

$$\{\mathbf{e}\} = [\mathbf{S}]\{\mathbf{s}\} \dots\dots\dots (4.7)$$

The constants of $[\mathbf{S}]$ are described as:

$$S_{11} = \frac{1}{E_{11}}$$

$$S_{22} = S_{33} = \frac{1}{E_{22}}$$

$$S_{44} = \frac{2(1 + \nu_{23})}{E_{22}}$$

$$S_{55} = S_{66} = \frac{1}{G_{12}}$$

$$S_{12} = S_{21} = S_{13} = S_{31} = \frac{-\nu_{12}}{E_{11}}$$

$$S_{23} = S_{32} = \frac{-\nu_{23}}{E_{22}}$$

where: E is the tensile modulus, G is the shear modulus, and ν is the Poisson ratio of the material. From the above, it can be seen that five engineering properties are required to describe fully the three-dimensional ply element depicted in Figure 4.1(a).

Laminates often consist of a variety of ply types and orientations. For the three-dimensional approach to be used, each ply is described separately and its stiffness properties are combined within a global stiffness matrix for the entire component being investigated. FEA is one method of doing such an analysis. However, due to the relative thinness of plies (of the order of 1 mm at the maximum), the number of brick elements required to describe a component would be excessive, so discretisation is often conducted on a laminate level to reduce the number of equations to a high but realistic level. A further simplification was demonstrated by Taufik, Barrau & Lorin (1999) when they used a virtual work approach to develop the stiffness matrix for an FRP beam of arbitrary cross-section. The analysis was

then compared favourably against unmodified FEA for the same beam. Taufik concluded that the method could be used as an alternative to FEA with the advantage of greater efficiency with no loss of accuracy. Furthermore, taking into account geometrical considerations, further simplifications can be introduced that greatly reduce computational effort without a major sacrifice of accuracy.

4.2.3 Two-dimensional analysis

Plies are thin compared to their length and width, so they are often assumed to be in a simple two-dimensional state of stress. For this situation the z-axis stresses and strains are ignored and equation (4.7) becomes

$$\begin{Bmatrix} \mathbf{e}_1 \\ \mathbf{e}_2 \\ \mathbf{g}_{12} \end{Bmatrix} = \begin{bmatrix} S_{11} & S_{12} & 0 \\ S_{21} & S_{22} & 0 \\ 0 & 0 & S_{66} \end{bmatrix} \begin{Bmatrix} \mathbf{s}_1 \\ \mathbf{s}_2 \\ \mathbf{t}_{12} \end{Bmatrix} \dots\dots\dots (4.8)$$

where \mathbf{g} is the absolute shear strain and only four engineering properties are required. The stiffness matrix is still particular to the orthogonal axis system, but can be transformed to any axis system to be investigated. Plies are stacked one upon the other to form a laminate. The combination of the individual ply property matrices into an equivalent plate property matrix may be achieved via a method commonly referred to as Classical Laminate Theory, described in Appendix A. This method is incorporated into many FEA packages. By ignoring the z-axis stresses and strains, assumptions are made; these assumptions are:

- the thickness of the laminate is constant and is much smaller than the length and width;
- displacements are small when compared with the laminate thickness;
- transverse shear strains are negligible;
- tangential displacements are linear functions of the z coordinate;
- each ply obeys Hooke's law; and
- transverse shear stresses are zero on the boundary surfaces.

The assumptions define the plate according to Kirchhoff's plate theory, where normals to the middle surface remain straight and normal during deformation. The result of this assumption is that shear stresses throughout the plate's thickness are ignored. Subsequently the displacements within the plate can be expressed as:

$$\begin{aligned}
u(x, y, z) &= -z \frac{\partial w_m(x, y)}{\partial x} \\
v(x, y, z) &= -z \frac{\partial w_m(x, y)}{\partial y} \dots\dots\dots (4.9) \\
w(x, y, z) &= w_m(x, y)
\end{aligned}$$

where u , v , and w are the displacements in the x , y and z directions respectively and w_m represents the displacement in the z -axis direction of the middle plane.

An improvement upon Kirchhoff's plate theory is Mindlin's plate theory, where rotation components, \mathbf{q}_x and \mathbf{q}_y , relative to the middle plate, after deformation, are included. The inclusion of these rotations allows for shear strains, so that equations (4.9) become:

$$\begin{aligned}
u(x, y, z) &= -z \frac{\partial w_m(x, y)}{\partial x} + z \mathbf{q}_y \\
v(x, y, z) &= -z \frac{\partial w_m(x, y)}{\partial y} - z \mathbf{q}_x \dots\dots\dots (4.10) \\
w(x, y, z) &= w_m(x, y) + z \frac{(\mathbf{q}_x^2 - \mathbf{q}_x^2 \mathbf{q}_y^2)/2 + \mathbf{q}_y^2}{2}
\end{aligned}$$

Most FEA programs use the latter Mindlin approach for their shell elements. However, those that combine this with classical laminate theory ignore shear through the thickness, reducing the method back to Kirchhoff's plate theory. This is significant because shear stresses through a plate and the associated deformations can be substantial in materials that have high anisotropy ratios (E/G), such as FRPs.

The incorporation of shear into classical laminate theory will provide a significant improvement in the method, consequently a number of researchers have concentrated upon the evaluation and improvement of the method in conjunction with FEA shell elements. For example, Chandrashekhara & Bangera (1993) used the ABD matrices from classical laminate theory (Appendix A) to develop a non-linear analysis technique. The technique incorporates iterations and convergence criteria that included the higher order shear deformation and geometric non-linearity. Comparisons were made for differing the ply orientations on theoretical models and substantial differences in results were noted between standard FEA and Chandrashekhara's formulation for beams with angle-ply orientations. Another approach was formulated by Kim, Davalos & Barbero (first published 1996) who used a layer-wise constant-shear beam theory, combined with classical laminate theory,

while formulating a new FEA element that allowed for the progressive failure of layered composite beams. The moment and shear stiffness were calculated and used to predict the failures of laminates. Comparisons with experimental testing provided favourable outcomes. This latter development was used and expanded by Lee et al. (1995) who incorporated non-linear material descriptions into the FEA elements.

These two-dimensional approaches give good approximations of real beam behaviour; however, they still rely on computer solution for even the simplest beam problem. A further simplification can be made that reduces the computational effort and provides a set of properties of an entire beam.

4.2.4 One-dimensional analysis

Plate theory can be further simplified for members whose depth (thickness) and width are small compared to their length. Such a member is a beam. The simplification is facilitated by making the further assumption that:

- normal and shear stresses and strains in the y-axis directions are not considered, so the only stress components present are \mathbf{s}_x and \mathbf{t}_{xz} .

For the beam element, (4.8) becomes:

$$\begin{Bmatrix} \mathbf{e}_x \\ \mathbf{g}_{xz} \end{Bmatrix} = \begin{bmatrix} S_{11} & 0 \\ 0 & S_{66} \end{bmatrix} \begin{Bmatrix} \mathbf{s}_x \\ \mathbf{t}_{xz} \end{Bmatrix} \dots\dots\dots (4.11)$$

so that the shear and normal stresses are independent. To describe a beam, only two effective beam property constants are therefore required (E and G). These properties are combined with the beam section properties: area (A), second moment of area (I), and torsion constant (J) for solution of a number of loading regimes.

4.2.4.1 Flexure

Stress versus strain

Based on classical beam theory, the strain distribution across the cross-section of a beam under flexure is linear, as depicted on Figure 4.3(a). For the case of an isotropic homogeneous beam, these strains may be multiplied by the modulus of the material to obtain the stress distribution, Figure 4.3(b). For isotropic materials, it is common practice to define failure by the maximum stress criterion, using the formula:

$$s = \frac{M}{Z} \dots\dots\dots (4.12)$$

where: M is the moment and Z is the section modulus ($Z = I / c$, where c is shown in Figure 4.3). However, FRP beams differ from their homogeneous counterparts because the ply and laminate properties vary throughout the section. Even in the linear elastic range, the stress distribution within the beam is not linear, rather it depends upon the location and modulus of the individual ply materials as shown on Figure 4.3. Due to this varied stress field, it is more convenient to specify the ultimate capacity of an FRP beam in terms of the maximum strain criterion rather than in terms of stresses.

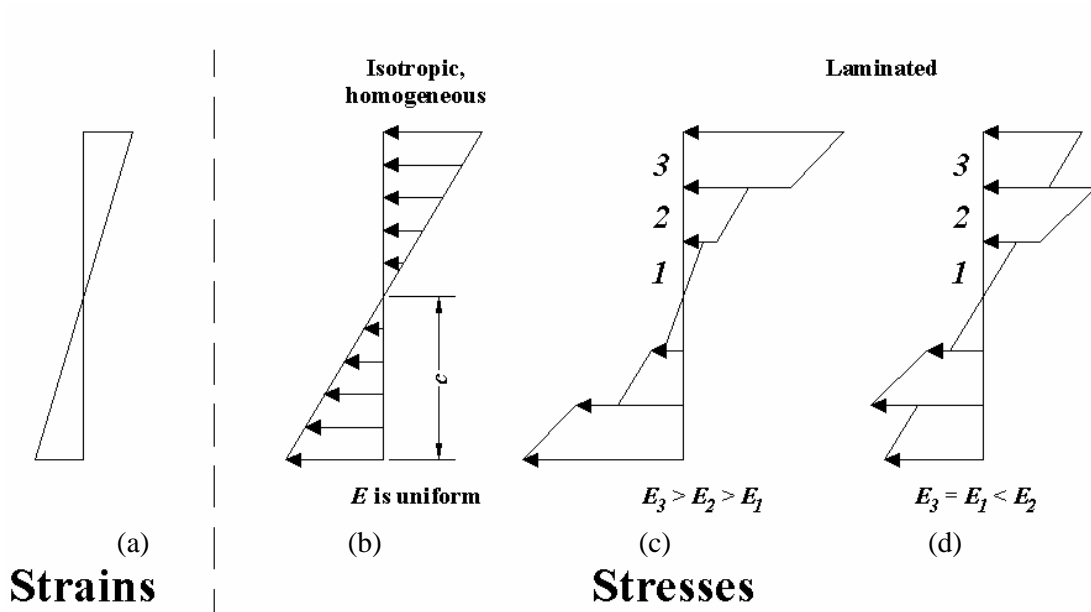


Figure 4.3 Strain and stress distributions throughout a beam in bending

Beam theory

In the one-dimensional approach, the assumptions of Kirchhoff’s plate theory remain and the shear stresses throughout the beam are ignored. For a pure flexure situation, this assumption is valid. However, as mentioned previously, shear is of importance when considering FRP, which therefore warrants the use of methods that include shear deformations. Such a method is Timoshenko’s beam theory (Timoshenko 1921).

Like Mindlin plate theory, Timoshenko's beam theory allows for the rotation of the plane section. Added to Timoshenko's beam theory is a shear adjustment factor (k) to allow for the non-uniform shear stress distribution at a section while retaining the one-dimensional approach. An example is a simply-supported beam of length L subject to three-point bending, with a load of P (Mallick 1997, p. 241). Equations (4.13) and (4.14) give the calculated deflection at mid-point, via the Euler-Bernoulli and Timoshenko methods, respectively.

$$\Delta = \frac{PL^3}{48EI} \dots\dots\dots (4.13)$$

$$\Delta = \underbrace{\frac{PL^3}{48EI}}_{\text{Moment}} + \underbrace{\frac{PL}{k4GA}}_{\text{Shear}} \dots\dots\dots (4.14)$$

It can be seen from (4.14) that the effects from shear can be added to the effects from pure bending.

Determination of engineering constants

Many researchers and manufacturers have concentrated on determining the engineering constants of FRP beams for use with Timoshenko's beam theory. Bank (1987) used an adaptation of the theory (adapted by Cowper (1966)) for thin-walled laminated beams. The bending and shear coefficients presented by Timoshenko were developed for composite materials. Based upon the longitudinal modulus of the materials, Bank calculated the coefficients for uniform thin-walled beams and used the transformed section of the beam to ascertain beam stiffness values. He concluded that Timoshenko's beam theory was appropriate. Bank's approach of using the longitudinal modulus for the calculation of the transformed section when analysing the beam for shear contradicts Kollbrunner & Basler (1969, p. 17) who showed that the use of the shear modulus was appropriate. This contradiction was not resolved, thereby casting uncertainty over Bank's conclusions.

In later investigations, Bank (1989) pointed out that the manufacturers gave full section engineering constants, such as E , G , and I , which were experimentally determined. He described how the coefficients are experimentally determined and demonstrated the method for two beams. Bank, Nadipelli & Gentry (1994) also determined the shear modulus of pultruded beams experimentally with the use of strain gauge rosettes. The formula

described used the first and second moments of area around the neutral axis to convert the strains into an appropriate modulus. Roberts (2001) further demonstrated the experimental determination of the engineering constants and expanded the scope to include torsion and buckling. Roberts tested three pultruded I-beams and determined the constants E and G in both cross-section axis directions as well as the torsion constant, J . Flexural modulus was determined using 3 and 4 point bending tests and the values obtained from both tests were within 3% of each other. However, comparison against the manufacturer's published properties were given and showed errors in the order of 8% to 38% for flexural modulus (manufacturer's values low) and 14% below to 17% above for shear modulus. Such a scatter in modulus values raises doubts as to the reliability of manufacturers' data and the level of quality control of the manufacturing process of the beams used by Roberts. Furthermore, Barbero, Fu & Raftoyiannis (1991) found that 'theoretical prediction of ultimate bending strength based on linear bending theory grossly overestimates the load-carrying capacity of the members when using the manufacturers' provided section properties. Additionally, Mottram (1991) found that deflections of beams were substantially lower than expected when using the manufacturers' quoted modulus value. All of which indicates that doubts as to the accuracy of manufacturers' specifications are widespread.

Experimental determination of the engineering constants requires prototyping and testing. Analytical determination alleviates the need for such a trial-and-error approach to FRP analysis. Theoretical formulations of beam characteristics have been derived or altered and subsequently investigated by Barbero, Fu & Raftoyiannis (1991), Kedward, Wilson & McLean (1989) and Taufik, Barrau & Lorin (1999). They have developed formula based upon kinematics and energy methods that can be incorporated into computer systems. These systems can then be used to determine properties of beam cross-sections. Barbero et al., whilst investigating the ultimate bending performance of a pultruded beam, used equivalent material properties that were formulated for laminates using the rule of mixtures. Barbero et al. pointed out 'that shear deformation effects are important'. Barbero's conclusion was confirmed by Patel, Tripathy & Pang (1993) when they used a strain energy formulation (which included shear components) to analyse a multi-celled box beam. Furthermore, Ascione, Feo & Mancusi (2000) showed that there was a marked increase in deflections when shear was included in Vlasov's classical thin-walled beam theory (Vlasov 1961).

Due to the importance of shear within FRP beams, Barbero, Lopez-Anido & Davalos (1993) adapted Timoshenko's beam theory, using kinematics and energy principles to formulate a method that required computer solution. Barbero et al. formulated kinematic equations for bending and shear stress distribution, as well as for the location of the shear

centre. Using the shear stress distribution, a shear correction factor was used with Timoshenko's beam theory. The results of the analysis were compared with three-dimensional models analysed with the FEA program ANSYS (ANSYS Inc. 1997), which produced favourable results.

Combination of material and section constants into one term

To account for the variety in modulus values of materials and orientations within an FRP beam, second moment of area, I , and modulus, E , were combined into one term, D_y , by Davalos, Qiao & Salim (1997) in an analysis approach that relied on classical laminate and Timoshenko's beam theory. The combination of the two constants, E and I , was considered as the only way to provide engineering constants to FRP sections that were built up using a number of fibre types or orientation, due to the different moduli of the individual fibres or orientations. Nagaraj & Gangarao (1997) conducted experiments on pultruded box and I-beams to determine the combined EI values of the beams. Subsequently, new beams were tested in three-point bending to verify the validity of an approximate classical lamination theory and FEA predictions. Results were in agreement with the predictions. Fibre orientation was shown to be important. Nagaraj & Gangarao used Barbero's methodology of a shear correction factor for predicting shear stiffness. However, Nagaraj & Gangarao ignored the contribution of the flanges of the beams when calculating the shear stiffness, with any error being absorbed within the shear correction factor.

The combination of E and I into one value continued with Barbero (1998) publishing basic beam formulae within a handbook, using the one term D_y in place of EI and shear correction factors F with k incorporated into the value GA . Barbero & DeVivo (1999) also used a shear stiffness factor of GA when investigating the performance of pultruded beam-columns.

4.2.4.2 Buckling

Pultruded beams have been confirmed to fail primarily due to flange buckling. Subsequently, more analysis methods that included the second-order failure modes were formulated and investigated. Mottram (1991) investigated box beams and tested them for compression-face buckling, tension material failure, compression material failure and shear failures, thereby expanding on Johnson's methodology (Johnson 1985) (which was adapted from Bulson's (1970) investigations of the stability of flat plates). The methodology required the use of given manufacturers' material and sectional coefficients I , E and G . Experiments were conducted which resulted in Mottram concluding that the section properties given by the manufacturers were suspect. Roberts' results (presented earlier)

indicate that Mottram's conclusions may be justified. Another approach was used when Gilchrist et al. (1996) investigated shear, lateral torsional buckling, warping, local flange and web buckling of pultruded I-sections. Gilchrist et al. used the shear moduli calculated with the use of a 'Laminate Analysis Program' (Centre for Composite Materials 1991) to determine deflections. A further approach was presented by Silvestre & Camotim (2001) who identified the eight most relevant cross-section buckling deformation modal shapes for laminated C-sections. Silvestre & Camotim's formulation used classical laminate theory to gain the section properties, which removed the need to rely on manufacturers' data or testing. However, Silvestre & Camotim gave no verification against experimental data and, as such, the formulation remains untested.

Further formulations with the use of kinematic assumptions were made and constitutive relationships developed with the use of laminate theory by Morey, Johnson & Shield (1998) in their formulation of a theory for the buckling of symmetric composite beams. Morey et al. found that the Timoshenko buckling load for laminated composite beams was 'inadequate for laminates that exhibit anti-clastic curvature' (The beam results do not include a stiffness effect - anti-clastic curvature. As the plate bends, the section bows. This bowed section is stiffer than a perfectly flat section.). Anti-clastic curvature would only be of major concern for thin wide flanges of beams, which are scarce in civil engineering systems. Therefore, Timoshenko's theory should be acceptable in most cases.

4.2.4.3 Lateral torsional buckling

A secondary failure mode of vital importance in determining the capacity of beams spanning between lateral restraints is the lateral buckling of the entire section. In a continuation of earlier investigations, Bank (1990) made use of transformed sections when modifying beam theory to include cross-sectional warping. Timoshenko beam theory was modified to provide an approximate method for the calculation of the beam twist. Bank noted that both shear and twist become more significant for beams having shorter spans and larger anisotropy ratios (E/G), thus highlighting the importance of considering shear and lateral torsional buckling deformations in FRP beams. Another attempt to formulate a buckling expression was conducted by Roberts (2001). Roberts expressed the lateral and local buckling modes using governing energy principles. The resultant equation was identical to the approximate solution by Timoshenko (1961). Roberts then obtained the engineering constants by testing pultruded beams. Roberts concluded that the constants obtained could be used in Timoshenko beam theory and buckling analysis.

In order to model lateral torsional buckling Loughlan & Ata (1995) discussed the torsion constant of open sections. Loughlan & Ata referenced Saint Venant theories to derive relationships. FEA was conducted, which correlated with the theory for general warping displacements, although errors appeared when investigating warping constants. A Z-section was used in the analysis and the theory presented was based on flat elements of symmetric laminates. Equivalent thickness was used in the theory via the use of the longitudinal modulus (not shear modulus as shown to be appropriate by Kollbrunner & Basler (1969)). Loughlan & Ata (1997a, b) continued investigations with box beams using the same methodology they had developed for open sections. The analysis method was compared against FEA and experimental results, with favourable comparisons. In later work, Loughlan & Ata (1998) pointed out that standard beam theory is shown to give erroneous predictions of the torsional response of the composite beams. However, this conclusion may not be valid, as the error could have been due to the use of the longitudinal modulus instead of the shear modulus when calculating the engineering properties.

Torsional and torsional buckling analysis have been conducted by Davalos & Qiao (1997), and Kabir & Sherbourne (1998) who have independently developed the same strain-energy-based formulations for lateral and distortional buckling of I-beams. Davalos & Qiao used total potential energy and strain energy methods to formulate the ABD matrix (named the $\alpha\beta\delta$ matrix by Davalos) for a universal column section. Davalos & Qiao then formulated rotation and displacement functions along the beam length for torsional buckling using shape functions (Ma & Hughes 1996). The new formulations were compared to three-dimensional FEA models and experimental data, with results that agreed. Alternatively, a new approach for open and closed sections was discussed separately by Massa & Barbero (1998) when formulating the stiffness matrix for a generic beam cross-section. Torsion and shear sectional properties of beams were derived as well as the principal axis for torsion of any segment. The method involved dividing the section up into a series of flat and curved portions. The mechanical property formulated was GA_s . The theory was compared against the results of FEA and experiments with favourable outcomes. Massa concluded that the combination of the shear modulus and shear area into one constant was advantageous.

Following a different approach, Kabir & Sherbourne (1998) discussed local and lateral buckling of a pultruded FRP I-beam. Buckling deformation was considered sinusoidal. Models based on the Cauchy stress tensor and Kirchhoff's theory, were used. The flange torsional rigidity was defined as GJ and the web analysed separately as a plate with post-buckling stiffness being considered. Kabir & Sherbourne showed that the post-buckling load at failure was greater than the load at the bifurcation point. The use of a

reduced value of E was verified against a reduced section-size approach. This method required programs to solve eigenvalue problems. Comparisons were made using an example of an FRP pultruded I-beam section. Good relationships between local and overall buckling were shown for the following three cases: flange buckling precipitates failure of the beam; flange buckling occurs prior to overall buckling, followed by failure of the beam; and overall buckling occurs followed by failure of the beam. Kabir & Sherbourne determined that the length of the beam was related directly to the failure mode that occurred and that the primary failure mechanism was often flange buckling. In a continuation of earlier investigations, Kabir & Sherbourne (1999) gave a theoretical analysis of buckling behaviour for plates and pultruded FRP I-beams using Rayleigh-Ritz, Galerkin and numerical methods. As in previous work, Kabir & Sherbourne concluded that ‘the compressive flange limits buckling strength’.

The one-dimensional approach has shown a wide variety of applications, with simplicity of calculation. Many researchers have reported good correlation between theoretical formulations and experimental results. Silvestre & Camotim (2001) used classical laminate theory to define beam-wall properties when they adapted a generalised beam theory to produce a formulation for thin-walled FRP members. Silvestre & Camotim illustrated the use of the formulations and noted, ‘in the context of linear stability analyses, the generalised beam theory is a rather elegant, insightful and efficient alternative to finite element and /or finite strip methods. In fact, general beam theory provides a general unified approach to accurately solve a wide range of problems ...’.

4.2.5 Time effects

So far, the discussion has concentrated upon short-term loading. In general, FRP’s are prone to undergo creep under sustained load since they contain a significant amount of polymeric material, which is visco-elastic in nature. These long-term creep effects are even more deleterious in GFRP, since glass fibres also undergo stress corrosion. Therefore, it is desirable to ascertain the performance of a beam with regards to time.

Analytical predictions of creep behaviour are problematic since it is a micro-level phenomenon with a large number of variables contributing to its rate. In addition, the variability of production methodologies employed in the manufacture of FRP components render idle the generalisation of any analytical prediction. Therefore, it is common practice to include long-term tests for any new FRP beam (Alwis 1998; Deskovic, Meier & Triantafillou 1995; Evans, Ningyun & Chandler 1990; Hoa 1995; Holmes & Rahman 1980; Lee et al. 1995; Mosallam & Bank 1991; Ningyun & Evans 1995). The determination of

long-term deflections has often been facilitated via experimental testing of completed components. Curve-fitting techniques have been employed, and models developed so that extrapolation of the trends can be performed.

Previous research (Hollaway & Howard 1985; Holmes & Rahman 1980) has indicated that sufficient data could be obtained over a 10000 hour loading period, so that extrapolation for longer periods could be valid. Hoa (1995) made use of Holmes & Rahman's observation that the majority of creep occurred in the first 1000 hours of loading. After loading a composite box beam for a period of 3 months (approximately 2200 hours), Hoa provided a design example to predict the long-term deflections. As no long-term experimental validation was given, Hoa's method may produce gross errors when extrapolated, due to the small amount of experimental data obtained.

In an attempt to reduce the need for full-scale testing, the continuum approach was employed by Mosallam & Bank (1991). Creep models were formulated based upon testing coupons cut from pultruded FRP beam webs and flanges. Mosallam & Bank conducted axial and shear coupon tests to formulate the models based upon the Boltzmann superposition principle (Ward & Hadley 1993, p. 51). These models were then compared against results obtained from full-scale testing of a frame constructed from pultruded sections, with favourable outcomes.

Deskovic, Meier & Triantafillou (1995) used three methodologies to study the creep behaviour of their beam: a rheological model for concrete creep combined with either Findley's power law (Findley & Worley 1951) or a continuum approach for polymer matrix creep. They assumed that the creep attributed to glass fibres could be ignored and would be inconsequential when compared to the concrete and polymer matrix. Subsequently, the polymer matrix was modelled, with allowance of the fibre fraction. Such an approach, while providing reasonable results for relatively short-term loading, may not be suitable for extrapolation into the longer term, as glass is subject to stress corrosion rupture.

It appears that such approaches can only provide indicative deflection prediction with no account of the strength limit state over time. Due to these fundamental limitations, the recommendation by Hogg (1998) that long-term creep tests be performed in order to gain a realistic expectation of structural adequacy is pertinent.

4.3 Shortcomings of current methodologies used to determine FRP beam section size

4.3.1 General

The traditional approach to FRP beam size determination within the aerospace and automotive industries relies upon close consultation and teamwork between material suppliers, manufacturers, the engineer and the end-user. Extensive FEA is conducted, followed by successive prototyping and testing, until the desired behaviours are observed. The costs involved in the process are considered acceptable or are able to be offset by the number of components produced. However, this arrangement is not the norm for civil engineering systems. Indeed, in most civil engineering situations, a single item is requested by the end-user and then designed by an engineer. The design is given to a manufacturer to produce and install. The engineer must specify clearly the materials and design, with the confidence that the manufacturer will produce the item with the same material characteristics specified in the design.

As it has already been pointed out, it is clear for cost and practical considerations that the traditional method is inappropriate in civil engineering applications. This has prompted researchers to recognise that a design methodology along the lines of current steel and timber design codes is required. This would allow civil engineers to provide a cost-effective FRP design service with confidence, expedition and safety (Head & Templeman 1990). For any design methodology to be considered complete, it needs to address: load and material characterisation, and methods to determine section size and geometry. Load and material characterisation fall outside the scope of this study and are not discussed herein. The determination of section size and geometry is however contingent upon analysis methods. Therefore, the techniques reflect the current understanding of behaviours and the shortcomings in the techniques highlight areas where further research is warranted. To determine the section size and geometry of an FRP beam all the behaviour types for the particular application under investigation need to be considered. For the simply-supported beam the behaviours that require consideration are: moment, shear, combined moment and shear, lateral torsional buckling, bearing, and creep. To simplify the determination process, it is standard practice to consider the behaviour types individually, and provide separate interaction rules. With this goal in mind, methodologies to determine section size, adapted from one-dimensional analysis methods, have been formulated. These techniques are discussed in the following sections.

4.3.2 Moment and shear

The two most common loading types that a beam must resist, to be considered structurally adequate, are moment and shear. Barbero, Fu & Raftoyiannis (1991), Barbero (1998), and Barbero & DeVivo (1999) have developed simple formula based upon elastic theory for design of FRP beams. In order to simplify the calculations, Nagaraj & Gagarao (1997) altered Barbero et al.'s methodology by ignoring the influence of secondary directions. The simplification made the assumption that the lamina in the beam is isotropic. In both cases, coefficients obtained from experimentation are required in order to perform the analysis. The manufacturer provided these coefficients. However, this methodology is practically cumbersome as the process requires prototyping and testing. Furthermore, as highlighted in the preceding sections, the use of manufacturers' data is questionable; the data should not be used until doubts as to its accuracy have been dissipated. An alternative approach for FRP beam size determination was developed by Van Erp (1999). The method is based upon the coupling of the forces in the top and bottom flanges. The method was found to be reasonably accurate within the linear elastic range, as subsequently demonstrated by experiment. Van Erp concluded that, for design purposes, such a result was acceptable as a practical starting method to estimate beam dimensions.

Two publications dedicated to FRP design that give governing rules for moment and shear capacity are the Structural Plastics Design Manual (American Society of Civil Engineers 1984) and the Eurocomp Design Code (Clarke 1996). Both are based upon the 'limit-state' design approach. The Structural Plastics Design Manual ignores the differing moduli in tension and compression of FRP. Section properties are determined via the use of an altered transformed section approach. The manual provides for checking against second-order effects, however it ignores shear deformation. The Eurocomp Design Code gives conservative design methodologies based on material and section coefficients. The latter recommends experimental determination of the section property coefficients, and does not give any method of their analytical determination. Shear capacity is given in terms of shear area, shear stress, and a partial safety factor for material resistance.

4.3.3 Combined moment and shear

Beams are rarely used in states of pure bending or pure shear. The most common combined loading in design is that of moment and shear. Interaction charts have been produced for sections of differing materials. These charts are in terms of the ultimate capacity of the section in a state of pure shear or pure bending. AS4100 steel structures code (Standards Australia 1998), AS3600 concrete structures code (Standards Australia 2001) and

the Eurocomp Design Code all give relationships that are ‘deemed to comply’. These relationships are graphically represented on Figure 4.4.

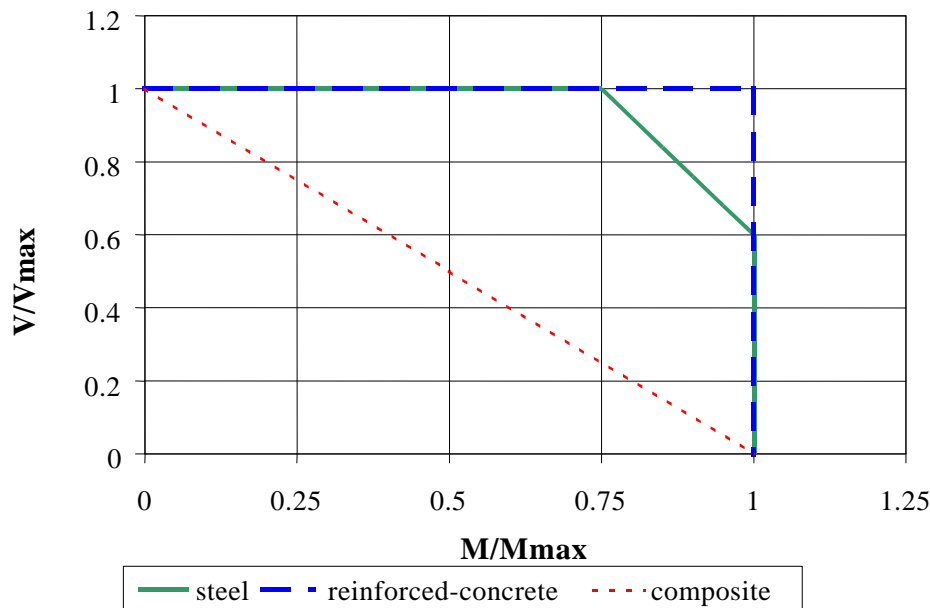


Figure 4.4 Published moment-shear interaction for steel, concrete and composites

As it appears from the curves, unlike steel and reinforced concrete, there is an interaction between bending and shear for FRP. Given the disparity in FRP beam design (pultrusion, box, combination of core materials, et cetera) this curve may be representative of the behaviour of one prototype but may not be generalised. Furthermore, the inclusion of core material may confer on the beam a behaviour similar to that of RC beams. As it appears from the literature, every prototype has a unique behaviour. Therefore, it is all the more important to investigate this synergy between shear and bending. This will be investigated in subsequent chapters.

4.3.4 Lateral torsional buckling

There are a number of ways to determine the critical buckling moment of a beam spanning between lateral restraints. Commonly, the ultimate strength in design is considered to be at the initiation of lateral torsional buckling. For example, the lateral torsional buckling of steel beams is assessed in terms of the reference buckling moment, coefficients for slenderness, the shape of the moment diagram, restraint type, and spacing. The reference buckling moment is determined by analytical formulation as shown by Gaylord, Gaylord & Stallmeyer (1992, p. 290). A similar approach was developed by Morey, Johnson & Shield (1998) for FRP beams with constant wall thickness. They formulated a simple beam theory

using virtual work methods. Morey et al. gave a formula for the non-dimensional buckling moment that is similar to Gaylord et al's equation. The Structural Plastics Design Manual and Eurocomp Design Code also use Gaylord et al's equation. However, two sets of coefficients, C_l for loading and restraint type, and K for effective length factor, have been added. The factors used are different from those used in steel design. The formula presented in the Eurocomp Design Code uses the fourth root instead of the square root in the calculation. However, this appears to be incorrectly typed as Clarke uses the same formula as presented in the Structural Plastics Design Manual (which uses the square root) when giving an example of the calculation. Regardless of which method is used, section properties of the beam are required to ascertain the lateral buckling moment. Therefore, the determination of these properties is necessary.

4.3.5 Bearing capacity

In general, FRP beams have a lower bearing capacity than their concrete or steel counterparts. Even though it is of primary importance in design, it is yet to attract a thorough investigation. So far, the approach adopted in design codes mimics that used in steel design. The Structural Plastics Design Manual and Eurocomp Design Code use similar formula as those shown by Gaylord, Gaylord & Stallmeyer (1992, p. 358). Both codes include the use of a bearing angle (α) of 45 degrees to determine a crushing and buckling length for a box section as depicted on Figure 4.5.

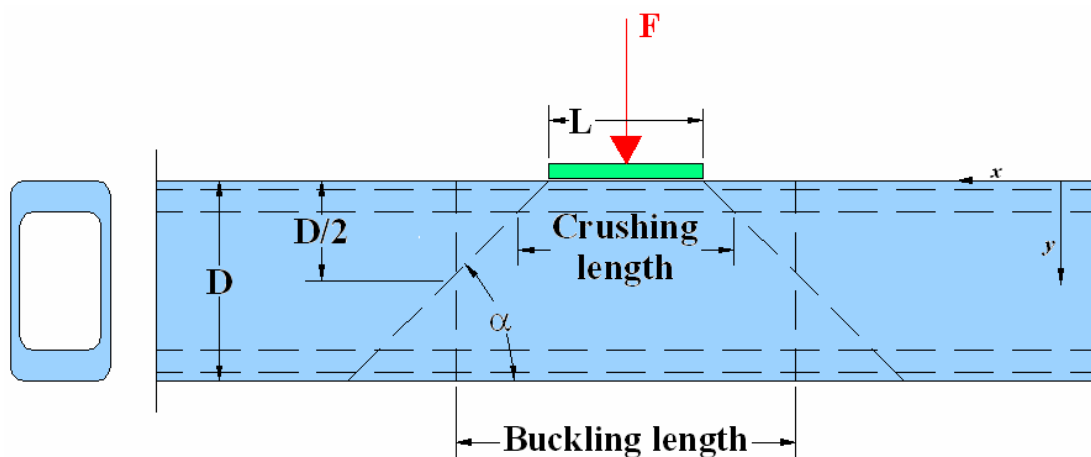


Figure 4.5 Bearing distribution angle

The stress distribution under the load is not uniform; the use of the angle however, simplifies the analysis. A 45 degree angle makes sense for an isotropic material such as steel. The

fibre orientation within FRP beams is likely to influence the stress distribution, and therefore warrants further investigation.

4.3.6 Creep and creep rupture

Creep deformations are difficult to characterise as the mechanisms are at the micro-mechanical level. However micro-mechanics modelling is inappropriate in design. Therefore design codes have adopted simplified creep formulations for use on most beams. In all cases, experimental verification is recommended because of the variability in FRP beam designs. Nonetheless, methods are given for approximate solutions based upon existing experimental data for particular mat types. The Structural Plastics Design Manual and Eurocomp Design Code employ a method where the modulus of the component is reduced over time. The graphs given on Figure 4.6 and Figure 4.7 have limitations, as they are only useful for the laminate types shown within them. The graphs were formulated from experimental results over 26000 hours for the Structural Plastics Design Manual and 10000 hours for the Eurocomp Design Code, and then extrapolated.

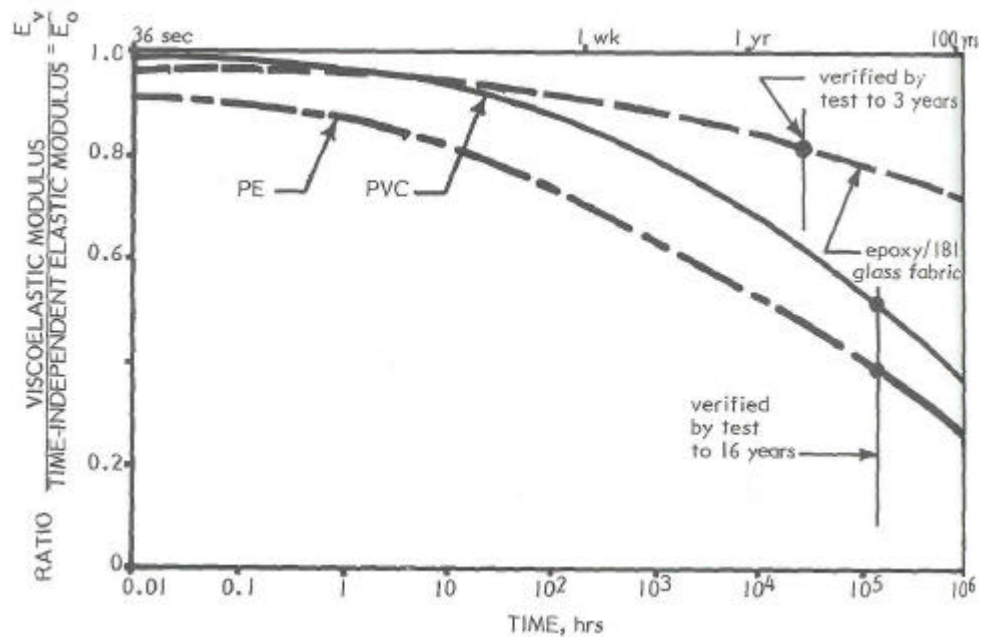


Figure 4.6 Indicative creep modulus versus time (American Society of Civil Engineers 1984, p. 210)

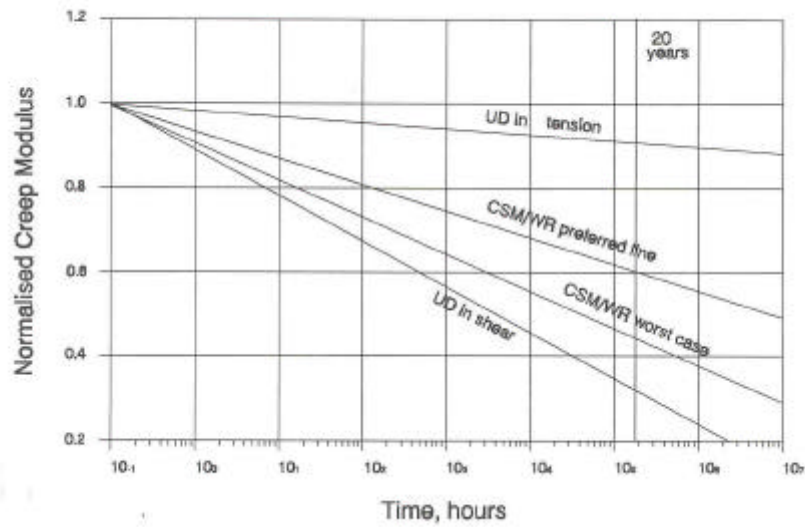


Figure 4.7 Indicative creep modulus versus time (Clarke 1996, p. 127)

Added to the uncertainty of creep is creep rupture in glass fibres, which must be taken into account to avoid catastrophic failures of structures. The Eurocomp Design Code provides a chart, shown on Figure 4.8, giving the reduction of tensile strength over time for specific glass laminate mats.

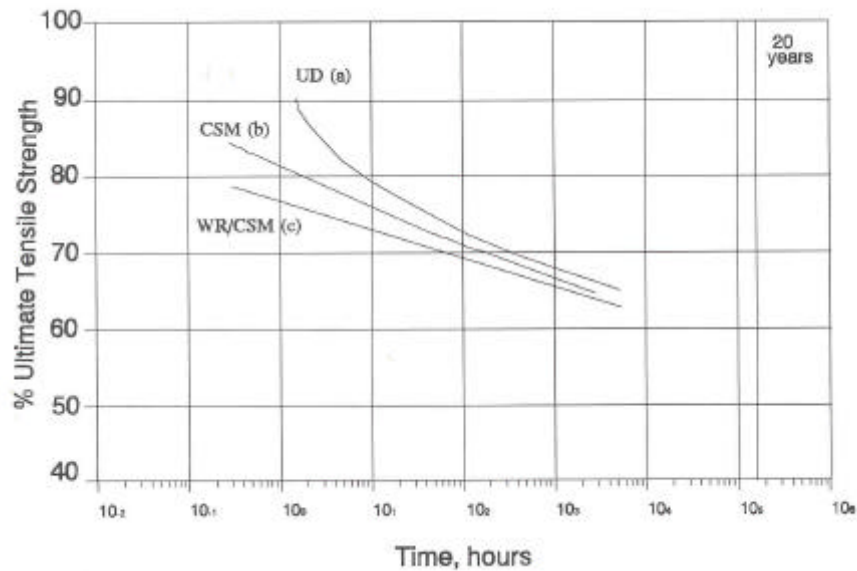


Figure 4.8 Tensile stress rupture of polyester composites (Clarke 1996, p. 128)

The graph appears to have the different mats converging and the lines becoming asymptotic to 50% of instantaneous ultimate strength. This then tends to correlate with the creep chart

to indicate that, for long-term use of glass fibres, the loads must be below 50% of the instantaneous ultimate failure load. Unfortunately, no definitive statement is given because there is a lack of data concerning long-term exposure. Likewise, the studies on unidirectional fibres (Phoenix 2000) are restricted to components where the main fibre direction is in line with the axis of principal stress. Again the data does not extend to over 10^4 hours. The Structural Plastics Design Manual gives factors of 50% and 40% for long-term loading in compression and tension respectively. The Civil Engineering Research Foundation recommends no greater than 25% of the instantaneous failure stress be placed upon components subject to long-term loadings (Karbhari & Chin 2001). This disparity in recommendations between codes that purport to give limit-state design rules and independent reports is of concern and requires further investigation prior to the widespread design of FRP components in civil engineering systems.

4.3.7 Ductility

Another area of concern for civil engineering structures is the one of failure/post-failure behaviour of a structure. This is often termed ductility. The word ductility has been given numerous meanings throughout the literature. The word refers primarily to a material characteristic. For a material to be considered ductile, increasing deflections are produced when continuously held at a yield stress level, that is, the strain continues to become larger as the material plastically deforms. Steel is an example of a material that exhibits ductility. Figure 4.9 shows a comparison between steel and unidirectional glass laminate. Generally, FRP materials do not plastically deform - and therefore are considered non-ductile - even though ductile behaviour of composite structures may still be achieved. What is sought in such a situation is that there is sufficient visual warning that the structure is failing; deflections of primary elements become sufficiently high to warn people of imminent failure. Furthermore, in dynamic loading situations, for example earthquake loading, energy absorbing behaviour is sought. There are two ways to provide the above-mentioned requirement for ductile structures using non-ductile materials: provision of pseudo-ductile components, and an overall structural design approach.

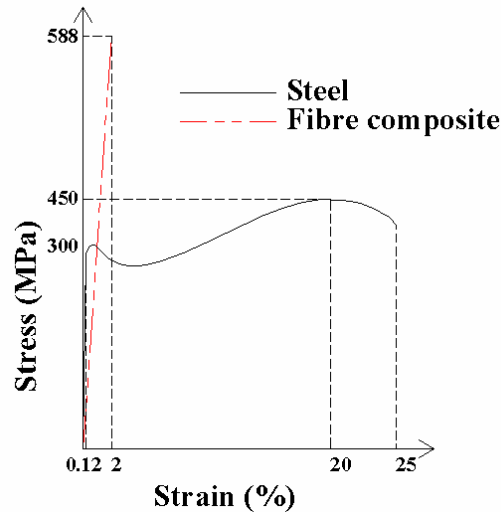


Figure 4.9 General stress – strain relationships of steel and FRP

Structural components produced from non-ductile materials can be designed to act in a pseudo-ductile manner. In the case of an FRP beam, the combination of carbon and glass fibres in the tension flange of the beam can produce such a result (Deskovic, Triantafillou & Meier 1995). The theory behind such an approach is to have the carbon-fibre fail first (at around 1% strain) and then the glass-fibres continue to take loads until their failure strain of 2% is reached. The disadvantages of this method are shock loading of the glass-fibres and cost. The glass-fibres must absorb the energy released by the failing of the carbon-fibres and associated kinetic energy produced by the sudden increase in deflection of the beam. A substantial amount of glass-fibre is therefore required in the beam to resist the static and dynamic loading. As a result, the beam has almost twice the required reinforcing for strength, which increases cost. The alternative is that engineers design structures with ductile failure in mind. Methods of doing so include the use of redundant load paths, avoidance of single-span simply-supported beams, design based upon providing large elastic deflections at overload, and jointing techniques that provide progressive failure. These are the methodologies currently employed for the design of timber structures. Non-ductile materials such as timber and concrete are commonly used in civil engineering structures. These structures meet the underlying requirement of ductility. Therefore, one has to bear in mind that it is the structure that needs to exhibit ductile behaviour not the material.

4.4 Conclusion

For FRP beams to be used and accepted in the civil engineering community, understanding of their behaviour must advance to the point where reliable and comprehensive lower-bound predictive models are available. This chapter has reviewed the

state of FRP beam analysis and design methodologies used for civil engineering structures. It appears that the advantage of tailorability of composite material has allowed many beam prototypes to develop. However, from an analysis view-point, this constitutes rather a disadvantage as no general methodology can be universally adopted. Nevertheless, it appears that the use of the three combined engineering section properties, namely EI , GA and GJ , provides an acceptable and coherent modelling approach applicable for the civil engineering field. Unfortunately, even this somewhat simplified analysis requires experimental determination of engineering section constants.

Experimental determination of the constants requires a large number of beams to be tested, for the results to be considered statistically representative. Furthermore, it is apparent that manufacturer-supplied constants are unreliable, and therefore are to be used cautiously. Likewise, the FEA methods are expensive from both a cost and resource perspective. An alternative method of determining engineering constants lies in the transformed section approach. This approach has been investigated and researchers gave contradictory conclusions as to the method's suitability. However, there are doubts to the validity of the conclusions, as it appears that some researchers have used the incorrect modulus when incorporating shear into the analysis. Therefore, further investigations into the transformed section approach are appropriate.

Coupled with the one-dimensional engineering properties are the methods to model behaviour. Shear deformation is not only significant in FRP beams but it acts in synergy with bending. Therefore, it cannot be ignored. As a result, methods, such as the Euler-Bernoulli beam theory alone, are inappropriate for FRP beam modelling. Timoshenko beam theory does include shear, subsequently researchers have investigated its potential for use with FRP beams. Its application has met with varied success ranging from inappropriate to appropriate. Interestingly, the researchers who reported that the theory is inappropriate are the same ones who appear to have used the incorrect modulus in the transformed section approach. It is therefore possible that Timoshenko beam theory, coupled with engineering constants obtained from the transformed section approach may be appropriate, and may constitute the framework for a comprehensive modelling method. To ascertain this, further investigations are warranted.

Another issue of concern for design with FRP is that of the long-term behaviour. This is particularly important for infrastructure applications where the structures are expected to perform for very lengthy periods of time. As it appears, there is a complete lack of data and/or through-life estimation models for periods of time in excess of 10^4 hours.

References

- Abu-Farsakh, G. A., Numayr, K. S. & Hamad, K. A. 1997, 'Micro-mechanical model for predicting the compressive strength of fibrous composite materials', *Composites Science and Technology*, vol. 57, no. 9-10, pp. 1415-1422.
- Alwis, W. A. M. 1998, 'Long-term deflection of RC beams under constant loads', *Engineering Structures*, vol. 21, pp. 168 - 175.
- American Society of Civil Engineers 1984, *Structural Plastics Design Manual*, American Society of Civil Engineers, New York.
- ANSYS Inc., 'ANSYS', ver 5.4, ANSYS Inc., Southpointe, Canonsburg PA 15317.
- Ascione, L., Feo, G. & Mancusi, G. 2000, 'On the statical behaviour of fibre-reinforced polymer thin-walled beams', *Composites Part B: engineering*, vol. 31B, no. 8, pp. 643 - 653.
- Ballinger, C. A. 1994, 'Specification needs for FRP composite products', in *3rd Materials engineering conference*, ed. A. S. o. C. Engineers, American Society of Civil Engineers, San Diego, CA, USA, pp. 56 - 63.
- Bank, L. C. 1987, 'Shear coefficients for thin-walled composite beams', *Composite Structures*, vol. 8, pp. 46 - 61.
- Bank, L. C. 1989, 'Flexural and shear moduli of full-section fiber reinforced plastic (FRP) pultruded beams', *Journal of Testing and Evaluation*, vol. 17, no. 1, pp. 40 - 45.
- Bank, L. C. 1990, 'Modifications to beam theory for bending and twisting of open-section composite beams', *Composite Structures*, vol. 15, no. 2, pp. 93 - 114.
- Bank, L. C., Nadipelli, M. & Gentry, T. R. 1994, 'Local buckling and failure of pultruded fiber-reinforced plastic beams', *Journal of Engineering Materials and Technology*, vol. 116, no. 2, pp. 233 - 237.
- Barbero, E. J. 1991, 'Pultruded structural shapes: Stress analysis and failure prediction.' in *Conference on Advanced Composites in Civil Engineering Structures*, ed. ASCE, ASCE, New York, pp. 194 - 204.
- Barbero, E. J. 1998, 'Construction', in *Handbook of Composites*, ed. S. T. Peters, Chapman & Hall, London, pp. 982-1003.
- Barbero, E. J. & DeVivo, L. 1999, 'Beam-column design equations for wide-flange pultruded structural shapes', *Journal of Composites for Construction*, vol. 3, no. 4, pp. 185-191.
- Barbero, E. J., Fu, S-H. & Raftoyiannis, I. 1991, 'Ultimate bending strength of composite beams', *Journal of Materials in Civil Engineering*, vol. 3, no. 4, pp. 292-306.

- Barbero, E. J., Lopez-Anido, R. & Davalos, J. F. 1993, 'On the mechanics of thin-walled laminated composite beams', *Journal of Composite Materials*, vol. 27, no. 8, pp. 806 - 829.
- Bulson, P. S. 1970, *The Stability of Flat Plates*, Chatto & Windus, London.
- Centre for Composite Materials, 'LAP: Laminate analysis program', ver 1, Imperial College, London.
- Chandrashekhara, K. & Bangera, K. M. 1993, 'Linear and geometrically non-linear analysis of composite beams under transverse loading.' *Composites Science and Technology*, vol. 47, pp. 399 - 347.
- Clarke, J. L. (ed.) 1996, *Structural Design of Polymer Composites; Eurocomp Design Code*, E & FN Spon, Chapman & Hall, London.
- Cowper, G. R. 1966, 'The shear coefficient in Timoshenko's beam theory', *Journal of Applied Mechanics*, no. 33, pp. 335-340.
- Davalos, J. F. & Qiao, P. 1997, 'Analytical and experimental study of lateral distortional buckling of FRP wide-flange beams', *Journal of Composites for Construction*, vol. 1, no. 4, pp. 150-159.
- Davalos, J. F., Qiao, P. & Salim, H. A. 1997, 'An engineering approach for design of FRP beams', in *Building To Last*, eds. L. J. Kempner & C. B. Brown, American Society of Civil Engineers, Portland, Oregon, pp. 1479 -1483.
- Davalos, J. F., Salim, P., Qiao, R., Lopez-Anido, R. & Barbero, E. J. 1996, 'Analysis and design of pultruded FRP shapes under bending', *Composites Part B: engineering*, vol. 27, no. 3/4, pp. 295 - 306.
- Deskovic, N., Meier, U. & Triantafillou, T. C. 1995, 'Innovative design of FRP combined with concrete: Long-term behavior', *Journal of Structural Engineering*, vol. July, pp. 1079-1089.
- Deskovic, N., Triantafillou, T. C. & Meier, U. 1995, 'Innovative design of FRP combined with concrete: Short-term behavior', *Journal of Structural Engineering*, vol. July, pp. 1069 - 1077.
- Evans, J. T., Ningyun, W. & Chandler, H. W. 1990, 'Creep of fibre composite beams in bending', *Acta Metallurgica Et Materialia*, vol. 38, no. 8, pp. 1565 - 1572.
- Findley, W. N. & Worley, W. J. 1951, *Some static, fatigue and creep tests of a glass fabric laminated with a polyester resin*, Engineering experimental section, University of Illinois, Illinois, 6389.
- Gaylord, E. H., Gaylord, C. N. & Stallmeyer, J. E. 1992, *Design of Steel Structures*, 3rd edn, McGraw-Hill, Singapore.
- Gilchrist, M. D., Kinloch, A. J., Matthews, F. L. & Osiyemi, S. O. 1996, 'Mechanical performance of carbon-fibre- and glass-fibre-reinforced epoxy I-beams: I.

- Mechanical behaviour', *Composites science and technology*, vol. 56, no. 1, pp. 37-53.
- Head, P. R. & Templeman, R. B. 1990, 'Application of limit state design principles to composite structural systems', in *Polymers and polymer composites in construction*, ed. L. C. Hollaway, Telford, pp. 73 - 92.
- Hoa, S. V. 1995, 'Creep of a Composite Box Beam with Design Implications', *Journal of Reinforced Plastics and Composites*, vol. 14, pp. 128 - 142.
- Hogg, P. J. 1998, 'Designing for creep in composites', in *Designing Cost-Effective Composites*, Professional Engineering Publishing Ltd., IMechE Headquarters, London, UK, pp. 93 - 106.
- Hollaway, L. C. & Howard, C. 1985, 'Some short and long term loading characteristics of a double layer skeletal structure manufactured from pultruded composites', in *Third international conference on composite structures*, Elsevier Applied Science, Paisley, Scotland, pp. 788 - 808.
- Holmes, M. & Rahman, T. A. 1980, 'Creep behaviour of glass reinforced plastic box beams', *Composites*, vol. 11, no. 2, pp. 79 - 85.
- Ivanov, I. & Tabiei, A. 2001, 'Three-dimensional computational micro-mechanical model for woven fabric composites', *Composite Structures*, vol. 54, no. 4, pp. 489-496.
- Johnson, A. F. 1985, 'Simplified buckling analysis for RP beams and columns', in *1st European conference on composite materials*, Bordeaux, p. 541.
- Jones, R. M. 1975, *Mechanics of Composite Materials*, McGraw-Hill, New York.
- Kabir, M. Z. & Sherbourne, A. N. 1998, 'Lateral-Torsional Buckling of Post-Local Buckled Fibrous Composite Beams', *Journal of Engineering Mechanics*, vol. 124, no. 7, pp. 754 - 764.
- Kabir, M. Z. & Sherbourne, A. N. 1999, 'Local Buckling of Thin-Walled Fibre Composite Beams Under Transverse Loading', *Canadian Journal of Civil Engineering*, vol. 26, no. 1, pp. 107 - 118.
- Karbhari, V. M. & Chin, J. W. 2001, *Gap Analysis for Durability of Fiber Reinforced Polymer Composites in Civil Infrastructure, Summary and Conclusions*, Available: [<http://www.cerf.org/research/summary/composit.htm>].
- Kedward, K. T., Wilson, R. S. & McLean, S. K. 1989, 'Flexure of Simply Curved Composite Shapes', *Composites*, vol. 20, no. 6, pp. 527-536.
- Kim, Y., Davalos, J. F. & Barbero, E. J. 1996, 'Progressive Failure Analysis of Laminated Composite Beams', *Journal of Composite Materials*, no. 30, p. 5.
- Kollbrunner, C. F. & Basler, K. 1969, *Torsion in Structures: An Engineering Approach*, Springer-Verlag, Berlin.

- Lee, J., Hollaway, L., Thorn, A. & Head, P. 1995, 'The structural characteristic of a polymer composite cellular box beam in bending', *Construction and building materials*, vol. 9, no. 6, pp. 333 - 340.
- Lee, J. J. & Kim, S. 2002, 'Lateral buckling analysis of thin-walled laminated channel-section beams', *Composite Structures*, vol. 56, pp. 391 - 399.
- Loughlan, J. & Ata, M. 1995, 'The restrained torsional response of open section carbon fibre composite beams', *Composite Structures*, vol. 32, no. 1/4, pp. 13 - 32.
- Loughlan, J. & Ata, M. 1997a, 'The analysis of carbon fibre composite box beams subjected to torsion with variable twist', *Computer Methods in Applied Mechanics and Engineering*, vol. 152, no. 3-4, pp. 373-391.
- Loughlan, J. & Ata, M. 1997b, 'The constrained torsional characteristics of some carbon fibre composite box-beams', *Thin walled structures*, vol. 28, no. 3/4, pp. 233 - 252.
- Loughlan, J. & Ata, M. 1998, 'Variable Twist Torsion Tests on Carbon Fibre Composite Beams', *Composite Structures*, vol. 42, no. 4, pp. 307 - 328.
- Ma, M. & Hughes, O. 1996, 'Lateral distortional buckling of mono-symmetric I-beams under distributed vertical load', *Thin walled structures*, vol. 24, no. 1, pp. 1 - 18.
- Mallick, P. K. (ed.) 1997, *Composites engineering handbook*, Marcel Dekker, New York.
- Massa, J. C. & Barbero, E. J. 1998, 'A Strength of Materials Formulation for Thin Walled Composite Beams with Torsion', *Journal of Composite Materials*, vol. 32, no. 17, pp. 1560 -1594.
- Morey, T. A., Johnson, E. & Shield, C. K. 1998, 'A Simple Beam Theory for the Buckling of Symmetric Composite Beams including Interaction of In-Plane Stresses', *Composites Science and Technology*, vol. 58, p. 1321 - 1333.
- Mosallam, A. S. & Bank, L. C. 1991, 'Creep and recovery of a pultruded FRP frame', in *Advanced composites materials in civil engineering structures*, eds. S. L. Iyer & R. Sen, American Society of Civil Engineers, Las Vegas, Nevada, pp. 24 - 35.
- Mottram, J. T. 1991, 'Evaluation of Design Analysis for Pultruded Fibre-Reinforced Polymeric Box Beams', *The Structural Engineer*, vol. 69, no. 11, pp. 211 - 220.
- Nagaraj, V. & Gangarao, H. V. S. 1997, 'Static Behavior of Pultruded GFRP Beams', *Journal of Composites for Construction*, vol. August, pp. 120-129.
- Nikkel, D. J. J. & Christensen, R. M. 1990, 'Micro-mechanical model for aligned fiber elastic-plastic composites', *European Journal of Mechanics, A/Solids*, vol. 9, no. 5, pp. 429-451.
- Ningyun, W. & Evans, J. T. 1995, 'Collapse of continuous fibre composite beams at elevated temperatures', *Composites*, vol. 26, no. 1, pp. 56 - 61.
- Patel, H., J., Tripathy, A. K. & Pang, S-S. 1993, 'Bending Analysis of a Laminated Composite Box Beam', in *Composite Material Technology*, eds. D. Hui, T. J. Kozik

- & O. O. Ochoa, The American Society of Mechanical Engineers, Houston, Texas, pp. 63 - 71.
- Phoenix, S. L. 2000, 'Modeling the Statistical Lifetime of Glass/Polymer Matrix Composites in Tension', *Composite Structures*, vol. 48, pp. 19-29.
- Qiao, P., Davalos, J. F. & Barbero, E. J. 1994, 'FRPBEAM: a computer program for analysis and design of FRP beams', ver CFC-94-191, Constructed facilities center, West Virginia University, Morgantown, West Virginia.
- Roberts, T. M. 2001, 'Mechanical properties and buckling of pultruded FRP profiles', in *International conference on FRP composites in civil engineering*, ed. J. G. Teng, Elsevier Science Ltd., Hong Kong, China, pp. 1435 - 1442.
- Silvestre, N. & Camotim, D. 2001, 'On the use of generalised beam theory to assess the buckling behaviour of thin-walled FRP members displaying arbitrary orthotropy', in *International conference on FRP composites in civil engineering*, ed. J. G. Teng, Elsevier Science Ltd., Hong Kong, China, pp. 1427 - 1434.
- Standards Australia 1998, *AS4100 - 1998 Steel Structures*, Standards Australia International Ltd., Sydney.
- Standards Australia 2001, *AS3600 - 2001 Concrete Structures*, Standards Australia International Ltd., Sydney.
- Taufik, A., Barrau, J. J. & Lorin, F. 1999, 'Composite Beam Analysis with Arbitrary Cross Section', *Composite Structures*, vol. 44, pp. 189-194.
- Timoshenko, S. 1961, *Theory of Elastic Stability*, 2nd edn, McGraw-Hill, New York.
- Timoshenko, S. P. 1921, 'On the correction for shear of the differential equation for transverse vibration of prismatic bars', *Phil Mag*, no. 41, pp. 744-746.
- Van Erp, G. M. 1999, 'Structural Design in Fibre Composites', in *Fibre Composites: Fancy Facade or Real Structural Alternative.*, eds. G. M. Van Erp & P. E. Simpson, University of Southern Queensland, Brisbane, Australia.
- Vlasov, V. Z. 1961, *Thin-walled elastic beams*, Pergamon, New York.
- Ward, I. M. & Hadley, D. W. 1993, *An introduction to the mechanical properties of solid polymers*, John Willry & Sons Ltd., West Sussex, England.
- Yang, S., Gokhale, A. M. & Shan, Z. 2000, 'Utility of microstructure modeling for simulation of micro-mechanical response of composites containing non-uniformly distributed fibers', *Acta Materialia*, vol. 48, no. 9, pp. 2307-2322.

Chapter 5 Conception of a new hybrid composite beam

5.1 Introduction

General

From the previous literature review, it has become evident that the discussed FRP beam designs do not provide the cost-performance behaviour necessary to be successful in civil engineering. Many beams tend to fail via a non-primary failure mode such as flange or web buckling, delamination of laminates, or collapse at point loads. These failure modes are difficult to predict with reasonable accuracy, thereby making capacity prediction complicated and imprecise. Furthermore, manufacturers have attempted to alleviate failure modes such as flange buckling by the addition of further laminates that are expensive and under-used from a structural point of view. In order to remedy the identified shortcomings of existing beam designs in an economical manner, firstly, each of the identified failure modes will be re-examined separately and solutions proposed. Secondly, the proposed solutions will be incorporated into a new beam design, the effectiveness of which will be examined through a detailed testing program. The incorporation of the proposed solutions are expected to lead to a significant improvement over traditional FRP beams and as such contribute to the wider use of FRP in infrastructure applications.

Proposed solution to flange buckling and associated delamination at the web-flange interface

Figure 5.1(a) shows a typical single web FRP beam. The single webs of these sections provide inadequate flange restraint. As a result, they are susceptible to flange buckling. It was shown in Chapter 3 that the solutions proposed by pultruders, such as thickening the flanges of their beams by using fillers or provision of extra webs, are not successful in eliminating the failure mode in a cost-effective way. Another solution in the form of a box beam, shown on Figure 5.1(b), was investigated by Ashby (1989). Although the web restraint provided by the box-shaped section is superior to the single web design, it was shown that it is still not sufficient to alleviate flange-buckling failures without significant thickening of the compression flange. The most promising solution, so far, as shown in Chapter 3 appears to be the combination of FRP with a structural core material, such as concrete or PFR. Figure 5.1(c) and (d) show two designs incorporating concrete and PFR respectively. Of these two core materials, PFR has superior adherence to FRP, absence of alkalinity, and a lower density. Therefore, PFR core will be adopted in the development of the new design.

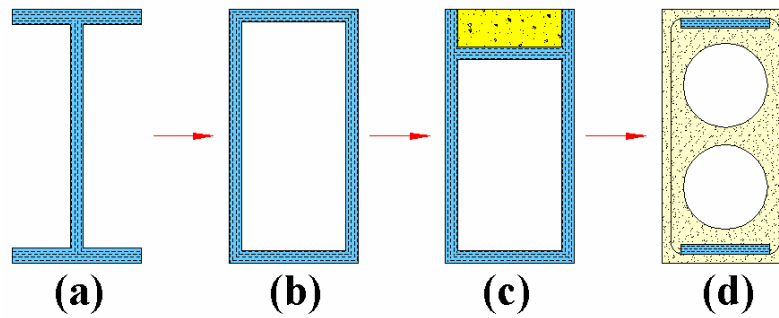


Figure 5.1 Progression of FRP beam designs to alleviate flange buckling

Control of web buckling

In addition to providing restraints against flange buckling, the addition of a core material also provides an effective solution to web buckling. Indeed, the incorporation of a core material in the webs adds to structural stability and reduces bearing pressures across the web. However, provision of core material throughout the beam, as shown in Figure 5.2(a), would be excessive in terms of structural efficiency as it contributes additional dead weight and increases the overall cost of the beam. Therefore, judicious placement of the core material in between web laminate layers, as shown on Figure 5.2(b), can provide for an effective solution. Such placement would make the webs an efficient sandwich structure with the laminates located where the highest strains are likely to occur.

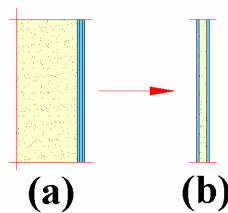


Figure 5.2 Placement of core between web laminates

Proposed solution to compressive failure under vertical loads

The inclusion of a core material does provide an economical solution to flange and web buckling. However, if the shape of the section is poorly designed, it may not stop the compressive failure of the beam under vertical loads. For example, circular voids in the beam as shown on Figure 5.3(a), through arch action, amplify stress concentrations formed within the section (Davey 1999). Subsequent studies (Ryan 2000) indicated that rectangular

holes are less likely to cause this problem. Therefore, the use of a rectangular void, as shown on Figure 5.3(b), will be used in the manufacture of the new beam. In addition, the use of rectangular voids can provide for a connecting member to be inserted.

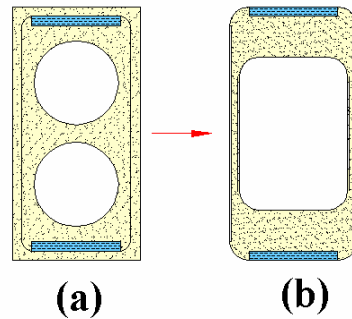


Figure 5.3 Rectangular void to reduce stress concentrations under compressive loading

Fibre orientation

One of the causes contributing to the preceding problems is poor fibre orientation within the beams. Some of the existing beams, in particular pultruded and filament wound, do not provide ideal fibre orientation. Laminates perform best when the fibres are aligned with the principal stress vectors. The principal stress vectors throughout a beam vary depending upon the loading arrangement and constraint conditions. For the general case of a beam in bending, an accepted simplification is to state that the flanges resist the moments and the webs resist the shear. Under such an assumption the principal stress vectors in the flanges and webs are respectively at 0 degrees and 45 degrees to the longitudinal axis of the beam. The fibre orientation in the flanges and webs of the new section therefore should be aligned with these principal stress vectors. Indeed, Kabir, Pandey & Sherbourne (1998) also concluded that such alignment is the optimum for bending, shear and lateral stability.

5.2 Description of the new beam

5.2.1 Section Design

Taking into account the aforementioned shortcomings, a new section design that incorporates the proposed solutions is shown on Figure 5.4. The beam section consists of two FRP RHS (Rectangular Hollow Sections), one inside the other. These RHS are created using two ‘U’ shaped laminates overlapping at the webs. The size of the inner RHS is determined by calculating the amount of core material required in the flanges and the webs

to avoid secondary failure modes. The primary role of the RHS is to confine the core material, which is placed within. In addition, the RHS have been designed to contribute to the shear and torsional stiffness of the beam. Under loadings of shear and torsion, the principal stress vectors are at ± 45 degrees. Therefore, the ideal fibre orientation for the inner and outer RHS is ± 45 degrees to the longitudinal axis. The flanges have an extra layer of reinforcement positioned inside the outer RHS. The purpose of this reinforcement is to provide resistance to compressive and tensile forces induced by bending moments. Therefore, fibres aligned with the longitudinal axis of the beam are the most effective. The webs have a similar construction as the flanges. If required, extra laminates with fibres at ± 45 degrees to the longitudinal axis of the beam can be provided within the core to provide extra shear resistance.

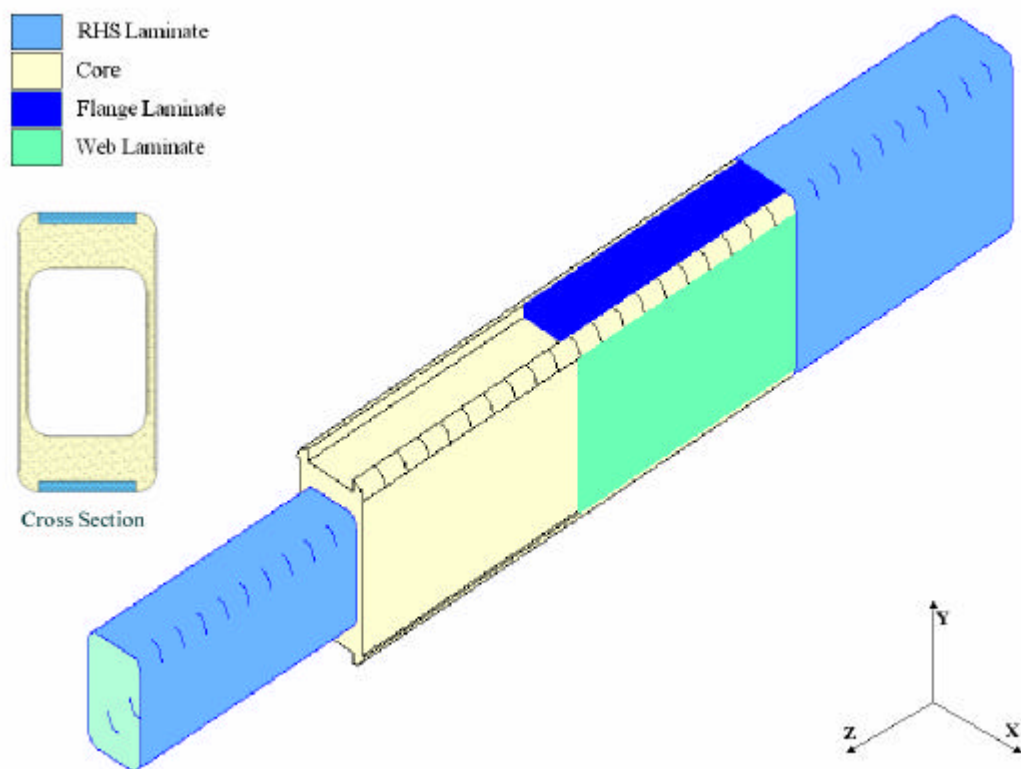


Figure 5.4 Exploded view of the beam

The 14 different laminates used in the section are labelled from L_1 to L_{14} (Figure 5.5) for further reference in the analysis of the beam. Due to the differing material behaviour of the constituents in compression and tension, distinct symbols are provided to the laminates on different sides of the neutral axis for ease of computation.

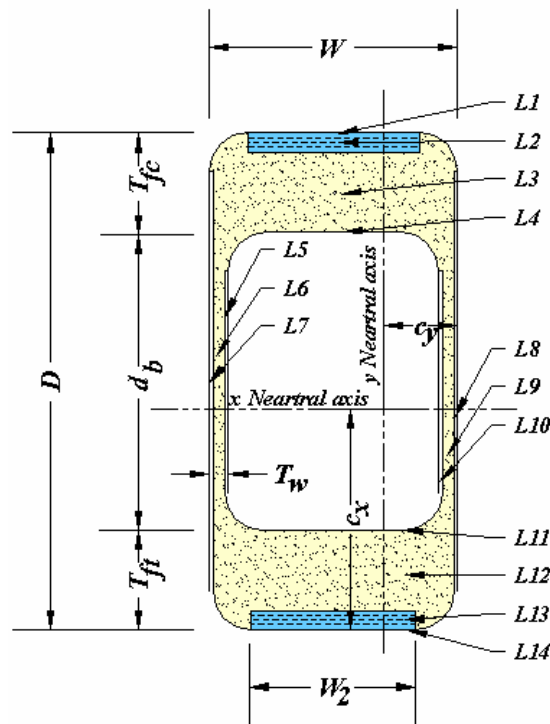


Figure 5.5 Beam dimensions and designations

5.2.2 Determination of section size of test beams

5.2.2.1 Span

Once an FRP specimen is under a certain size, its failure strength increases for any further reductions in size (Bazant, Daniel & Li 1996; Curtin 2000; Tabiei & Sun 1999). It is therefore important to ensure that test specimens are sufficiently large to ensure they do not give results that are unrepresentative of larger structures. However, testing of large beams (for example 400 mm deep by 5000 mm long) was considered impractical due to the high costs associated with the large quantities of materials involved, the time required for their manufacture and the need to test on a machine that requires special staff to operate it. The use of relatively small beams removes such restrictions as they can be tested using simple universal testing machines such as the Avery Universal Testing Machine (Avery Ltd.) pictured on Figure 5.6. Test beams with a span of 600 mm, and a cross-section of 65 mm × 33 mm were chosen for the experimental part of this thesis. This size beam provides for laminates larger than those tested in standard tensile and compressive tests. To determine whether the core material was likely to exhibit any size-effect, a comparison with concrete was used because of its resemblance with PFR. Concrete specimens are considered large enough, not to suffer from size-effect, when the cross-sectional width of a component is at

least four times the size of the aggregate within the concrete (Neville 1981, p. 564). Therefore size effects in the PFR should not be expected provided the core has a thickness in excess of 0.625 mm. The smallest core size is located in the webs, which have a width-to-particle-size ratio of 16:1, which is well in excess of the minimum for concrete. Another consideration is the surface area contact between the PFR and Laminates. As the beam is increased in size, surface area contact increases proportionately to the scale while the area of laminate may increase proportional to the square of the scale. Shear stress across the PFR / Laminate interface will remain proportional to the capacity of the beam. Therefore, the shear stress should remain constant provided the beam design is optimum. Consequently it is assumed that any size effects in the test beams can be considered negligible.

The use of relatively small test beams made it possible to manufacture a large number of test specimens for different loading conditions and variations in cross-sectional dimensions.



Figure 5.6 Avery Universal Testing Machine

5.2.2.2 Selection of test beam depth

The depth of a beam has a direct effect upon its deflection at failure. For the 4-point testing arrangement used in this thesis, a safe limit of 25 mm deflection was adopted to avoid fouling of the beam against the testing machine bed and measurement fixtures. Based on the

maximum strain criterion, a beam depth of 65 mm would fail within the adopted limit of deflection. Therefore, a beam depth of 65 mm was chosen.

5.2.2.3 Width

The criteria used to determine the width for the test beams were the bending and shear capacities, the minimisation of material, and lateral stability. To provide an adequate bending capacity, particularly important when testing for shear, unidirectional laminates, referred as L_2 and L_{13} on Figure 5.5, are required. The number, the placement, and the lateral size of the laminates influence the section width. A further factor that influences the amount of unidirectional laminate, and thereby the section width, is the amount of shear reinforcement provided. This is because of the synergy between bending and shear. Therefore, the amount of unidirectional reinforcement can only be determined once the quantity of shear reinforcement is chosen. The choice of this shear reinforcement was based upon minimising material use in the test beam. Hence, the shear resisting U-shaped RHS laminates were set to the minimum amount possible, namely one ply: $L_1 = L_4 = L_{11} = L_{14} = 1$ ply, which, as shown on Figure 5.5, yields $L_5 = L_7 = L_8 = L_{10} = 2$ plies. With this amount of shear reinforcing, a moment capacity of no less than $2.5 \times 10^6 \text{ N.mm}$ is required to ensure shear failure. This capacity was determined using the analytical formulations described in the next Chapter. To achieve this moment capacity areas of 89 mm^2 of unidirectional laminate are required for each of L_2 and L_{13} . A further restriction is imposed by the hand lay-up method of manufacturing the laminates. A limit of seven plies was imposed because that is the maximum number of plies that can be laid by hand in one session. As shown on Figure 5.7, using this maximum results in the minimum overall cross-sectional area for the beam. With seven plies, each 0.56 mm thick, the width of the unidirectional laminate corresponds to 22.7 mm. To allow for the wrapping of the RHS laminates a radius of 5 mm to the corners of the beam was required. This resulted in a 32.7 mm overall beam width. With these dimensions, the beam has an aspect ratio of 2 to 1. To determine if the beam, with this aspect ratio, would be laterally stable, the critical lateral torsional buckling moment was calculated, as detailed in the next Chapter. The critical lateral torsional buckling moment was well in excess of the designed moment capacity of the beam. Therefore, the beam will be laterally stable.

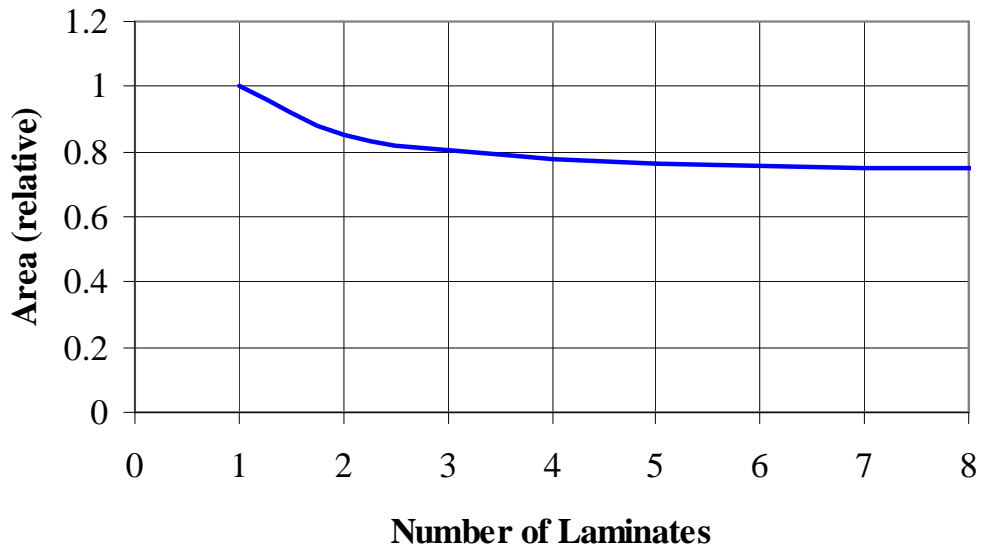


Figure 5.7 Number of unidirectional laminates versus cross-sectional area for the FRP beam

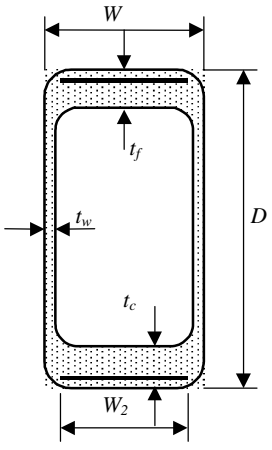
5.2.2.4 Flange and web core dimensions

The only constraint on the amount of core within the flanges and webs is a manufacturing practicality. For injection moulding of the beams, a minimum core thickness of 2 mm was considered feasible. Analysis of the beam, detailed in the next Chapter, was undertaken to determine if more than the minimum core thickness was required. Indeed, the analysis revealed that the optimum flange core thickness (L_3 and L_{12}) is 7.5 mm, while a web core thickness (L_6 and L_9) of 2.5 mm would be needed to prevent buckling failures. Therefore, these latter dimensions were adopted in the beam design.

5.2.2.5 Final beam dimensions

As described, the overall dimensions of the beam were dictated by testing arrangements, material availability, time constraints and manufacturing techniques. Once the beam dimensions were finalised, which were set at 65 mm by 33 mm, a mould and mandrels were machined to the required dimensions. Subsequently, no changes to the external dimensions of the beam were possible. Furthermore, production of the beams to the same dimensions makes comparison of results possible. The final dimensions of the beam and its components are given on Table 5.1.

Table 5.1 Nominal beam dimensions

<i>Cross-section</i>	<i>Dimensions</i> (mm)	<i>Number of Laminates</i>
	$D = 65$ $W = 33$ $w_2 = 23$ $L_3 = L_{12} = 7.5$ $L_6 = L_9 = 2.5$ $t_f = 11.76$ $t_c = 11.76$ $t_w = 3.18$	$L_1 = L_{14} = 1$ $L_2 = L_{13} = 7$ $L_4 = L_{11} = 1$ $L_5 = L_{10} = 2$ $L_7 = L_8 = 2$

5.3 Materials

The choice of materials used in the production of the beams was mainly dictated by their availability at the University of Southern Queensland. The E-Glass reinforcement was kindly donated by Colan Pty. Ltd. (Colan Products). In order to avoid the excessive cure shrinkage that characterises polyester and vinyl-ester resins, ADR246TX resin with ADH160 hardener (ATL Composites Pty Ltd.) was chosen as the matrix material. ADR246TX is a DGEBA-based epoxy blend with the addition of BisF epoxide, which is a viscosity modifier. The resin also includes a thixotropic additive to reduce resin drain from laminates during lay-up. As to the core material, it is made of a mixture of resin and fly ash micro-spheres. The laminates used on the test beams are designated in section 5.4.1.

5.3.1 E-Glass

The E-Glass incorporated into the beams was in the form of mats: unidirectional, plain weave, and double-bias as outlined in Table 5.2.

Table 5.2 E-Glass mat properties

<i>Name</i>	<i>Code</i>	<i>Manufacturer</i>	<i>Mass (g/m²)</i>	<i>Density of glass (kg/m³)</i>
Unidirectional	MU4500K127	Colan Pty Ltd	450	2540
Plain weave	AF251	Colan Pty Ltd	165	
Double-bias	MX6000A127	Colan Pty Ltd	600	

5.3.2 Laminate properties

Prior to construction of the beams, the individual components (the laminates and core material) were tested to obtain their respective mechanical properties. Testing was conducted using an MTS 810 shown on Figure 5.8.



Figure 5.8 MTS 810 Material Test System Machine

Specimens were made and tested in accordance with international standards ISO 527-4, 527-5, 604, 14126 and 14129 (International Organization for Standardization). The obtained results together with those provided by Humphreys (2000, pers. comm.) and Ellis (2001, pers. comm.) are compiled in Table 5.3. Average values are given, followed by the standard

deviation in brackets. The scatter in the specimen results was as low as 7% for shear properties, and as high as 22% for the tensile properties. The major reason for this scatter is the variability of fibre fraction as is expected with the hand lay-up technique (Ayers 2001, p. 224).

Table 5.3 Laminate properties

<i>Name</i>		Unidirectional		Plain weave
<i>Code</i>		<i>MU4500K127</i>		<i>AF251</i>
<i>Density (kg/m³)</i>		1740		1510
<i>Thickness (mm)</i>		0.56		0.17
<i>Direction</i>		11	22	11 and 22
<i>Tensile</i>	<i>Failure stress (MPa)</i>	516.4 (69.3)	47.1 (3.88)	169.6 (38.4)
	<i>Failure strain (%)</i>	1.965 (0.154)	1.11 (0.725)	1.475 (0.106)
	<i>Modulus (MPa)</i>	26705 (1808)	9894 (1990)	11502 (910.9)
<i>Compressive</i>	<i>Failure stress (MPa)</i>	448.1 (62.7)	127.0 (20.89)	263.0 (38.8)
	<i>Failure strain (%)</i>	1.65 (0.235)	2.47 (0.654)	1.920 (0.126)
	<i>Modulus (MPa)</i>	33363 (2990)	10184 (1746)	13700 (141.5)
<i>Shear</i>	<i>Failure stress (MPa)</i>	47.2 (3.95)		50.2 (1.55)
	<i>Failure strain (%)</i>	1.39 (0.02)		2.5 (0.059)
	<i>Modulus (MPa)</i>	3009 (107.5)		2017 (36.71)
<i>Poisson ratio, (ν_{12})</i>		0.27		0.24

The properties of the double bias mat were obtained by Ellis (2001, pers. comm.) and its properties are reported on Table 2.5.

5.3.3 Core properties

The PFR core consists of ADR246TX epoxy resin mixed with ‘SLG’ fly-ash microspheres (Envirospheres Pty. Ltd.), which are a by-product from coal-fired power stations. The name PFR ‘Particulate Filled Resin’ for the core material was coined by Van Erp (1999). A ratio of micro-spheres to matrix of 1:2 (33% fly-ash) by mass was used. This ratio was found, by Van Kerkwyk (2000, pers. comm.), to be the optimum as far as strength-versus-workability is concerned. The use of the epoxy resin provides a gel time of over one hour.

The PFR behaviour was initially assumed to be linear isotropic (Ayers & Van Erp 2000). However, subsequent material property investigations, as part of this study, revealed that the core material exhibits a quasi-linear stress-strain behaviour in compression, and a non-linear behaviour in tension.

When tested in compression the material shows a relatively linear behaviour to a strain of 1.5%, after which a substantial non-linear behaviour is observed to failure. This can be seen on Figure 5.9. The response and failure mode observed under compressive loading is very similar to that displayed by concrete. Part of this behaviour may be explained by the high value of its Poisson’s ratio, of the order of 0.4, resulting in an increase of its effective cross-sectional area. However, as shown on Figure 5.9, an insignificant change in the graph results when the stresses are adjusted to include the Poisson effect. Consequently, the Poisson effect can be ignored in the one-dimensional analysis. During the experiments the PFR within the beam will not undergo compressive strains over 1.5%, the non-linear behaviour could be ignored here. Therefore, the compressive behaviour of the PFR has been modelled as linear in this thesis with an average Modulus of Elasticity of 5160 MPa .

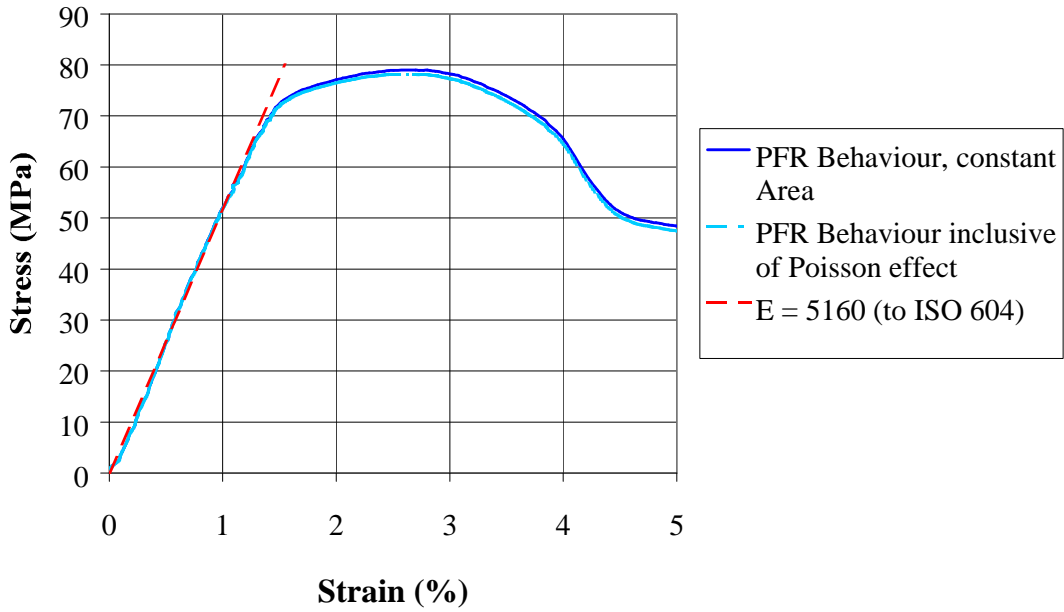


Figure 5.9 Non-linear stress strain behaviour of the PFR in compression

In tension, as shown on Figure 5.10, the material appears to lose its stiffness as the strain is increased. The cross-sectional area is reduced in size, and polymer chains may straighten and slide around the particles. The Poisson effect, as with compression, is minor; this can be seen on Figure 5.10 where the curves for constant area and that inclusive of Poisson effect overlap. Unlike, in compression, the PFR stress-strains behaviour becomes non-linear at an early stage within the beam. This non-linearity is taken into account in this thesis. For FEA it is possible to use the non-linear stress-strain data directly as input. In order to incorporate the non-linear material behaviour into the transformed section analysis of the next Chapter, an effective modulus, based on the original unstrained cross-sectional area, is adopted. The modulus is approximated by the following formula (shown on Figure 5.10):

$$E_t = C_{ta} + C_{tb} e \dots\dots\dots (5.1)$$

Where:

$$C_{ta} = 4740 \text{ MPa and}$$

$$C_{tb} = -134680 \text{ MPa}$$

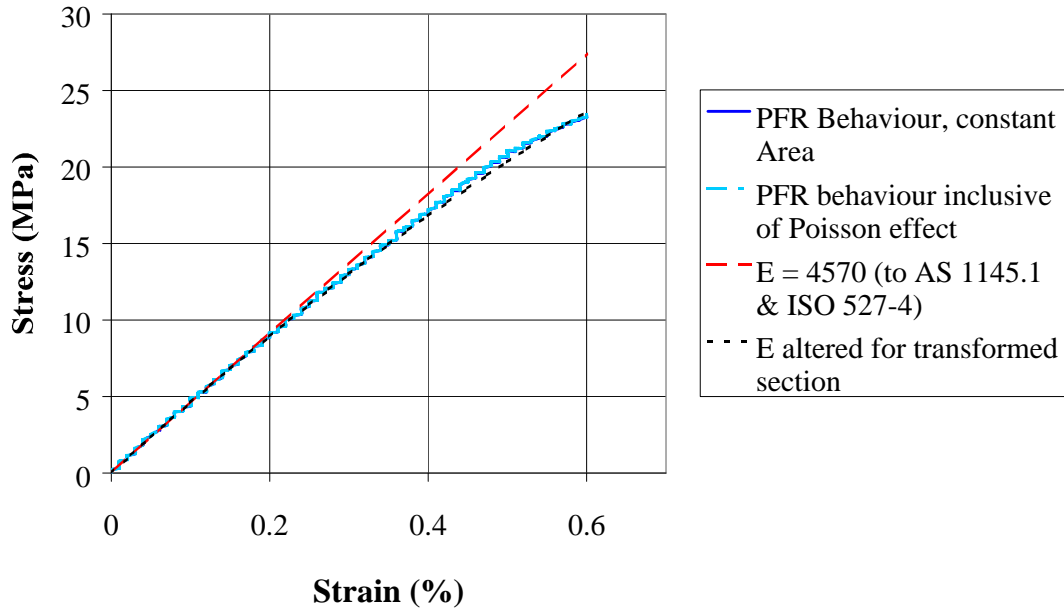


Figure 5.10 Non-linear stress strain behaviour of the PFR in tension

The properties of the PFR are summarised on Table 5.4, and they will be used for the remainder of the study.

Table 5.4 The properties of PFR

PFR	<i>Failure Stress (MPa)</i>	<i>Failure Strain (%)</i>	<i>Modulus (MPa)</i>	n
<i>Tension</i>	23.6	0.6	$4740-134680e_t$	0.4
<i>Compression</i>	79	2.7	5160	
<i>Shear*</i>	54.3	3.6	1510	

* Calculated

5.4 Production processes

5.4.1 Material Use

A unidirectional mat was used for the flange laminates L_2 and L_{13} . A double-bias cloth, with ± 45 degrees fibre orientation, would have been the ideal choice for the RHS if a light grade were available. Unfortunately, the lightest grade available was a 600 g/m^2 mat. Analysis, as detailed in the next Chapter, revealed that using a 600 g/m^2 double-bias mat would result in a section without a need for core material in the webs. As a lighter double-bias mat was not available, plain weave fabric was substituted, and used for all the RHS

laminates. This substitution made it possible to observe the contribution of the core material to buckling resistance of the webs. However, extra shear reinforcement was required for the investigation of the pure moment behaviour of the beam, as dictated by the 4-point-test arrangement. So, the double-bias mat was used in areas of the beam not under investigation to ensure shear failure would not occur.

In addition to the materials used to manufacture the beams, a sacrificial material, called peel ply, is required in the production process. Peel ply is a woven fabric consisting of nylon threads coated with a silicone-based release agent. Its use ensures that effective bonding of fully-cured laminates is achieved by keeping the bond surface clean. Furthermore, its removal inhibits the formation of a smooth outer layer of resin, thus ensuring that the PFR bonds well to the laminates.

5.4.2 Production

For the preliminary study, the adopted manufacturing process was based on a form-and-pour methodology, using timber formwork as shown on Figure 5.11. The production process involved the lay-up of the inner RHS over a timber folding wedge mandrel. The unidirectional reinforcement (L_2 and L_{13}) was laid up on a table to cure at ambient temperature before being cut to size, and placed in the mould. Once the mould was assembled, the inner RHS (including mandrel to stop any buckling of the thin inner RHS) was placed in it, and spacers made from PFR were positioned to ensure the RHS could not move. The core material was then mixed and poured over the inner RHS. The beams were poured to a slightly higher level than required in order to be machined to a standard size. The beams required 48 hours ambient cure prior to de-moulding to avoid any damage to the core. Once cured, each beam was retrieved from the mould, and the mandrel was removed. The top web surface was machined to size using a drill press with diamond cutter. The outer RHS layers were laid over the core. The completed beam was heat-cured in an oven for 8 hours at 80 °C. However, this process was not continued for it had many disadvantages. Among them were: the excessive manufacture time, the lack of dimension control with the open mould as well as the mould's short life span. For these reasons, another process appropriate to the available resources was devised. This process consists of a combination of hand lay-up and injection moulding, and is described in Appendix B.



Figure 5.11 Form and pour beam production

5.5 Summary

A new FRP beam has been developed by proposing solutions to the shortcomings of existing designs. These solutions were integrated into a new FRP beam design. It is anticipated that this new design will not suffer from the premature failures that characterise the existing designs. Based on the availability of materials and testing equipment, the dimensions of the test beams were selected. The materials incorporated within the beam were disclosed and properties quantified. The process used to manufacture the beams was also briefly described.

References

- Ashby, M. F. 1989, *On material and shape*, Engineering Department, University of Cambridge, Cambridge, England.
- ATL Composites Pty Ltd., 27 Gibbs St., Labrador QLD 4215 Australia.
- Avery Ltd., Birmingham, England.
- Ayers, S. R. 2001, *Material foundations for the application of fibre composite materials in civil and structural engineering*, Ph.D., University of Southern Queensland.
- Ayers, S. R. & Van Erp, G. M. 2000, 'Development of a new core material for composites in primary structural applications', in *ACUN-2*, eds. S. Bandyopadhyay et al., University of New South Wales, Sydney, pp. 247 - 252.

- Bazant, Z. P., Daniel, I. M. & Li, Z. 1996, 'Size effect and fracture characteristics of composite laminates', *Journal of Engineering Materials and Technology, Transactions of the ASME*, vol. 118, no. 3, pp. 317 - 324.
- Colan Products, 441 Logan Rd., Stones Corner QLD 4120 Australia.
- Curtin, W. A. 2000, 'Dimensionality and size effects on the strength of fiber-reinforced composites', *Composites Science and Technology*, vol. 60, no. 4, pp. 543 - 551.
- Davey, S. 1999, *The fabrication of a fibre composite floor slab*, Fibre composite design and development, University of Southern Queensland, Toowoomba, Australia.
- Envirospheres Pty. Ltd., PO Box 497 Lindfield NSW 2070 Australia.
- International Organization for Standardization, *International Standard*, International Organization for Standardization, Case Postale 56 CH-1211 Geneve 20 Switzerland, Geneve.
- Kabir, M. Z., Pandey, M. D. & Sherbourne, A. N. 1998, *Optimal Fibre Orientations in Lateral Stability of Pultruded I-Section Composite Beams*, Department of Civil Engineering, University of Waterloo, Waterloo, Ontario, Canada, N2L 3G1.
- Neville, A. M. 1981, *Properties of concrete*, 3rd edn, Pitman Publishing Ltd., London.
- Ryan, H. 2000, *Investigation of the compressive behaviour and the optimum cross-section of a fibre composite girder-web*, Undergraduate, University of Southern Queensland.
- Tabiei, A. & Sun, J. 1999, 'Statistical aspects of strength size effect of laminated composite materials', *Composite Structures*, vol. 46, no. 3, pp. 209 - 216.
- Van Erp, G. M. 1999, 'A New Fibre Composite Beam for Civil Engineering Applications', *Composites Fabrication Journal*, vol. July, pp. 30 - 33.

Chapter 6 Analytical modelling of the FRP beam behaviour

6.1 Introduction

In Chapter 3 it was shown that traditional FRP beams often fail long before the ultimate load-carrying capacity of the reinforcing fibres is achieved. This is inefficient and wasteful from a resources perspective. The main purpose of the new beam design is to avoid these early failure modes in a cost-effective manner. If the dimensions of the beam are poorly chosen, these secondary failure modes may still occur or excessive quantity of materials may be used. Therefore, an efficient method of analysis is required so that the test beams can be designed and a testing program developed. It was revealed in Chapter 4 that there is some confusion as to the applicability of formulae based upon classical beam theory and thin-walled beam theory. However, it appears that the confusion is related to the method of application of the formulae, not to the assumptions on which the formulae are based. It is therefore reasonable to expect that these methods will yield useful results. In this Chapter, formulae from classical beam theory and thin-walled beam theory, coupled with the transformed section approach, will be adjusted to allow for laminate properties. The formulae identify the critical parameters that govern the different failure modes of the new beam. Furthermore, a simple method to allow for cracking of the core material, commonly used in reinforced concrete analysis, will be incorporated into the analysis so that load – deflection curves can be generated. The formulae are then used to develop a testing program that is described in the next Chapter - the results of which will validate/invalidate the analysis methods adopted in this Chapter.

6.2 Pure bending

6.2.1 Moment curvature behaviour

The behaviour of an FRP beam incorporating PFR is somewhat similar to that of a reinforced concrete (RC) beam. As shown on Figure 6.1, the FRP beam progresses through an initial linear elastic segment (region 1) before cracking of the core material, which results in a reduction in stiffness (region 2). With increasing load, the stiffness continues to deteriorate. However, unlike for RC beams, there is no tangible ‘yield plateau’ because of the linear-elastic behaviour of the glass reinforcement. Therefore, the beam continues to sustain increasing load until it ultimately fails (point 3).

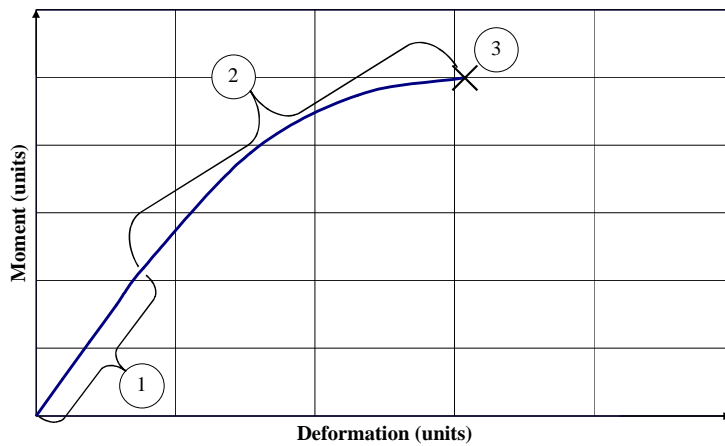


Figure 6.1 FRP beam: load deformation behaviour

Beam behaviour is well described by the moment-curvature relationship. In the linear-elastic range, this relationship can be expressed as:

$$\mathbf{k} = \frac{M}{EI} \dots\dots\dots (6.1)$$

where: \mathbf{k} is the curvature of the beam, M is the moment, and EI is the stiffness. As is common for reinforced concrete beams, a similar expression can be also used for the cracked stage of the FRP beam (region 2):

$$\mathbf{k} = \frac{M}{EI_{effective}} \dots\dots\dots (6.2)$$

where $EI_{effective}$ lies between $EI_{un-cracked}$ and $EI_{cracked}$. In order to derive an expression for $EI_{effective}$ it is useful to determine these upper and lower boundaries first.

6.2.2 Un-cracked beam behaviour

To account for the different materials in the cross-section, the transformed section approach is used (Warner, Rangan & Hall 1989 p. 103). The transformed section for the un-cracked FRP beam, together with the strain and stress distributions, are represented on Figure 6.2. The dissimilar width of the core material in the compression zone, relative to that in the tensile zone, is related to the different moduli of elasticity of FRP and PFR in compression and tension.

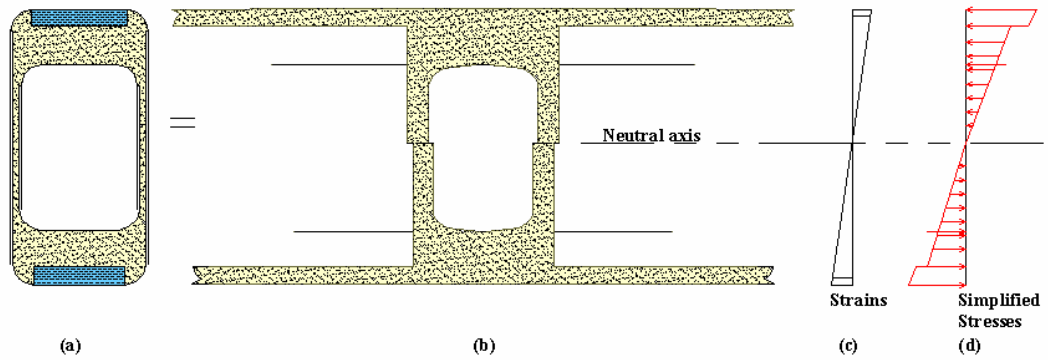


Figure 6.2 Transformed section of the un-cracked FRP beam

In line with standard beam theory, the strain distribution through the depth of the cross-section is assumed linear. However, due to the different moduli of elasticity of the beam materials, the stress distribution throughout the FRP beam’s cross-section is not linear, as shown on Figure 6.2d. It is therefore easier to describe the behaviour of the individual laminates in terms of strain. When using the transformed section approach, strains can be calculated by altering the standard moment-stress relationship formula for homogeneous isotropic materials:

$$s_{(y)} = \frac{My}{I} \dots\dots\dots (6.3)$$

by substitution of Hooke’s law

$$s = Ee \dots\dots\dots (6.4)$$

resulting in:

$$e_{(y)} = \frac{My}{EI} \dots\dots\dots (6.5)$$

where: $s_{(y)}$ and $e_{(y)}$ are respectively the stress and strain at a distance y from the neutral axis, and I and E are respectively the second moment of area and reference modulus of the transformed section. By comparing the strains throughout the cross-section against the PFR capacity it can be determined when cracking is likely to occur. However, equation (6.5) must be used iteratively as the tensile behaviour of the PFR is non-linear.

As discussed in Chapter 5 the PFR displays a non-linear behaviour. Taking this effect into account in the simulation of the behaviour of the un-cracked FRP beam requires an iterative transformed-section approach. Based on the calculated tensile modulus of elasticity, the transformed section can be updated at each iteration. The details of this approach are presented in Appendix C.1. The results of the simulation are shown on Figure 6.3 together with the average result from the tests. It can be seen that the iterative approach results in a slightly better estimate of the deflection compared to the constant modulus approach.

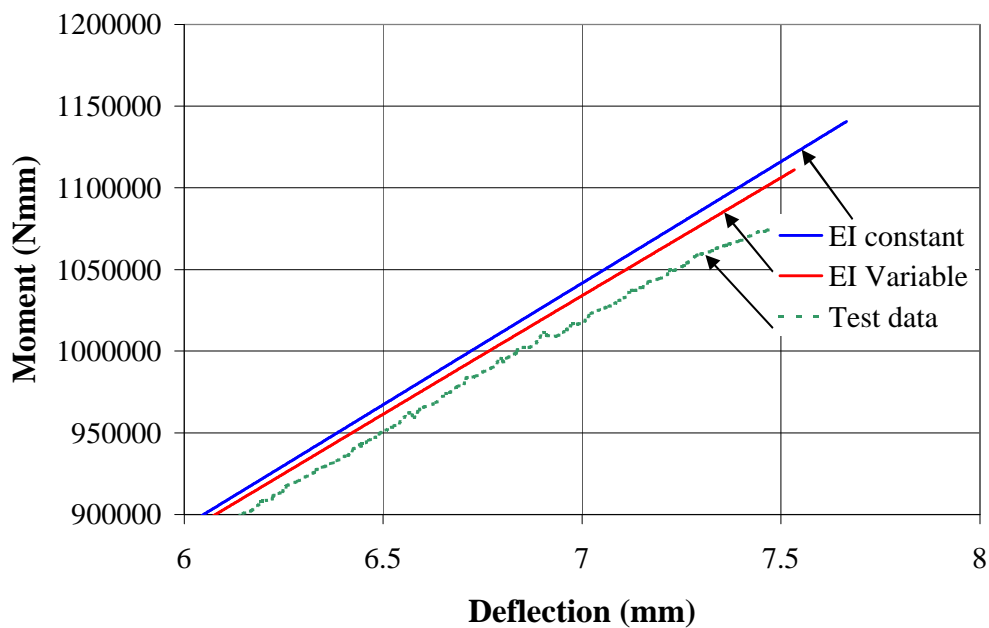


Figure 6.3 Comparison between the use of a constant and variable stiffness of the un-cracked FRP beam

The formulae and iterative method describe the beam behaviour prior to the occurrence of cracking in the core material. However, the ultimate capacity of the beam will be in excess of the cracking moment since the unidirectional laminates, within the beam, have a higher tensile failure strain than that of the core. It is therefore necessary to incorporate into the model the effects of core cracking upon load deformation behaviour.

6.2.3 Effects of cracking of the PFR material on the behaviour of the beam

Cracking of the core material has a significant influence on the overall stiffness and failure performance of the FRP beam. Accurate modelling of this phenomenon is extremely

difficult and requires sophisticated software. In this chapter a more simplistic approach based upon limiting strain criterion is adopted. This approach infers that a crack initiates first at the interface between the bottom laminate and the core material. Associated with this crack is local de-bonding at the interface, as shown on Figure 6.4.

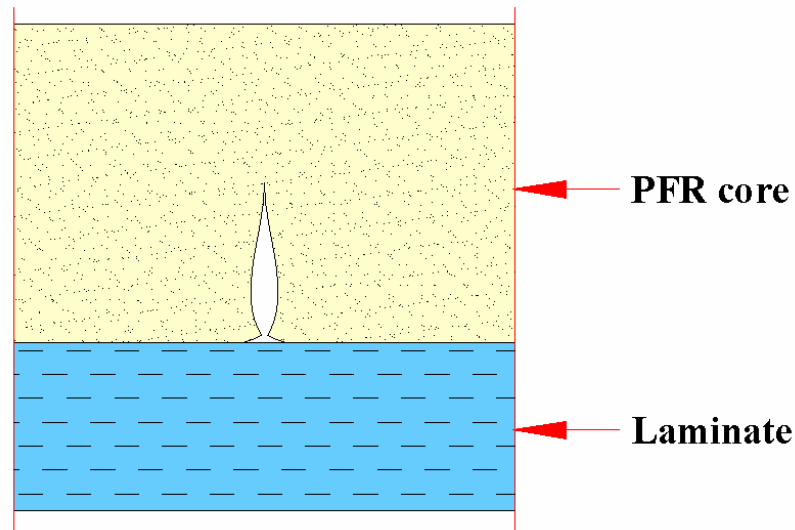


Figure 6.4 Close-up of cracking with associated de-bonding

Once a crack has formed, the laminates become the principal tensile load-carrying element at that location. The exact behaviour of this process - and its influence on strength and stiffness - is very complex. As with RC beams, analysis can be simplified significantly by disregarding any tensile contribution of the core material to the strength and stiffness at the position of a crack. The transformed section, at the position of a crack, is shown on Figure 6.5. For the sake of clarity, the stress contribution of the web laminates is omitted from Figure 6.5d. By ignoring the tensile capacity of the core material, the neutral axis shifts up the beam, and the overall stiffness at that location is reduced.

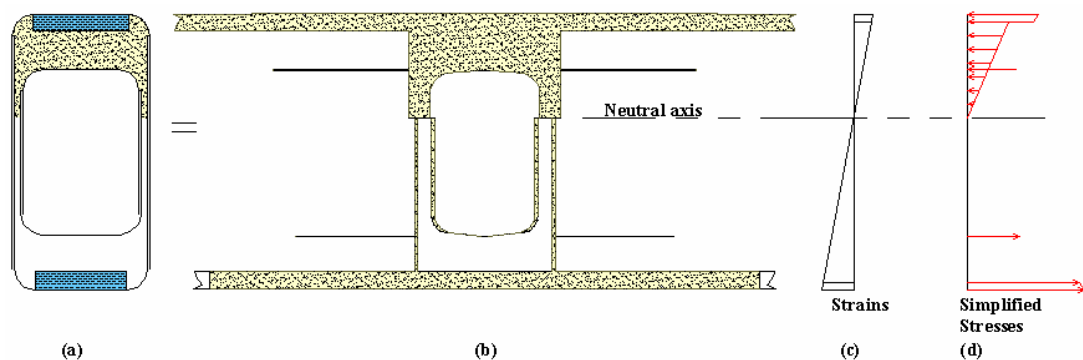


Figure 6.5 Transformed section of cracked FRP beam

Effective stiffness of the beam

Once the limiting strain is exceeded, cracks in the PFR material initiate at weak points in the laminate-PFR interface. As a result, the number of cracks along the length of a beam increases with rise in applied moment. This progressive formation of cracks reduces the beams' effective stiffness, $EI_{effective}$, which progresses from the un-cracked state, $EI_{un-cracked}$, towards the fully cracked state, $EI_{cracked}$. However, the stiffness will always remain slightly higher than $EI_{cracked}$ because the beam is a composite of cracked and un-cracked segments as shown on Figure 6.6 (Springolo & Van Erp 2001).

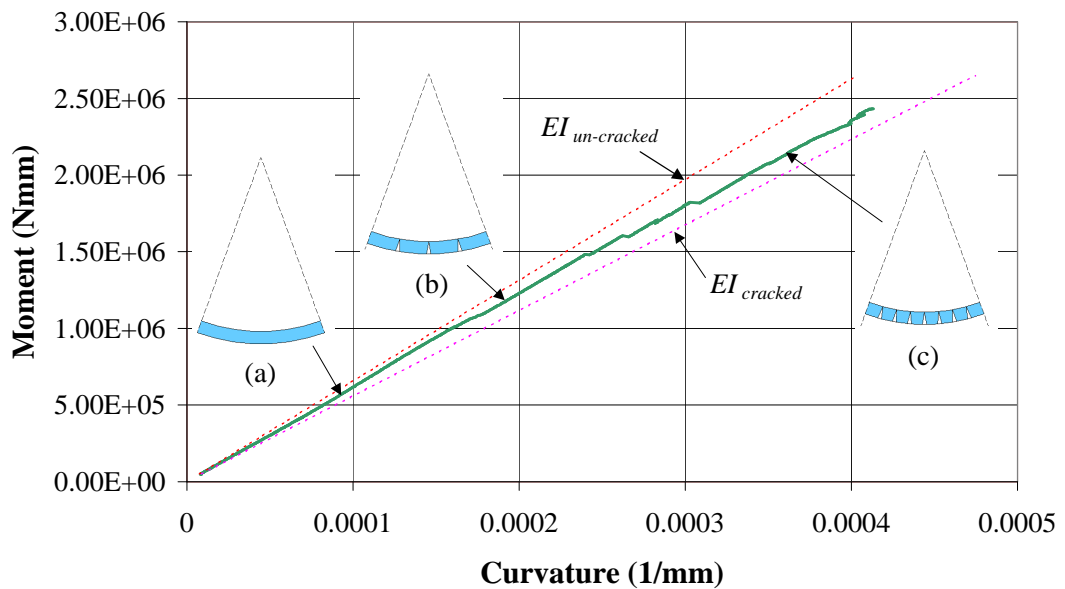


Figure 6.6 Moment-curvature of the FRP beam

The behaviour shown on Figure 6.6 is similar to the well-known behaviour of RC beams (Branson 1963, 1997; Kordina & Quast 1971). Given the similarity, it is likely that the approach developed for RC beams will yield reasonable estimates for the effective stiffness of the FRP beam. Figure 6.7 shows the stiffness prediction for the FRP beam using the approach developed for RC beams by Branson (1963, 1997). Based upon experiments, Branson proposed an empirical expression for the beam stiffness:

$$EI_{effective} = EI_{cracked} + (EI_{un-cracked} - EI_{cracked}) \left(\frac{M_{cracked}}{M} \right)^3 \dots\dots\dots (6.6)$$

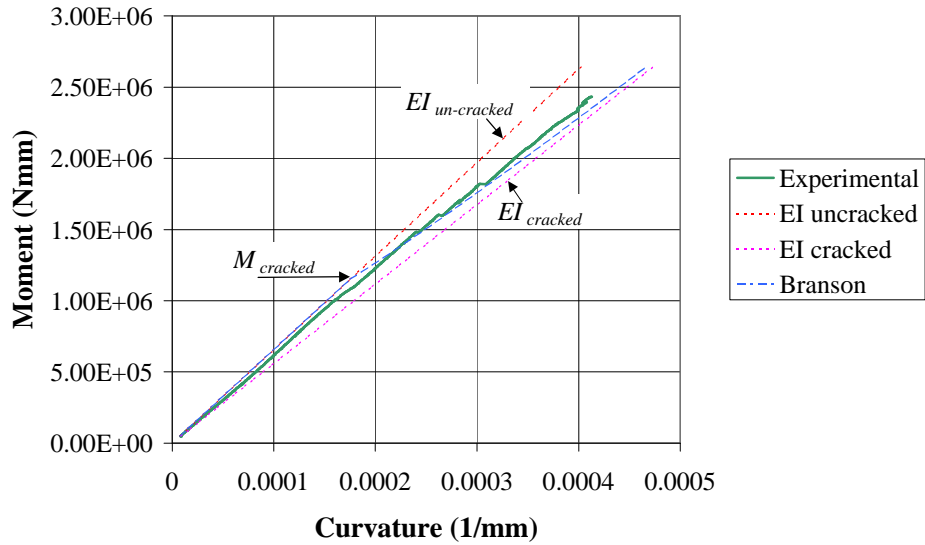


Figure 6.7 Moment-curvature of the FRP beam, and the Branson model

In the Branson model, the calculation of $EI_{effective}$ requires the cracking moment ($M_{cracked}$). In the present case, the un-cracked stiffness is a function of the strain in the core material. As a result, the determination of $M_{cracked}$ requires the solution of a fourth-order polynomial. However Kordina and Quast (1971) proposed a simpler approach for the evaluation of the effective stiffness. This approach assumes the moment-curvature relationship to be bi-linear as shown on Figure 6.8. The effective stiffness is obtained as the slope of the curve in the cracked region.

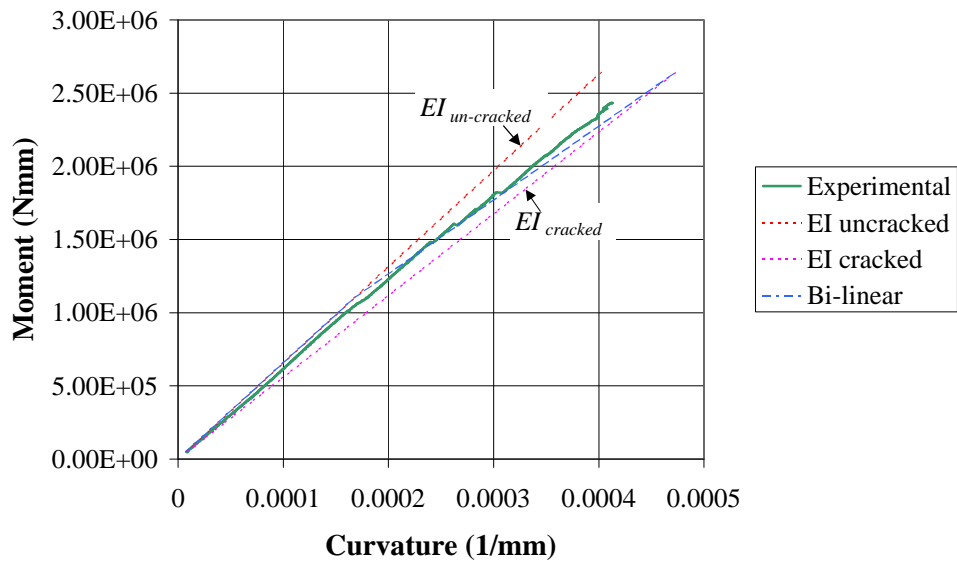


Figure 6.8 Moment-curvature of the FRP beam and the bilinear model

Assuming that the ultimate failure of the FRP beam is caused by tensile laminate rupture, the bilinear approximation can be used to express the effective stiffness in terms of tensile strains:

$$EI_{effective} = EI_{un-cracked} - (EI_{un-cracked} - EI_{cracked}) \frac{(e_t - e_{ft12})}{(e_{ft13} - e_{ft12})} \dots\dots\dots (6.7)$$

Therefore, the effective distance to the neutral axis corresponds to:

$$c_{effective} = c_{un-cracked} + (c_{cracked} - c_{un-cracked}) \frac{(e_t - e_{ft12})}{(e_{ft13} - e_{ft12})} \dots\dots\dots (6.8)$$

where: e_{ft12} and e_{ft13} are respectively the tensile failure strains of laminates L_{12} and L_{13} , and e_t is the highest tensile strain in the core material at a given load.

Equations (6.7) and (6.8) appear to describe with reasonable accuracy the flexural behaviour of the beam, which lies somewhere between the cracked and un-cracked states.

6.2.4 Primary failure modes

6.2.4.1 General

For the most cost-effective use of FRP materials, within the beam, the full capacity of the laminates should be reached prior to any other failure mode occurring. Indeed, it is one of the aims of this study that the developed beam fails in a primary mode. Therefore, it is important that the ultimate failure loads are estimated so that a comparison with the experimental results can be performed.

6.2.4.2 Critical components

The unidirectional laminates (L_2 and L_{13}) are the stiffest elements within the beam and they attract the majority of the resultant tensile and compressive forces generated by the applied bending moment. The rupture of any of these laminates will cause the total collapse of the beam, as the remaining materials are incapable of absorbing the released energy. Consequently, the two primary failure modes of the beam are either tensile or compressive failure of the unidirectional laminates. Due to the characteristics of these laminates, both these failure modes are brittle in nature, and they occur at the locations of highest strain. The

point of highest strain in the laminate happens at the location of a previously formed crack in the PFR.

6.2.4.3 Tensile failure of the bottom unidirectional laminate

The failure of the bottom laminate (L_{13}) creates a hinge in the beam, which becomes therefore a mechanism. When the strain distribution through the depth of the beam is assumed to be linear, the curvature at failure can be expressed as:

$$k = \frac{e_{ft13}}{c_{cracked} - t_{14}} \dots\dots\dots (6.9)$$

where $c_{cracked}$ is the distance from the bottom of the beam to the neutral axis, and t_{14} is the thickness of the bottom exterior RHS laminate. Substitution of (6.9) into equation (6.1) results in the following expression for the failure moment, M_f :

$$M_f = \frac{e_{ft13}EI_{cracked}}{c_{cracked} - t_{14}} \dots\dots\dots (6.10)$$

The full capacity of the bottom unidirectional laminate is realised when this failure moment occurs and the resulting failure moment, M_f , will lie upon the ideal moment – curvature curve unless compressive failure of the top unidirectional laminate precipitates failure.

6.2.4.4 Compressive failure of the unidirectional laminate

Unlike in the tensile zone, where the PFR is assumed totally cracked, all the materials above the neutral axis resist the compressive force imposed on the section. Of these materials, the unidirectional laminate, L_2 , resists the majority of load. This laminate has the lowest failure strain. Its failure is accompanied by the total collapse of the beam. Therefore, the failure moment for this failure mode can be expressed as:

$$M_f = \frac{e_{fc2}EI_{cracked}}{D - c - t_1} \dots\dots\dots (6.11)$$

where: e_{fc2} is the compressive failure strain of the unidirectional laminate, D is the depth of the beam, t_1 is the thickness of the top outer RHS laminate, and the effect of the PFR is encompassed within $EI_{cracked}$.

6.2.4.5 Predominant primary failure mode

As mentioned in Chapter 5 the materials within the FRP beam have compressive moduli that are higher than their respective tensile moduli. This, coupled with the core cracking, causes the neutral axis of the beam to rise. Due to this shift in neutral axis, the tensile strains are higher than the respective compressive strains. Furthermore, the unidirectional laminates have a higher failure strain in compression than in tension. As a result, tensile failure will always be predominant. Therefore, the amount of tensile unidirectional laminate is the critical parameter governing primary failure. However, if a very small amount of tensile reinforcement is provided, tensile failure may occur immediately after the first crack in the core material. The beam discussed in Section 3.2.2.4 is a typical example of such behaviour (Van Erp 1999). In such situations, both the core material and unidirectional laminate contribute to the moment capacity. To avoid such premature failure, in a static loading regime, the test beams are provided with sufficient tensile laminate so that $M_f \gg M_{cracked}$.

6.2.5 Secondary failure modes

6.2.5.1 General

A range of secondary failure modes may precede the aforementioned primary failure modes. In many instances, the predominant cause of these secondary failure modes is the lack of sufficient web and flange restraint.

The beam section is comprised of flanges and relatively thin webs surrounding a void. Due to this geometry, moment buckling of the webs and compression buckling of the top flange may occur. In addition, increased curvature of the beam induces compressive forces in the webs. Similar forces also occur at locations where the beam is externally loaded or supported. Associated with these forces are the failure modes shown on Figure 6.9:

- (a) compression buckling of the webs;
- (b) crushing of the webs;
- (c) tearing of the web laminates;
- (d) laminate failure in the flanges;
- (e) punching shear of the core in the flanges; and
- (f) longitudinal cracking of the core in the flanges.

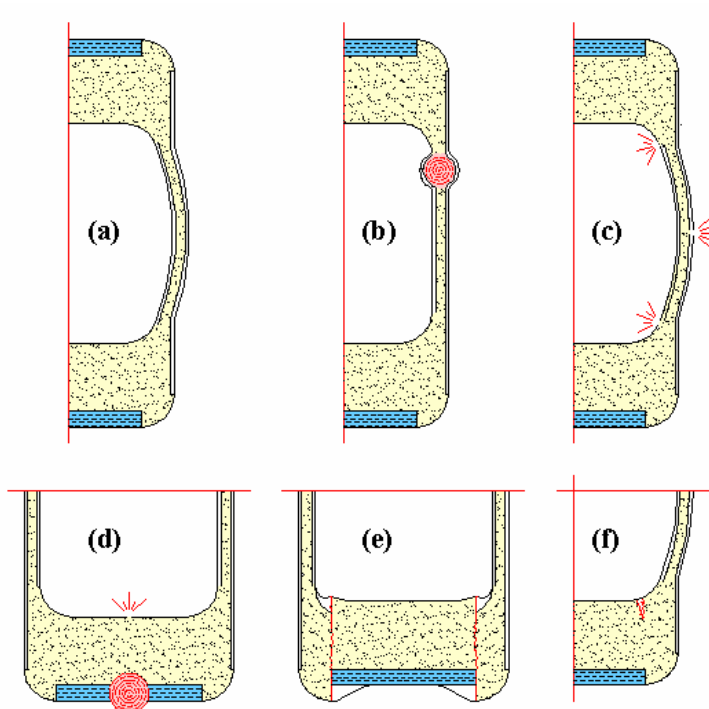


Figure 6.9 Some secondary failure modes in bearing

Potentially, any of these failure modes could precede the primary failure mode discussed before. Due to the complex boundary conditions and the resulting multidimensional stress states within the beam's cross-section, the failure loads are difficult to predict. However, using standard linear-elastic thin-walled beam theory, approximate solutions and the key parameters governing such failures can be obtained.

6.2.5.2 Moment buckling of the webs

As represented on Figure 6.10, compressive and tensile stresses are induced in the relatively thin webs. The compressive stresses may cause localised buckling of the web as shown on Figure 6.11.

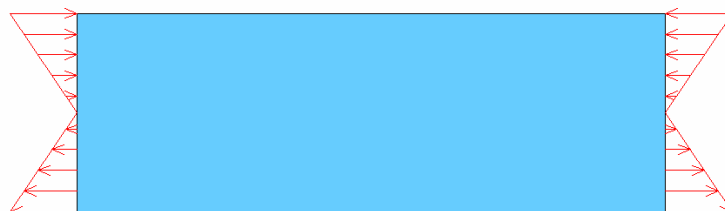


Figure 6.10 Stresses upon the web

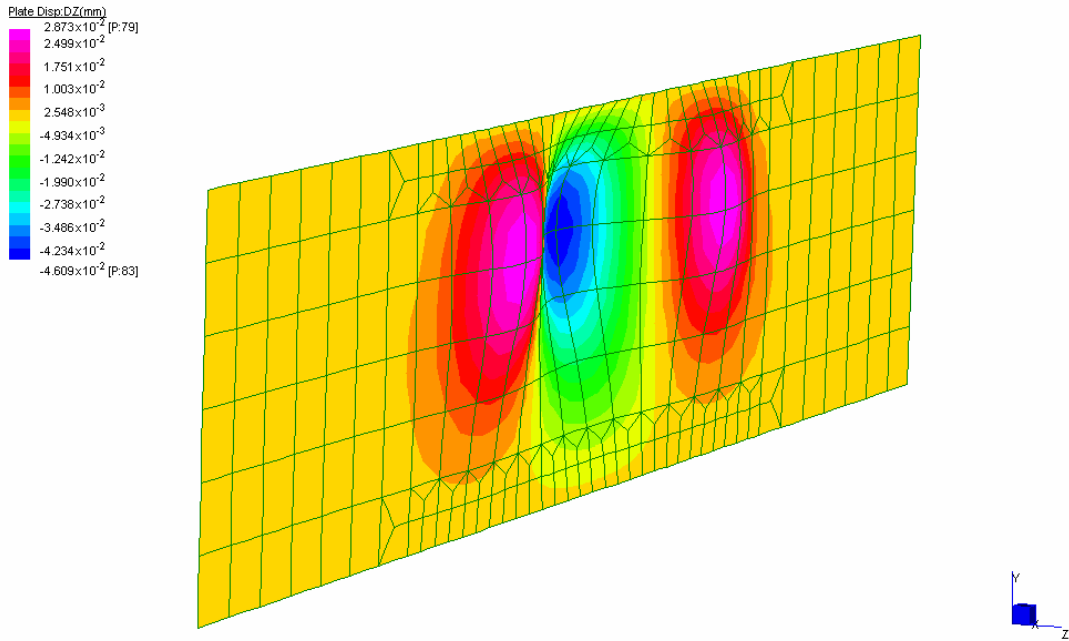


Figure 6.11 Moment buckling of web specimen

This type of buckling behaviour results in a reduced effective stiffness of the web and, therefore, accelerated failure of the beam. The rigidity of the connection between the web and the flanges has a major influence on the magnitude of the buckling load. In the case of thin-walled steel beams, a lower boundary approach is generally adopted to deal with the uncertainty in the boundary condition. A hinged connection between the web and the top flange is assumed. However, this approach underestimates the real buckling capacity of the web, and results in a conservative estimate for the buckling load. In the case of the present FRP beam, the core material at the web-flange interface may crack, resulting in a boundary condition similar to a hinge. Therefore, treating this boundary as hinged is appropriate. Its analytical treatment is based upon formulations developed for flat plates (Timoshenko, 1969) and transforming the section about its local axis. When these formulae are adopted for the sandwich structure of the web under consideration, they result in:

$$s_{mb.cr} = \frac{k_2 p^2 E}{12(1 - \nu_w^2)} \left(\frac{t_w}{d_b} \right)^2 \dots\dots\dots (6.12)$$

where: E is the reference modulus of the transformed section, ν_w is the Poisson ratio of the entire web of which the derivation is given in Appendix C.2, t_w is the thickness of the web, and d_b is the depth of the void in the FRP beam. The coefficient k_2 equals 23.8 for simple

supports. Using Hooke's law, expression (6.12) can be altered so that the critical moment buckling strain is expressed as:

$$e_{mb.cr} = \frac{23.8p^2}{12(1-n_w^2)} \left(\frac{t_w}{d_b} \right)^2 \dots\dots\dots (6.13)$$

From this equation, it is apparent that the web thickness, t_w , has a major impact upon buckling capacity.

The compressive strain in the web, at any given moment, can be calculated by substituting the relevant dimensions into equation (6.5) as follows:

$$e_{mb} = \left(D - c - \sum_{i=1}^4 t_i \right) \frac{M}{EI_{effective}} \dots\dots\dots (6.14)$$

To determine whether moment buckling of the web is likely, the results of equations (6.13) and (6.14) are compared. The onset of web moment buckling can be expected if $e_{mb} \geq e_{mb.cr}$. If moment buckling precipitates primary failure of the beam, extra core material can be added to increase t_w and thereby increase the buckling capacity of the web.

6.2.5.3 Compression buckling of the top flange

Under pure bending, the top flange of the beam is subjected to uniform compression as shown on Figure 6.12. In the case of a relatively thin top flange, this may result in local buckling as schematically depicted on Figure 6.13.



Figure 6.12 Stresses upon the flange

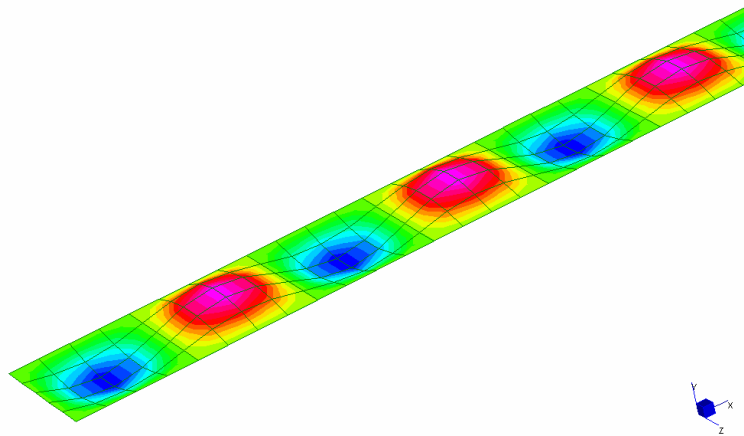


Figure 6.13 Compression buckling of the flange

When the top flange buckles, its stiffness decreases, causing the neutral axis of the beam to move towards the tension flange. The result of this shift is an increase in compressive strain in the buckled flange, and therefore accelerating failure of the beam. To minimise the possibility of this failure mode, core material (L_3) is added to the flanges of the beam. However, this failure may still occur if the thickness of core material is insufficient. To identify the key parameters for the flange buckling resistance, the buckling capacity of the flange is estimated.

The asymmetry of the flanges adds further complication to the analysis. By ignoring this asymmetry, the theory of plate buckling can be extended to the loading condition of flange compression buckling. Using the same rationale as for moment buckling of the webs, simply-supported edge conditions were assumed herein. This results in exactly the same form as equation (6.12) for critical compression buckling stress (Bulson 1970, p. 452) with a k_2 equalling 4 for simply-supported edges. The critical buckling strain for the sandwich panel flange then becomes:

$$e_{cb,cr} = \frac{4p^2}{12(1-\nu_f^2)} \left(\frac{t_f}{W - 2t_w} \right)^2 \dots\dots\dots (6.15)$$

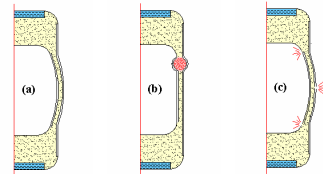
where: ν_f is the Poisson ratio of the flange, of which the derivation is similar to that given in Appendix C.2, t_f is the thickness of the flange, and W is the width of the beam. From equation (6.15), it is apparent that web and flange thickness are key parameters. Of these two, flange thickness has a dominant influence upon the buckling strain.

The strain of the compression flange can be calculated by substituting the relevant dimensions into equation (6.5) as follows:

$$e_1 = \frac{M(D - c)}{EI_{effective}} \dots\dots\dots (6.16)$$

The onset of flange buckling can be expected if $e_1 \geq e_{cb,cr}$.

6.2.5.4 Web failures (a), (b) and (c)



When the beam deforms as shown on Figure 6.14, or is subjected to an external bearing load, vertical compression forces are generated in the webs of the beam as shown on Figure 6.15.

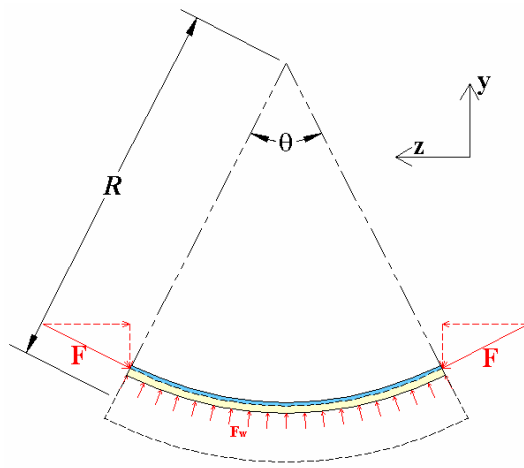


Figure 6.14 Top flange of curved beam: vertical force component

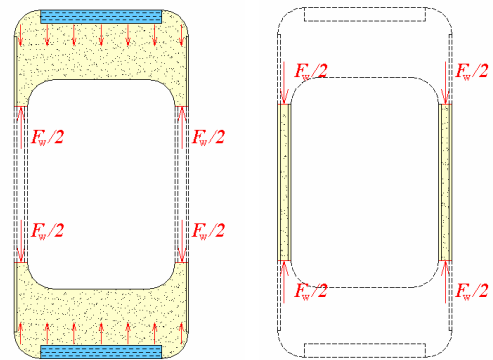


Figure 6.15 Secondary forces in flanges and webs

If the compressive force, noted F_w , is due to bending, then it is directly proportional to the curvature of the beam as detailed in Appendix C.3. The expression for F_w is obtained as:

$$F_w = \frac{\sum_{i=1}^4 e_i E_{ci} t_i w_i}{\left(EI/M - (D-c) + t_f/2 \right)} \dots\dots\dots (6.17)$$

However, for a point or bearing plate loading F_w is expressed as a linear function of the force applied and the depth of the beam as follows (Clarke 1996):

$$F_w = \frac{F}{L + 2y/\tan \alpha} \dots\dots\dots (6.18)$$

Where F is the force applied to the beam, y is the depth away from the applied force, and α is the stress distribution angle as shown on Figure 6.16. For buckling and crushing of the webs, the expression for F_w is often simplified to:

$$F_w = \frac{F}{\text{Buckling_length}} \dots\dots\dots (6.19)$$

and

$$F_w = \frac{F}{\text{Crushing_length}} \dots\dots\dots (6.20)$$

respectively. The use of this simple linear function will be further discussed in Section 6.6.

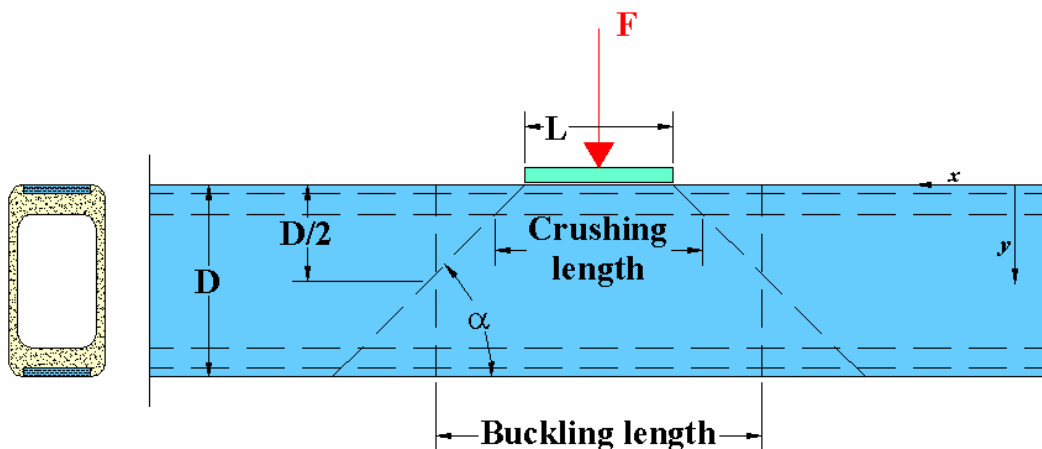


Figure 6.16 Standard determination of web dimensions for bearing capacity prediction

The force, F_w , is transmitted to the webs via the flanges. This causes a second-order moment (similar to the P- Δ effect in columns) into the beam cross-section, and results in an uneven stress distribution. Because of this second-order moment, the webs bow outwards and the flanges inwards as shown on Figure 6.17. The resulting moment diagrams have the form shown on Figure 6.18.

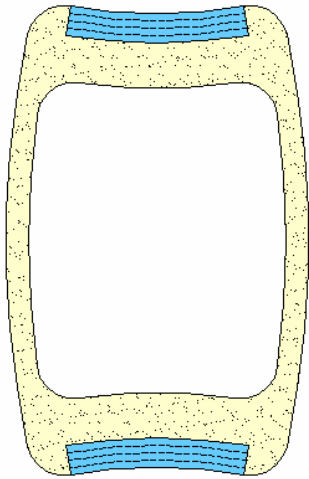


Figure 6.17

Deformed shape of beam due to the vertical force F_w

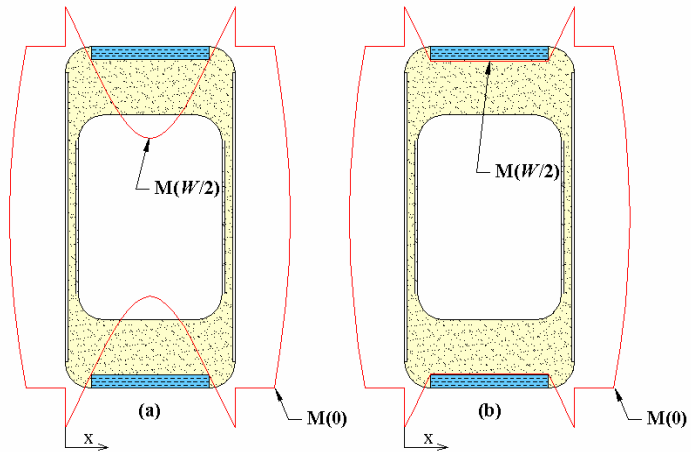


Figure 6.18 Moment diagrams throughout beam section; due to beam curvature (a) and bearing load (b)

The stiffnesses, EI_w and EI_f , of the web and flange segments are determined using the transformed section approach. Once obtained, they are used to determine the moment distributions in the cross-section caused by the beam curvature and bearing load respectively as:

$$M(0) = \frac{-F_w W}{8} \left(3 + \frac{(EI_w)^2 + 12(EI_f)^2}{2EI_w EI_f} \right) \dots\dots\dots (6.21)$$

$$M(W/2) = \frac{F_w W}{8} \left(4 + \frac{(EI_w)^2 + 12(EI_f)^2}{2EI_w EI_f} \right) \dots\dots\dots (6.22)$$

and

$$M(0) = \frac{F_w a}{2} \left(1 - \frac{\left(1 + \frac{a}{2W} \right)}{\left(1 + \frac{EI_w}{EI_f} \right)} \right) \dots\dots\dots (6.23)$$

$$M\left(\frac{W}{2}\right) = \frac{F_w a \left(1 + \frac{a}{2W} \right)}{2 \left(1 + \frac{EI_w}{EI_f} \right)} \dots\dots\dots (6.24)$$

where a is the distance from the edge of the beam to the location of load contact as shown on Figure 6.19, and W is the overall width of the beam.

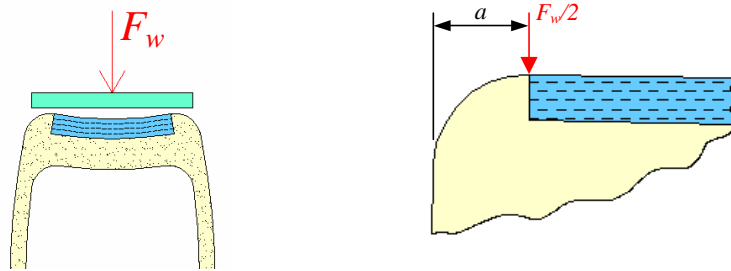


Figure 6.19 Bearing plate loading

The possible failure modes due to these actions are compression buckling, crushing, or tearing of the webs. Failure of the webs would severely affect the integrity of the beam and result in overall failure.

Compression buckling capacity of the webs (a)



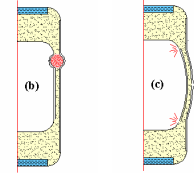
Buckling of the web under the compressive load, F_w , can be approximated using the classical Euler buckling formula as follows:

$$F_{w.cr} = 2 \frac{p^2 EI_w}{(k_l L)^2} \dots\dots\dots (6.25)$$

where L is the length of the element, and k_l is the effective length factor allowing for boundary conditions, which in this case have been assumed as pinned. Increasing core

thickness results in a higher buckling capacity, therefore, as with moment buckling, the thickness of the web is an important parameter. However, the presence of the second-order moment caused by the force F_w may place the webs in a state of lateral instability, which can result in premature buckling or their crushing or tearing.

Crushing or tearing of the web (b) and (c)



The web may also collapse due to compressive or tensile failure of one of its constituents. The determination of this type of failure is dependent on the strain distribution throughout the web. The vertical strains distribution caused by F_w can be obtained with an FE analysis as shown on Figure 6.20. The strains are not uniform across the web, they are higher on the inside edge.

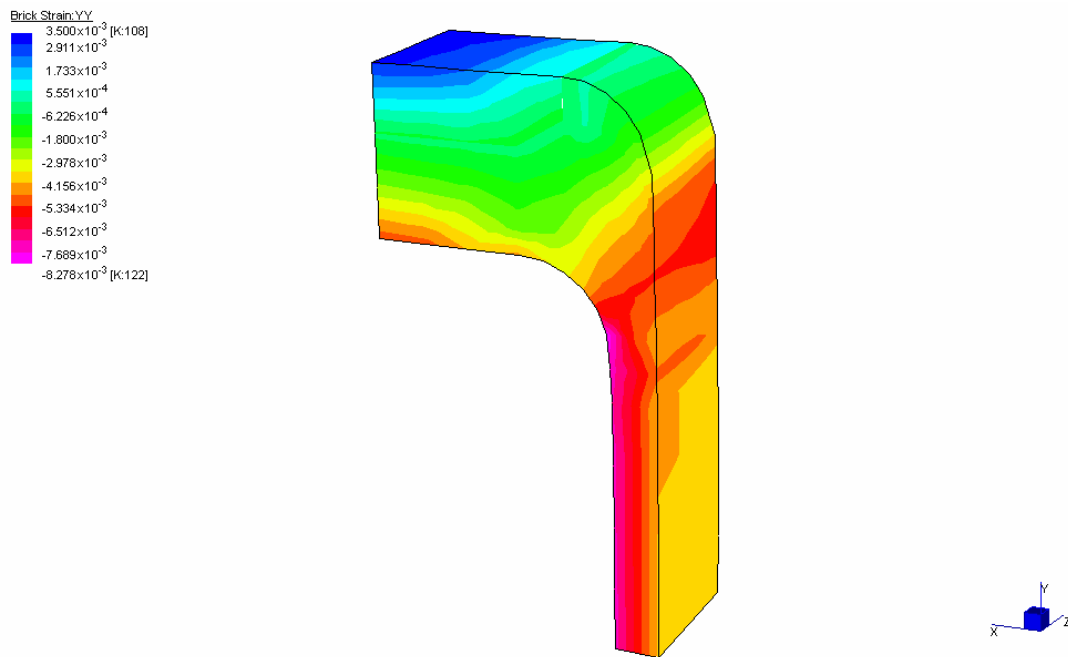


Figure 6.20 FEA model cross-section of the FRP beam under bearing load

The strains acting on the external and internal faces of the web can be estimated using the transformed section approach. The initial fibre compressive strain can be calculated as follows:

$$e_{cb,c} = \frac{M_{(0)}(t_w - c_w)}{EI_w} + \frac{F_w}{2EA_w} \dots\dots\dots (6.26)$$

and tensile strain as follows:

$$e_{cb,t} = \frac{M_{(0)}c_w}{EI_w} - \frac{F_w}{2EA_w} \dots\dots\dots (6.27)$$

where: A_w is the transformed area of the web, and E is the reference modulus of the transformed section. In both equations, the thickness of the webs has a major influence upon I_w and A_w , thereby also having a significant influence upon the magnitude of strains produced. Provided that:

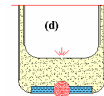
$$e_{cb,c} \leq \min(e_{fc5}; e_{fc6}; e_{fc7}), \dots\dots\dots (6.28)$$

and

$$e_{cb,t} \leq \min(e_{ft5}; e_{ft7}) \dots\dots\dots (6.29)$$

failure of the web should not occur.

6.2.5.5 RHS laminate failure within the flanges (d)



High values of the bending moment in the flanges, as depicted in Figure 6.18, could result in the failure of the RHS laminate and the core material, which in turn may cause the beam to split along its longitudinal axis. In addition, the associated shear forces could also cause the unidirectional laminate to punch into the void of the beam.

The resulting transverse strains in laminates L_1 and L_4 are proportional to the thickness of the flange, and can be calculated per unit length of beam, using equation (6.5), as follows:

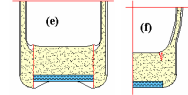
$$e_{1(x)} = \frac{-M_{(x)}(t_f - c_f)}{EI_f} \dots\dots\dots (6.30)$$

and

$$e_{4(x)} = \frac{M_{(x)}c_f}{EI_f} \dots\dots\dots (6.31)$$

where: t_f is the thickness of the flange, c_f is the distance from the bottom of the flange to the neutral axis of the flange, and EI_f is the stiffness of the flange (in the transverse direction). These estimated strains are compared with the capacities of the laminates L_1 and L_4 to determine whether failure is likely. Since the PFR material has a lower tensile failure strain than the laminates, it is expected to fail first.

6.2.5.6 Longitudinal cracking of the core in the flanges (e) and (f)



Part of the force F_w is also transferred to the webs through the core material. As a result, it is also subjected to shear and flexure. The transverse shear stress in the core resulting from the curvature of the beam can be calculated as follows:

$$t_{xy3(x)} = \frac{F_w \left(\frac{1-x}{2} - \frac{x}{W} \right)}{t_{3(x)}} \dots\dots\dots (6.32)$$

Additional shear stresses caused by external bearing plate loading can be calculated as follows:

$$t_{xy3} = \frac{F_w}{2t_3} \text{ for } 0 \leq x \leq a \text{ and } t_{xy3} = 0 \text{ for } x > a \dots\dots\dots (6.33)$$

The critical shear stress in the core material occurs at the web-flange interface. Since the core material has been assumed isotropic, the principal strains within can be determined using Mohr's circle:

$$e_{11,22} = \frac{e_x + e_y}{2} \pm \sqrt{\left(\frac{e_x - e_y}{2} \right)^2 + \left(\frac{t_{xy3}}{2G_3} \right)^2} \dots\dots\dots (6.34)$$

where: e_x are calculated using equation (6.31), e_y is taken as zero, and G_3 is the shear modulus of the PFR. From equations (6.31) and (6.33) it is apparent that the thickness of the flange is a major factor that governs the principal strain calculated in equations (6.30) to (6.34).

The obtained values calculated can then be checked against the failure strain of the PFR to estimate when failure is likely to happen. An initial crack in the core reduces the

shear area and amplifies the shear stresses as calculated in equation (6.32) leading to an accelerated overall failure of the flange.

6.2.5.7 Other failure modes

Sandwich structures that use foam as a core material suffer from web wrinkle and dimpling. The PFR used in the present beam has a higher stiffness than Nomex honeycomb, which is known not to experience these failure modes. Therefore, these failure modes are unlikely, and will not be considered in this study.

6.3 Pure shear

6.3.1 Shear-deformation behaviour

Like in the preceding section, the transformed section approach is also used to model shear behaviour and its applicability will be assessed by comparing predictions against the results from the tests, detailed in the next Chapter. The shear modulus, G , is now used in conjunction with the widths of the lamina to produce the transformed section. The behaviour of the beam under shear loading is as shown on Figure 6.21. The shear stiffness of the beam, GA , is initially that of the un-cracked section (region 1). The first cracks in the PFR appear at a loading of:

$$V_{cracked} = \frac{t_{f6} A_t G}{1.785 G_6} \dots\dots\dots (6.35)$$

where: t_{f6} is the failure shear stress of the core, A_t is the transformed area of the un-cracked section, G is the reference modulus of the transformed section, G_6 is the shear modulus of the core, and the denominator 1.785 allows for the non-uniform stress distribution throughout the section as determined in Section 6.3.2.

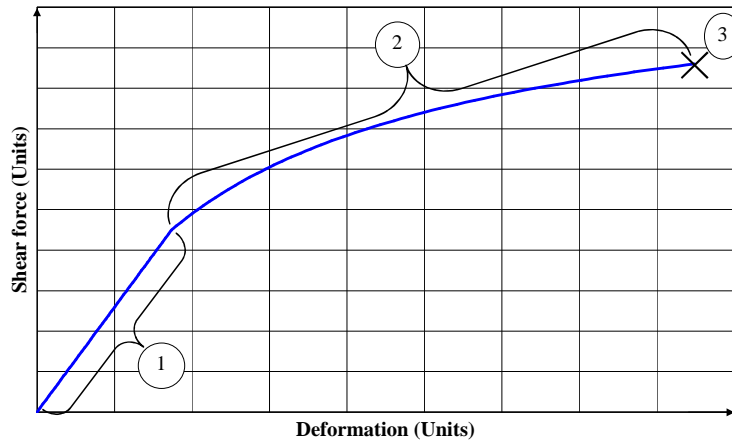


Figure 6.21 FRP beam; shear load deformation behaviour

Once cracking occurs, the beam becomes a hybrid of cracked and un-cracked sections. The beam continues to accept further loading until failure of the web laminates (point 3). The behaviour of the beam and the progression of cracks is similar in nature to that discussed for pure bending in Section 6.2.3. Using the same bilinear relationship adopted in Section 6.2.3, the effective shear stiffness for region 2 can be estimated as:

$$GA_{effective} = GA_{un-cracked} - (GA_{un-cracked} - GA_{cracked}) \frac{(V - V_{cracked})}{(V_{ultimate} - V_{cracked})} \dots\dots\dots (6.36)$$

where $V_{ultimate}$ is determined in Section 6.3.3.

Assuming small deformation theory, the obtained effective stiffness can be used to estimate shear deformations as detailed in Appendix C.5.

6.3.2 Shear stress distribution

According to ISO 14129 (International Organization for Standardization), shear failure of an FRP is considered to occur at a shear strain of 0.05. However, as tests reveal, shear behaviour of FRP materials is often characterised by yielding. In the opinion of the author, failure may be better defined through the use of a limiting stress criterion, which characterises the onset of yielding.

The stress distribution throughout a beam undergoing shear loading is not uniform. The variation in stresses is characterised by the shear flow throughout the section, which can be estimated using the following equation (Beer & Johnston 1985, p. 243):

$$t_y = \frac{VQ_y}{It_y} \dots\dots\dots (6.37)$$

where: t_y is the shear stress at the location a distance y from the neutral axis, V is the shear force acting on the beam, Q_y is the first moment of the area above y to the neutral axis, I is the second moment of area of the section, and t_y is the width of the section at the distance y . By ignoring shear lag, the equation gives an average shear stress across the width of the section. Indeed, shear lag can be considered negligible for thin sections such as the FRP beam webs as reported by Beer & Johnston (1985, p. 243). Furthermore, FEA confirmed that the shear lag was negligible.

Using equation (6.37), two cases were modelled, respectively ignoring and allowing for the cracking of the core material. The obtained distributions are shown on Figure 6.22.

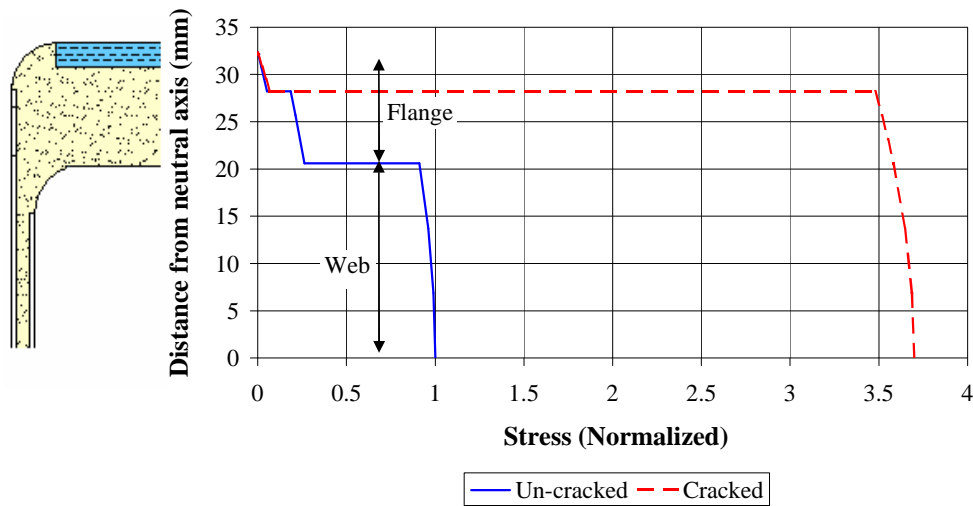


Figure 6.22 Shear stresses throughout the beam cross-section

It can be seen that the shear stresses within the web laminates are much higher when cracking of the core is considered. Furthermore, for both cases, it can be seen that the maximum shear stress value occurs in the webs. Hence, it is a common and reasonable practice to ignore flange contribution to shear resistance in box beams. However, for the sake of completeness, flange contributions are considered herein.

Calculation of the maximum shear stress is often facilitated by the introduction of a shear correction factor, k_3 , to the average shear stress. This average shear stress is calculated by:

$$t_{ave} = \frac{V}{A_t} \dots\dots\dots (6.38)$$

The shear correction factor can be estimated by comparing the values obtained from equations (6.37) and (6.38). Figure 6.23 shows the variation of k_3 along the depth of the beam.

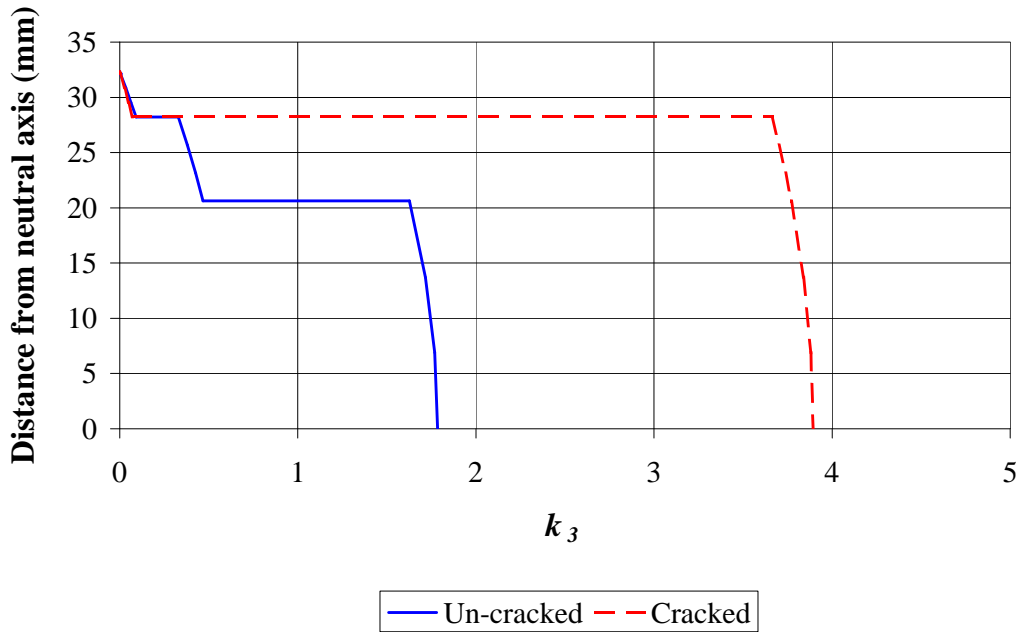


Figure 6.23 Shear correction values throughout the beam

It appears from these values that the maximum shear stress in the webs can be calculated respectively for the un-cracked and cracked transformed sections as:

$$t_{un-cracked} = 1.785 \frac{V}{A_t} \dots\dots\dots (6.39)$$

and:

$$t_{cracked} = 3.893 \frac{V}{A_{t,c}} \dots\dots\dots (6.40)$$

where $A_{t,c}$ is the transformed area of the cracked section. Determination of the individual laminate stresses is then achieved by multiplying the stresses, calculated with equations (6.39) and (6.40), by the transformation ratio for the particular laminate as follows:

$$t_i = \frac{G_i}{G} t \dots\dots\dots (6.41)$$

where: t_i is the shear stress in laminate i , G_i is the shear modulus of the laminate, G is the reference shear modulus used for the transformed section, and t is the shear stress calculated from equation (6.39) or (6.40). These stresses can then be compared with the capacities of the laminates to assess whether failure is likely to occur at the given shear loading.

Once the stresses in the beam have been determined, the failure modes can be defined with reference to these stresses.

6.3.3 Shear-induced failure modes

6.3.3.1 Cracking of the core

Excessive shear stresses in the beam can lead to a number of failures taking place. In particular, due to its brittle nature, cracking of the core material is likely to occur when the maximum shear stress in the web exceeds the failure shear stress of the PFR as shown in equation (6.35). It is expected that cracking will be initiated in the middle of the web where the shear stresses are the highest. Once the PFR is cracked, the web and flange laminates provide the only resistance to failure at crack locations, as they constitute the main shear reinforcement of the beam. With the addition of load, the cracks extend into the flanges causing a localised shear dislocation in the beam as shown on Figure 6.24. As a result, the inner RHS is no longer constrained by the core, and is prone to delaminating and buckling. Whereas the outer RHS laminate is still restrained and continues to resist the loading until it fails in a tensile mode.

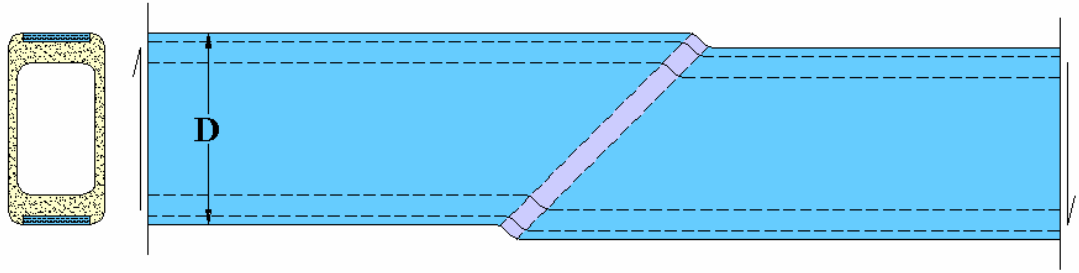


Figure 6.24 Exaggerated localised shear dislocation caused by cracking of the PFR

6.3.3.2 Shear failure of the webs

Failure of the web is expected when the shear stress in the outer RHS laminate exceeds its shear capacity, which is determined as:

$$3.893 \frac{VG_7}{A_{t,c}G} \geq t_{f7} \dots\dots\dots (6.42)$$

where t_{f7} is the shear capacity of the web laminate as determined using ISO 14129. However, experimental results, as will be detailed in Chapter 7 reveal that the shear capacity of the web laminates is higher than that estimated using ISO 14129. It was found that the shear strength of the web laminates is governed by fibre fracture. Therefore, equation (6.42) is reformulated to include fibre fracture, as detailed in Section 7.4.2.2, and results in:

$$3.893 \frac{VG_7}{A_{t,c}G} \geq s_{f7} f_{f7} \cos 45 \dots\dots\dots (6.43)$$

Using the latest equation, a prediction of the ultimate shear capacity of the beam can be obtained as:

$$V_{ultimate} = \frac{A_{t,c} s_{f7} f_{f7} G \cos 45}{3.893 G_7} \dots\dots\dots (6.44)$$

6.3.3.3 Shear buckling of the webs

The thinner the web, the higher the likelihood that web buckling will precede shear failure. The principal stresses caused by shear are shown on Figure 6.25.

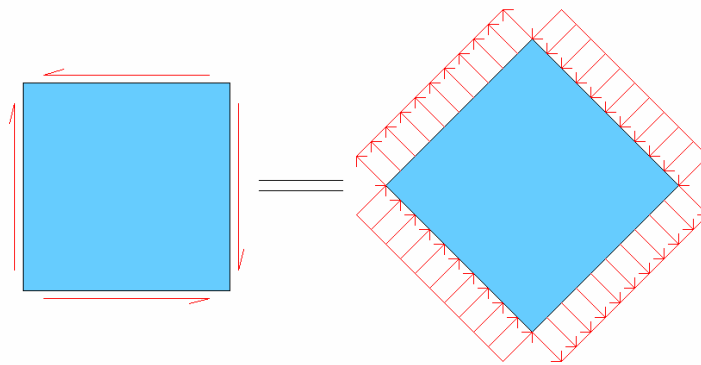


Figure 6.25 Principal stresses on the webs

The compressive component of these principal stresses may cause buckling of the web, which is shown on Figure 6.26. This type of buckling reduces the stiffness of the webs and leads to premature failure of the beam.

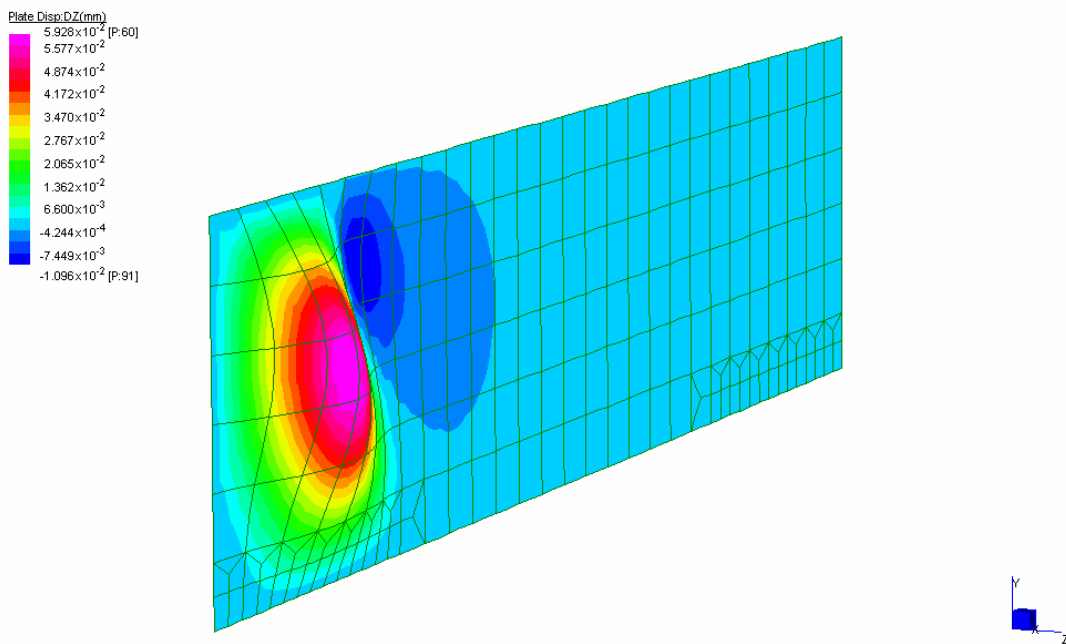


Figure 6.26 Shear buckling of web specimen

Using a hinged boundary assumption, as adopted in Section 6.2.5, a lower boundary solution for the critical shear buckling stress can be obtained as (Bulson 1970, p. 451):

$$s_{sb.cr} = \frac{5.35Gp^2 \left(\frac{t_w}{d_b} \right)^2}{12(1-n_w^2)} \dots\dots\dots (6.45)$$

where: the parameter 5.35 is based upon thin-walled plate theory for a plate with simply-supported restraints, t_w is the thickness of the web, d_b is the depth of the void, and ν_w is the Poisson ratio of the web as formulated in Appendix C.2. Comparison of the critical buckling and the maximum shear stresses within the web, respectively obtained using equations (6.39) and (6.40), provides an indication as to when shear buckling of the web is likely to occur. It is apparent from equation (6.45) that the web thickness has a major affect upon capacity, as a substantial rise in capacity can be achieved by a slight increase in web thickness.

6.3.3.4 Flange failure

While the webs resist the majority of the shear loading, the flange laminates also provide some resistance to shear. As a result, they are susceptible to undergoing the following failure modes: shear failure of the laminates (L_1 , L_2 or the core), and punching shear of the flange into the hollow core of the beam. Furthermore, the fibre orientation and geometry of the laminates do not provide any restraint against fibre pull-out, therefore the ISO 14129 recommended shear capacity applies.

Laminate failure in the flanges may happen when the shear stress exceeds the shear capacities of the outer laminates (L_1 or L_{1d}), the unidirectional laminate (L_2 or L_{13}), and the core (L_3 or L_{12}); their respective failure criteria are given as:

$$\frac{VG_1}{335.676A_{t,c}G} \geq t_{f1}, \dots \dots \dots (6.46)$$

$$\frac{VG_2}{13.922A_{t,c}G} \geq t_{f2} \dots \dots \dots (6.47)$$

and

$$\frac{VG_3}{2.138A_tG} \geq t_{f3} \dots \dots \dots (6.48)$$

where t_{fi} is the failure shear stress of laminate i, and the coefficients in the denominators are obtained from the shear flow diagrams represented on Figure 6.23. In case of failure of the flanges, the shear force is entirely resisted by the webs. However, as the web carries most of

the shear, this is unlikely since the shear loads required to cause flange laminate failures are well in excess of the webs' shear capacity.

Punching shear of the flange into the beam hollow core splits the beam into two parts along the longitudinal axis. Such a catastrophic failure can happen if the shear stress within the flange exceeds the shear strength of the core in the flange:

$$\frac{V}{2.138A_t} \frac{w_2 \sum_{i=1}^4 G_i t_i}{4 \left(\frac{t_{f3}}{t_{f1}} (t_1 + t_4) + t_2 + t_3 \right)} \frac{1}{G} \geq t_{f3} \dots\dots\dots (6.49)$$

It is apparent from equation (6.49) that flange thickness can be increased with subsequent increase in capacity.

6.4 Moment-shear interaction

6.4.1 Deformation behaviour

Since FRP beams are known to experience high shear deformations (Bank 1987, 1989; Barbero, Fu & Raftoyiannis 1991; Davalos et al. 1996; Kilic, Aktas & Dirikolu 2001; Nagaraj & Gangarao 1997), it is therefore necessary to include the effect of shear in describing their deformation under load, which warrants resorting to Timoshenko beam theory. According to this theory, the total deflection of a beam under a combined loading of moment and shear can be separated into two additive components, namely flexural and shear:

$$\Delta_t = \Delta_m + \Delta_s \dots\dots\dots (6.50)$$

where Δ_t is the total deflection, Δ_m is the moment deflection, given as:

$$\Delta_m = \frac{M(3La - 4a^2)}{6EI_{effective}} \dots\dots\dots (6.51)$$

and Δ_s is the shear deflection, given as:

$$\Delta_s = \frac{Va}{GA_{effective}} \dots\dots\dots (6.52)$$

for a beam in 4-point bending, where M is the moment and V is the shear force imposed on the beam. The values L and a are shown on Figure 6.27.

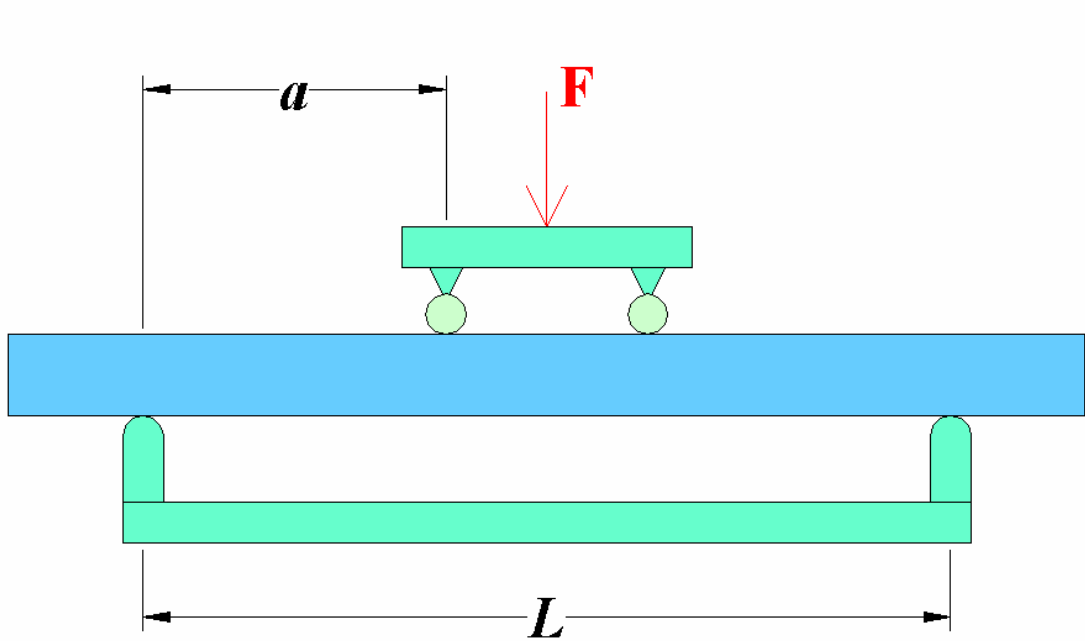


Figure 6.27 Beam in 4-point bending

6.4.2 Shear-moment capacity

6.4.2.1 General

As previously discussed in Section 4.3.3, there is a synergy between the actions of moment and shear in FRP: the introduction of a moment into a beam affects the shear capacity and vice versa. Methods for predicting the moment-shear interaction of homogeneous beams exist in the literature (Beer & Johnston 1985; Clarke 1996; Dym & Shames 1973; Gaylord, Gaylord & Stallmeyer 1992; Hibbeler 1991). The three most used methods in structural engineering: principal stress determination, linear relationship, and elliptical relationship are described below. A diagrammatic comparison between the models is given on Figure 6.29 at the end of this section.

6.4.2.2 Principal stress determination (Mohr's circle)

For an infinitesimally small isotropic element, failure under a combined load occurs when the principal stresses within the element exceed the respective capacity of the material. These principal stresses can be determined from the tensile, compressive and shear stresses acting on the element by the use of Mohr's circle:

$$s_{1,2} = \frac{s_z + s_y}{2} \pm \sqrt{\left(\frac{s_z - s_y}{2}\right)^2 + t_{zy}^2} \dots\dots\dots (6.53)$$

where s_y is taken as zero for a beam in combined bending and shear. The angle the first principal stress makes with the z-axis can be determined by solving for q as:

$$\tan 2q = \frac{2t_{zy}}{s_z - s_y} \dots\dots\dots (6.54)$$

However since principal stresses are known to rotate, equations (6.53) and (6.54) are better written in terms of strain as follows:

$$e_{11,22} = \frac{e_z + e_y}{2} \pm \sqrt{\left(\frac{e_z - e_y}{2}\right)^2 + \left(\frac{g_{zy}}{2}\right)^2} \dots\dots\dots (6.55)$$

and

$$\tan 2q = \frac{g_{zy}}{e_z - e_y} \dots\dots\dots (6.56)$$

where g_y is engineering shear strain.

Through the use of the transformed section approach, it is possible to simulate the FRP beam as homogeneous isotropic medium. Cracking of the core will precipitate failure of the beam. Therefore, the cracked section is used in the analysis. Figure 6.28 diagrammatically depicts a combination of the shear and bending strains, resulting in a varied strain distribution throughout the beam cross-section. The critical location depends on the ratio of moment to shear. However, unlike a real homogeneous isotropic section, the angle the principal strain makes with the direction of the fibres in the laminates is of

paramount importance. The most critical situation happens when the first principal strain is normal to fibre direction. For each moment shear combination, the principal strains and their directions can be established, and compared with the material capacity to determine the critical location. By altering the magnitude of shear and moment loading, an interaction diagram can be produced.

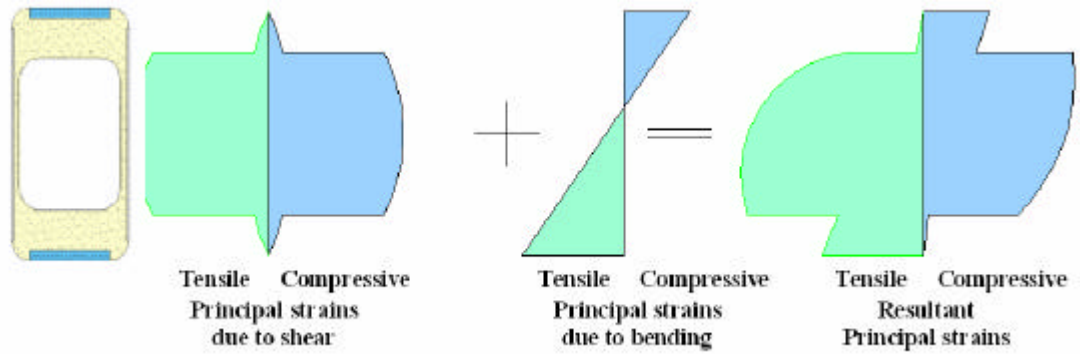


Figure 6.28 Principal strains of the transformed FRP beam

The flowchart of this method is given in Appendix C.7, and the obtained results are shown at the end of this section. Simpler methods are available and are discussed below.

6.4.2.3 Empirical models

Linear relationship (Eurocomp)

A linear relationship has been adopted by the Eurocomp design code (Clarke 1996). It uses the following formula:

$$1 \geq \frac{V}{V_{u0}} + \frac{M}{M_{u0}} \dots\dots\dots (6.57)$$

for the determination of a moment-shear interaction diagram. Where V_{u0} and M_{u0} are respectively the ultimate capacities of the beam in pure shear and moment.

Elliptical relationship (General)

When considering isotropic materials, the linear relationship mentioned above is conservative and is often replaced with an elliptical derivation that has its roots in the Mohr's circle method. For an isotropic material the general form is as follows:

$$1 \geq \left(\frac{V}{V_{u0}} \right)^2 + \left(\frac{N}{N_{u0}} \right)^2 \dots\dots\dots (6.58)$$

where N is the axial force applied. Given that the primary failure mechanism for the beams in flexure is one of an axial failure, the substitution of moment for axial force in equation (6.58) may be acceptable, therefore equation (6.58) becomes:

$$1 \geq \left(\frac{V}{V_{u0}} \right)^2 + \left(\frac{M}{M_{u0}} \right)^2 \dots\dots\dots (6.59)$$

This relationship is quadratic and allows higher combined loadings than the Eurocomp method. This method is also used for combined web buckling calculations (Bulson 1970, p. 451).

6.4.2.4 Comparison of models

Figure 6.29 is a plot of the interaction diagrams of the models described above. It is apparent from the diagram that none of the methods correlate. The Mohr's and elliptical methods are similar, the difference being due to the Mohr's method taking account of the FRP beams' constituent materials. All models show a degree of synergy between moment and shear, but this is highly pronounced for the Eurocomp model. Now that a number of models have been defined, they will be compared against FEA and experimental data in the remaining chapters to ascertain their applicability to FRP beam design.

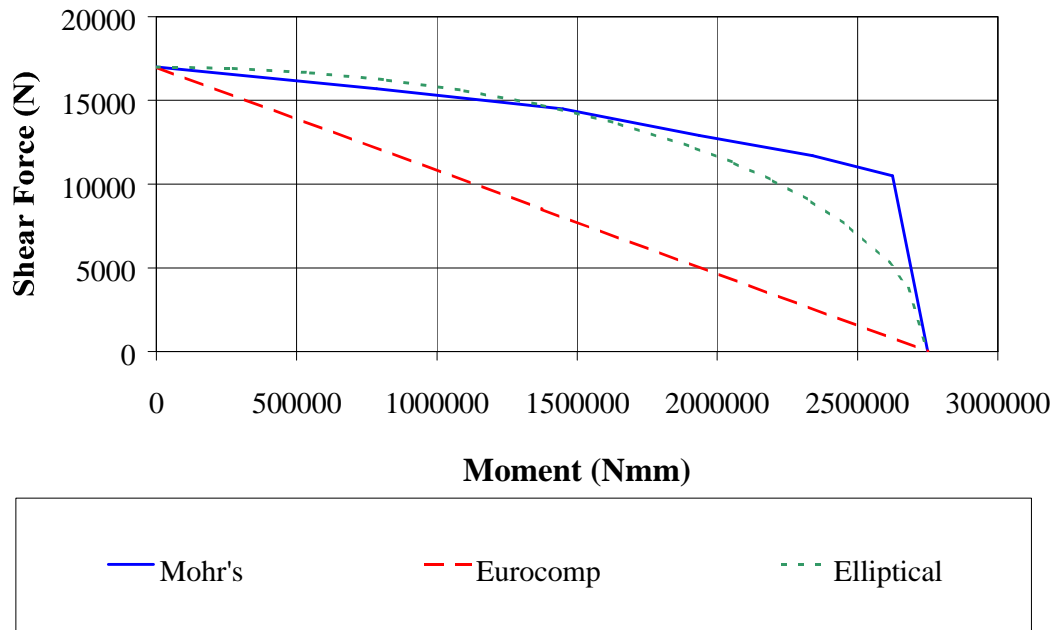


Figure 6.29 Moment-shear interaction diagrams

6.5 Lateral torsional resistance of the beam

6.5.1 General

Due to load eccentricities and geometrical imperfections, a beam tends to twist towards its weaker axis. This lateral torsional buckling often precipitates bending failure. Consequently, it can become the primary failure mode of a beam in flexure. To avoid this scenario, lateral restraints are often provided. Determination of restraint locations is dependent upon the critical buckling load, which is a function of the un-restrained span, and the section properties of the beam. The torsion constant of the section is of particular importance when it comes to the study of lateral torsional buckling. Once determined, a simple one-dimensional analysis can be formulated.

6.5.2 Determination of the torsion constant

Torsion or twisting in a section induces shear stresses. In the case of a rectangular hollow section, such as the present FRP beam, the shear stresses induced within the flanges and webs will be of a different magnitude. The differences in magnitude are due to the dissimilarity in the size, spatial location, and make-up of the flanges and webs. The core material could fail in tension from these shear stresses, and the section would continue to sustain further loads until ultimate failure. The mechanisms of pure shear discussed in

section 6.3 are applicable here. Distortional warping of the cross-section is prevented by the applied boundary conditions used in the experimental set-up. As a result, there is no change in length of the beam and the cracks in the PFR remain closed. As a result, torsional deformation behaviour does not display distinct cracked and un-cracked responses. Therefore, the torsion constant, J , for this particular set-up can be assumed to be independent of the applied loading.

The rotation of the section can now be calculated using a one-dimensional analysis. For thin-walled box beams, the determination of the torsion constant and rotations can be found in (Beer & Johnston 1985, p. 143; Heins 1975, p. 51):

$$\boldsymbol{f} = \frac{TL}{4A^2G} \oint \frac{ds}{t} = \frac{TL}{JG} \dots\dots\dots (6.60)$$

This results in the well-known Saint Venant torsion constant formula:

$$J = \frac{4A^2}{\oint \frac{ds}{t}} \dots\dots\dots (6.61)$$

where: T is the applied torque, L is the length of the beam, G is the shear modulus of the beam, \boldsymbol{f} is the angle of rotation as shown on Figure 6.30, the integral in the denominator is taken along the centre line of the wall section (for example, the integral of an RHS with dimensions $D \times W$, web thickness t_w and flange thickness t_f equals:

$$2 \left(\frac{(D - t_f)}{t_w} + \frac{(W - t_w)}{t_f} \right),$$

and

$$A = (D - t_f)(W - t_w) \dots\dots\dots (6.62)$$

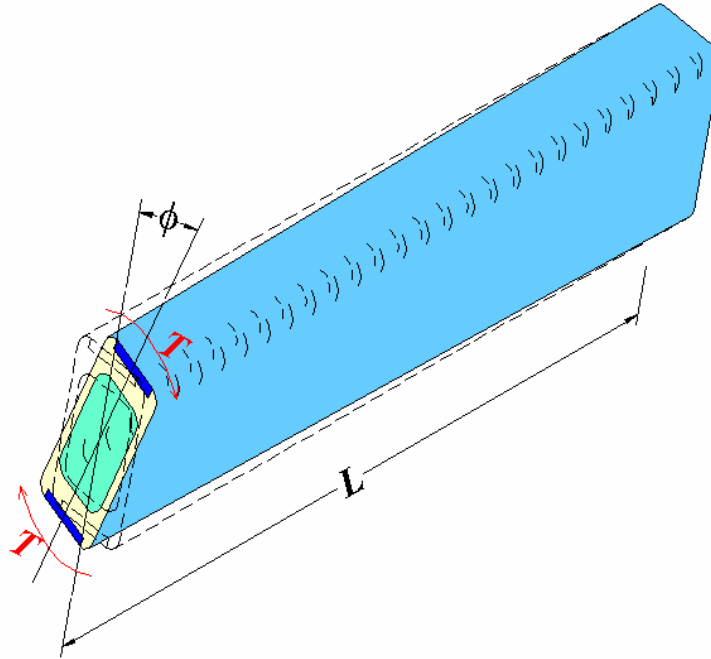


Figure 6.30 Torsional rotation of the beam

Through using the transformed section approach, the above formulae may be applied to determine the shear constant and deformations of the beam. Because of the geometry of the section, the transformation is carried out in a cylindrical coordinate system about the centre of rotation of the beam. A simplification is to set the transformed flanges to the y-axis transformation formula:

$$t_{ii} = t_i \frac{G_i}{G} \dots\dots\dots (6.63)$$

and the webs to the x-axis transformation formula:

$$w_{ii} = w_i \frac{G_i}{G} \dots\dots\dots (6.64)$$

Where: t_{ii} is the transformed thickness, w_{ii} is the transformed width, G_i is the shear modulus, of laminate i, and G is the reference modulus of the transformed section. A justification of this approach is given by Kollbrunner & Basler (1969 p. 17).

The resulting torsion constant can now be used within the model to estimate lateral torsional buckling behaviour.

6.5.3 Simplified analysis of lateral torsional buckling

The behaviour of an unrestrained beam to an increasing moment is illustrated on Figure 6.31. Minor imperfections in the beam and loading arrangement can result in the beam twisting slightly with increased loading. In region 1, as depicted on the graph, the behaviour of the beam is stable. However, as the end of region 1 is approached, the rotation of the section increases markedly. At this critical loading, the beam is no longer stable, as it continues to twist without addition of further loading, which ultimately results in its failure.

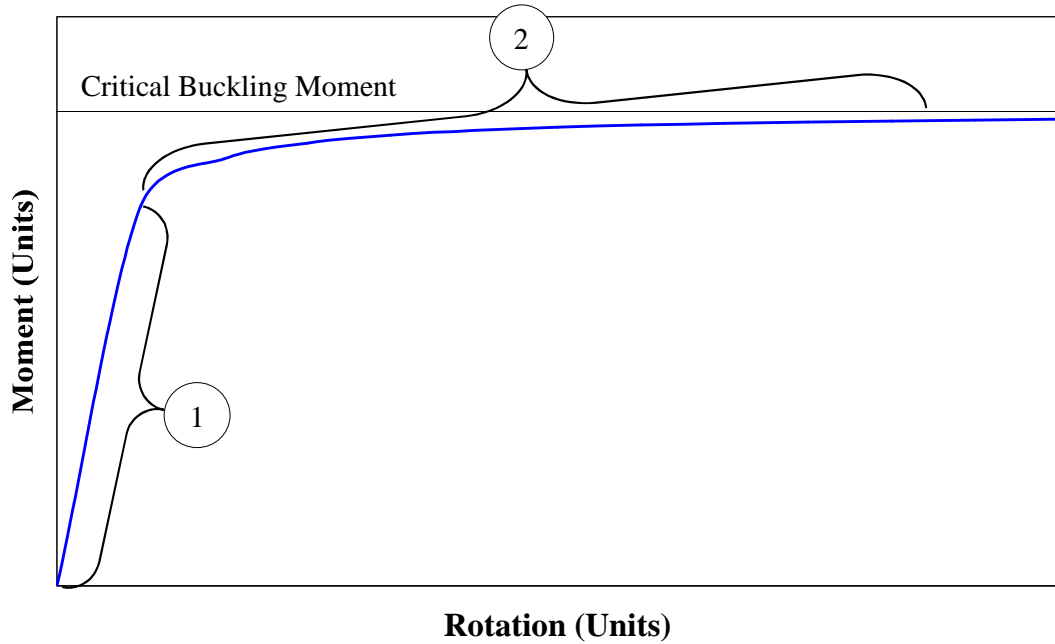


Figure 6.31 Lateral buckling behaviour of the FRP beam

6.5.3.1 Analytical formulation of lateral torsional buckling behaviour

Figure 6.32 represents the free end of the cantilever beam with an applied load, P . Due to the large displacements, the updated configuration, and the additional torque, Pdx , are obtained iteratively.

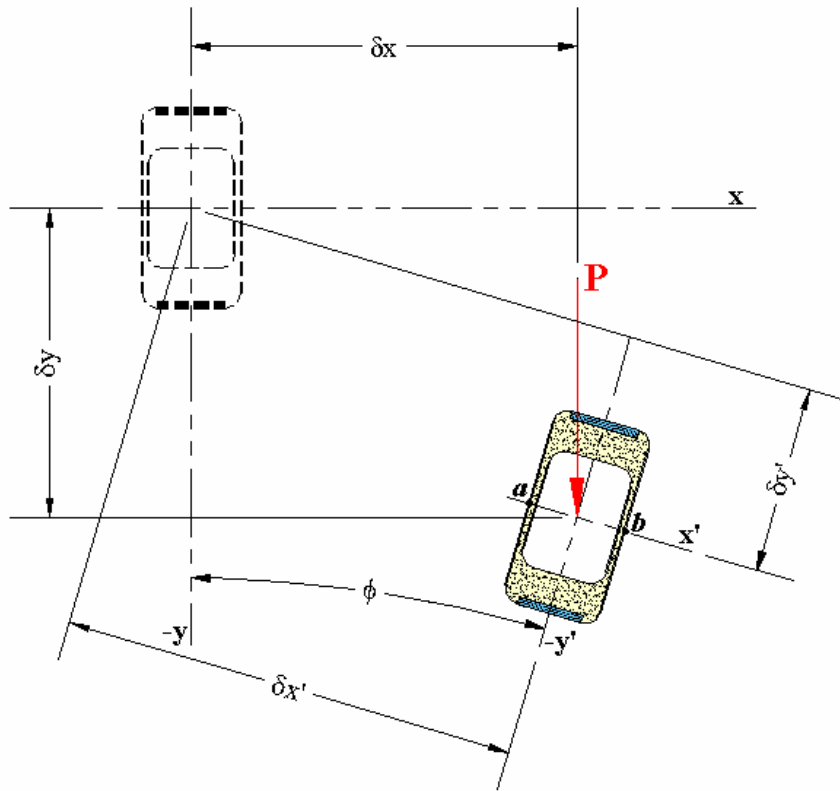


Figure 6.32 Deflections of a beam undergoing lateral torsional buckling

The derivation of the iterative approach is detailed in Appendix C.8 and results in expressions for the x-axis deflection, y-axis deflection and rotations respectively equalling:

$$\mathbf{d}x = \frac{L^3 P}{3} \sin\left(\frac{P \mathbf{d}x L}{4GJ}\right) \cos\left(\frac{P \mathbf{d}x L}{4GJ}\right) \left[\frac{1}{EI_y} - \frac{1}{EI_x} \right] \dots\dots\dots (6.65)$$

$$\mathbf{d}y = P \left[\left(\frac{L^3}{3EI_y} + \frac{L}{GA_s} \right) \sin^2\left(\frac{P \mathbf{d}x L}{4GJ}\right) + \left(\frac{L^3}{3EI_x} + \frac{L}{GA_s} \right) \cos^2\left(\frac{P \mathbf{d}x L}{4GJ}\right) \right] \dots\dots (6.66)$$

and

$$\mathbf{f} = \frac{P \mathbf{d}x L}{4GJ} \dots\dots\dots (6.67)$$

where L is the cantilever length, EI_x and EI_y are respectively the bending stiffness of the beam in the x and y directions, and $\mathbf{d}x$, $\mathbf{d}y$, and \mathbf{f} are shown on Figure 6.32.

Equations (6.65), (6.66) and (6.67) are solved for \mathbf{dx} , \mathbf{dy} , and \mathbf{f} . If the torsional resistance of the beam is greater than the average applied torque, $P\delta x/4$, the beam will not buckle and \mathbf{f} will converge to zero. The onset of buckling is observed if \mathbf{f} does not result in zero. The critical buckling moment is asymptotic to the resulting graph of Moment versus \mathbf{f} as shown on Figure 6.31.

6.5.3.2 Critical buckling moment formulae

The previously developed approach describes the load deformation path of the beam under torsional buckling. However, from a designer point of view only the critical buckling load is of interest. This can be obtained using equations based upon Euler buckling theory. Many equations for the critical buckling moment have been presented in design literature. Following is a discussion of a generalised approach along with the one specifically developed for FRP beams.

Generalised approach

According to Gaylord, Gaylord & Stallmeyer (1992, p. 290), the critical lateral torsional buckling moment of a steel beam is given as:

$$M_{cr} = \sqrt{\frac{P^2}{L^2} EI_y GJ + \frac{P^4}{L^4} EI_y EI_{warp}} \dots\dots\dots (6.68)$$

where: M_{cr} is the critical buckling moment, L is the length of the beam between lateral restraints, EI_y is the stiffness of the beam about the y-axis, GJ is the torsional stiffness of the beam, and EI_{warp} is the warping stiffness of the beam. For an RHS, I_{warp} is taken as zero as the section is doubly symmetric.

This formula is for the specific case of a simply-supported beam subjected to pure moment loading. To allow for other loading and boundary conditions equation (6.68) is altered to:

$$M_{cr} = C_b \sqrt{\frac{P^2}{L_{ef}^2} EI_y GJ + \frac{P^4}{L_{ef}^4} EI_y EI_{warp}} \dots\dots\dots (6.69)$$

where the coefficient C_b is incorporated to allow for the loading arrangement on the beam and L_{ef} is the effective length of the beam, which is related to the end restraints. Gaylord et al. gives a range of 1.28 to 1.71 for C_b , and L_{ef} equalling L for the cantilever beam.

FRP beam

The Eurocomp Design Code presents a formula for lateral torsional buckling specifically for FRPs. Clarke (1996, p. 91) cites the formula as:

$$M_b = \frac{\sqrt[4]{\frac{P^6}{L_{ef}^6} E^3 I_y^3 GJ + \frac{K P^8}{L_{ef}^8} E^4 I_y^3 I_{warp}}}{C_1} \dots\dots\dots (6.70)$$

where: $K = 0.5$ for fully-fixed end condition, and C_1 is depending upon K , and the loading arrangement. For a cantilever with point load at its end $K = 0.5$ and $C_1 = 1.0$.

The factors given by Clarke are only applicable to simply-supported doubly-symmetrical beams that are loaded through their shear centre. However, as shown on Figure 6.33, the use of the equation does not yield satisfactory results when compared against the analytical and the generalised approach.

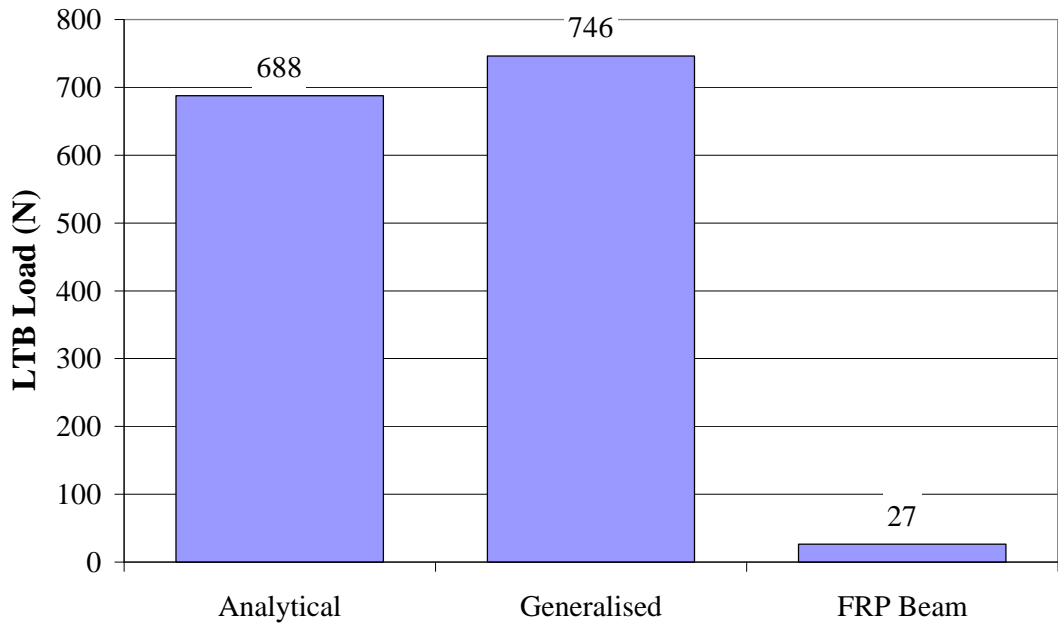


Figure 6.33 Comparison of methods to determine the critical buckling moment of the FRP beam

6.6 Determination of the bearing stress distribution angle

Analytical solutions for the bearing stress distribution angle (α , Figure 6.16) are based on Boussinesq theory, which is only valid for isotropic materials (Timoshenko 1969 p. 97). However, the present FRP beam is anisotropic, and a new approach is devised to obtain the stress distribution angle. First, assuming the beam with isotropic material properties, a finite element analysis is carried out. Once the FE analysis is validated with Boussinesq theory, it is applied to the real beam with anisotropic material properties. The results are then plotted and interpreted.

Figure 6.34 shows the validation of the FE analysis with Boussinesq theory. It can be seen that there is a good agreement between the two.

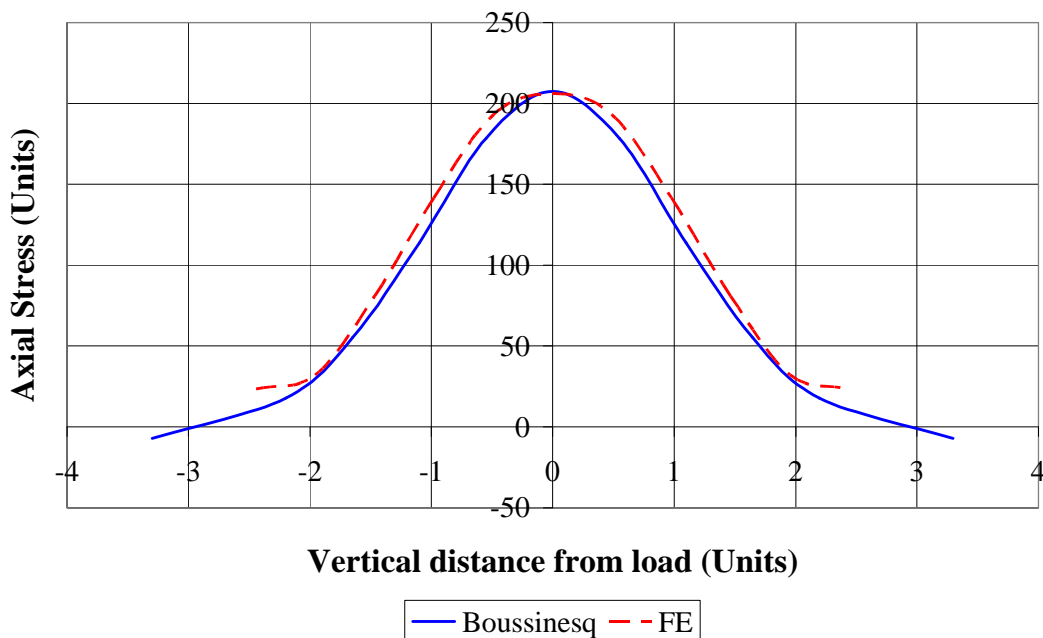


Figure 6.34 Comparison of FEA and analytical solution of the in-plane stresses at centre depth of a beam subject to 3-point bending

Considering the correlation between the analytical and FEA for the isotropic beam, it is reasonable to expect that the FEA will also provide indicative results for the orthotropic beam. The material properties in the FE model are therefore replaced with the beam's true laminate and core properties. The orthotropic laminates within the FRP beam affect the stress distribution as shown on Figure 6.35. The distribution is highly non-linear. The use of the 95th percentile line (44 degrees) is however warranted above the neutral axis where crushing failure is likely.

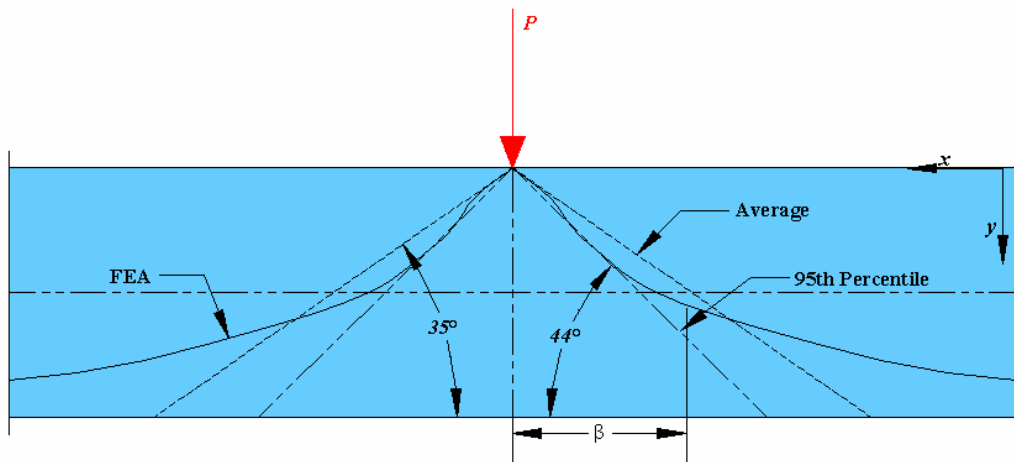


Figure 6.35 Stress factor ($D/2b$) as a function of beam depth for an orthotropic beam

Using this distribution angle, estimates of compressive strains within the beam can be obtained by using the transformed section approach, which yields the maximum strain as:

$$e_y(y)_{\max} = \frac{P}{E w_{b,t}(y) \frac{2y}{\tan a}} \dots\dots\dots (6.71)$$

where: E is reference Young's modulus of the transformed section and $w_{b,t}(y)$ is the transformed bearing width at the point of calculation. Stresses of the individual laminates can then be obtained by simply multiplying the strains by the particular laminate's modulus. Once the stress distribution is obtained, it can be used to either estimate the failure load or size the required bearing plates.

6.7 Key parameters

From the bending and shear investigations it became apparent that the thicknesses of the flanges and webs greatly affect the performance of the beam. Indeed, providing adequate thickness to the flanges and webs could avert all the investigated second-order failure modes. The core material is comparatively cheap compared to the laminates, and it does not have a key function as regards to the primary failure modes. Therefore, for the present beam, the key parameters are the flange and web core thickness. Altering the flange thickness, as shown on Figure 6.36 and Figure 6.37, has a minor affect upon shear capacity, as the webs provide the majority of the shear resistance of the beam. This shear-core thickness relationship is identical for top and bottom flanges. The moment-core thickness relationship is however different for the top and bottom flange. There is an optimum value for top flange

core thickness. Below the optimum, the beam is susceptible to flange buckling and punching failures. Once the thickness rises above the optimum, beam capacity falls due to the rise in neutral axis and proportional rise in tensile strains in the bottom laminate.

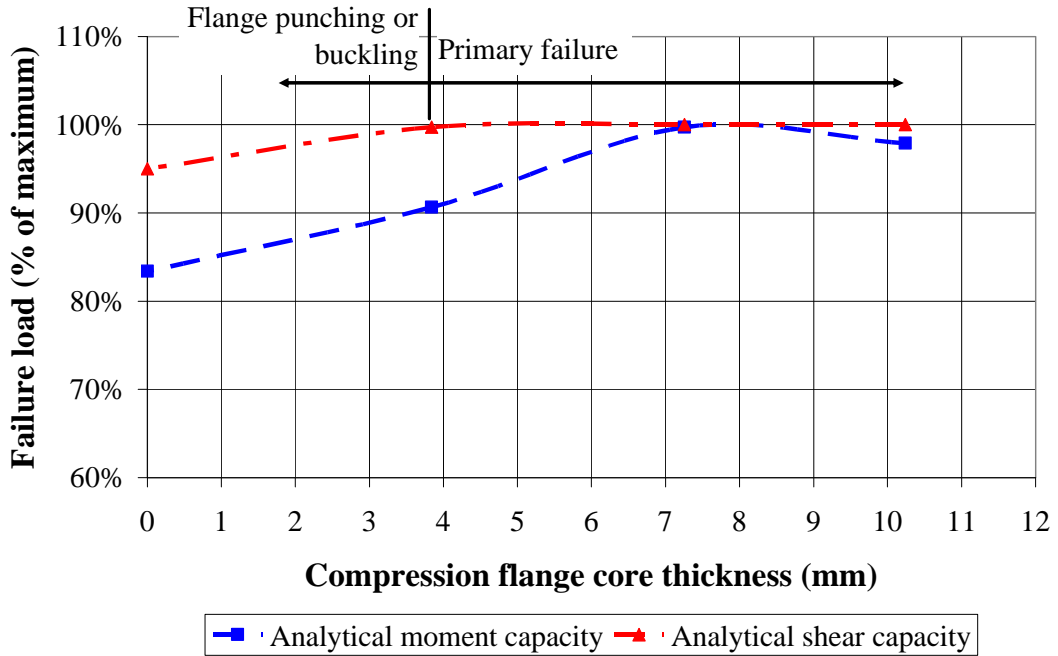


Figure 6.36 Effect on capacity by varying top flange core thickness

The thickness of core material in the bottom flange is less influenced by neutral axis shift due to the cracking of the core. However, as shown on Figure 6.37, insufficient material results in lower capacities of the beams due to the prevalence of bottom flange punching. The capacity of the beam does rise above the primary value (100%) for excessive amounts of core material (when compared to the bottom laminate) as beam failure then coincides with cracking of the core.

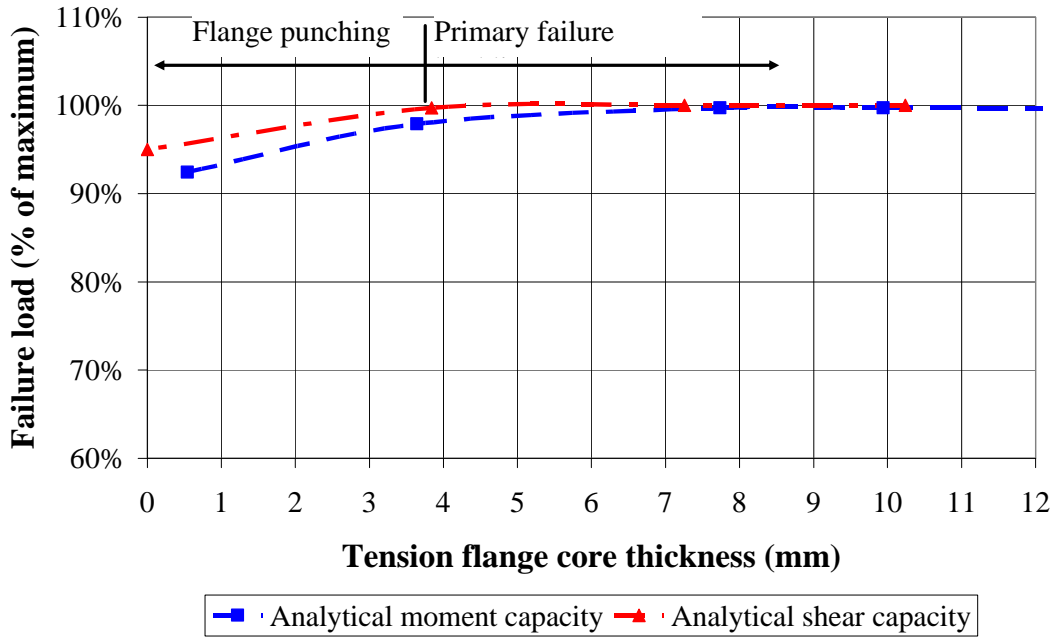


Figure 6.37 Effect on capacity by varying bottom flange core thickness

When web thickness is varied, both shear and moment capacity display significant responses as shown on Figure 6.38. In both cases, primary failure occurs once the web thickness is over a critical dimension.

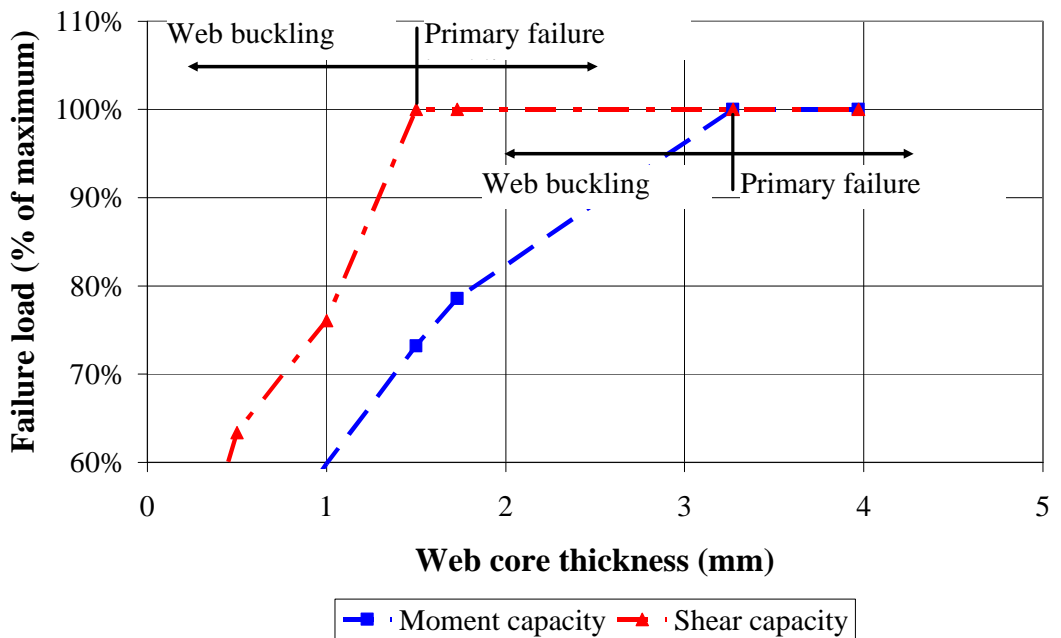


Figure 6.38 Effect on shear and moment capacities by varying web thickness

6.8 Conclusions

The bending behaviour of the beam has been modelled using the transformed section approach in conjunction with the Euler-Bernoulli beam theory. An altered stiffness approach is used to account for cracking of the core material. The resulting formulation is then used to estimate beam curvature and the resulting strains within the beam elements. Due to the difference in the moduli of the materials and the cracking of the core, the maximum strain through the section was found to be higher in tension than compression. As a result, the primary failure in bending was found to be the tensile rupture of the unidirectional reinforcement in the bottom flange. However, given the geometry of the section, failure modes that include:

- moment buckling of the webs;
- compression buckling of the top flange;
- compression buckling of the webs;
- crushing of the webs;
- tearing of the web laminates;
- laminate failure in the flanges;
- punching shear of the core in the flanges; and
- longitudinal cracking of the core in the flanges

are also possible. These were investigated using the thin-walled plate theory. It was confirmed that these secondary failure modes all have one parameter in common: core thickness. As a result, they all can be averted by the judicious placement of the core material within the flanges and webs, leaving the beam to fail in the aforementioned primary tensile failure mode. The formulae presented for the pure flexure behaviour have been incorporated into a program to predict the behaviour of the beam.

The thin-walled beam theory was also used to investigate the behaviour of the beam under shear loading. It was found that the laminates constitute the main shear reinforcement of the beam, particularly those placed in the webs, as the core material cracks before ultimate failure. However, if insufficient core material is provided within the webs and flanges, secondary failure modes such as buckling of the webs and punching shear of the flange could precede primary shear failure. The formulae presented in this section have also been incorporated into a program to predict the behaviour of the beam when loaded in pure shear. In addition, it has been used with the aforementioned bending program to investigate the

combined moment – shear loading. The combined model was found to replicate the known synergy between shear and bending.

Lateral instability is another reason for secondary failure of FRP beams. Using the transformed section, an iterative method describing the load deformation behaviour was developed. This approach has been also incorporated into two programs to respectively predict the torsional and lateral torsional buckling behaviour of the beam.

The stress distribution under a bearing load has been estimated using the finite element method. It was found that the fibre orientation within the FRP beam has a significant effect upon the bearing stress distribution. Maximum stresses under a loading point decrease in a highly non-linear manner below the neutral axis of the beam. However, above the neutral axis where crushing is more likely to happen, the stress distribution can be approximated with a straight line.

References

- Bank, L. C. 1987, 'Shear coefficients for thin-walled composite beams', *Composite Structures*, vol. 8, pp. 46 - 61.
- Bank, L. C. 1989, 'Flexural and shear moduli of full-section fiber reinforced plastic (FRP) pultruded beams', *Journal of Testing and Evaluation*, vol. 17, no. 1, pp. 40 - 45.
- Barbero, E. J., Fu, S-H. & Raftoyiannis, I. 1991, 'Ultimate bending strength of composite beams', *Journal of Materials in Civil Engineering*, vol. 3, no. 4, pp. 292-306.
- Beer, F. P. & Johnston, E. R. 1985, *Mechanics of Materials*, McGraw-Hill Ryerson Ltd, Singapore.
- Branson, D. E. 1963, *Instantaneous and time-dependent deflections of simple and continuous reinforced concrete beams*, Alabama Highway Research Report Bureau of Public Roads, Alabama, 7.
- Branson, D. E. 1997, *Deformation of concrete structures*, McGraw-Hill, New York.
- Bulson, P. S. 1970, *The Stability of Flat Plates*, Chatto & Windus, London.
- Clarke, J. L. (ed.) 1996, *Structural Design of Polymer Composites; Eurocomp Design Code*, E & FN Spon, Chapman & Hall.
- Davalos, J. F., Salim, P., Qiao, R., Lopez-Anido, R. & Barbero, E. J. 1996, 'Analysis and design of pultruded FRP shapes under bending', *Composites Part B: engineering*, vol. 27, no. 3/4, pp. 295 - 306.
- Dym, C. L. & Shames, I. H. 1973, *Solid Mechanics, a variational approach*, McGraw-Hill Kogakusha, Tokyo.

- Gaylord, E. H., Gaylord, C. N. & Stallmeyer, J. E. 1992, *Design of Steel Structures*, 3rd edn, McGraw-Hill, Singapore.
- Heins, C. P. 1975, *Bending and Torsional Design in Structural Members*, Lexington Books, Lexington, Massachusetts.
- Hibbeler, R. C. 1991, *Mechanics of Materials*, Maxwell Macmillan International, New York.
- International Organization for Standardization, *International Standard ISO14129*, International Organization for Standardization, Case Postale 56 CH-1211 Geneve 20 Switzerland, Geneve.
- Kilic, O., Aktas, A. & Dirikolu, M. H. 2001, 'An investigation of the effects of shear on the deflection of an orthotropic cantilever beam by the use of anisotropic elasticity theory', *Composites science and technology*, vol. 61, no. 14, pp. 2055 - 2061.
- Kollbrunner, C. F. & Basler, K. 1969, *Torsion in Structures: An Engineering Approach*, Springer-Verlag, Berlin.
- Kordina, K. & Quast, U. 1971, *Bemessung von schlanken Bauteilen - Knicksicherheitsnachweis (Design of slender reinforced concrete members - stability check)*, Beton-Kalender, Berlin.
- Nagaraj, V. & Gangarao, H. V. S. 1997, 'Static Behavior of Pultruded GFRP Beams', *Journal of Composites for Construction*, vol. August, pp. 120-129.
- Springolo, M. & Van Erp, G. M. 2001, 'Development of a new fibre composite beam', in *Technology Convergence in composites applications*, eds. S. Bandyopadhyay, N. Gowripalan & N. Drayton, University of New South Wales, Sydney, Australia, pp. 124 - 131.
- Timoshenko, S. 1969, *Theory of Elasticity*, 3rd edn, McGraw-Hill, New York.
- Van Erp, G. M. 1999, 'A New Fibre Composite Beam for Civil Engineering Applications', *Composites Fabrication Journal*, vol. July, pp. 30 - 33.
- Warner, R. F., Rangan, B. V. & Hall, A. S. 1989, *Reinforced concrete*, 3rd edn, Longman Australia Pty Ltd.

Chapter 7 Experimental characterisation of the beam behaviour

7.1 Introduction

The objective of this chapter is to continue the study of the behaviour of the developed beam through a comprehensive testing program designed to test for primary and secondary failure modes. The experimental set-ups are described in the following sections. In particular, the behaviours in bending, shear, combined bending and shear, buckling, and lateral torsional buckling will be investigated. The experimental results will validate/invalidate the critical parameters governing the behaviour of the beam as identified in the preceding Chapter. Furthermore, the data will be used for comparison with the FE analysis described in the next Chapter.

7.2 Strain distribution throughout the section

The formulae developed in the previous chapter were based on the assumption that the strain distribution throughout the section was linear. To validate/invalidate this assumption, a beam, designated B6, was manufactured with six strain gauges embedded within the section at mid-span, and tested in 4-point bending. These strain gauges were located as shown on Figure 7.1.

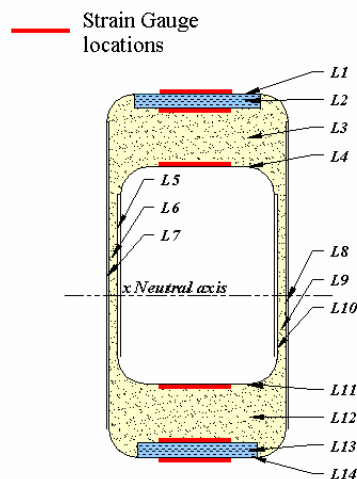


Figure 7.1 B6 strain gauge locations

Figure 7.2 shows the analytical predictions obtained, assuming a linear strain distribution throughout the section, as well as the readings from the strain gauges. It can be clearly seen that there is excellent agreement, which seems to indicate that the assumption of a linear strain distribution is valid for the beam as tested. The test beams used throughout the experimental program are of a similar size to the beam tested, a linear strain assumption should therefore be valid for those beams also.

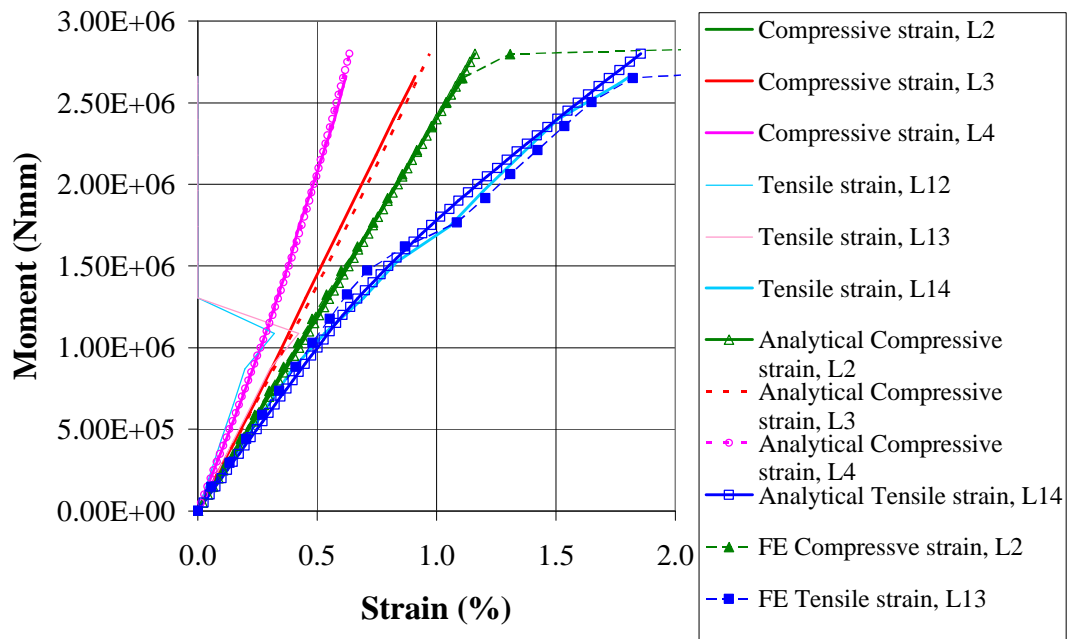


Figure 7.2 Moment-strain relationship of beam B6

7.3 Bending

7.3.1 General

The bending tests were designed to monitor the moment-curvature relationship, and investigate the following failure modes: tensile laminate failure, moment buckling of the web, compression buckling of the top flange, compression buckling of the webs, punching of the flange into the void, and flange core cracking. Furthermore, as identified in the analytical approach, web and flange thickness constitute parameters of concern, and where possible, beam geometry was varied to investigate their effects. For instance, to test for moment and compression buckling of the webs, separate specimens were produced with thin webs. In addition, to verify the analytically determined optimum size of the section, a range of beams, with differing flange thicknesses, was also tested. These specimens were

produced with a variety of cross-sections as listed in Table 7.1 and shown on Figure 7.3. One set of beams, designated (a) in Figure 7.3, was manufactured with no core material in the bottom flange to instigate punching of the flange laminates in the webs. To investigate compression buckling, a set of beams, designated (e) in Figure 7.3, was produced without core material in the top flange. A set of beams, designated (c) in Figure 7.3, was manufactured to the optimum dimensions defined by the analytical analysis. To confirm the analytical optimum, a further two sets of beams were produced, designated (b) and (d) on Figure 7.3, with geometries between the extremes of (a) – (c) and (c) – (e).

Table 7.1 Beam dimensions

Beam series designation	Predicted failure	Type (Figure 7.3)	Average dimensions					
			D (mm)	W (mm)	w_2 (mm)	t_{fc} (mm)	t_{ft} (mm)	t_w (mm)
B4	Flange core shear	(a)	63.7	34.7	20	17.8	4.8	3.2
B5	Tensile laminate	(b)	63.7	34.6	21.9	14.5	7.9	3.4
B6	Tensile laminate	(c)	65.3	34.9	23.1	11.5	11.8	3.4
B7	Tensile laminate	(c)	65.4	33.3	21.5	11.6	12	3.2
B8	Tensile laminate	(d)	63.3	34.3	20	8.1	14.2	3.5
B9	Compression buckling	(e)	63.1	34.2	21.9	4.1	17.5	3.4

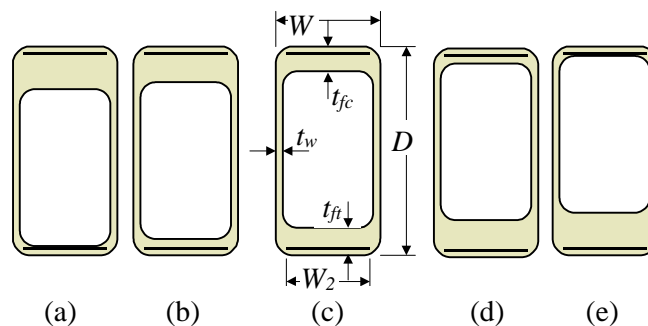


Figure 7.3 Beam geometries

Compression crushing of the top flange is another failure mode associated with bending. However, it was not tested directly, as both the analytical and FEA predicted that this failure mode would not occur. Instead, the compressive strains were monitored in the tests, and compared with the laminate capacity, given in Chapter 5 to assess the likelihood of this failure mode.

7.3.2 Beam tests

A 4-point bending arrangement was chosen as this method provides for pure moment to be observed between the load points. All beams were loaded using a deformation control rate of 5 mm/minute, which equates to 1 mm/minute along the length of the tensile unidirectional laminate. A schematic representation of the testing arrangement is shown on Figure 7.4. An attachment to the machine was used for the loading points. The steel bearing points were rounded with a radius of 15 mm and slide plates were placed upon them to allow horizontal slip of the specimen during testing. The span (L) was 600 mm and the loading span (L_s) was 200 mm for all the beams.

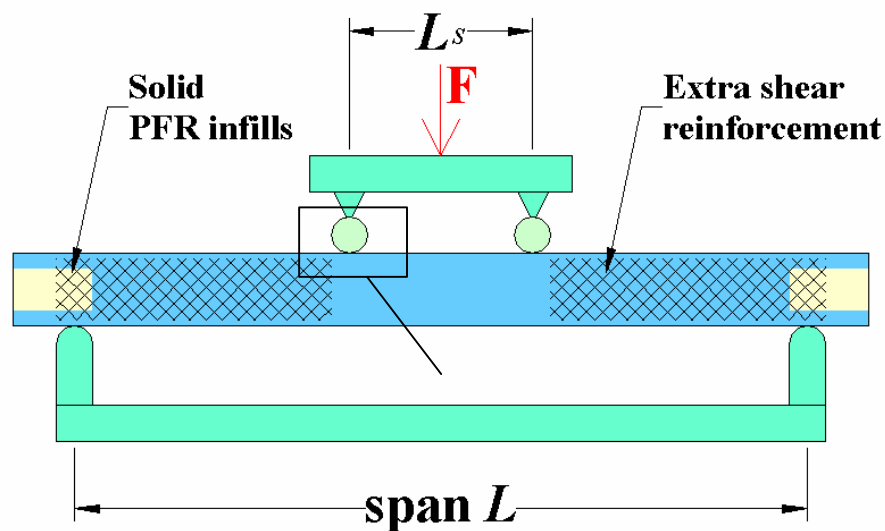


Figure 7.4 Loading arrangement of beams

To avoid premature failure of the beam, which may result from stress concentrations at the support and loading points, the ends of the beams were filled with PFR and bearing plates were designed to distribute the loads into the beam evenly. Furthermore, through consideration of the different stiffness of the steel bearing plates and the beam, the plates were designed so that they would bend with the specimen. The bearing plates are 125 mm long at the ends of the beam. At the inner loading points, as shown on Figure 7.5, the plates have a different size and design. They are made up of two 3 mm mild steel plates on top of each other, with a rubber spacer on the beam. The top and bottom plate lengths being 25 mm and 75 mm respectively. The 2 mm thick rubber spacer is used to ensure no stress concentrations result from point contact between the plates and the beam. To avoid probable failure in shear, extra reinforcement is added as shown on Figure 7.4.

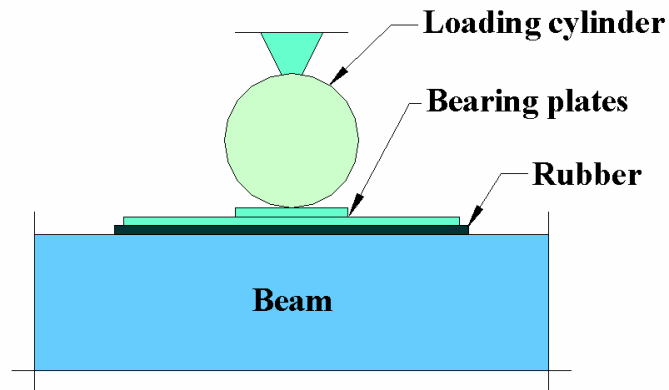


Figure 7.5 Loading plates for beam tests

The primary failure predictions are based upon strain values within the unidirectional laminates. These strains were therefore monitored with the use of strain gauges located at the top and bottom flanges of the beam. To install the strain gauges, resin was poured onto the plain weave mat at the locations where they were to be positioned. Once cured, the resin was filed and sanded flat to present a smooth adhering surface for the cyano-acrylate base glue. Load application was carried out through a 110 *kN* load cell. Both the strain gauges and load cell were connected to a data logging system. Data was recorded at 0.1-second intervals for post-processing.

Tensile failure of the unidirectional laminate

The majority of the beams failed due to tensile rupture of the bottom laminate, as predicted by the analytical approach. As shown on Figure 7.6, all the beams showed a similar strain behaviour. Initially, the behaviour is linear elastic until the first tensile failure of the core material is encountered. As the load is increased, the tensile strains exhibit a non-linear behaviour while the compressive strains remain essentially linear. The changing tensile modulus of the core material causes the observed non-linearity in the tensile strains. Furthermore, it can be noticed that the tensile cracking of the core occurs at around 0.6% tensile strain, which corresponds to the ultimate tensile strain of the core material as obtained in Section 5.3.3. This is also the cause for the reduction in the stiffness of the beams as shown on the average moment curvature graph on Figure 7.7. During the tests, audible signs of cracking kept occurring until failure. This was accompanied with substantial deflection reaching 19.6 *mm*, which corresponded to an average ratio of $L / 30$.

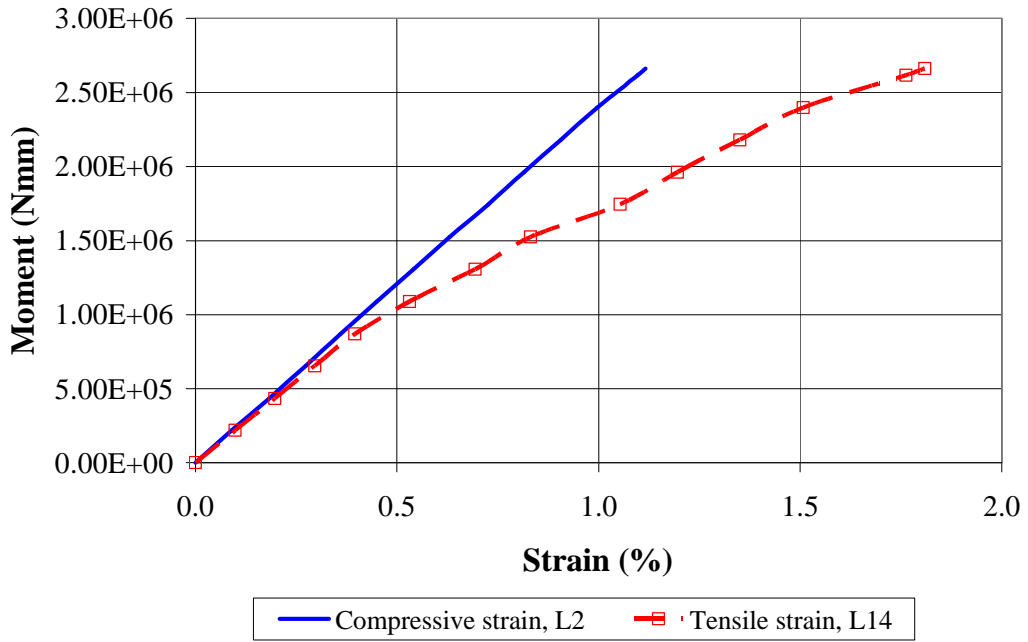


Figure 7.6 Typical moment-strain relationship of the test beams

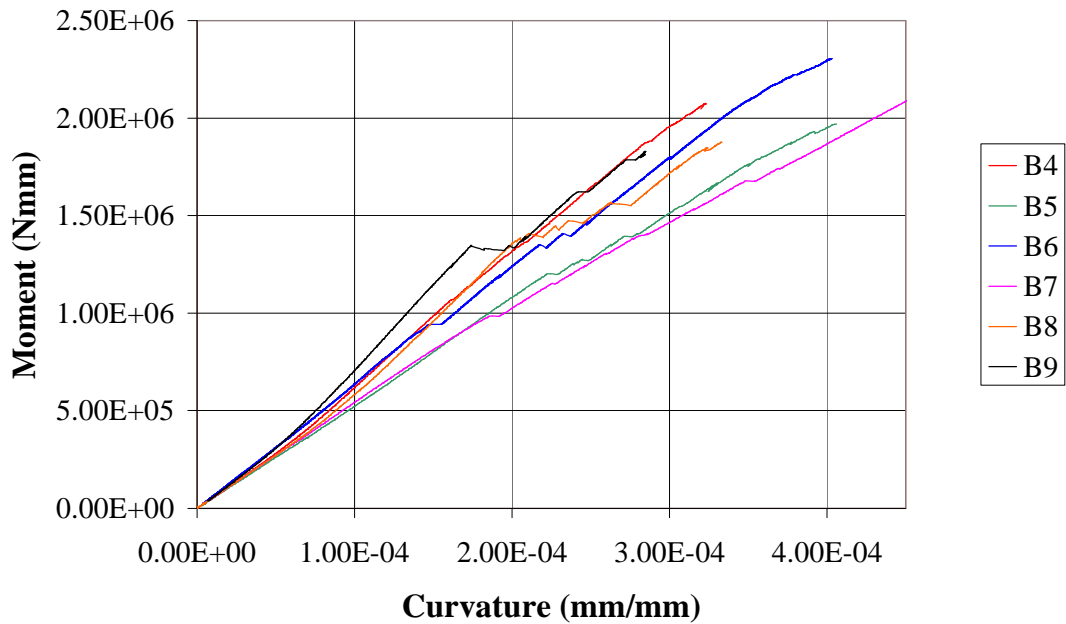


Figure 7.7 Moment-curvature relationship of the test beams

The tested beams (B7) were of the symmetric geometry as shown on Figure 7.3(c). Five of the ten beams tested were fitted with strain gauges. The average failure moment was recorded as $2.4105E6 \text{ N.mm}$, which was over predicted by the analytical method by 10.9%. Figure 7.8 shows that the analytical predictions of the tensile strain are in good agreement

with the experimental results, 'S1 to S5'. Analytical modelling of the strains was within 5% of experimental observations.

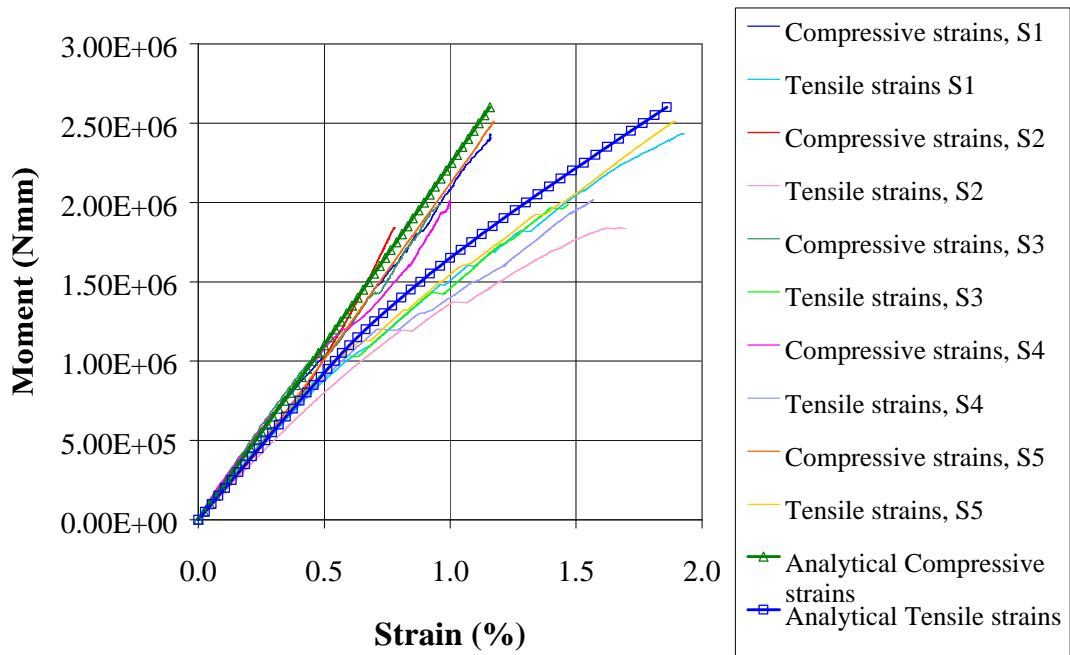


Figure 7.8 Moment-strain relationship of beam series B7

The second series designated B5, as shown on Figure 7.3(b), was manufactured with a reduced amount of core material in the bottom flange. This small amount was sufficient to resist the second-order shear punching of the bottom laminates, allowing the beam to fail by rupture of the unidirectional laminate. The average failure moment was recorded as 2.425E6 *N.mm* as shown on Figure 7.9. It can be seen that the analytical method predicted a failure moment 9.3% higher, which is excellent given the simplistic nature of the analytical method. Furthermore, modelling of the strains was within 10% of all the results.

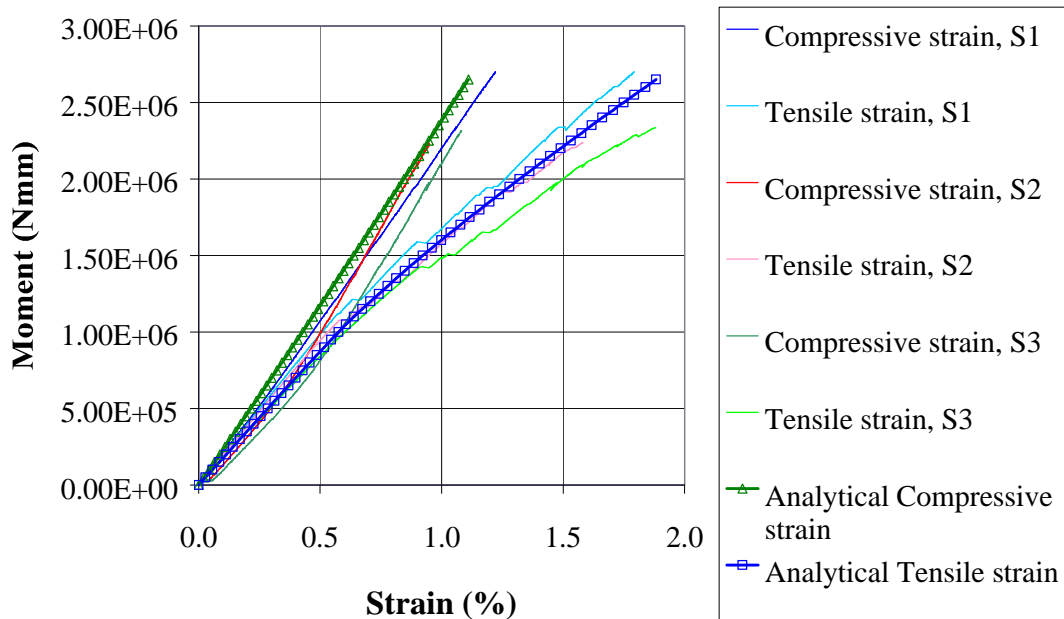


Figure 7.9 Moment-strain relationship of beam series B5

The results obtained from tests on the series with reduced amount of core material in the top flange, designated B8 ((d) on Figure 7.3), showed that the small amount of core material was sufficient to resist bearing stresses, as well as providing sufficient compressive reinforcement restraint. Indeed, all the beams failed in the tension zones. The average failure moment was $2.112E6 \text{ N.mm}$. The analytical predictions were 18.4% higher than the average recorded maximum failure moment. Upon examination of the beams, it was found that they had red stains within the unidirectional laminates. The stain came from a red thread incorporated into a new batch of unidirectional mat used for the beams. Subsequent laminate testing confirmed a reduction in the failure capacity in the order of 12% for this batch of unidirectional ply (Ellis 2001, pers. comm.) Using the new failure strain of the laminate in the analytical theory resulted in a prediction that was only 6 % higher than the average.

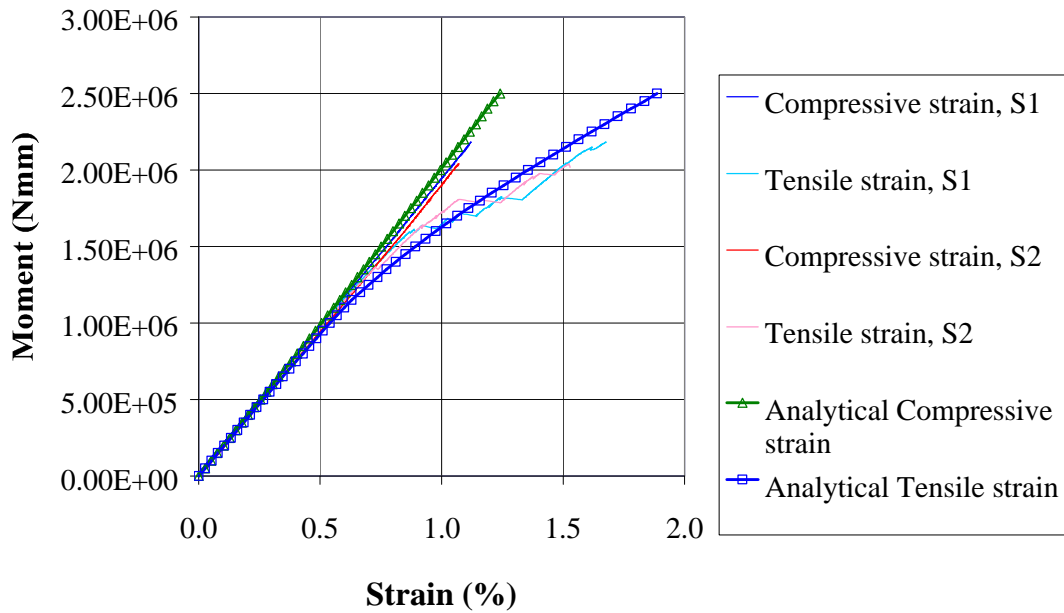


Figure 7.10 Moment-strain relationship of beam series B8

Compressive failure of the unidirectional laminate

All the tests revealed that the compressive strains at failure were lower than their tensile counterparts. This is due to the higher modulus of the laminates in compression and the introduction of core material in the flange. Therefore, primary compressive failure of the unidirectional laminate was not possible for the developed FRP beam.

Compression buckling of the top flange

The results obtained from tests on the series with no core material in the top flange, designated B9 ((e) on Figure 7.3), showed that the beams failed prematurely as a result of the lack of sufficient compressive restraint. Failure in both beams occurred under a loading point indicating that bearing stresses caused the initial buckling in the laminate. The average failure moment was $2.048E6 \text{ N.mm}$. These failures highlighted the sensitivity of the top flange to the loading arrangement. As shown on Figure 7.11, this buckling affected the compressive strains as soon as the load was placed on the beam.

When the core material in the tensile flange reached its limiting strain, a shift in the tensile strain occurred as can be also noticed on Figure 7.11. This resulted in a sudden-dynamic-localised load redistribution to the unidirectional reinforcement. However, this beam absorbed the released energy since sufficient unidirectional reinforcement was provided.

The analytical model predicted a bearing failure that was 8% higher than the experimental average. Analytical tensile strain predictions are within 4% of the results.

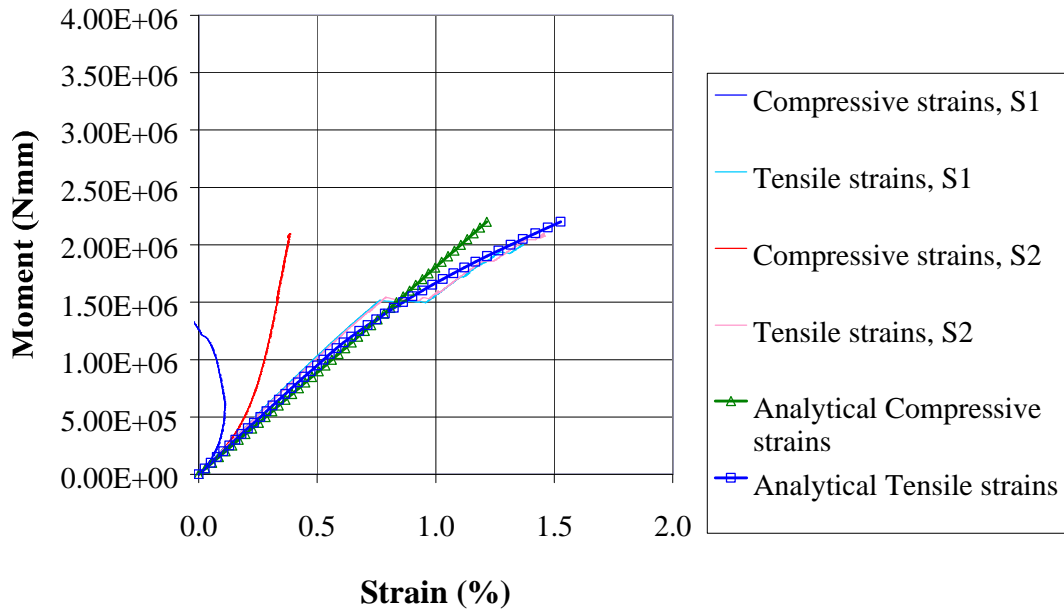


Figure 7.11 Moment-strain relationship of beam series B9

Longitudinal cracking of the core in the flanges

The beams designated B4, were produced with minimal core material in the bottom flange as shown on Figure 7.3(a). As a result, they failed prematurely. The failure was the result of the bottom flange punching into the hollow void of the beam. It was caused by the existing shear loading combined with second-order shear forces resulting from the significant bending deflection of the beam. The analytical model predicted this failure mode with reasonable accuracy as shown on Figure 7.12. The average failure moment was $2.365E6 \text{ N.mm}$. The analytical prediction was 5.7% higher. The tensile strains were predicted within 11 % of the experimental results.

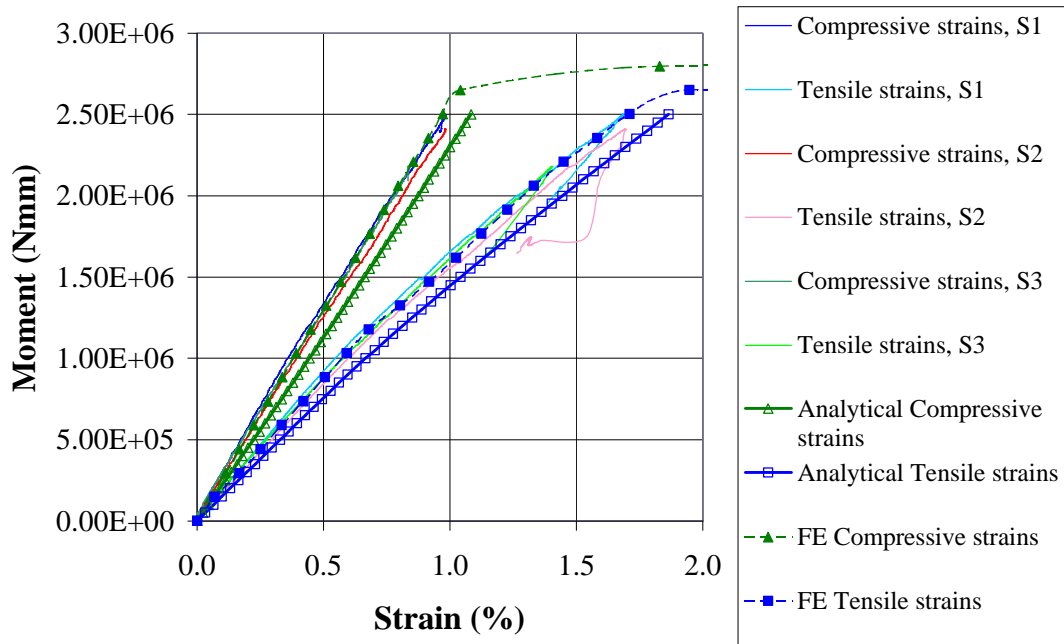


Figure 7.12 Moment-strain relationship of beam series B4

7.3.3 Moment buckling of the webs

Inducing moment buckling of the web in the beam was experimentally problematic. Altering the web thickness would not only require new mandrels to be manufactured but also would result in the thickness of the core in the webs being less than the required 2 mm. Furthermore, it would cause difficulties in injection moulding as well as inducing size effects. Since the analytical model is based upon a simply-supported plate, it was therefore considered worthwhile to manufacture a separate web specimen to simulate the condition of simply-supported end restraints, so the results could be compared directly with the analytic estimate. In order for the specimen to be loaded in 4-point bending, it was made 1100 mm long, 150 mm high and 3.9 mm wide. Furthermore, it was made with a laminate lay-up identical to the beam's web; with two layers of the plain weave material on each side of the core. Extra laminates of unidirectional glass were added in locations of high bearing, tensile, and shear stresses, as shown on Figure 7.13, to ensure that failure due to moment buckling would prevail.

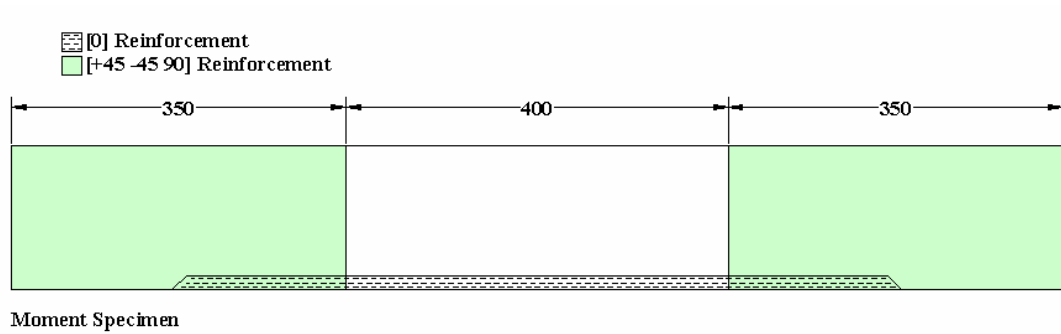


Figure 7.13 Extra reinforcement on web specimen

To provide lateral restraints to the top and bottom edges of the specimen, sacrificial sandwich panel stiffeners were used. However, to account for their added moment resistance, they were individually tested so their added strength could be quantified. The lateral restraints were made to act independently from the buckling specimen, so that their effect could be deducted. Figure 7.14 and Figure 7.15 show respectively a cross-section of the test specimen and a photograph of the experimental set-up.

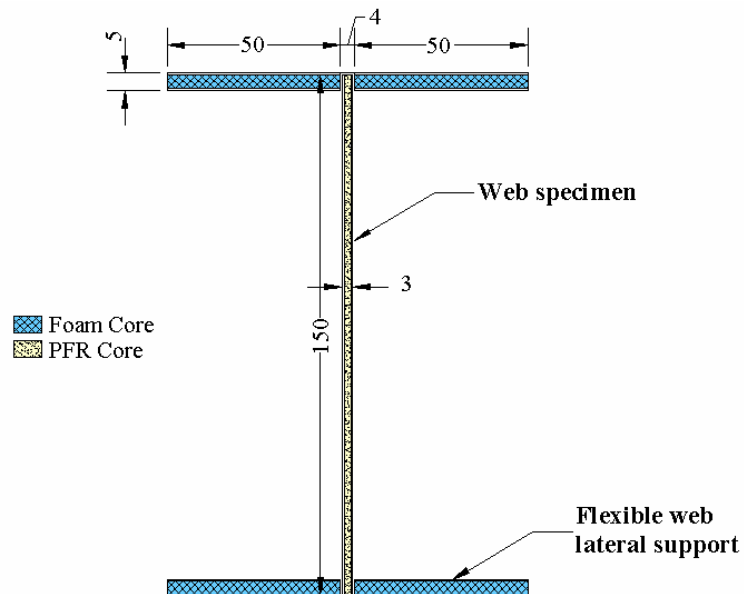


Figure 7.14 Web specimen testing

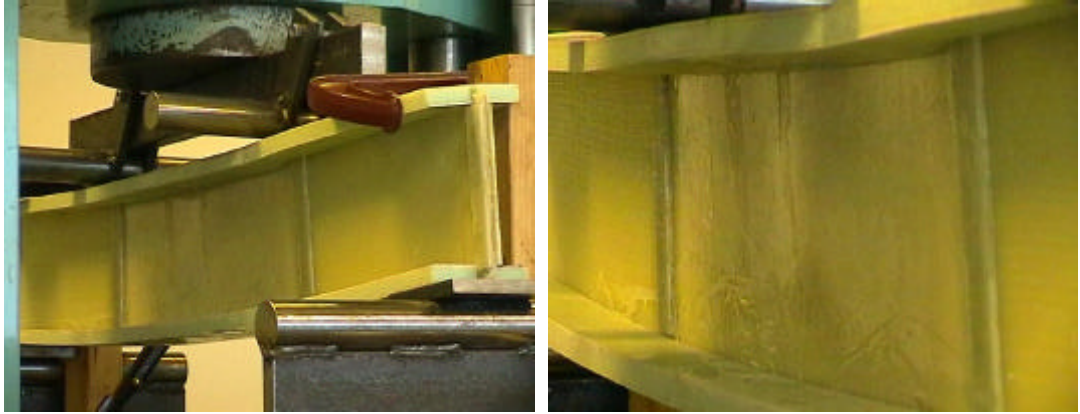


Figure 7.15 Testing web buckling specimen

The first buckling signs of the web were noticed at a load of 9.8 *kN*. Buckling initiated at the top of the specimen, indicating that the lateral restraints had allowed some lateral movement. As a result the observed buckling load can be attributed to an edge condition somewhere between free and simply-supported. This load lies in-between the two analytical values, as can be seen on Figure 7.16. This tends to confirm that the testing arrangement had not provided sufficient lateral restraint to the top of the specimen.

As the load was increased, the lateral restraints inhibited additional lateral deformation of the top edge. The specimen continued to buckle in a mode consistent with simply-supported edges until failure. Failure was initiated by a laminate tearing due to the buckling. The ultimate failure load was consistent with the simply-supported edge conditions. The observed first buckling was 11% lower, and failure load was 1.2% higher, than the analytical prediction. Therefore, the analytical method provided a reasonable estimate of the buckling load.

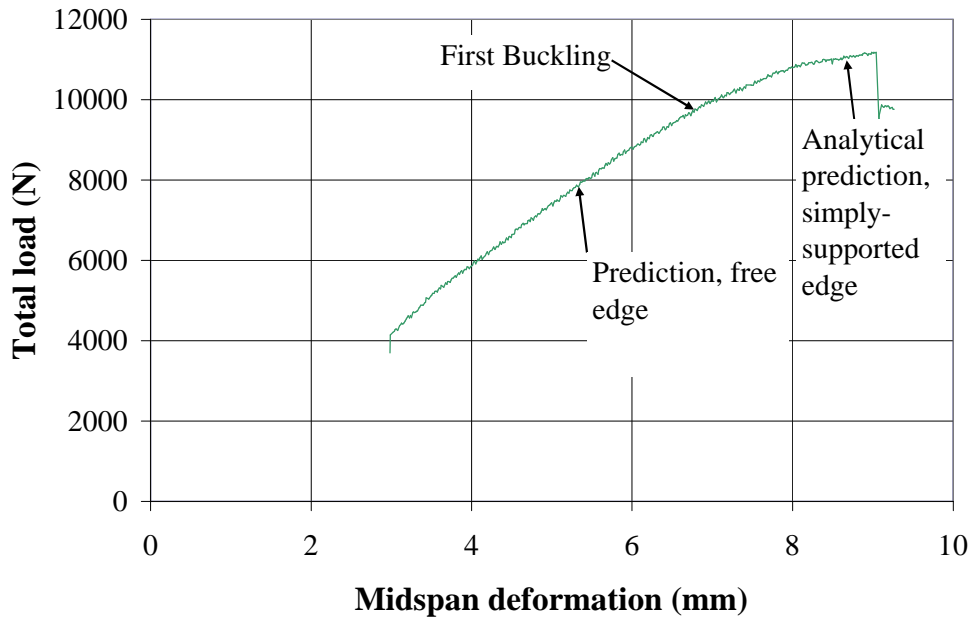


Figure 7.16 Failure of web

7.3.4 Compression buckling of the webs

The analysis indicated that moment loading of the beam would not instigate compression buckling of the webs. Therefore, to determine the buckling capacity of the webs, flat test specimens were made and tested. Six specimens were produced with a lay-up of two layers of plain weave placed on each side of the core. The dimensions of the specimens are detailed in Appendix D.9. To measure the respective strains and determine the onset of first buckling, strain gauges were used. The gauges were glued at the level of the longitudinal axis, and orientated parallel to it. Both ends of the specimens were held firm (encastè) within the grips of the testing machine so that the boundary behaviour of the web could be observed. For this arrangement equation (6.25) is amended to:

$$P_{cr} = \frac{p^2 EI_w}{(k_1 L)^2} \dots\dots\dots (7.1)$$

where: P_{cr} is the critical buckling load.

The machine was operated in deformation control mode, at a rate of 1 mm per minute.

The buckling of the specimens was accompanied by cracking of the core material near the jaw restraints. Once buckled, the specimens only accepted a small increase in load before failure. Individual results are presented in Appendix E.2. Figure 7.17 shows the experimental results together with the theoretical Euler buckling load. The experimental results lie between the two analytical predictions of $k_l = 1$ and $k_l = 0.5$, indicating that the boundary condition of the webs is in-between simply-supported and encastré. This demonstrates that substantial resistance to rotations remains at the boundary even though the core is cracked. Indeed, the boundary did not act like a pinned restraint. The equivalent k_l value from the experiments is 0.6. Therefore, the assumption of pinned ends is conservative and can be considered as a lower bound prediction of buckling capacity.

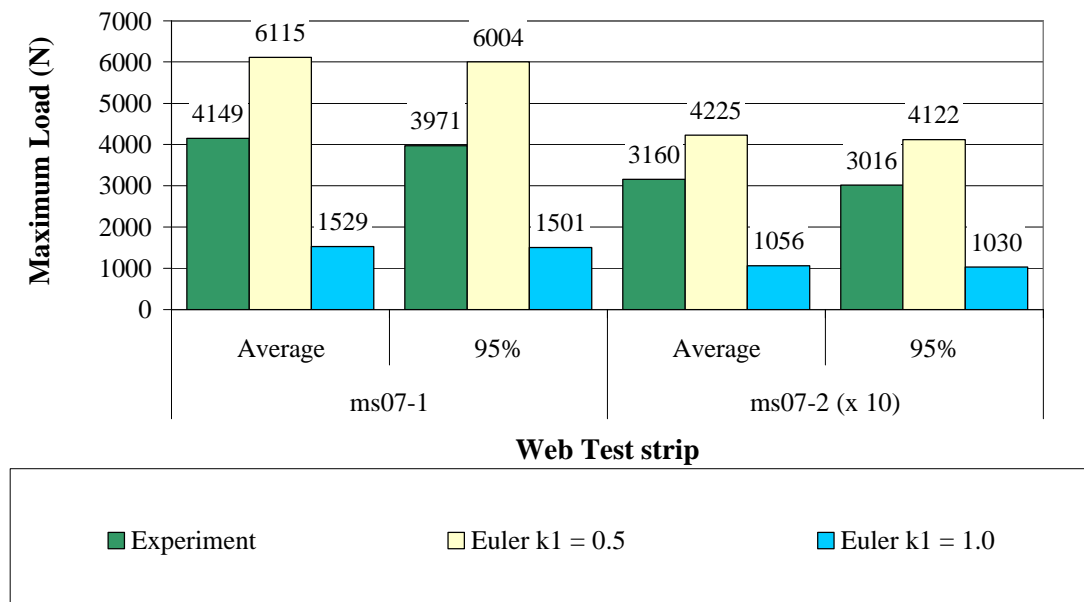


Figure 7.17 Buckling loads of web test strips

7.3.5 Characterisation of the local bearing capacity

To be able to resist concentrated point loads, the local bearing capacity of an FRP beam is of paramount importance as was noted with the premature failure of the B9 series. Indeed, the lack of appropriate bearing capacity can lead to failure of the beam either through punching shear or tensile cracking of the core material.

Due to the reduced amount of core material in the flanges, punching shear was initiated in beam B4 as described in Section 7.3.1. However, to induce longitudinal tensile cracking of the core, separate beam specimens loaded in compression were required. These

specimens were, 50 mm in length, with cross-sectional dimensions similar to the B7 series. The specimens were loaded across the entire length like a beam on rigid foundation.

Failure of all the beams was initiated by the cracking of the core material in the flanges. Once the core cracked, the beams' load capacity dropped as the flanges pushed into the hollow void precipitating the buckling of the webs. The individual results for the beams are presented in Appendix E.3. The analytical solution provides reasonably good estimates, of the failure load, within 3% as can be seen on Figure 7.18.

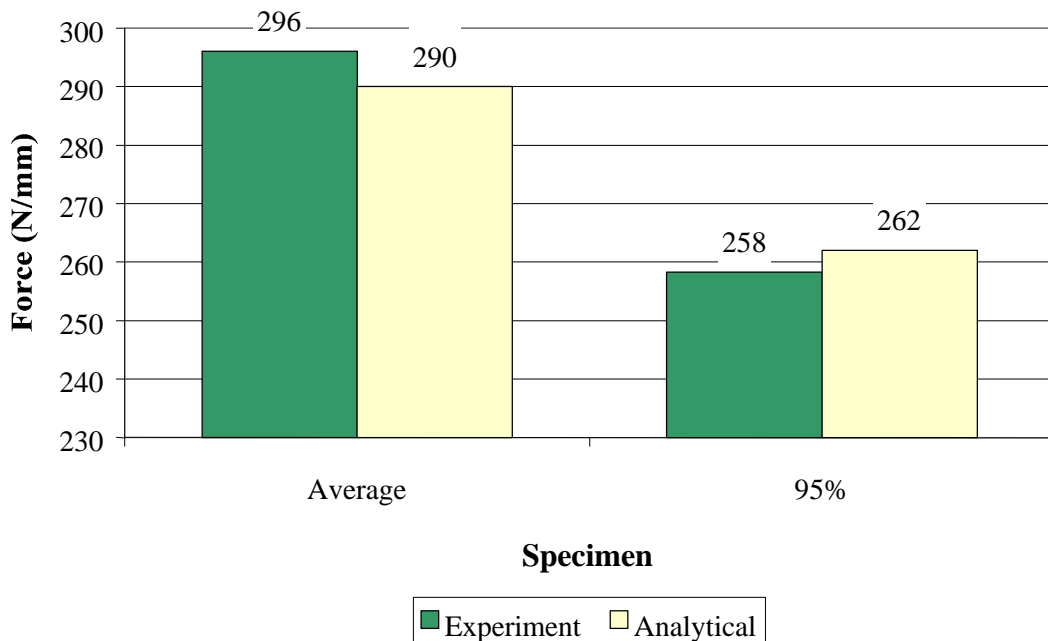


Figure 7.18 Comparison of beam crushing capacity and analytical solution

It appears therefore that the core material dominates the behaviour of the beam when its cross-section is loaded in compression. The analytical model was capable of predicting both the failure mode and load.

7.4 Shear

7.4.1 General

Characterisation of the shear behaviour of the PFR beam was achieved through combined moment-shear tests, and individual testing of web specimens in tension at 45° with respect to the fibre orientation. Furthermore, to investigate the shear buckling capacity of the webs, individual specimens were also tested in 4-point bending.

7.4.2 Beam shear capacity

7.4.2.1 Estimation of beam shear capacity by testing under combined moment and shear loading

The combined moment-shear tests were carried out in a 4-point bending arrangement as this allows for the independent measurement of the bending stiffness as follows:

$$EI_{test} = \frac{VaD}{e_c + e_t} \dots\dots\dots (7.2)$$

where D is the depth of the beam, and the determination of the pure bending deflection as:

$$\Delta_m = \frac{(e_c + e_t)(3La - 4a^2)}{6D} \dots\dots\dots (7.3)$$

The pure bending deflection can then be deducted from the total deflections to obtain the shear deflection component.

Theoretically, as discussed in Section 6.3.1, the moment and shear deformations at the loading point were given as:

$$\Delta_m = \frac{Va(3La - 4a^2)}{6EI_{effective}} \dots\dots\dots (6.51)$$

and

$$\Delta_s = \frac{Va}{GA_{effective}} \dots\dots\dots (6.52)$$

where V is the shear force acting on the beam, a is as shown on Figure 7.19, Δ_m and Δ_s are respectively the moment and shear deformation. These theoretical values can be compared with the experimental results. The total theoretical deformation is obtained by summing the results calculated from equations (6.51) and (6.52).

The testing arrangement is shown on Figure 7.19. To measure the shear strains in the webs, strain rosettes were glued at the sides of the beams as shown on the Figure. It

should be noted that in this series of tests, shear failure of the beams was not inhibited by either filling the hollow core at the ends of the beam with core material or adding extra web laminates to strengthen the beams as done in the flexural tests.

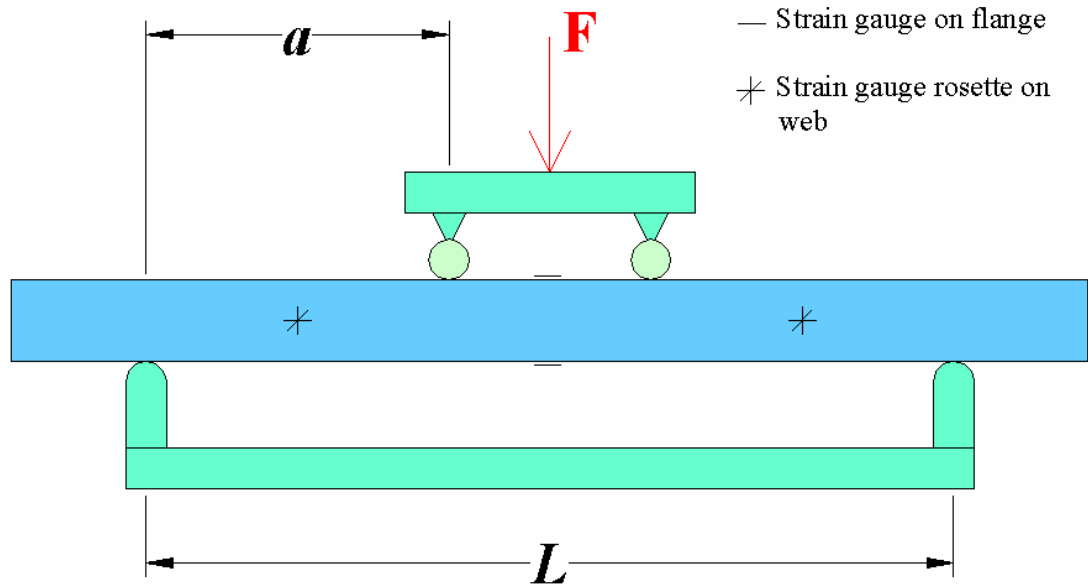


Figure 7.19 Moment-shear testing set-up

The strain rosettes represented on Figure 7.20 were glued at 0, 45, and 90 degrees to the horizontal. The absolute shear strain was then obtained by post-processing the data from these three strain gauge readings as follows (Hibbeler 1991 p. 470):

$$g_{xy} = 2e_{45} - (e_0 + e_{90}) \dots\dots\dots (7.4)$$

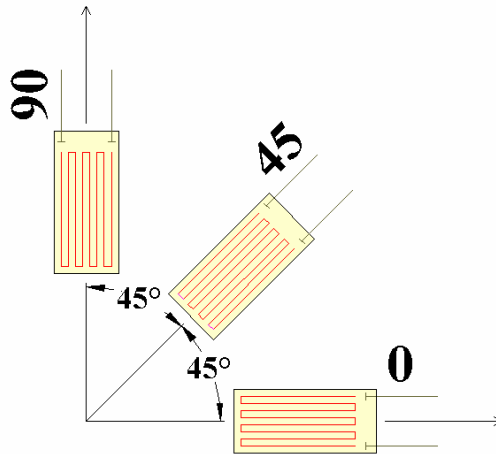


Figure 7.20 Strain gauge rosette arrangement

Table 7.2 shows the average dimensions of the beams tested.

Table 7.2 Shear test beam dimensions

<i>Cross-section</i>	<i>Average Dimensions (mm)</i>	<i>Number of Laminates</i>	<i>Description</i>
	$D=65.0$ $W=34.3$ $w_2=22.5$ $t_f=12.0$ $t_c=12.0$ $t_w=4.0$	$L_1=1$ $L_2=7$ $L_4=1$ $L_5=2$ $L_7=2$ $L_8=2$ $L_{10}=2$ $L_{11}=1$ $L_{13}=7$ $L_{14}=1$	<p>All beams were made to the same sizes. Four batches of six beams were produced. To reduce the possibility of obtaining erroneous results, due to manufacturing differences, one beam from each batch was used in each series.</p>

By altering the span of the beams, the overall behaviour of the FRP beam in bending and shear could be investigated (discussed in Section 7.5). Furthermore, as can be seen on Table 7.3, the series 6 have the shortest lever arm, which makes it the closest possible to a pure shear test. Therefore, it is used to estimate the ‘pure’ shear strength of the beams.

Table 7.3 Shear testing beam spans

<i>Beam series</i>	<i>Span L (mm)</i>	<i>Lever arm a (mm)</i>
1	700	300
2	710	255
3	620	210
4	530	165
5	340	120
6	350	75

All the beams in this series showed a similar behaviour. The measured deflections were almost linear up to the first form of cracking in the core material, either through shear or bending. The cracks were typically neat and did not affect the web laminates. Both the shear area and stiffness decreased, and the deformations increased accordingly. If shear cracking occurred first, the beams continued to accept further loading until the occurrence of flexural cracking, or vice versa, after which total failure was imminent for most of the beams in the series. However, a small number of beams continued to accept further loading before ultimate failure. In all cases, total failure was due to the web laminates de-bonding from the core and subsequently buckling. The respective average and maximum failure shear for the series 6 beams were recorded as 14427 and 16711 *N*. These results will be compared with those obtained from web tests and the analytical solution in Section 7.4.2.3. Complete results for each beam are presented in Appendix E.5

The normalised strains from the rosettes shown on Figure 7.21 indicate a significant variation between the experimental results. This is due to the complex nature of the moment-shear interaction of the beams. Also included on the Figure is the analytical prediction of the pure shear strains. It can be clearly seen that the latter lies within the spread of the experimental results, which indicates that the shear flow throughout the beam can be reasonably estimated using the analytical model.

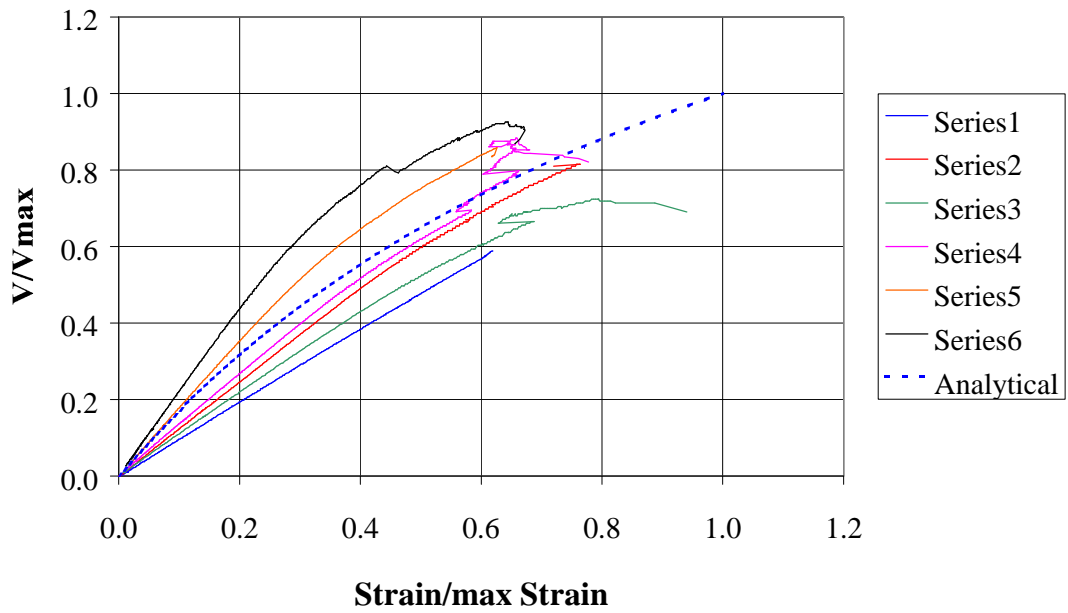


Figure 7.21 Shear loading versus shear strain (normalised based upon maximum values from each series)

In addition, the results from the combined moment-shear tests were post-processed using equations (7.2) and (7.3) to obtain the shear deflections. These are plotted on Figure 7.22. Similarly, these results indicate the same spread in the experimental results. It can also be seen that the analytical prediction of the pure shear behaviour lies within the experimental range of results.

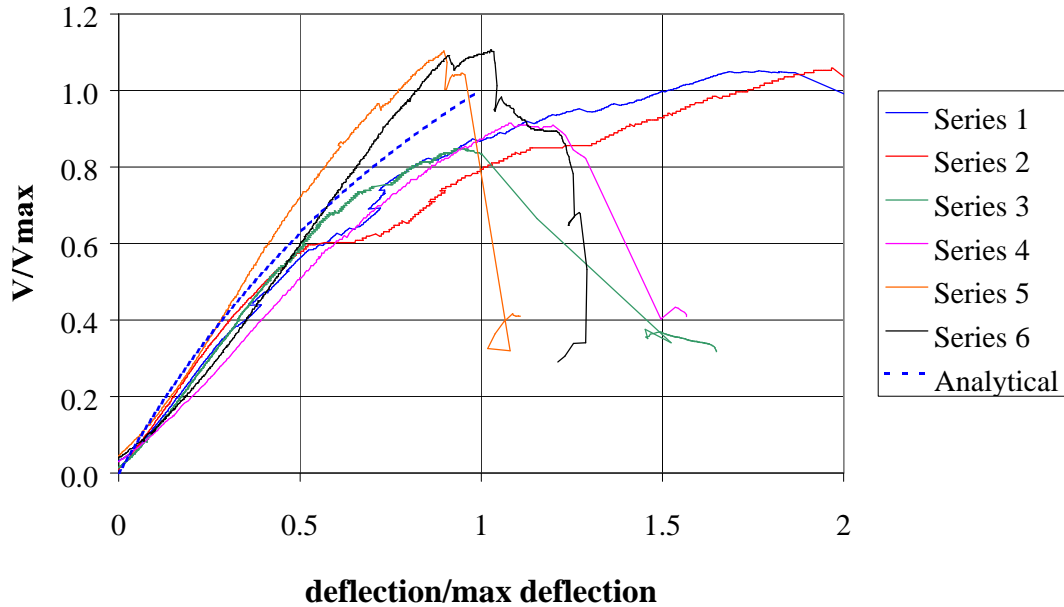


Figure 7.22 Normalized shear loading versus deflection

7.4.2.2 Determination of beam shear capacity by testing web specimens

A different method for the determination of the beam's shear capacity is through testing individual specimens in tension, at a 45-degree orientation, as they contribute the most to its shear strength. The specimen lay-up is identical to the webs in the beam: 25 mm wide by 250 mm long. The orientation of the fibres within the specimen was at 45 degrees to the applied force as required by ISO 14129. To avoid core crushing, at the jaw grip areas, extra laminates were used at both ends. Initial testing results revealed that the specimens had a tendency to break near the jaw grips of the testing machine (specimens S1). To avoid this failure, new specimens were made with two extra laminates added, and tapered at the ends. Figure 7.23 shows schematically the specimen's lay-up.



Figure 7.23 Section geometry of web shear specimens

The determination of beam shear capacity is obtained with equation (6.40) re-arranged as follows:

$$V = \frac{A_{t.c} t_{fw}}{3.893} \dots\dots\dots (7.5)$$

where t_{fw} is the experimentally-determined shear failure stress of the web laminates.

Both sets of experiments showed a similar failure pattern. The first sign of damage was the cracking of the core. The cracks were perpendicular to the applied load. With further increase in the applied load, initial failure of one side laminate took place with the glass fibres fracturing, leaving a perpendicular tear across the specimen, as can be seen on Figure 7.24 (a). Once the first laminate failed, the total load was redistributed to the second one. The generated eccentricity in the loading caused the remaining laminate to de-bond from the core. The fibres then pulled out from the matrix resulting in a fracture plane at 45 degrees to the applied load, as can be seen on Figure 7.24 (b). Results from individual test specimens are presented in Appendix E.4.

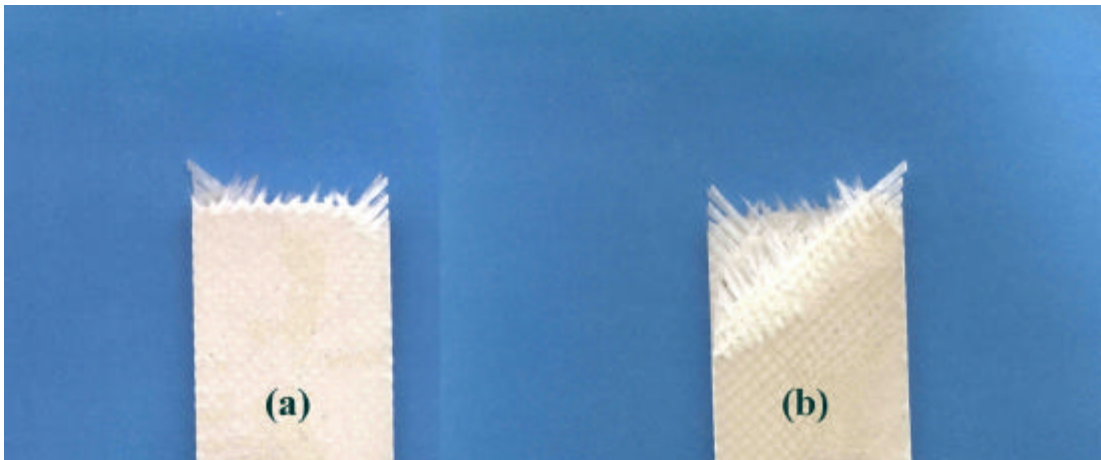


Figure 7.24 Web specimen failure

Figure 7.25 shows the stress-strain behaviour of the specimens. Both series of tests display an initial linear response until cracking occurs in the core, which was then followed by a slightly non-linear response. The difference in the initial stiffness of the two series is due to the addition of the extra laminates at the ends of the specimens ‘S2’.

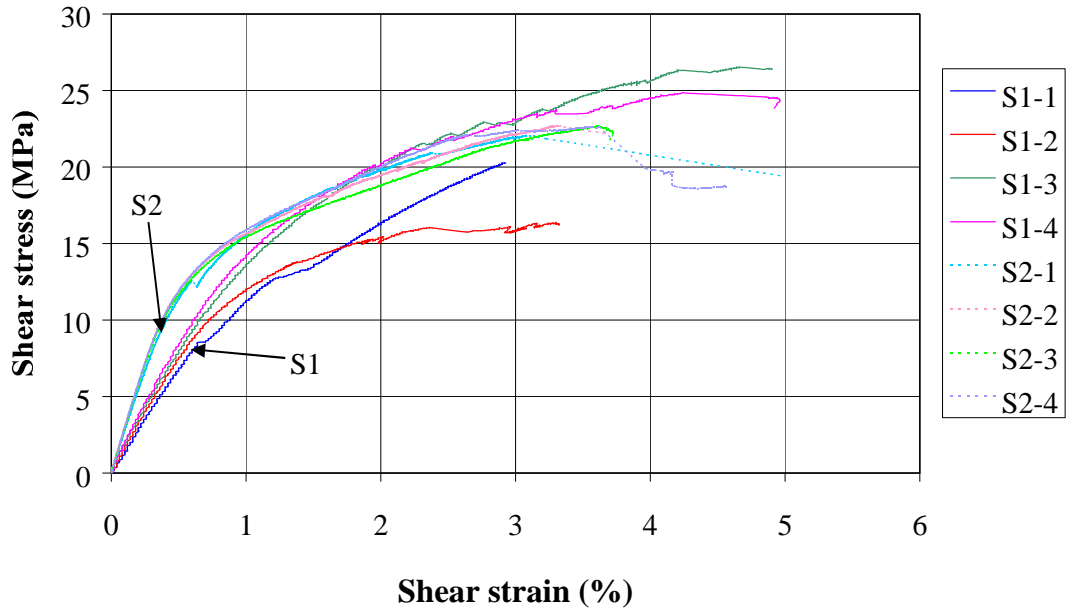


Figure 7.25 Shear stress-strain behaviour of web specimens (inclusive of core)

The shear strength of the specimens does not equal the shear strength of the glass laminates as shown on Figure 7.26.

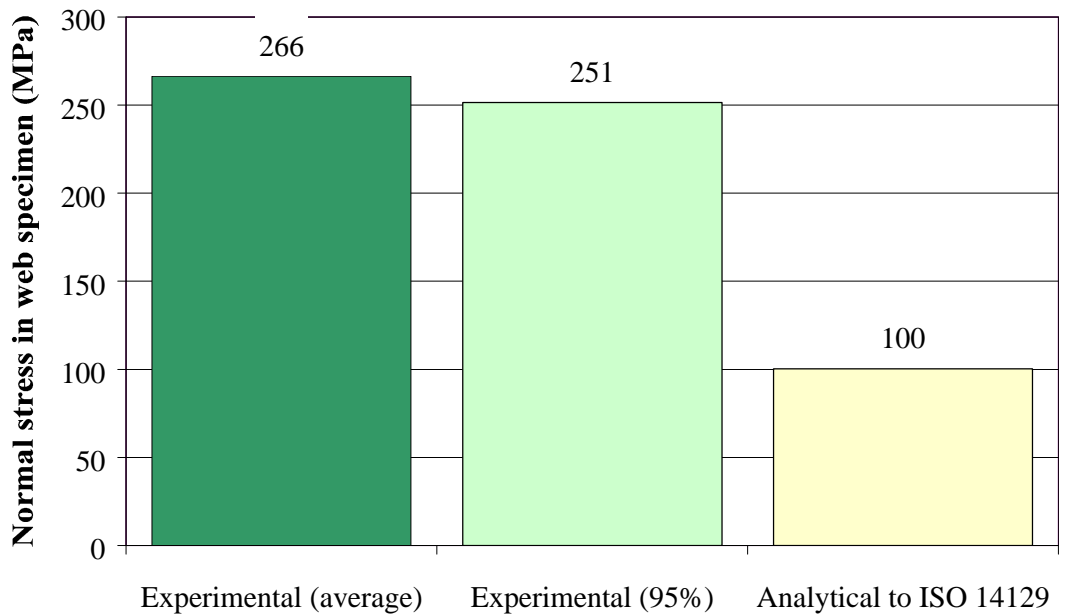


Figure 7.26 Failure of webs in shear and ISO 14129 prediction

From the above described experiments, the obtained shear strength of the glass laminate is 125 MPa , which is far higher than the shear capacity of the laminates when tested separately without the addition of a core material, 50.2 MPa as described in section 5.3.2. This increase in the shear capacity can be explained by the addition of the core material, which inhibits plastic deformations in the laminate resin. This causes the fibres to rupture, at a crack in the core, instead of pulling out, as happens in a standard shear test on a laminate carried out according to ISO 14129.

In the light of this new finding, it is necessary to take into account fibre fracture in the analytical determination of the shear capacity of the laminates within the beam as follows.

The capacity of the glass fibres of any laminate can be determined by:

$$s_{fi} = \frac{s_{fii}}{S_i f_{fi}} \dots\dots\dots (7.6)$$

where S is the ratio of fibres aligned in the direction of the force applied (for the plain weave $S = 0.5$). Therefore:

$$s_{f7} = 169.6 \text{ MPa}$$

This is for a fibre mass fraction of 0.5. The equivalent volume fraction, when using density of resin and glass of 1100 kg/m^3 and 2540 kg/m^3 respectively, is:

$$f_{f7} = 0.3022$$

The resulting failure stress for the glass along its length can then be calculated as:

$$s_{f7} = \frac{169.6}{0.5 \times 0.3022} = 1122.4 \text{ MPa}$$

Noting that the fibres, in the shear specimens, initially act as tension members at 45 degrees to the direction of the load (as shown on Figure 7.27(a) and the free body diagram (b)), the effective area normal to the fibres is:

$$f_{f7} \cos 45$$

and the capacity of the specimens may be determined as:

$$s_{f.lam} = s_{f7} f_{f7} \cos^2 45 \dots\dots\dots (7.7)$$

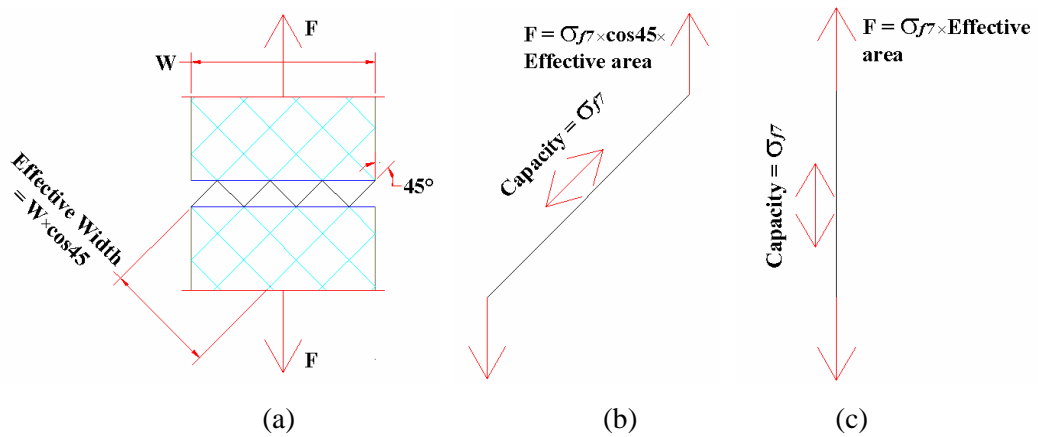


Figure 7.27 Free body diagrams of the initial and final fibre orientation at a crack in the core

However, as the load is applied, the fibres align themselves with its direction, as shown on Figure 7.27(c). Therefore, the final failure stress of the laminate will be:

$$s_{f.lam} = s_{f7} f_{f7} \cos 45 \dots\dots\dots (7.8)$$

The analytical stress prediction, equation (7.8), will be termed the amended analytical prediction henceforth.

Figure 7.28 shows the experimental results together with the initial and amended analytical formulations. It appears that the amended analytical formulation provides better estimates of the ultimate shear capacity of the webs, which are within 9.8% of the experimental results.

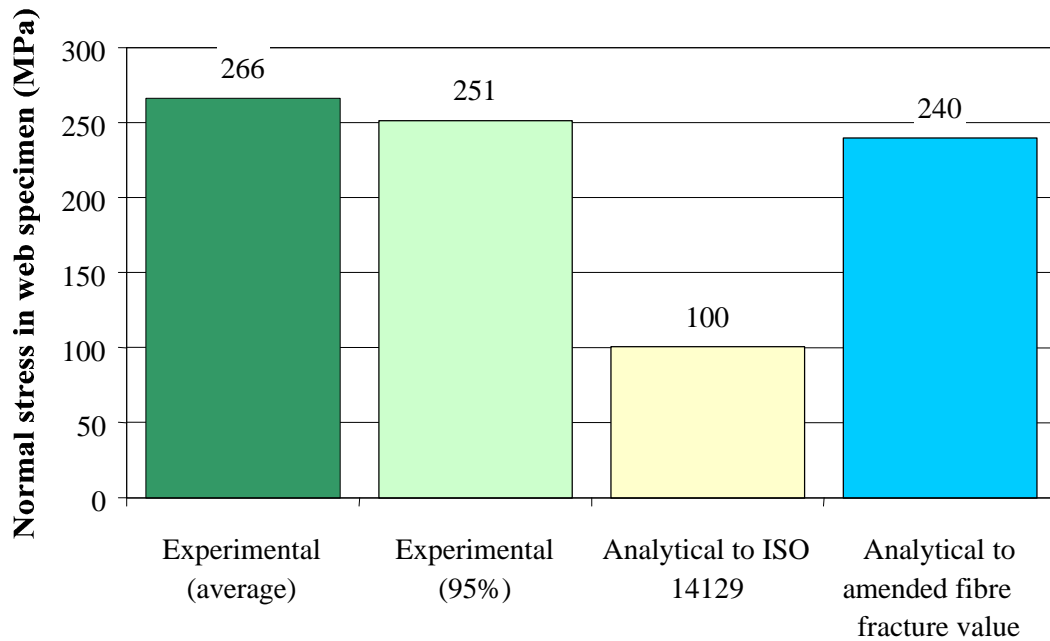


Figure 7.28 Failure of webs in shear and analytical prediction

Based upon the experimentally-obtained results, and the use of equation (7.5), the ultimate shear capacity of the beam is estimated to 18840 *N*.

7.4.2.3 Comparison of results and the analytical solution for the pure shear capacity of the beam

The results from the two experimental methods, described above, for the determination of the pure shear capacity of the beam are shown together with the analytical predictions on Figure 7.29.

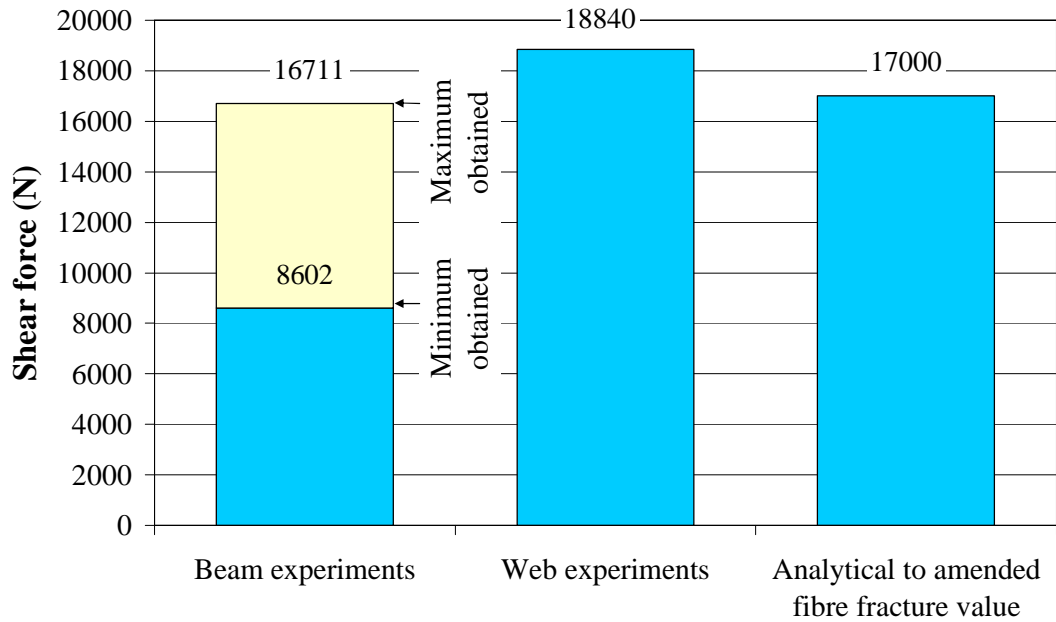


Figure 7.29 Comparison of ultimate shear capacities and predictions

It can be seen that the maximum shear capacity obtained by testing the beam is 11.3 % lower than that obtained by testing the web specimens. This difference may be attributed to the expected synergy between moment and shear. This is an important aspect of FRP beam behaviour, and will be discussed in detail in section 7.5. It therefore appears reasonable to take the pure shear capacity as that calculated from the web experiments, where combined loading was not present. On the other hand, the analytical prediction of the pure shear capacity is 9% below the latter experimental value, which can be regarded as reasonably accurate.

7.4.3 Shear buckling capacity of the webs

As discussed in Section 7.3.3, it is not practical to induce buckling of the web in the beam. Therefore, a specimen was made in such a way as to ensure shear buckling was the dominant failure mode. The web specimen is identical to that described in Section 7.3.3. Extra laminates of unidirectional glass were provided in locations of high bearing and tensile stresses as shown on Figure 7.30.

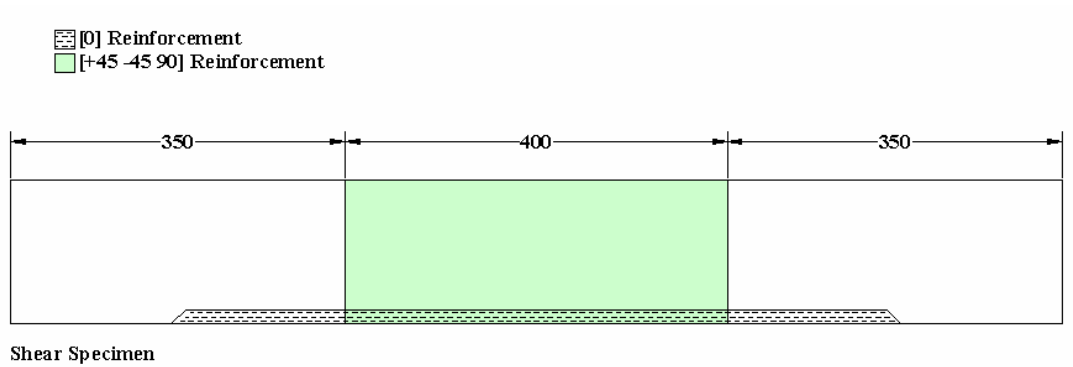


Figure 7.30 Extra reinforcement on web specimen

The sacrificial sandwich panel stiffeners, described in Section 7.3.3, were also used to ensure the web top and bottom edges of the specimen remained laterally restrained.

First buckling took place at a load of 15 *kN*. Contrary to testing for moment buckling, the lateral restraints effectively restrained the top and bottom of the specimen. Figure 7.31 shows the buckling of the specimen at a load of 16 *kN*.

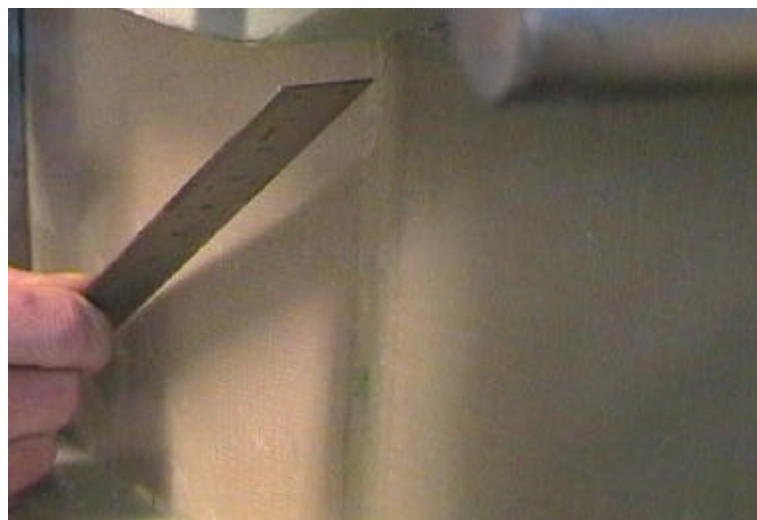


Figure 7.31 Shear buckling of test specimen

The load-deformation curve is shown on Figure 7.32. It can be noticed that the specimen is still capable of carrying further loading even after first buckling has occurred. Ultimately failure happens with the tearing of the laminate. The analytical approach predicts a first buckling load of 13.8 *kN*, which is approximately 8.3% lower than the observed buckling load.

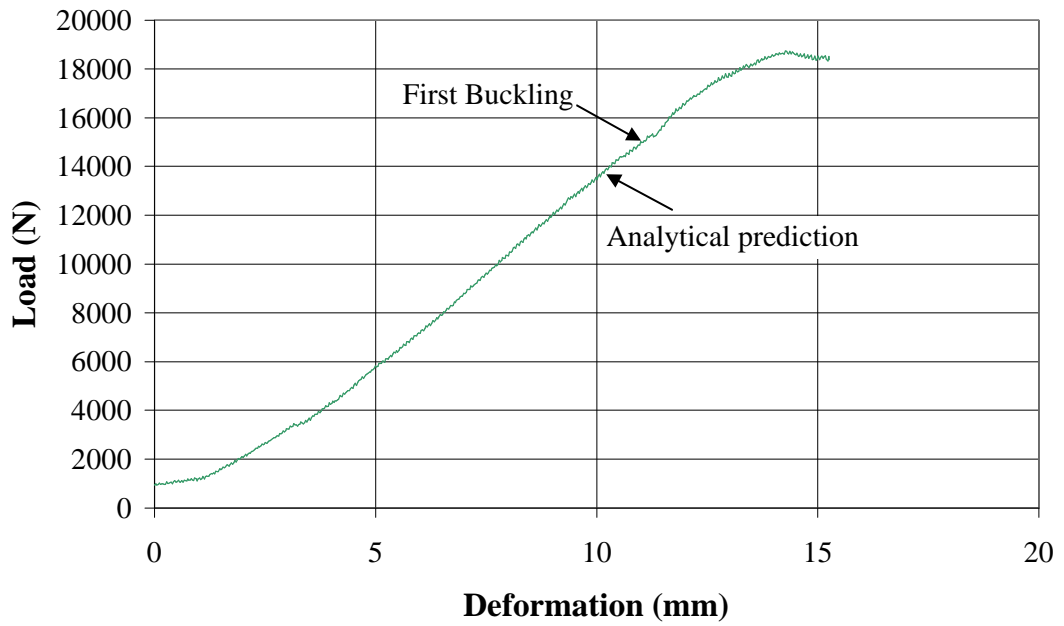
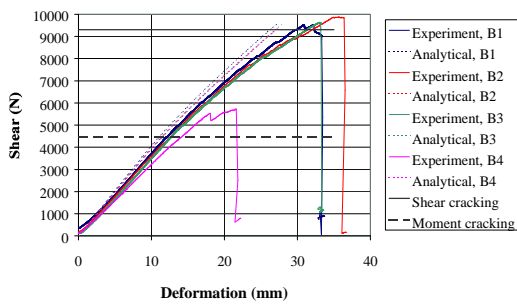


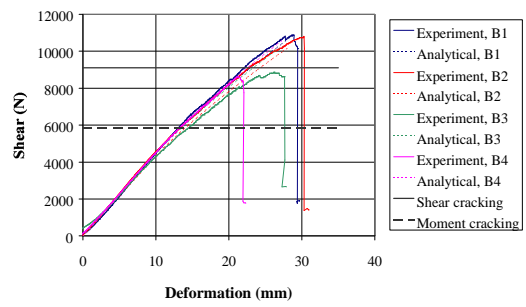
Figure 7.32 Load versus deformation of shear buckling specimen

7.5 Combined moment and shear

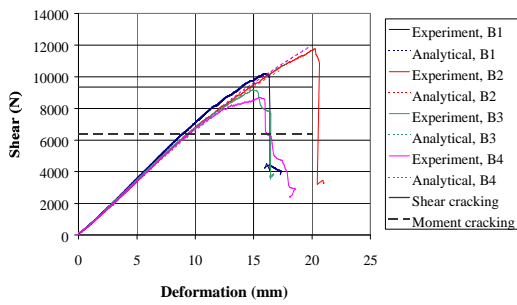
For the sake of comparison, the results from the combined flexure-shear tests described in Section 7.4.2.1 are shown on Figure 7.33 as well as the theoretical predictions represented by dotted lines. It can be seen that the analytical model provides reasonable estimates of the individual beam behaviours for all the test series.



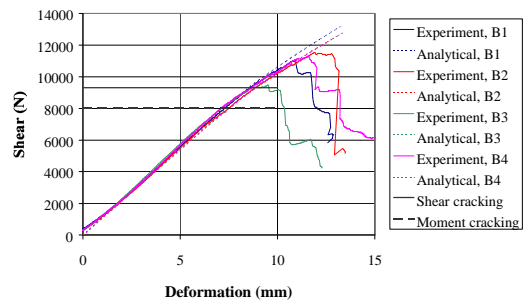
Series 1 (300 mm lever arm)



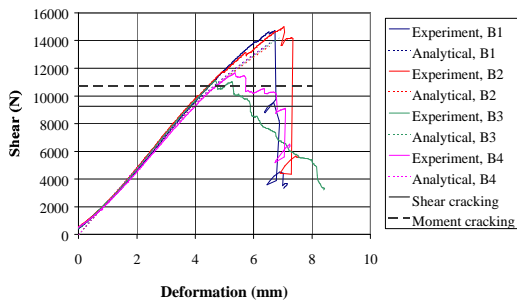
Series 2 (255 mm lever arm)



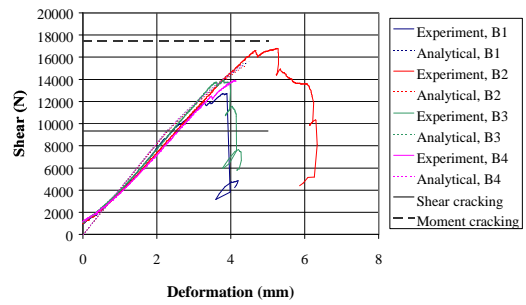
Series 3 (210 mm lever arm)



Series 4 (165 mm lever arm)



Series 5 (120 mm lever arm)



Series 6 (75 mm lever arm)

Figure 7.33 Total deformations of beams

The data from all the beams are plotted on Figure 7.34, along with the predictions from the models such as Eurocomp, Mohr's circle, and Elliptical. As it appears, there is a large discrepancy between the results. However, a broad trend is noticeable comprising many failures coinciding with the occurrence of shear cracking at a load of 9.275 kN after moment cracking has occurred at a load 1.318 kN.m.

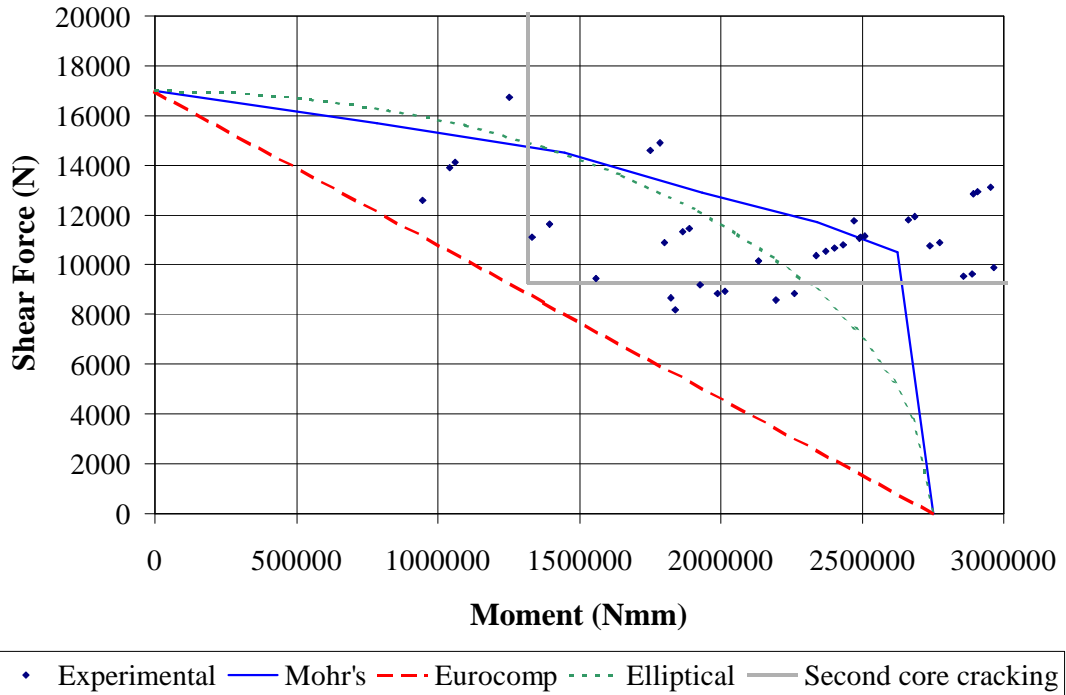


Figure 7.34 Moment versus shear

From the data presented above, it appears that the performance of the beams is greatly influenced by the moment-shear interaction. Pure shear loading results in a neat crack being formed without causing premature failure. However, with the presence of bending, the shear crack is accompanied with localised crushing of the core in the compressive zone, leading to the buckling of the RHS web laminate, thus resulting in premature failure. Therefore, under combined moment shear loading, the appearance of shear cracking in the core material marks the onset of instability in the beam behaviour, and this should be taken as its ultimate capacity:

$$\text{if } V > V_{cr} \text{ then } M \text{ must be } < M_{cr} \text{ or}$$

$$\text{if } M > M_{cr} \text{ then } V \text{ must be } < V_{cr} \dots\dots\dots (7.9)$$

where: M_{cr} and V_{cr} are the moment and shear loading at which cracks occur respectively.

When comparing the experimental averages with the different models using least squares method, it appears that the Mohr's circle methodology is the closest to the experimental data. This was somehow expected since this method takes into account the laminate orthotropic properties. A lot of failure points lie inside the Mohr's circle prediction

while no points lie within the Eurocomp approach thus making the latter appropriate for design purposes.

7.6 Lateral torsional buckling

The analytical determination of the lateral torsional buckling moment is dependent upon the torsion constant of the beam. Therefore, preliminary torsion tests were carried out to determine the torsion constant of the beam prior to the investigation into its lateral torsional buckling. The two sets of experiments are described below.

7.6.1 Torsion constant

To determine the torsion constant, eight beams were manufactured and tested. The beams were tested in a jig made from 12 mm steel plate for the clamping mechanisms, and 16 mm plate for the base and sides as shown on Figure 7.35.

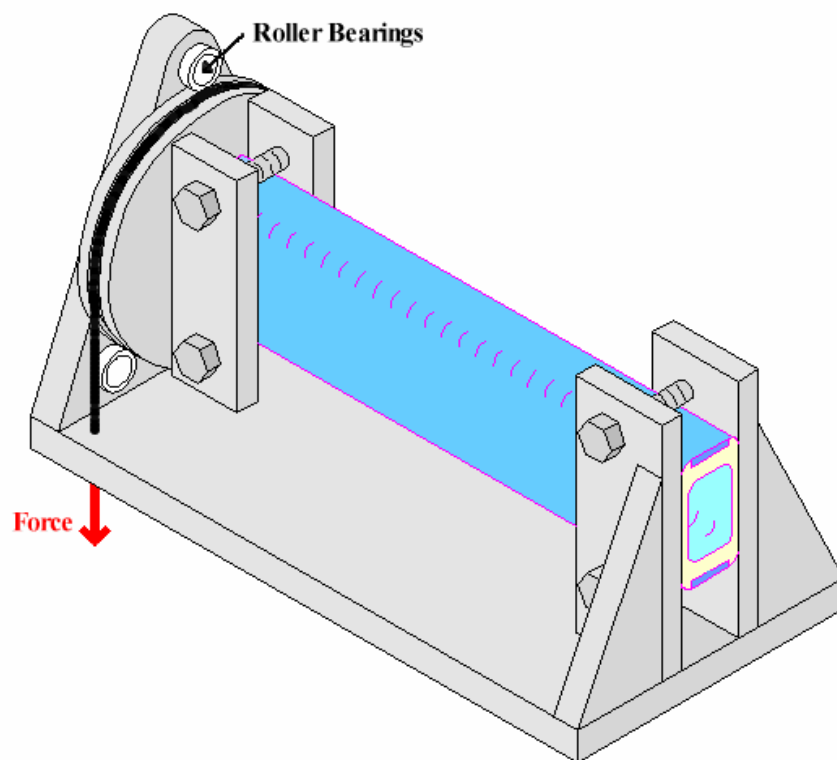


Figure 7.35 Torsion testing arrangement

One end of the beam was clamped to the jig and the other end was clamped to a circular platen. The platen was seated in-between three roller bearings. A cable was fixed to the platen, and attached to the Avery testing machine, so that a torque could be applied. The jig

was firmly fixed to the Avery testing bed to ensure that jig deformations were negligible. Rotations were manually measured and recorded at intervals of 1000 *N* force on the cable. Figure 7.36 shows a beam undergoing testing.

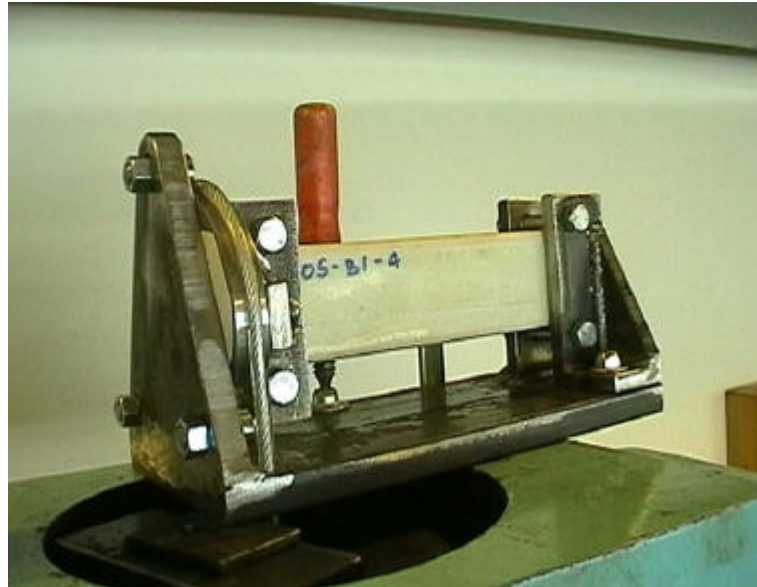


Figure 7.36 Beam undergoing torsion testing

The response of the beams was linear elastic until failure as shown on Figure 7.37. In most cases, de-bonding of the outer RHS laminate along the flange-web interface precipitated ultimate failure. This occurred at (or before) cracking of the core commenced.

The irregularity in the results could be attributed to the inaccuracy in the manual measuring method. The analytical method predicts the rotations well. The prediction that the core would be restrained from cracking due to the torsional shrinking of the beam appears to be justified since cracking was only heard at failure.

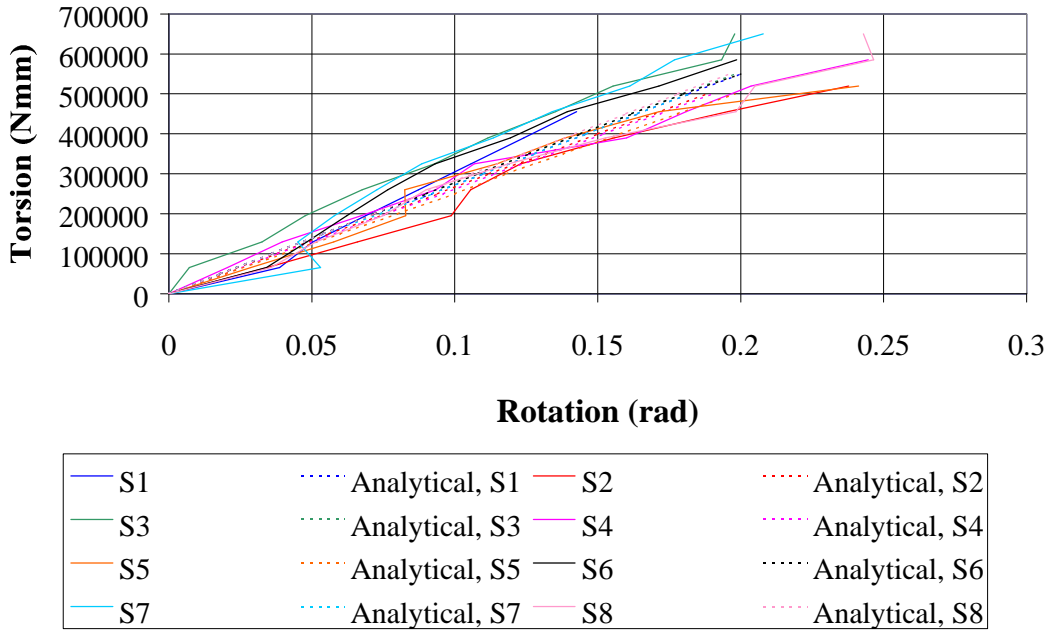


Figure 7.37 Torsion versus rotation angle

The use of the transformed section method in combination with the one-dimensional analysis provided reasonable results. This indicates that the torsion constant, calculated from the transformed section, is accurate and can be used in the lateral torsional buckling analysis.

7.6.2 Lateral torsional buckling behaviour

Testing for lateral torsional buckling did not require the destruction of the beam as necessary information could be obtained before the specimen was damaged. Therefore, only one test specimen was manufactured. This consisted of a 2.4 metre beam loaded as a cantilever with a point load at the free end. The other end was clamped to the bed of the Avery universal testing machine, so that no rotations could occur. Figure 7.38 shows the testing arrangement.

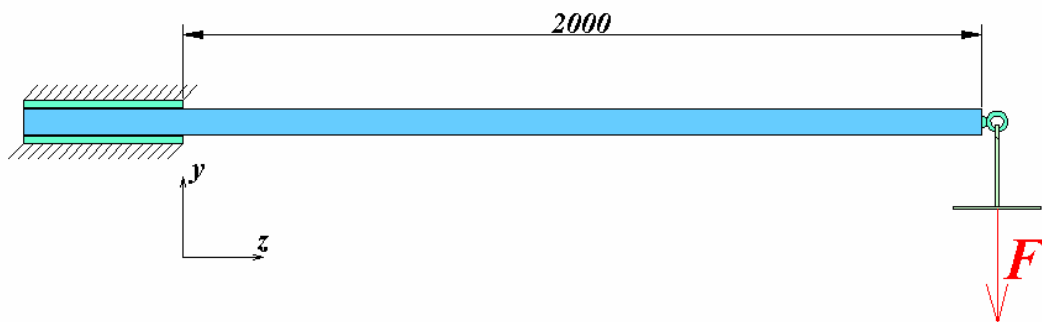


Figure 7.38 Test set-up for lateral torsional buckling

Although the test set-up appears simple, it proved quite a challenge when measuring the required quantities such as: displacements in the x and y direction as represented on Figure 7.38, and rotations around the z and x axes. Static measuring devices, such as LVDT's, were deemed inappropriate, as they influenced the beam's behaviour. It was therefore decided to measure only the rotations by adhering clinometers to the end of the beam. Two clinometers were used: one to measure z-axis rotation and the other to measure x-axis rotation. Since the two clinometers would twist out of plane during the experiment, an algorithm to compensate for this was pre-programmed into the data-logger to allow for any out-of-plane rotation of the clinometers.

The beam was loaded using calibrated weights, and allowed to settle upon each subsequent loading. A photograph of the beam close to maximum loading is shown on Figure 7.39. The maximum stable end loading that could be placed upon the beam was 665 N, any loading above this limit resulted in unstable behaviour.

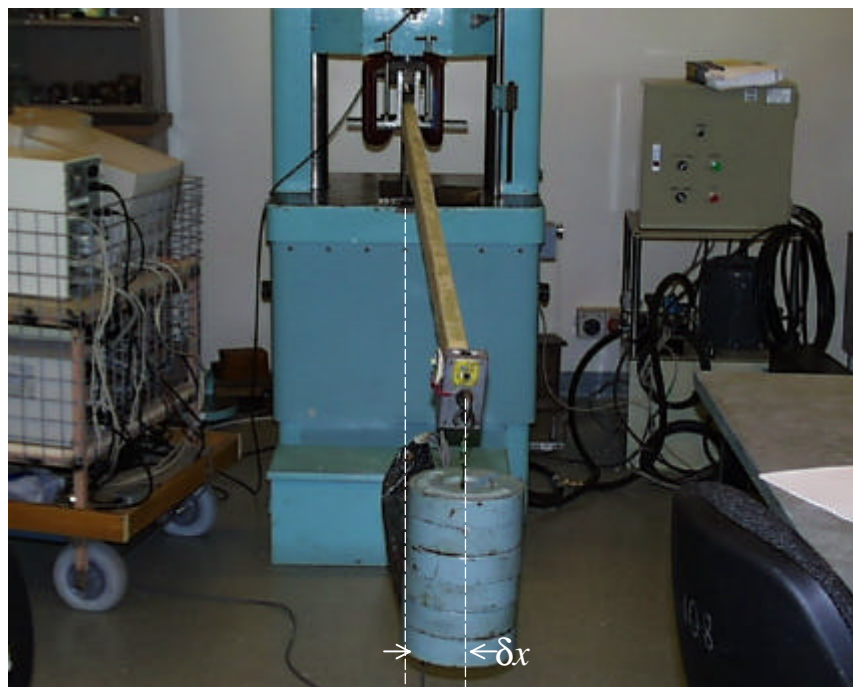


Figure 7.39 Cantilever beam, lateral torsional buckling

The test results are plotted on Figure 7.40 together with the theoretical predictions. A linear regression of the initial data points indicates that the critical loading, which signifies the onset of major lateral torsional buckling is 528 N, while the critical load is approximately 700 N.

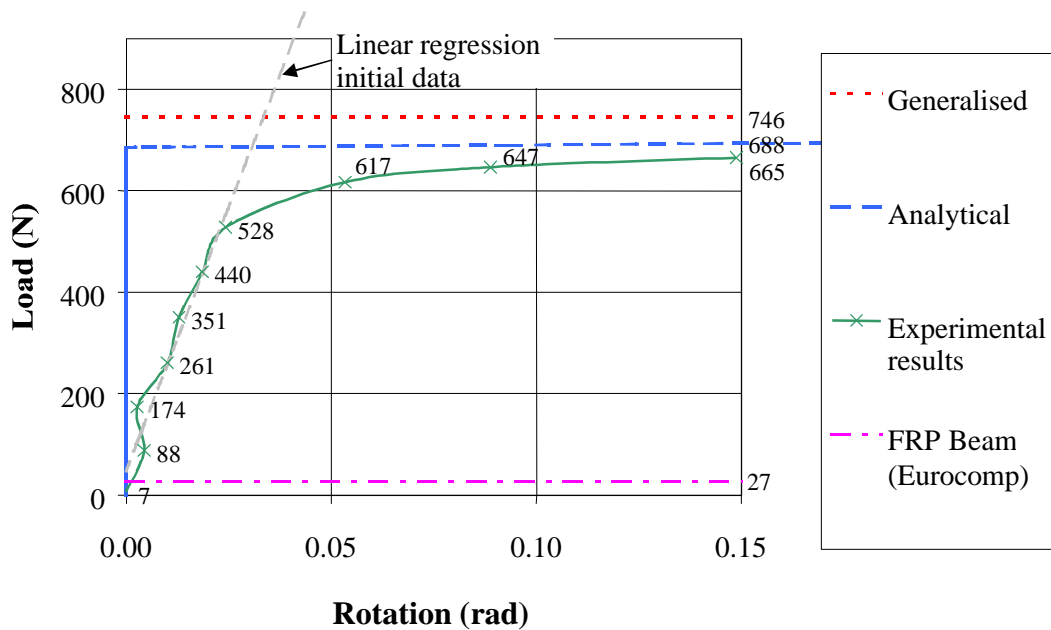


Figure 7.40 z-axis rotation of cantilever beam

Comparing these experimental values with the predictive methods shows that the FRP beam formula cited in the Eurocomp code is clearly non-representative of the beam behaviour. The analytical model, while unable to account for initial imperfections, provides a reasonably good estimate of the critical load. The generalised method slightly overestimates the buckling capacity.

7.7 Bearing stresses distribution angle

To determine the distribution angle under bearing stresses, a series of beams were tested with varying-sized loading platens ranging from 14 to 63 *mm*. Two types of tests were conducted to determine the distribution angle. First, beams, BB1, were tested in three-point bending with an overall span of 400 *mm*. Whereas beams, BB2, were tested as beams on rigid foundation. Included with the data of these tests, are the results of beams that failed in bearing when conducting other tests such as bending. All the tested beams displayed a similar pattern, they failed due to core cracking at the web-flange interface as discussed for the fully compressed specimens in Section 7.3.5. The individual results are presented in Appendix E.7.

The experimental results along with the analytical predictions are shown on Figure 7.41. The simple analytical approach predicts lower failure loads, which are within 12% of

the experimental. This deviation from experimental results is to be expected since a linear stress distribution was assumed in the analytical formulation. However, such a simplistic approach has its advantages since it yields reasonable results with ease in calculation.

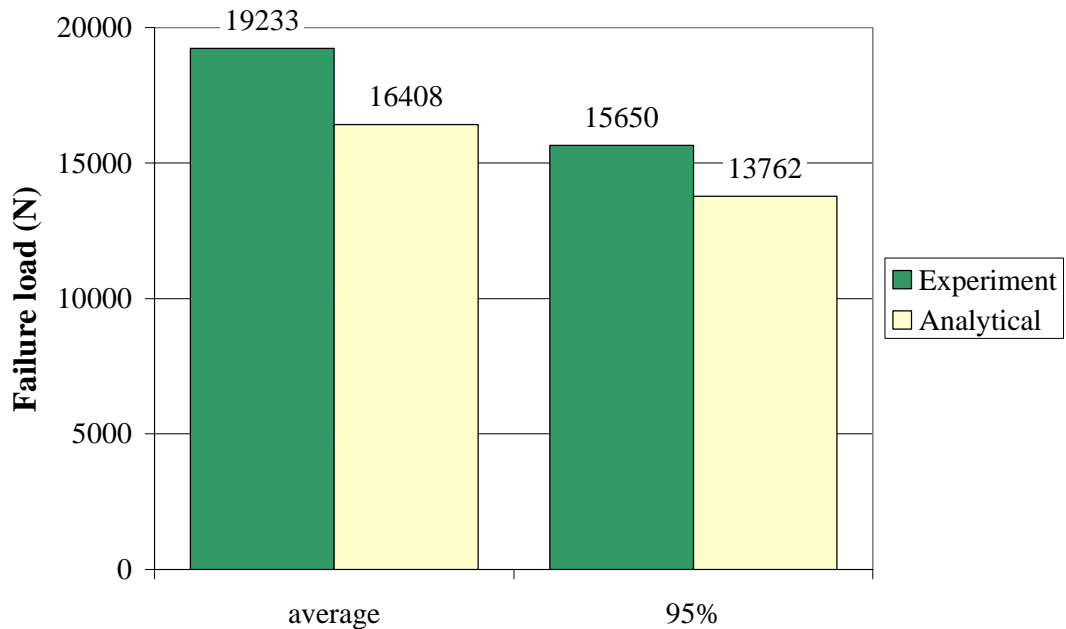


Figure 7.41 Failure loads for beams versus model predictions

A clear trend between bearing distance and capacity can be seen in the results shown on Figure 7.42. Analysis of the results revealed that a bearing angle of 39 degrees corresponded to failure. The analytical value of 44 degrees is conservative when compared to the angle obtained experimentally. This appears to indicate that the stress distribution fans out to a greater extent than predicted using the analytical analysis.

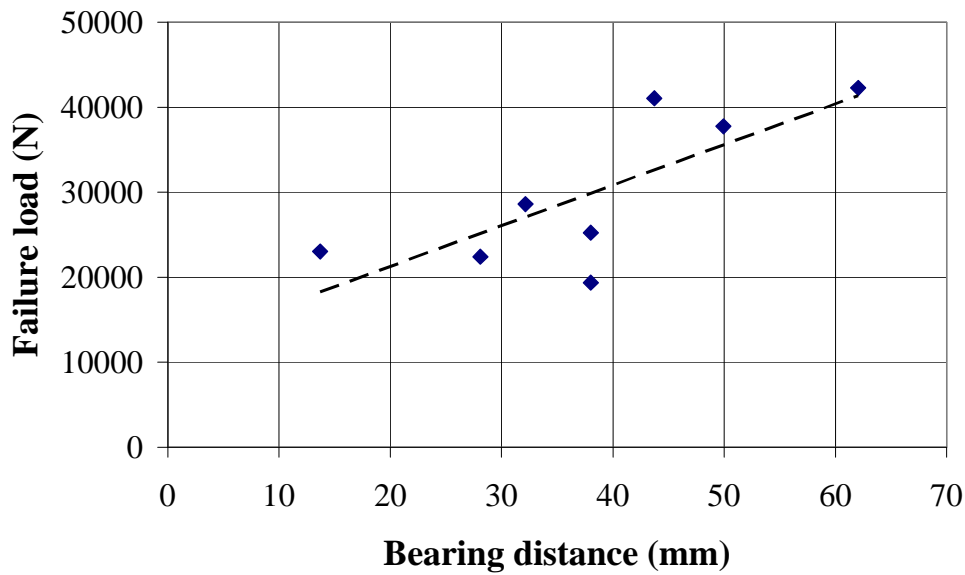


Figure 7.42 Failure load and bearing distance of fully-supported series

7.8 Creep

The only reliable way to investigate the creep behaviour of FRP components is to carry out long-term tests. The main objective of the following experiments was to assess whether the creep behaviour of the FRP beam conforms to the general model for FRP materials. Two sets of beams were manufactured to characterise long-term behaviour. The first set, B1, consisted of five beams that were tested in 4-points bending, with displacement control at a rate of 5 mm per minute to determine short-term failure load and deflections. The second set of beams, B1c, was subjected to sustained loadings over a long period in excess of 16000 hours. To conform to the recommendations of the Eurocomp design code, one of the beams was loaded with 60% of short-term capacity. The load levels for the remaining two beams were determined using serviceability criteria. For instance, to cause a deflection equal to 1/200 span required a loading of 20% of short-term capacity. However, for long-term serviceability limit, it was considered that a loading level of 20 % was excessive, therefore the last beam was only loaded at 10% of short-term capacity. Furthermore, testing beams with different load levels would validate/invalidate the assumption of linearity between creep strains and stress. Figure 7.43 shows the experimental set-up. The loads were applied to the beams by means of steel weights hanging from the ends of the lever arm amplifying the loads by a factor of 10. The tests were carried out in a fully-enclosed building with a yearly temperature fluctuation of 10 °C. Centreline beam

deflections were measured on a regular basis. Figure 7.44 shows photographs of the experimental set-up.

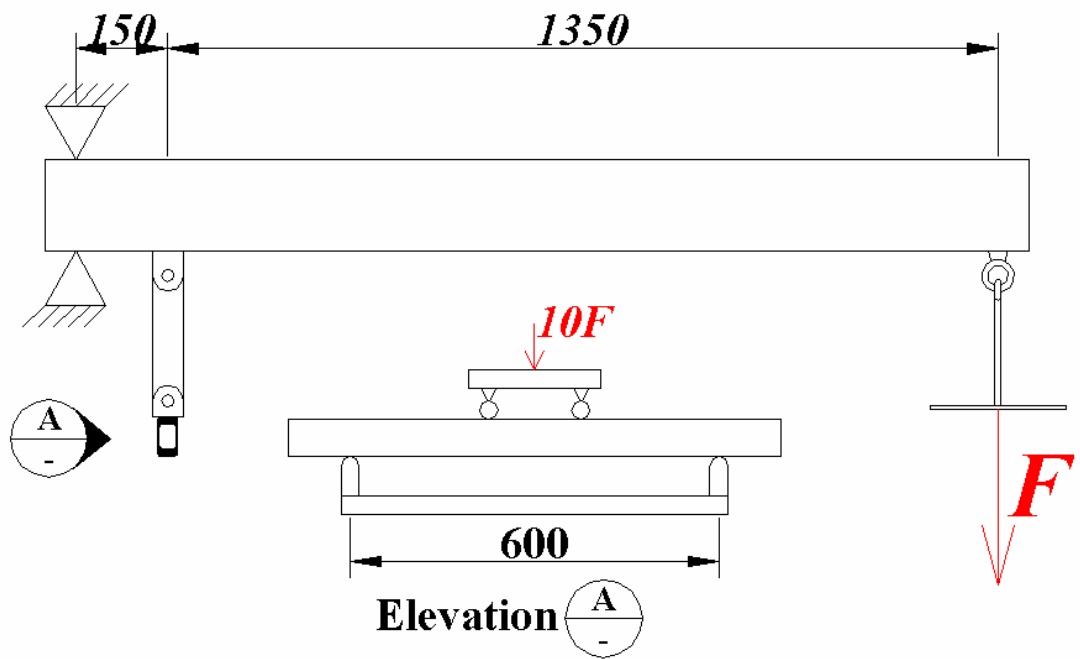


Figure 7.43 Test regime for long-term loading of the beams



Figure 7.44 Beams undergoing sustained loading

The testing is ongoing, results, to date, are presented below.

The control specimens, B1, behaved in a similar manner as the beams tested for bending as described in Section 7.3.2. In general, failure was due to tensile rupture of the bottom laminate in the flange. The average failure moment was $3 \times 10^6 \text{ N.mm}$ corresponding to a centreline deflection of 18.3 mm . The results are presented in Appendix E.8.

Figure 7.45 shows a plot of the available results for the sustained loaded beams, Bc, at the time of writing in the form of central deflections versus time for the three beams. It is apparent that a large amount of the creep deflection occurs within the first 1000 hours as noted by Hoa (1995). It is also clear that substantial deformations continue beyond 2000 hours period.

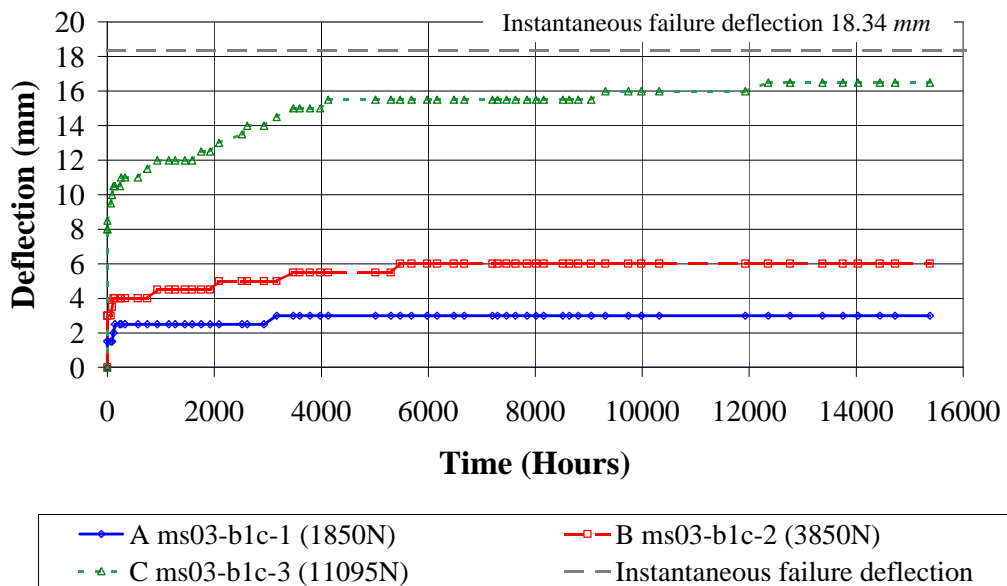


Figure 7.45 Time versus deflection for the three beams tested

When the deflections are normalised with respect to initial instantaneous deflection as shown on Figure 7.46, it appears that the creep strains as a proportion of the initial deflections are independent of load level. Also represented on Figure 7.46 is the Findley's power law calibrated for the results. This indicates that the creep behaviour of the tested beams, with a large amount of Particulate Filled Resin, is similar to that displayed by classic FRP beams.

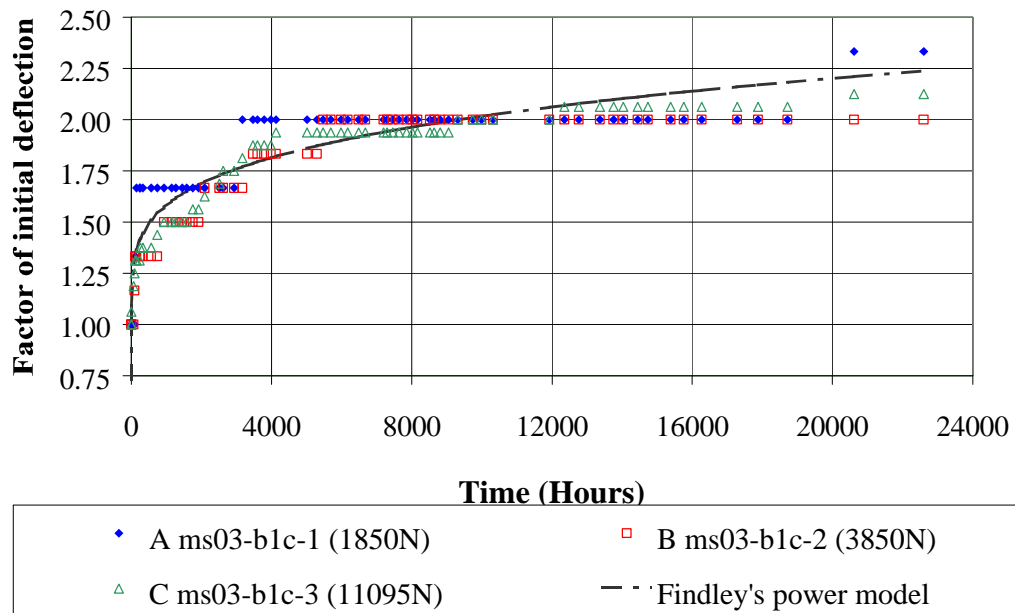


Figure 7.46 Time versus factor of initial deflection

However, since the duration of the creep tests is only 16000 hours (equivalent to 22 months), it is too early to draw any valid conclusions about long-term behaviour. It is reasonable to assume that the creep strains are the results of different phenomena such as: creep of the matrix, creep of the PFR and stress rupture in the fibres. However, in the long-term, which of these factors dominates creep behaviour remains unclear.

7.9 General Discussion

From the above tests, it appears that there is an optimum thickness of core material for the beam under generalised loads. This can be seen by observing the plot of failure load versus amount of core material in the compression flange (Figure 7.47), which clearly indicates the optimum to be 8 mm. At this value, the primary failure mode in the FRP beam is that of tensile failure of the unidirectional reinforcement. When the amount of core material in the compression flange is below the optimum, the beam is susceptible to punching shear, compression flange buckling and bearing failures, thereby lowering its ultimate capacity. On the other hand, if the compressive core thickness is higher than the optimum, a drop in strength results. This is due to the neutral axis shifting towards the compressive flange, inducing higher tensile strains for the same value of moment.

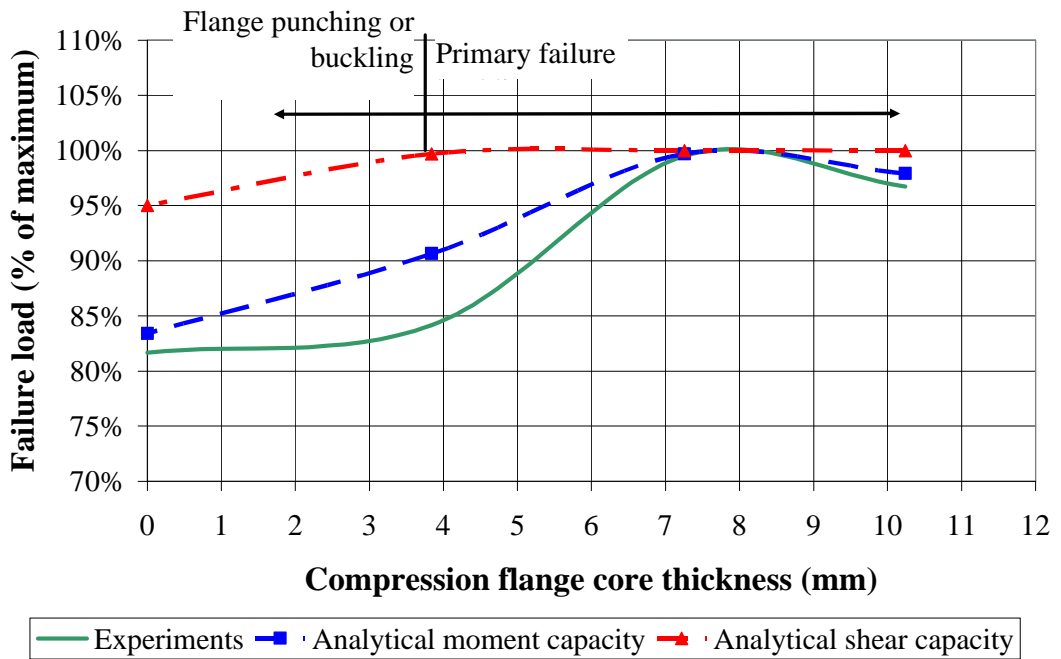


Figure 7.47 Compression flange core thickness versus failure load

As shown on Figure 7.48, there is also an optimal minimum core thickness for the tensile flange. While beams B5 demonstrated that a core thickness of 3.6 mm, or more, prevented the punching shear failures witnessed in beam series B4, an optimum performance is reached when the core material is above 7.5 mm thick. The thickness of the core material in the tensile flange does not influence ultimate strength provided more than the minimum core material is provided, and the beam is not significantly under-reinforced. Therefore, provision of equal material in the top and bottom flange can be achieved, making the beam doubly symmetric.

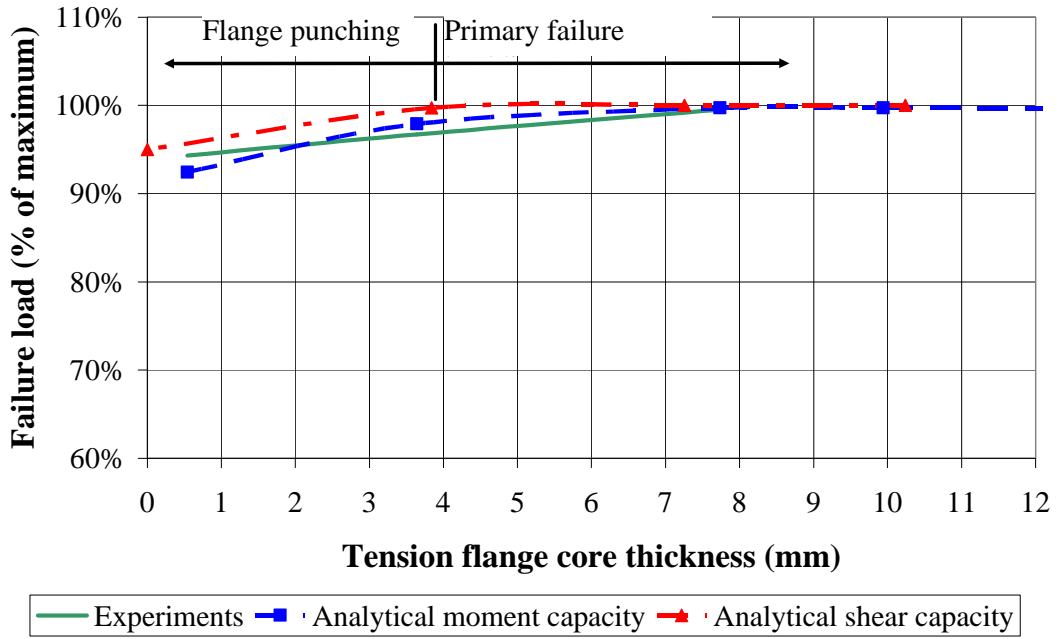


Figure 7.48 Tension flange core thickness versus failure load

Core material placement in the webs also has a marked effect upon beam behaviour. As shown on Figure 7.49, there is a clear relationship between capacity and web thickness, which closely agrees with the analytical prediction.

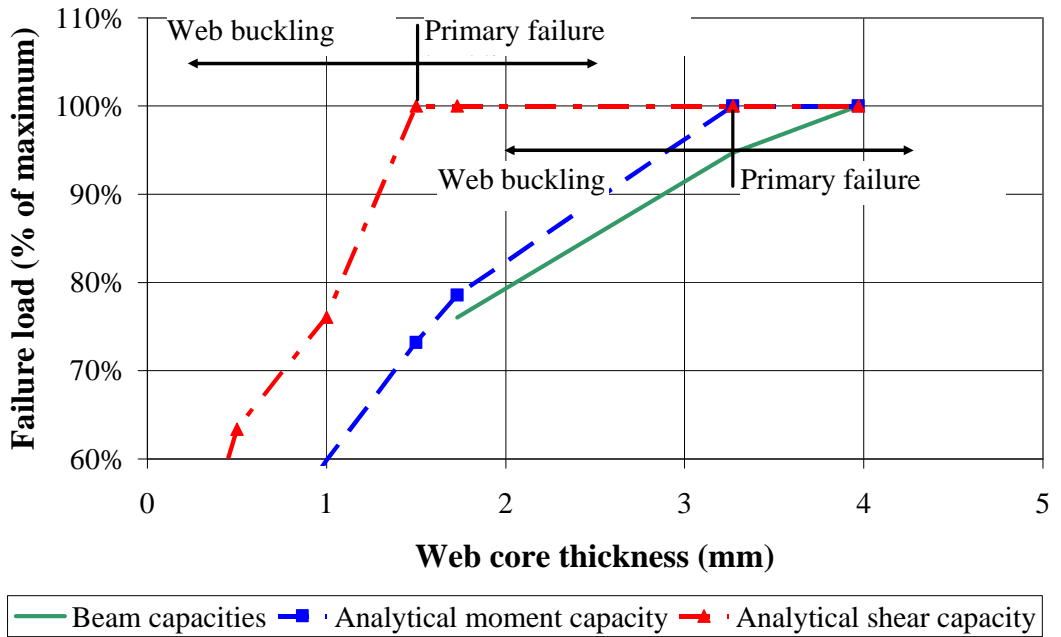


Figure 7.49 Web core thickness versus failure load

7.10 Conclusions

The mechanical response of the developed FRP beam has been thoroughly investigated both experimentally and analytically. Particular emphasis was put on identifying the sources of primary and secondary failure modes. Furthermore, the experimental results were used to validate the analytical method developed in the previous chapter. Overall, the analytical results compared very well with their experimental counterparts, thus validating the underlying assumptions.

The primary failure mode in bending was due to the rupture of the unidirectional laminates, as predicted by the analytical method. The load deformation behaviour is linear elastic until the first tensile cracking of the core material is encountered. As the load is increased, the tensile strains exhibit a non-linear behaviour while the compressive strains remain essentially linear. It was also found that the quantity and location of the core material affect the behaviour of the beams. For instance, a small amount placed in the bottom flange was sufficient to resist the second-order shear punching of the bottom laminates in bending, allowing therefore the primary failure mode to dominate. Furthermore, the inclusion of core material in the webs and flanges provides an effective restraining mechanism to the laminates, thereby alleviating second-order failures.

The shear resistance of the beam is enhanced by the provision of a PFR core sandwiched between the laminates in the webs. The core material plays a double role. First, it provides a restraint against buckling of the webs, and second it inhibits plastic deformations in the laminate resin, thus causing the fibres to rupture instead of pulling out, as happens in a standard shear test on a laminate carried out according to ISO 14129. As a result, the overall load carrying capacity of the beam is increased. The shear behaviour of the beam is well-predicted by the analytical method when fibre rupture is included in the formulation.

The moment-shear interaction was found to have a significant influence on the behaviour of the beam. Pure shear on its own does not result in premature failure. However, when associated with bending, the shear crack is accompanied by localised crushing of the core in the compressive zone leading to the buckling of the RHS web laminate, thus resulting in premature failure. Therefore, under combined moment-shear loading, the combination of shear and moment cracking in the core material signals the onset of instability in the beam behaviour, and the corresponding load should be taken as its ultimate capacity. The analytical modelling predicted this behaviour reasonably well. In particular, it accurately

predicts when each type of cracking will occur. However, the ultimate capacity was slightly over-estimated due to the simplifying assumptions used.

The torsional behaviour of the beam was found to be linear up to failure. The torsion constant, calculated from the transformed section, resulted in predictions of rotations that closely agreed with the experimentally observed values, thus validating the adopted approach. The lateral torsional buckling response of the beam was found to follow the general Euler theory. The critical buckling load was modelled well using the analytical method.

When considering the bearing capacity of the beam under concentrated loads, the low tensile failure strain of the core is the limiting factor. Cracking of the core material in tension reduces the shear area of the flanges, thus increasing the buckling length of the webs. The determination of the stress distribution angle, often used in design, depends upon the specific architecture of the beam in question. For the developed beam, the value of 45 degrees, as suggested by the Eurocomp design code, was found to be conservative compared to the experimentally determined value of 39 degrees.

The long-term behaviour of the beam under sustained loading was found to follow the general trend of FRP behaviour as reported in the literature. From the limited experimental data, it appears that the creep performance of the beam is independent of load level. Findley's power model was found to fit the data. However, extrapolation to long-term behaviour may be considered as unreliable at the moment since the duration of the creep tests is only 16000 hours (equivalent to 22 months). It is reasonable to assume that the creep strains result from different phenomena such as: creep of the matrix, creep of the PFR and stress rupture in the fibres. However, in the long-term, which of these factors dominates creep behaviour remains unclear.

The loading arrangements investigated in this Chapter constitute a broad area of investigation. The investigations into each area were exploratory in nature and therefore conducted to a limited detail. As previously noted, all these areas could, in themselves, constitute entire doctoral studies. However, this broader approach was taken in order to ascertain the validity of the new beam so that the fundamentals of the beam behaviour could be established, providing a base from which further research could continue.

References

Hibbeler, R. C. 1991, *Mechanics of Materials*, Maxwell Macmillan International, New York.

Ho, S. V. 1995, 'Creep of a Composite Box Beam with Design Implications', *Journal of Reinforced Plastics and Composites*, vol. 14, pp. 128 – 142

Chapter 8 Non-linear finite element modelling of the FRP beam behaviour

8.1 Introduction

Predominantly, finite element analysis (FEA) has been the method of choice for FRP analysis. Most commercial finite element (FE) packages include capabilities to analyse laminated plate structures, albeit of simplified nature. However, they are of limited value for detailed numerical investigations incorporating complex non-linear behaviour of FRP. As a result, a significant amount of research has been directed to improving numerical techniques that could be incorporated into FEA (Ascione, Feo & Mancusi 2000; Barbero, Lopez-Anido & Davalos 1993; Davalos & Qiao 1997; Davalos et al. 1996; Haj-Ali & Kilic 2002; Taufik, Barrau & Lorin 1999). However, these techniques have yet to be proven and to be adopted by commercial FE packages. A different approach based on the scripting capability of the ABAQUS finite element software (Hibbitt, Karlsson & Sorensen Inc. 2002) is proposed to model the non-linear behaviour of the FRP beam. The obtained results will be compared to those obtained with another commercial package Strand7 (G+D Computing 2000) as well as with the analytical predictions.

8.2 Modelling the complex behaviour of the FRP beam

8.2.1 Limitations of standard FE software

A simple linear finite element analysis of the behaviour of the beam requires the descriptions of the material properties of the laminates and those of the core. More elaborate analyses that include non-linear effects must take into account the different behaviours in compression and tension in all the materials, the build-up of damage in the constituents such as fibre rupture and matrix cracking in the laminates, and cracking in the core material.

Most commercial FE packages are limited in their ability to model such complex phenomena. For instance, Strand7 does not allow for the modelling of progressive damage in the constituents, or materials with different behaviours in tension and compression. On the other hand, with the use of scripting and user-defined sub-routines, these complex behaviours can be effectively incorporated within ABAQUS.

8.2.2 Description of the FE models

8.2.2.1 Modelling the FRP beam using Strand7

Most commercial FE software use shell elements to model laminates. This is relatively accurate provided the shell elements remain comparatively thin. However, as shown on Figure 8.1, in the present case the unidirectional laminates cannot be considered thin when compared to the size of the beam. In addition, if shell elements are to be used, shear throughout the laminates will be ignored. Therefore, to avoid mesh discrepancies, that would arise when combining shell and brick elements to model respectively the laminates and the core material, the laminates are modelled as orthotropic brick elements to produce a more realistic model as shown on Figure 8.2.

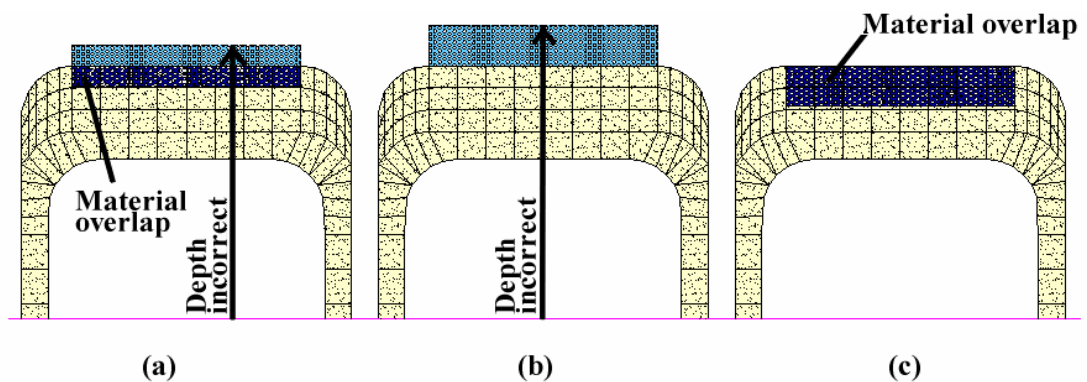


Figure 8.1 Use of thick shell elements results in inaccurate models due to overlapping materials

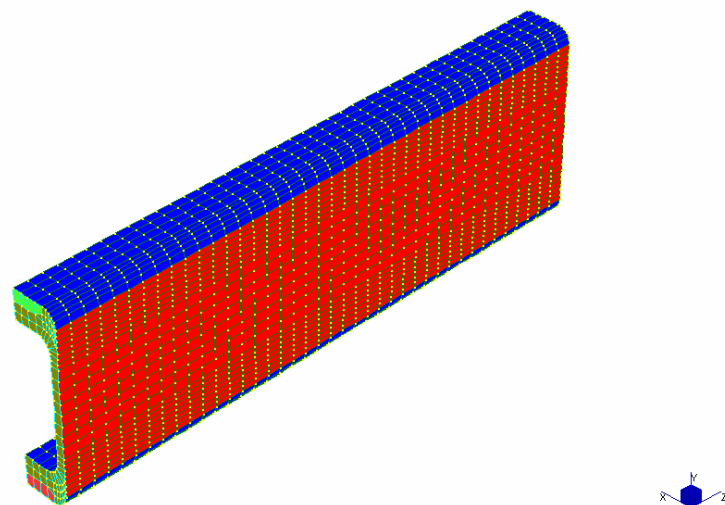


Figure 8.2 Model with orthotropic bricks for flange laminates

Another difficulty encountered with finite element analysis of the present beam relates to the different behaviours in tension and compression of the constitutive materials. For instance, Strand 7 does not allow for different material properties in tension and compression. Therefore, a solution consisting of assigning the compressive properties, tensile properties, and average properties respectively to the compressive laminates, tensile laminates and web laminates, where the position of the neutral axis was unknown, was devised. This approach can be considered suitable for bending, where a fair estimate of the stress distribution can be assumed, however, it is quite impractical for other loadings where the stress distribution cannot be estimated, *à priori*, such as buckling. In these situations, average properties are used throughout.

In addition to the differing material properties in tension and compression, FRPs undergo progressive damage during loading. The damage is due to matrix cracking, fibre-matrix de-bonding and fibre breakage. Algorithms based on continuum damage mechanics have been formulated (Chang et al. 1989) to account for such damage. However, standard FE packages, such as Strand7, do not offer a mechanism to incorporate these algorithms. On the other hand, core cracking may be simulated by the manual removal of brick elements. This could be achieved by running several individual models with increasing number of pre-defined cracks present in the core material. The models are analysed incrementally, and the results compiled. However, the de-bonding at the PFR-laminate interface cannot be modelled with this arrangement. Furthermore, the interaction behaviour between core material and laminates is yet to be quantified, and is the subject of continuing investigation by Ellis & Van Erp (2001). Given the current state of knowledge, this de-bonding behaviour cannot be modelled reliably, regardless of the FEA package chosen.

To determine the practicality of the manual brick elements removal method, it was trailed on one beam. Figure 8.3 shows the core of a model with bricks removed for bending analysis. The spacing of the pre-defined cracks was determined using existing formulations (Humphreys 2001).

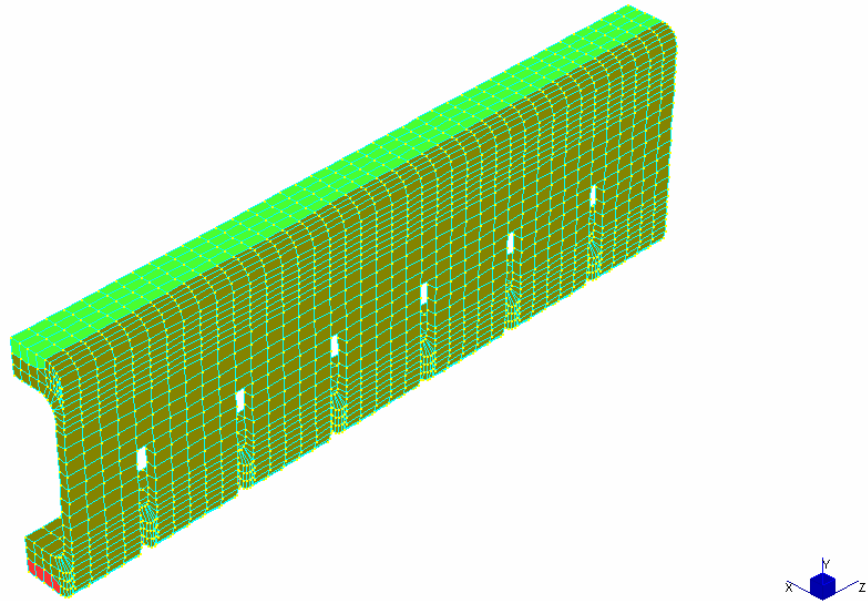


Figure 8.3 Finite element model of the core with brick elements removed to simulate cracking of a beam in bending

The results, shown on Figure 8.4 in the form of tensile and compressive strains, display larger strains and lower failure load when compared to the un-cracked solid models. The method also took a considerable amount of time to manually remove the elements, run the successive analysis and compile the results, making it impractical. In addition, removal of the elements provides no stiffness in the x , y and xy directions, which is not realistic. Furthermore, the removal of the brick elements in the core material causes individual plate elements to span the crack, which causes a problem with convergence of the solution. Therefore, manual removal of bricks was not continued and Strand7 was not further used to predict bending or shear behaviour of beam.

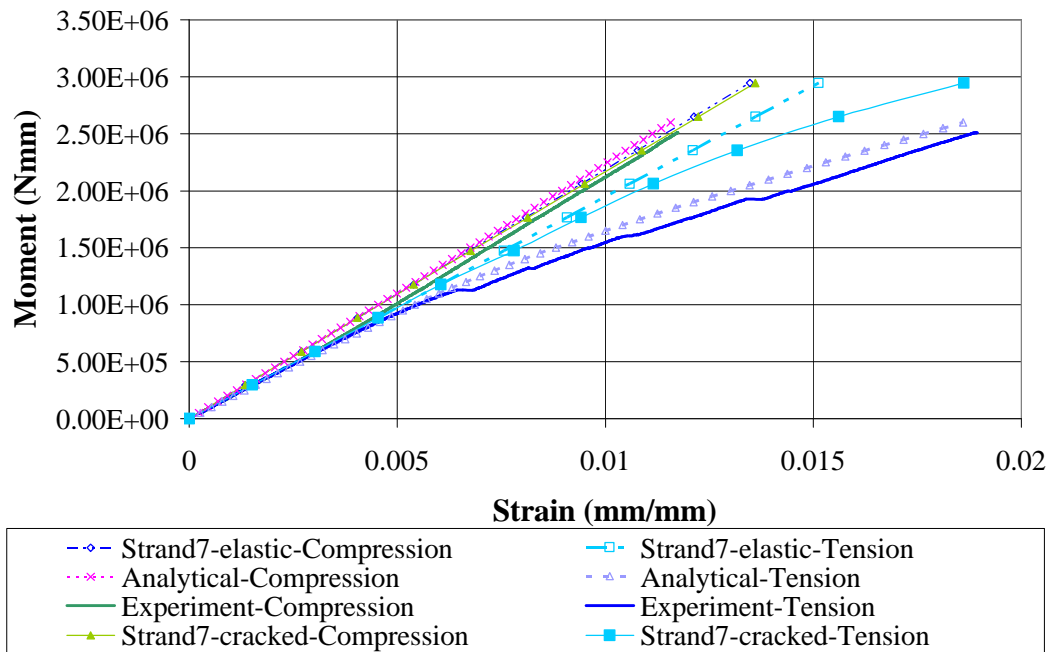


Figure 8.4 Comparison of Strand7, analytical solution, and experimental results

8.2.2.2 Modelling the FRP beam using ABAQUS

Unlike Strand7, ABAQUS is a general finite element software with non-linear capabilities. In particular, whenever a material definition is not supported, the user is provided with the ability to script or use external sub-routines.

Because of the ability to script within ABAQUS, using the Python language (Van Rossum 2002), an algorithm taking into account the progressive damage within the constituents is proposed. To account for the different material properties in tension and compression, a linear elastic analysis with homogeneous properties is run to identify stress states within the beam. Material properties were then assigned correspondingly. Because of changes in the model, caused by modelling the damage at different parts of the beam throughout the analysis, this process is updated at each iteration, depending on the stress states obtained at the previous iteration. The cracking in the core material is modelled using a smeared crack approach. When the strain in the core material exceeds a limiting value, the elastic modulus is put to zero at the offending Gauss point. Damage in the laminates is modelled by means of an external Fortran sub-routine implementing the damage model of (Chang et al. 1989). Furthermore, initial material properties throughout the beam model are varied to imitate the heterogeneous nature of the materials so that stress concentrations may form, providing the sites for crack initiation and laminate failure. A flow chart of the process is given on Figure 8.5.

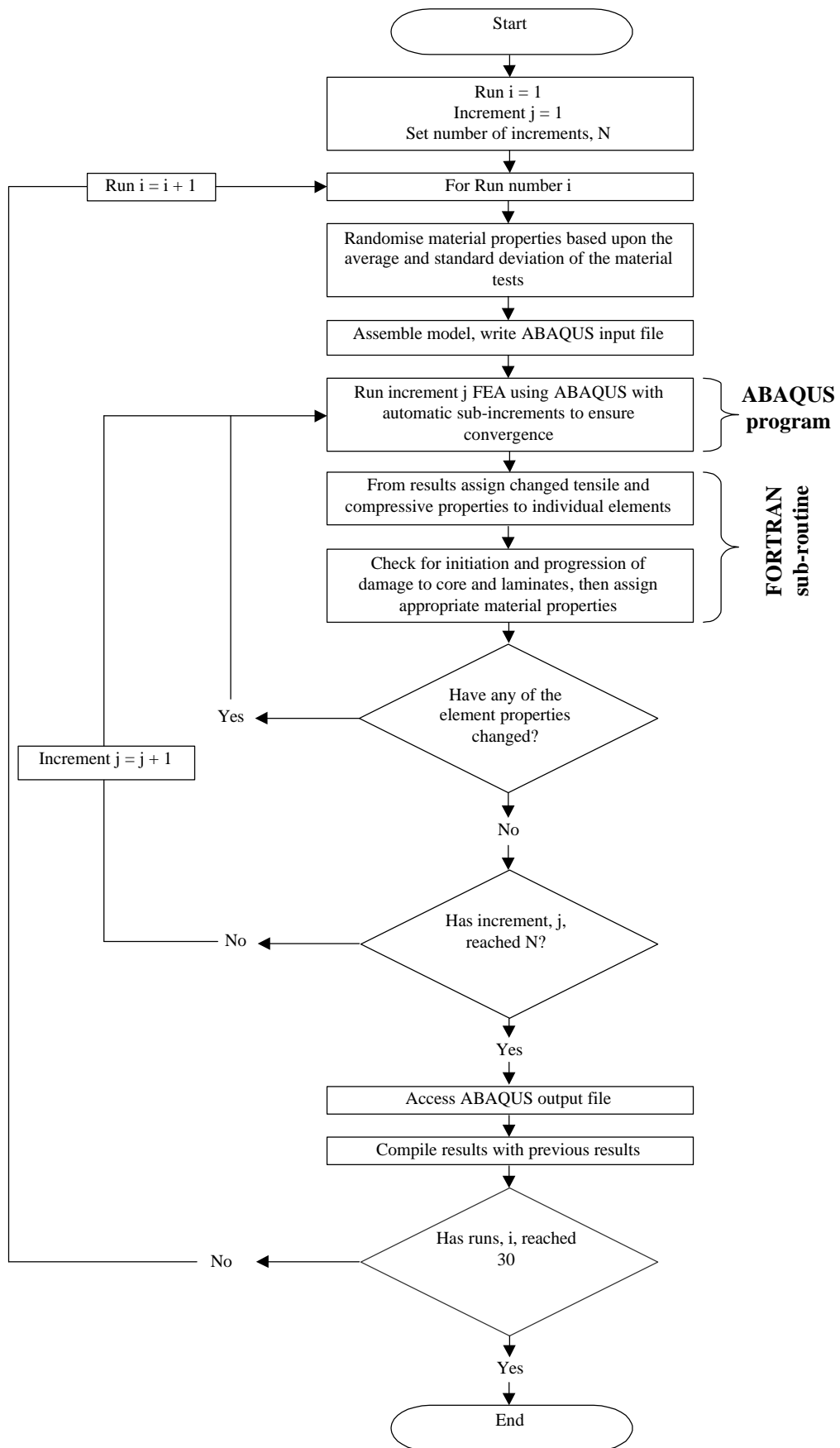


Figure 8.5 Flow chart of Python script

Material properties were randomly assigned to the brick and shell elements in the models. The distribution was based upon the average and standard deviation recorded in testing the laminates and PFR. To ensure that results were statistically valid, 30 models, each with a different randomisation sequence, were analysed for each loading configuration. Both the assigning of tensile and compressive properties, and the modelling of progressive failure was achieved within ABAQUS via a user-defined FORTRAN sub-routine (Appendix F.1). The core material cracking and FRP tensile capacities were based on a maximum strain criterion. To simulate the cracked behaviour of an element, the tensile and shear moduli, respectively parallel and perpendicular to the direction of failure, were re-set to one. The 10 different principal strain states possible, for a brick element, and corresponding material properties are given in Table 8.1.

Table 8.1 Material properties for failure modelling

Principal strain state C = compression, T = tension, and F = failed in tension			Material properties C = compression modulus, T = tension modulus, ✓ = original non-failed value used, and ✗ = failure value used (1 for E and G , 0 for n)								
e_{11}	e_{22}	e_{33}	E_{11}	E_{22}	E_{33}	n_{12}	n_{13}	n_{23}	G_{12}	G_{13}	G_{23}
C	C	C	C	C	C	✓	✓	✓	✓	✓	✓
T	C	C	T	C	C	✓	✓	✓	✓	✓	✓
F	C	C	✗	C	C	✗	✗	✓	✗	✗	✓
T	T	C	T	T	C	✓	✓	✓	✓	✓	✓
F	T	C	✗	T	C	✗	✗	✓	✗	✗	✓
F	F	C	✗	✗	C	✗	✗	✗	✗	✗	✗
T	T	T	T	T	T	✓	✓	✓	✓	✓	✓
F	T	T	✗	T	T	✗	✗	✓	✗	✗	✓
F	F	T	✗	✗	T	✗	✗	✗	✗	✗	✗
F	F	F	✗	✗	✗	✗	✗	✗	✗	✗	✗

To model the progressive matrix, shear, and compressive failure of the laminates, the existing formulations by Chang et al. (1989), detailed in Appendix F.2, were also incorporated within a user-defined FORTRAN sub-routine. The obtained results for the beam loaded in bending are shown on Figure 8.6. It can be seen that there exists an excellent correlation with both the experimental and analytical results. Furthermore, the FEA and analytical ultimate capacity predictions agree very well with the experimental results.

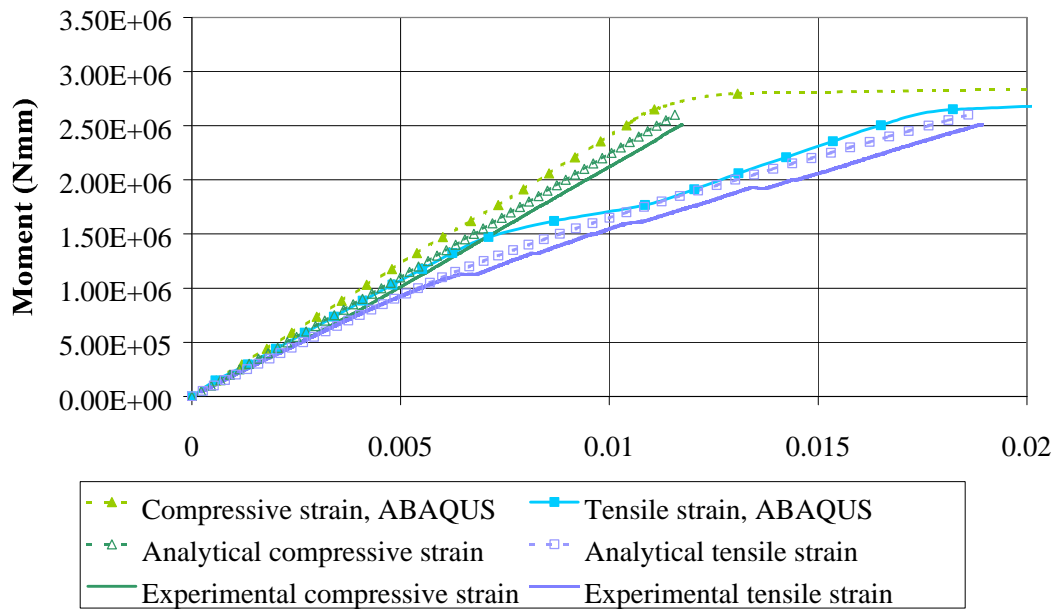
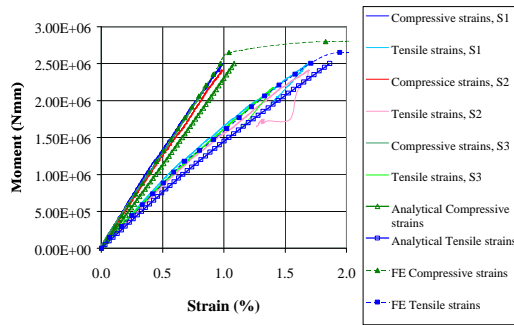
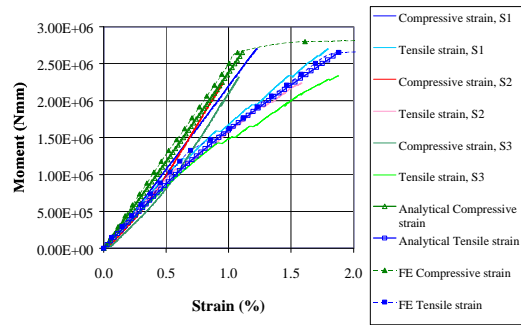


Figure 8.6 FE model versus analytical and experimental results

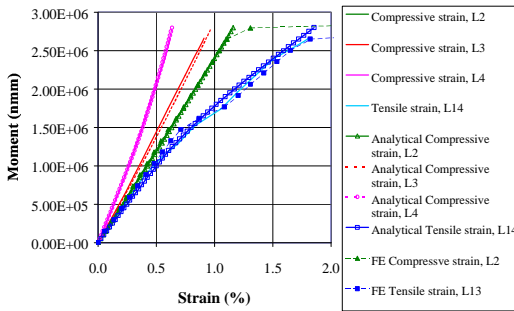
The difference in the analytical and FEA predictions of tensile strains, between moments of $1E6$ to $1.75E6$ $N.mm$ on Figure 8.6, could be attributed to the fact that the FEA model does not provide for core-laminate de-bonding. As mentioned previously, the characterisation of this phenomenon is still under investigation. However, the FEA results converge to the analytical predictions above a moment of $1.75E6$ $N.mm$, which is of prime importance as far as prediction of loading capacity is concerned. As can be seen in Figure 8.7, the FEA predictions are consistent for all the beam geometries tested.



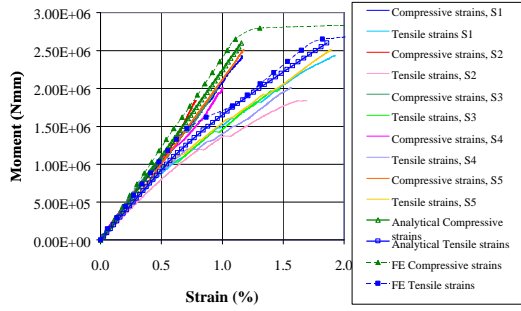
Beam series B4



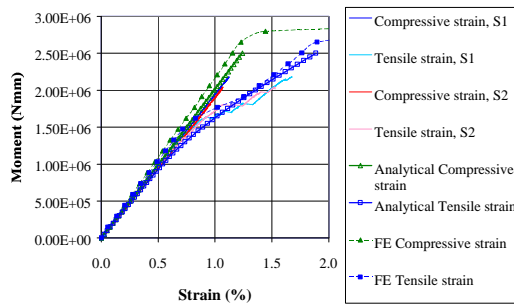
Beam series B5



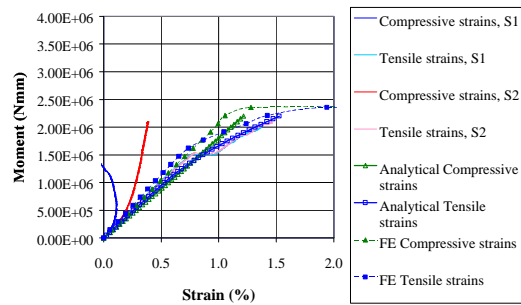
Beam series B6



Beam series B7



Beam series B8



Beam series B9

Figure 8.7 FE model versus analytical and experimental results for changing flange core thickness

8.3 Models under specific loading regimes

8.3.1 General

In the following sections, the algorithm developed above using the ABAQUS software is used to model the beam behaviour in a range of loading regimes.

8.3.2 Moment buckling of the webs

Testing for web buckling required the manufacture and testing of separate web specimens as described in the previous Chapter. These specimens are modelled as per the 4-

point bending testing arrangement. The first buckling mode, as predicted by the model, is shown on Figure 8.8. Comparison of results, as shown on Table 8.2, shows that the analytical and ABAQUS solutions are similar and agree well with the experimental results.

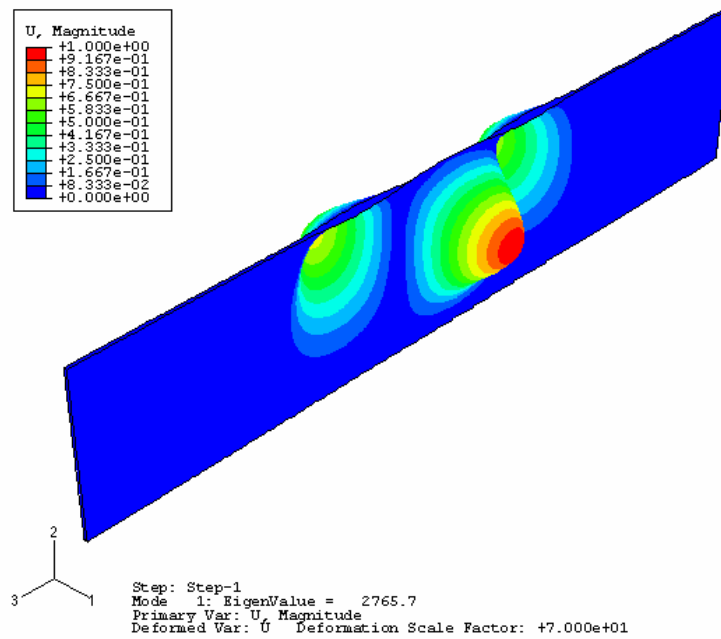


Figure 8.8 Moment buckling of the web specimen

Table 8.2 Moment buckling predictions

	Analytical	FEA	Experimental
<i>Buckling Moment</i> ($\times 10^5 N.mm$)	9.66	9.68	Buckled at: 8.60 Failed at: 9.72

8.3.3 Compression buckling of webs

To study compression buckling, two more web specimens were manufactured and tested as detailed in the previous Chapter. In the testing arrangement, the compressive loads were applied using grip joints, which restrict end rotations. In the FE model, these boundary conditions are modelled as fixed ends.

The first buckling load results are listed in Table 8.3. The FE analysis predicts buckling forces that lie between the simply-supported and fixed-ends boundary conditions used in the analytical analysis. However, the FE results are around 25% lower than the experimentally observed buckling load. This lower prediction could be attributed to the lack

of de-bonding modelling in the FE scripting. As a result, a small number of elements near cracks at the core-laminate interface fail in the models, with a subsequent reduction in local stiffness.

Table 8.3 FE model indicates that true boundary condition of web is between simply-supported and fixed-ends restraints

		Analytical	FEA	Experiments	Analytical
		$k_I = 1$	$k_I = 0.5$	$k_I = 0.5$	$k_I = 0.5$
<i>Buckling Force (N)</i>	ms07-1	1529	3010	4149	6115
	ms07-2	106	245	316	423

8.3.4 Longitudinal cracking of the core in the flanges

Numerical and experimental modelling of punching failure of the laminates required a change in the geometry of the beam to avoid the dominance of other failure modes such as tensile failure. This was achieved by minimising the amount of the core material in the bottom flange. As a result, once loaded in bending, the modified beam fails through punching of the compressive laminates into its hollow core. Figure 8.9 shows the FE model of the modified section. The obtained FE results show excellent agreement with their analytical and experimental counterparts as shown on Table 8.4.

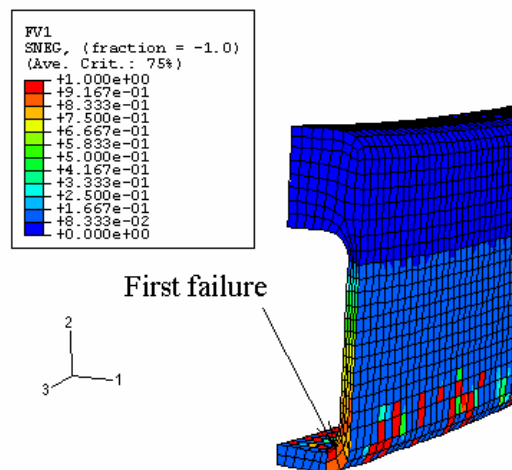
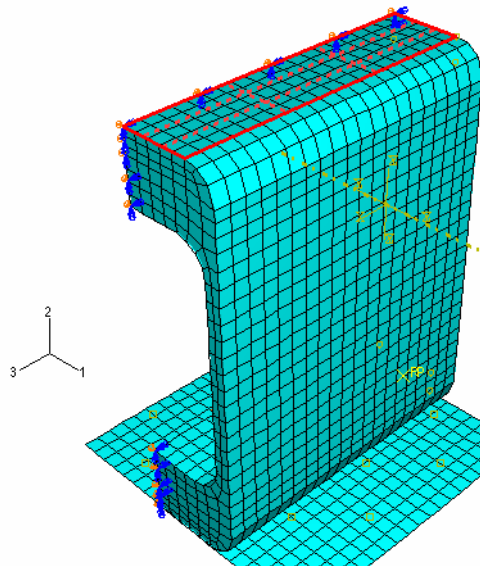


Figure 8.9 Modified beam to force punching shear dominant

Table 8.4 Predictions of punching capacity in modified beam

	FEA	Experiments	Analytical
<i>Failure Load</i> ($\times 10^6$ N.mm)	2.50	2.51	2.65

However, to model cracking of the core in a standard symmetric beam, uniformly distributed compressive loads along the length of the beam, as represented on Figure 8.10, had to be applied to make this failure mode dominant. As a result, the beam is under a state of plane strain, and a strip of the beam as shown on Figure 8.11 is analysed with corresponding boundary conditions. The FE model predictions reported on Table 8.5, show good agreement with the analytical solution and experimental results. Furthermore, failure of the core was predicted to initiate at the web-flange interface as shown on Figure 8.11 and observed in the experiments.

**Figure 8.10** Uniformly distributed load on symmetric beam**Table 8.5** Predictions of PFR failure within the flanges

	FEA	Analytical	Experiments
<i>Failure Load</i> (N/mm)	285	290	299

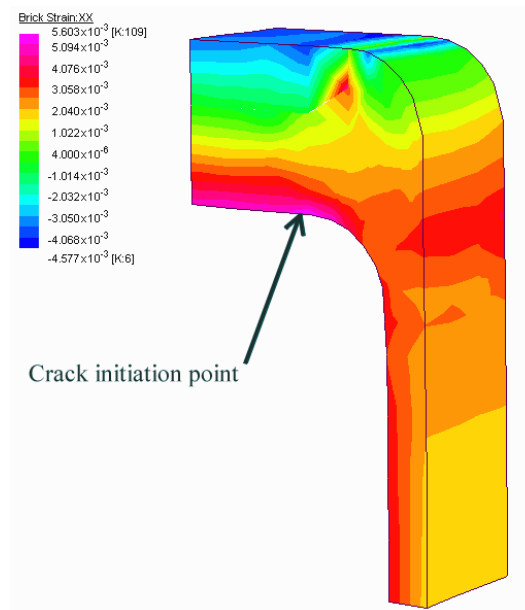


Figure 8.11 FEA results, longitudinal cracking of the core material

8.3.5 Shear

For the determination of shear behaviour, three sets of models were analysed:

- long thin-web specimens to determine the web capacity;
- web specimens for determination of critical buckling capacity; and
- entire beam for prediction of overall performance.

The three models are described below.

8.3.5.1 Web shear strength

Since the webs constitute the main shear bearing elements of the section, separate web specimens designed and tested according to ISO 14129 were modelled. The first consisted of a sandwich structure with the core modelled as brick elements and the laminates as shell elements. This model gave similar predictions of failure loads as those obtained with the analytical solution using the ISO 14129 determined shear capacity of the web laminates. When the web material properties of the model were altered to allow for fibre constraint the analysis resulted in a substantially higher shear capacity, which is identical to the amended analytical prediction, equation (6.43), which is only 10% below the experimentally observed capacity.

Table 8.6 Comparison between web shear models

	Initial analytical, FEA (to ISO 14129)	Amended analytical and FEA	Experiments
<i>Normal failure stress in web specimen (MPa)</i>	100	240	266

8.3.5.2 Shear buckling of the webs

To model shear buckling, a web specimen similar to that used to test for moment buckling, was modelled. The first predicted buckling mode is shown on Figure 8.12. As with moment buckling, comparison of the results, as reported on Table 8.7, shows good agreement between the analytical, FE and experimental results.

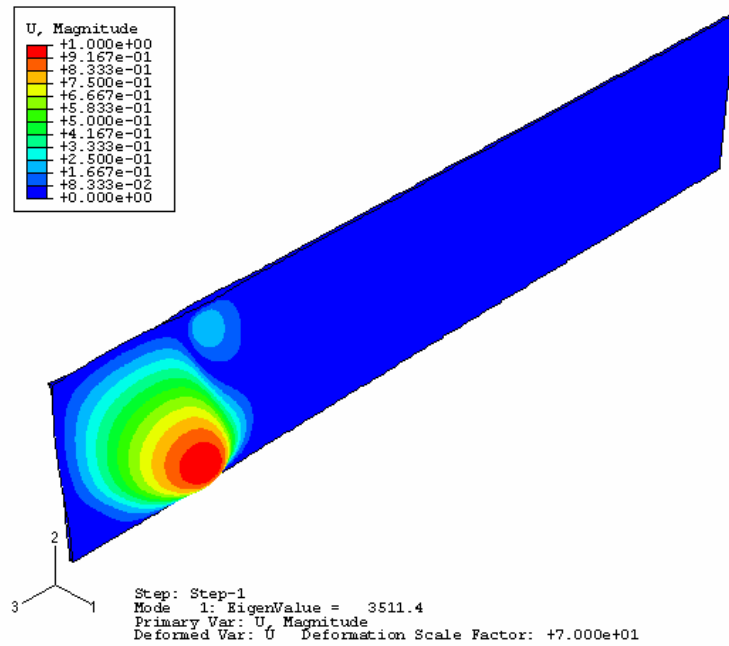


Figure 8.12 Shear buckling of web specimen

Table 8.7 Shear buckling predictions

	Analytical	FEA	Experiments
<i>Shear Load (N)</i>	6871	7023	Buckled at: 7500 Failed at: 9370

8.3.5.3 Overall beam performance

Due to symmetry, only half of the beam is discretised as shown on Figure 8.13.

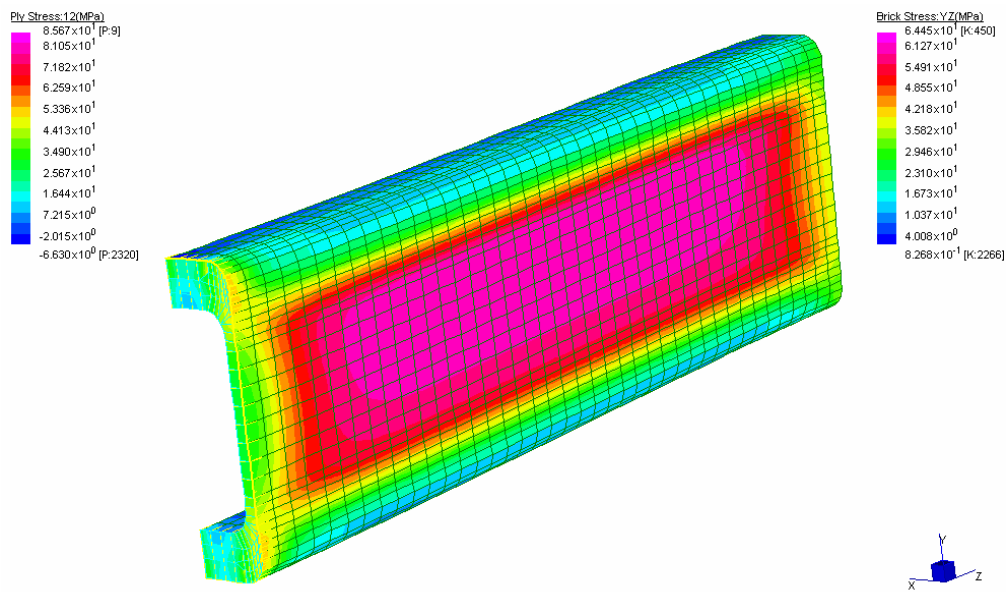


Figure 8.13 FEA results, shear stress throughout beam

The obtained results are shown on Figure 8.14. Again, the FE results show good agreement with the analytical solution. The relatively small discrepancies in the results could be attributed due to the way the used brick elements fail at the interface between core and laminates.

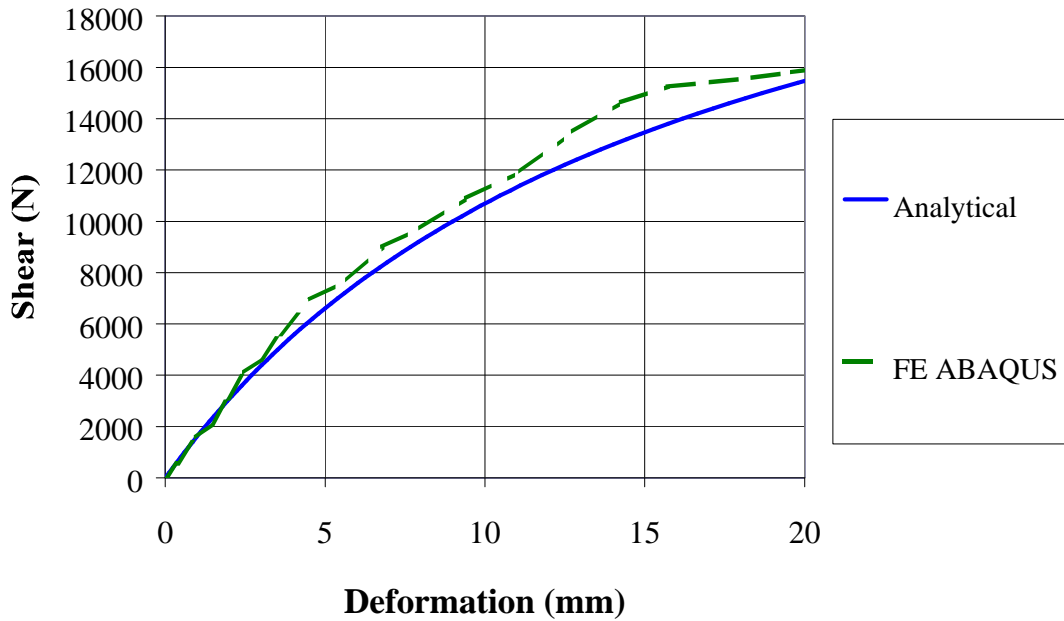


Figure 8.14 Comparison of FE model deflections of the beam under shear loads.

8.3.6 Combined moment and shear

Six beams loaded in 4-point bending were analysed. Due to symmetry, only half spans were modelled. The lengths of the span were successively reduced to obtain the interaction diagrams between moment and shear. Figure 8.15 shows the two extremes of the model geometries.

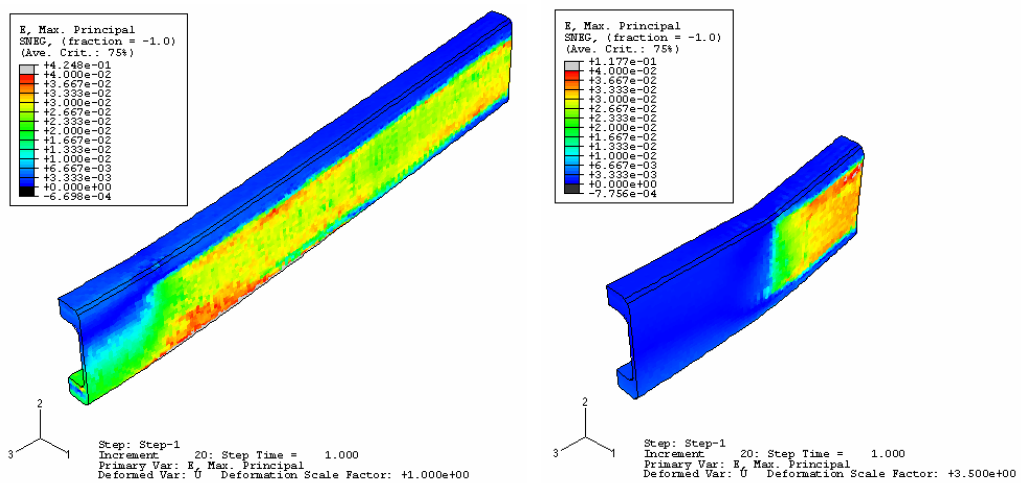


Figure 8.15 Models of 4-point bending.

The obtained failure predictions, together with the analytical and experimental results, are plotted on Figure 8.16. It can be seen that the FEA results reproduce the trend of the experimental shown as dots on the plot. However, the FE results correlate with the analytical results only at either high shear-and-low moment or low shear-and-high moment. Furthermore, the general trend shown by the FE results seems to follow occurrences of cracking in the core material as experimentally observed and modelled in the FE via the fortran subroutine.

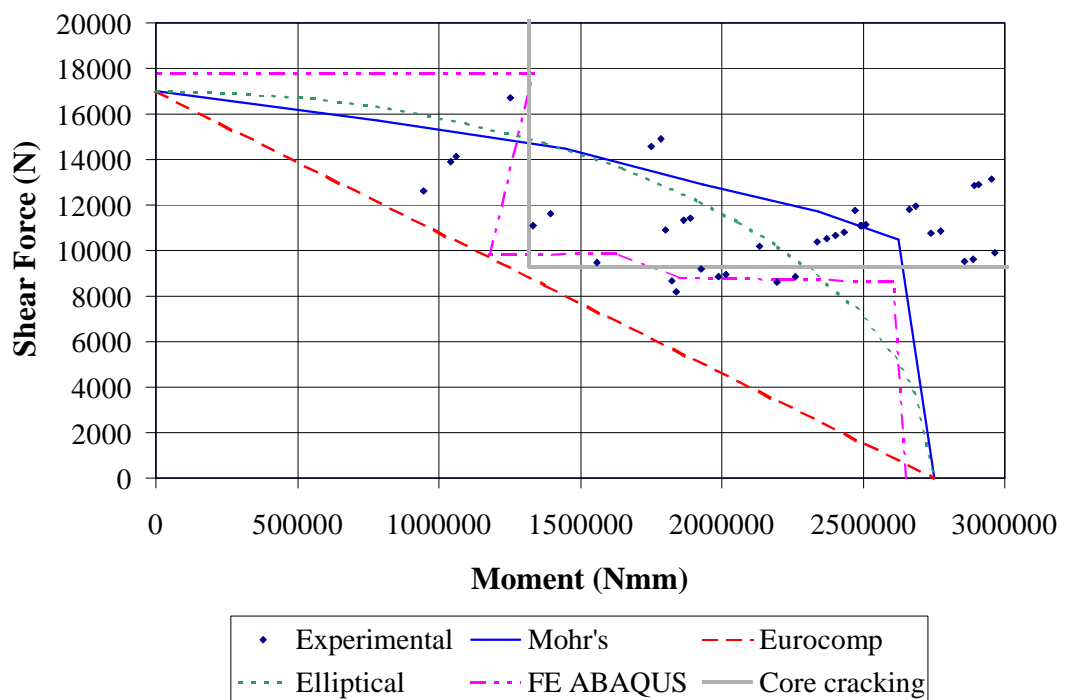


Figure 8.16 Comparison of combined loading models

8.3.7 Lateral torsional buckling

Due to the nature of the torsional response of the beam, no symmetry in modelling was used. This was done to avoid defining complex boundary conditions. Two models, torsion and lateral torsional buckling (LTB), are analysed.

8.3.7.1 Torsion constant

For the first model, one end of the beam was restrained while an arbitrary torque of $2e6 \text{ N.mm}$ was applied to the other end. To reproduce the experimental set-up, the end sections of the beam were restrained from warping. The obtained results, as reported on Figure 8.17, show good agreement with the analytical and experimental results.

Furthermore, the analysis revealed that the cracking of the core has a minimal effect upon torsion response, and the torsion constant is load independent.

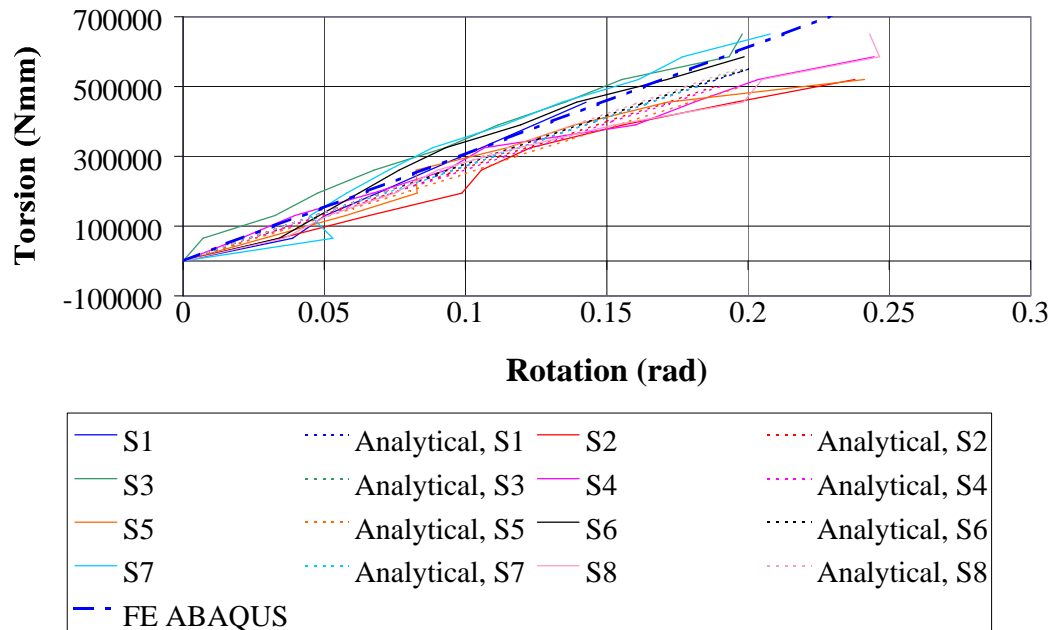


Figure 8.17 Comparison between torsion models showing a linear response

8.3.7.2 Lateral torsional buckling

In line with the experimental set-up, a two-meter long cantilevered beam was modelled. The model was solved to obtain the eigenvalues. Figure 8.18 shows the first predicted buckling mode.

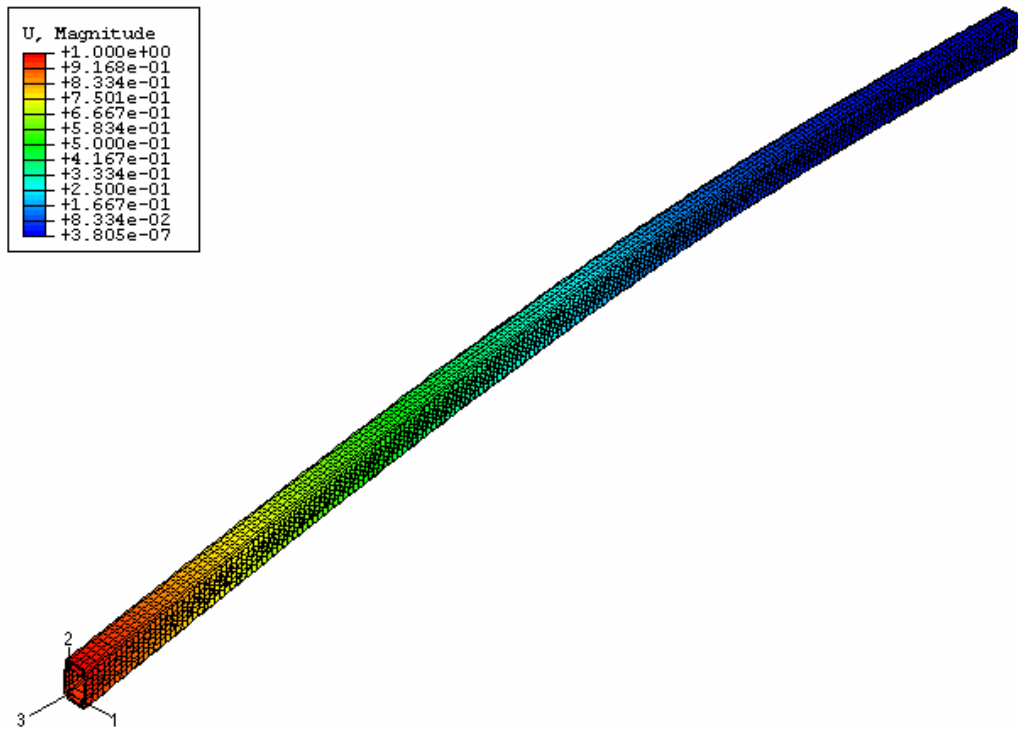


Figure 8.18 Finite element results for first positive eigenvalue

As shown on Figure 8.19, there is some variability between the experimental, theoretical and FEA results. The Eurocomp formulation for FRP beams is substantially lower than the other methods. The remainder of the predictions lie within 27% of each other. The FEA is within 11% of the critical moment as observed in the experimentation.

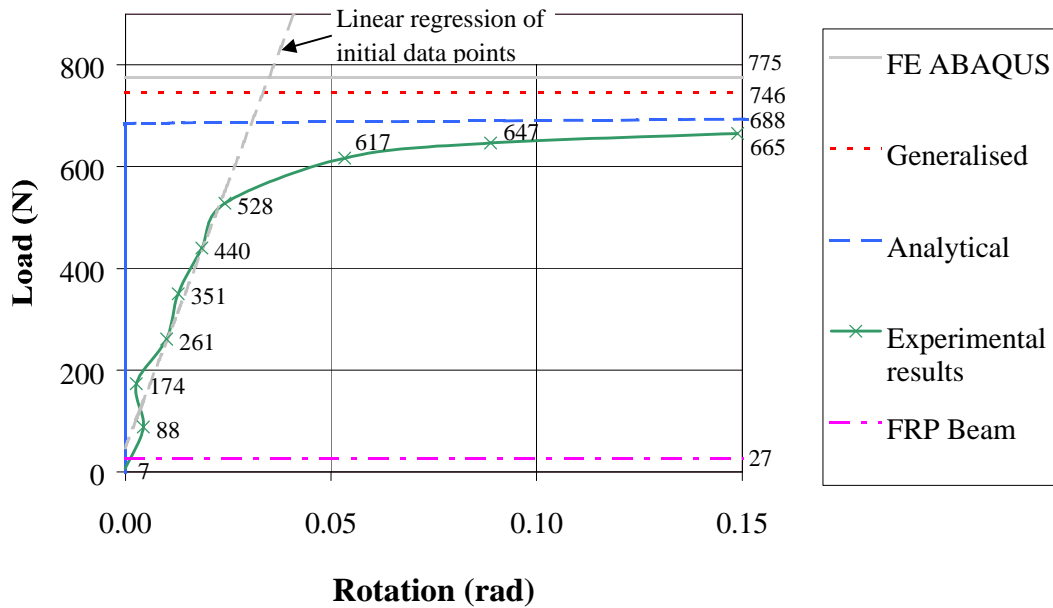


Figure 8.19 Comparison of LTB predictions

8.4 Conclusions

Detailed finite element analysis of the present beam made of a combination of FRP laminates and core material is a very complex task. The formulation of such behaviour is yet to be incorporated in available commercial software. However, with the ability to script and the use of external sub-routines, this complex behaviour, which includes phenomena such as:

- different compressive and tensile properties of the materials;
- core tensile cracking failure prior to ultimate failure of the beam; and
- progressive damage of FRP laminates,

can be incorporated with relative ease in a Python script calling ABAQUS as an FE solver.

The obtained results using the developed algorithm compare well with the analytical and experimental results. In particular, the developed FE approach captured well the synergy between shear and bending better than any other method. Depending on the characterisation of the de-bonding behaviour between the core and the laminate interface, this phenomenon can be easily included in the FE approach.

References

- Ascione, L., Feo, G. & Mancusi, G. 2000, 'On the statical behaviour of fibre-reinforced polymer thin-walled beams', *Composites Part B: engineering*, vol. 31B, no. 8, pp. 643 - 653.
- Barbero, E. J., Lopez-Anido, R. & Davalos, J. F. 1993, 'On the mechanics of thin-walled laminated composite beams', *Journal of Composite Materials*, vol. 27, no. 8, pp. 806 - 829.
- Chang, F., Lessard, L., Chang, K. & Liu, S. 1989, 'Damage tolerance of laminated composites containing a hole and subjected to tension or compression', in *34th International SAMPE Symposium and Exhibition - Tomorrow's Materials: Today*, Publ by SAMPE, Covina, CA, USA, Reno, NV, USA, pp. 559-568.
- Davalos, J. F. & Qiao, P. 1997, 'Analytical and experimental study of lateral distortional buckling of FRP wide-flange beams', *Journal of Composites for Construction*, vol. 1, no. 4, pp. 150-159.
- Davalos, J. F., Salim, P., Qiao, R., Lopez-Anido, R. & Barbero, E. J. 1996, 'Analysis and design of pultruded FRP shapes under bending', *Composites Part B: engineering*, vol. 27, no. 3/4, pp. 295 - 306.
- Ellis, G. E. & Van Erp, G. M. 2001, 'Right angle fibre composite joints for civil engineering applications', in *Technology Convergence in Composites Applications*, eds. S. Bandyopadhyay, N. Gowripalan & N. Drayton, University of New South Wales, Sydney, Australia, pp. 102-110.
- G+D Computing, 'Strand7', 2000, ver 1.5.3, G+D Computing, Sydney.
- Haj-Ali, R. & Kilic, H. 2002, 'Nonlinear behavior of pultruded FPR composites', *Composites Part B: engineering*, vol. 33, pp. 173 - 191.
- Hibbitt, Karlsson & Sorensen Inc., 2002, 'ABAQUS', ver 6.3.1, Hibbitt, Karlsson & Sorensen, Inc., Pawtucket.
- Humphreys 2001, *Crack propagation in PFR*, University of Southern Queensland, Toowoomba.
- Taufik, A., Barrau, J. J. & Lorin, F. 1999, 'Composite Beam Analysis with Arbitrary Cross Section', *Composite Structures*, vol. 44, pp. 189-194.
- Van Rossum, G., 'Python', 2002, ver 2.2.2, Python Software Foundation

Chapter 9 Conclusions and recommendations

9.1 Review of research

The purpose of this thesis was to develop, test and analyse a new FRP beam that would suffer less from second-order failures than traditional FRP beams and whose behaviour could be readily predicted. First a review of existing FRP beam designs was presented in Chapter 3. It was found that most beams, manufactured solely from FRP, suffered some form of deficiency in structural behaviour, with second-order failures being predominant. These failure modes are due to geometric design of the section and manufacturing techniques. Currently, the most successful section designs are those that combine FRP with a core material, such as concrete. These concrete-filled beams appear to have solved many problems inherent to existing designs. However, bonding of the concrete to the FRP has emerged as a major concern of this concept. Replacement of cementitious concrete with polymer concrete appeared to be a promising solution.

In addition to an optimum section design, reliable and comprehensive lower-bound predictive models must also be made available for FRP beams before they will be accepted by the civil engineering community. The state of FRP beam analysis and design methodologies, used for civil engineering structures, was reviewed in Chapter 4. It was found that the tailorability of composite material could be more of an inconvenience than an advantage when developing a general methodology that can be universally adopted for the diverse prototypes being designed. Nevertheless, it appears that the use of the three combined engineering section properties, namely EI , GA and GJ , provides an acceptable and coherent modelling approach applicable for the civil engineering field. Unfortunately, it was also found that even this somewhat simplified analysis requires experimental determination of the engineering section constants.

Drawing upon the knowledge gained in the literature review, a new FRP beam design, addressing the shortcomings of existing beams, was developed. The new beam incorporates FRP and a sturdy PFR core material. The design, the materials used, as well as the manufacturing techniques were reviewed in Chapter 5. In order to optimise the design, an analytical model of its behaviour was presented in Chapter 6. The model is based on classical beam theory. The engineering section properties were determined using the transformed-section approach. The cracking of the core material was modelled through an altered-stiffness approach commonly used to model reinforced-concrete structures. The

model revealed that secondary failure modes have all one parameter in common: core thickness. As a result, they all can be prevented by the judicious placement of the core material within the flanges and webs, leaving the beam to fail in the primary tensile failure mode by rupture of the tensile laminates.

To validate the analytical model and increase the understanding of the structural behaviour of this new beam design, a comprehensive experimental program was undertaken as described in Chapter 7. It was found that the analytical model agreed relatively well with the experimental results, thus validating the underlying assumptions. In particular, the tests revealed that the placement of the core material in the webs and flanges averted most of the secondary failure modes. The tests also revealed that the pure shear capacity of the web laminates was governed by fibre fracture, not fibre pull-out as was generally assumed. Altering the analytical model to account for this fibre failure under shear provided good agreement with the experimental results. A further finding was that the core within the webs caused a premature failure under a combined loading of moment and shear. This complex phenomenon combining cracking, crushing, de-bonding and buckling in the webs under moment and shear was beyond the simple analytical formulation. To investigate this complex behaviour further a detailed non-linear finite element analysis of the beam was carried out. The analysis combined the scripting power of the Python language with the non-linear analysis ability of the ABAQUS software to incorporate the different compressive and tensile properties of the materials, the tensile cracking in the core material, and the progressive damage in the FRP laminates. The obtained results compared well with the experimental and analytical results. In particular, the developed FE approach captured well the synergy between shear and bending better than any other method.

9.2 Main findings

The major findings of this study can be summarised as follows:

- Beams manufactured solely from FRP often fail via a second-order failure mode such as flange or web buckling, delamination of laminates, or collapse at point loads.
- A combination of a closed-section design which incorporates a structural core material, such as concrete or particulate filled resin, appears to be a cost-effective method to increase flange and web thickness in order to eliminate second-order failures.

- The addition of the core material to the flanges and webs of the newly-developed beam alleviates the premature buckling failures observed in the existing designs, thus constituting an improvement in overall beam performance.
- Failures from point loads, and combined moment – shear interaction, are dominated by buckling failure due to the cracking of the core material.
- The pure shear capacity of the web laminates is governed by fibre fracture rather than fibre pull-out as is described in codes and the literature.
- The formulae, as described in Chapter 6, show very good agreement with experimental results. These formulae were initially developed for designing the experimental program. In light of this observed accuracy, these formulae could constitute the basis for design of FRP beams.
- The behaviour of the beam is well-described using advanced non-linear finite element analysis that incorporates non-linear damage progression in the constituents.
- Predictive models from current design codes were found to be obsolete in some aspects such as shear and moment interaction, which suggests that the development of codes and guidelines is seriously lagging behind, and further research is needed.

9.3 Recommendations for further research

Each loading arrangement investigated in this thesis could, in its own right, constitute a doctoral study. This broad approach was taken in order to ascertain the validity of the new beam so that the fundamentals of the beam behaviour could be established, providing a base from which further research could continue. Accordingly, through the course of this study, it has become apparent that the understanding of a number of areas is limited and requires further investigation. A summary of the key topics identified for further research is provided below.

The present investigation concerned a beam with small dimensions that fitted with the available resources. Throughout the design phases every precaution was taken so as to eliminate size effect. However, this can only be ascertained with the conduct of large scale testing and analysis.

The testing regime was conducted mainly under static loads. The response of the beam under dynamic loading remains to be investigated.

Although some data on the behaviour under sustained load (22 months) has been obtained, it is yet unclear whether these data could be extrapolated to long-term durations in excess of fifty years as common requirements for infrastructure applications. Further research is urgently needed into the durability of composite systems.

Another concern for the design of FRP beams is the provision of connections with other structural elements. Beams are rarely used in isolation, connections to columns and other framing members are required to transfer loads and ensure structural stability. Connecting FRP members presents specific issues due to the nature of failure of FRP, such as bearing failure of one bolt in a bolt group and delamination of connecting angles.

The core material exhibited a non-linear response to tensile loadings. This was modelled in this study by fitting a curve to the experimentally-obtained data. However, the mechanisms of its behaviour, particularly its response under sustained loading, are yet to be fully understood, and the development of a material behaviour law is required. For instance, the capacity of the FRP beam when undergoing combined moment and shear loading appeared to be limited by web failures due to the core cracking. It is apparent that the beam becomes unstable once moment and shear cracking occur simultaneously. The mechanisms involved are complex and were not investigated herein. Detailed investigation of the cracking mechanisms in the core material within the webs may provide improvements in design.

Appendices

Appendix A. Classical Laminate Theory

Using small displacement theory we have for each ply:

$$\{\mathbf{e}\} = [S]\{\mathbf{s}\} \dots\dots\dots (A.1)$$

Where:

$\{\boldsymbol{\varepsilon}\}$ = average strain;

$[S]$ = strain-stress stiffness matrix,

$$[S] = \begin{bmatrix} \frac{1}{E_{11}} & \frac{-\nu_{21}}{E_{22}} & 0 \\ \frac{-\nu_{12}}{E_{11}} & \frac{1}{E_{22}} & 0 \\ 0 & 0 & \frac{1}{G_{12}} \end{bmatrix};$$

E_{11} = Modulus of elasticity of the ply in its principal direction;

E_{22} = Modulus of elasticity of the ply in the direction at 90° to its principal direction;

ν_{12} = Poisson's ratio (noting that $E_{11}\nu_{21} = E_{22}\nu_{12}$);

G_{12} = shear modulus; and

$\{\boldsymbol{\sigma}\}$ = average stress.

Rearranging equation (A.1) results in:

$$\{\mathbf{s}\} = [S^{-1}]\{\mathbf{e}\} \dots\dots\dots (A.2)$$

By denoting $[S^{-1}] = [Q]$ equation (A.2) becomes:

$$\{\mathbf{s}\} = [Q]\{\mathbf{e}\} \dots\dots\dots (A.3)$$

Resulting in the stress-strain stiffness matrix:

$$[Q] = \begin{bmatrix} \frac{E_{11}}{1 - \nu_{12}\nu_{21}} & \frac{\nu_{21}E_{11}}{1 - \nu_{12}\nu_{21}} & 0 \\ \frac{\nu_{12}E_{22}}{1 - \nu_{12}\nu_{21}} & \frac{E_{22}}{1 - \nu_{12}\nu_{21}} & 0 \\ 0 & 0 & G_{12} \end{bmatrix} \dots\dots\dots (A.4)$$

The matrix $[Q]$ is in terms of the ply's principal axis. If the ply within the laminate is at any angle, other than 0° , to the global axis, then the above matrix will need to be transformed to give stiffness properties of that ply in the global coordinate system. The transforming is done as follows:

$$[\bar{Q}] = [T^{-1}][Q][R][T][R^{-1}] \dots\dots\dots (A.5)$$

Where:

$[\bar{Q}]$ = transformed stress-strain stiffness matrix;

$[T]$ = transformation matrix,

$$[T] = \begin{bmatrix} \cos^2 \mathbf{q} & \sin^2 \mathbf{q} & 2 \sin \mathbf{q} \cos \mathbf{q} \\ \sin^2 \mathbf{q} & \cos^2 \mathbf{q} & -2 \sin \mathbf{q} \cos \mathbf{q} \\ -\sin \mathbf{q} \cos \mathbf{q} & \sin \mathbf{q} \cos \mathbf{q} & \cos^2 \mathbf{q} - \sin^2 \mathbf{q} \end{bmatrix};$$

\mathbf{q} = angle between plies principal axis and laminate global axis; and

$[R]$ = conversion matrix from tensor strain to engineering strain,

$$[R] = \begin{bmatrix} 1 & 0 & 0 \\ 0 & 1 & 0 \\ 0 & 0 & 2 \end{bmatrix}.$$

All individual ply matrices can be transformed into the global coordinate system using the above methodology. The individual ply property matrices are combined into an equivalent laminate property matrix. The matrix is termed the ABD matrix, where A, B and D are 3x3 matrices. The values are as follows:

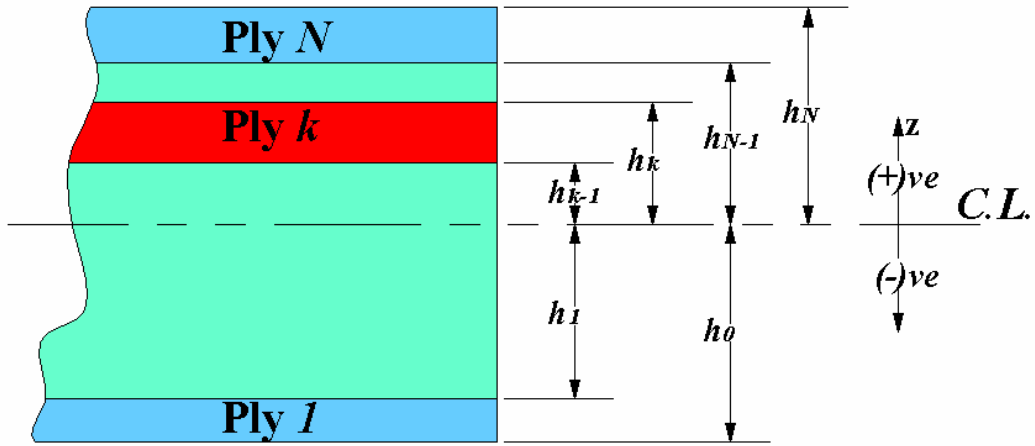


Figure A.1 Measurement of ply in a laminate. (Swanson 1997)

$$A_{ij} = \sum_{k=1}^N (\bar{Q}_{ij})_k (h_k - h_{k-1}) \dots\dots\dots (A.6)$$

$$B_{ij} = \sum_{k=1}^N (\bar{Q}_{ij})_k \frac{h_k^2 - h_{k-1}^2}{2} \dots\dots\dots (A.7)$$

$$D_{ij} = \sum_{k=1}^N (\bar{Q}_{ij})_k \frac{h_k^3 - h_{k-1}^3}{3} \dots\dots\dots (A.8)$$

Where:

k = ply number;

h_k = distance from centroid of laminate to centroid of ply k (mm) (depicted in Figure A.1); and

N = total number of plies in laminate.

The ABD matrix is the equivalent load stress-strain stiffness matrix of the laminate. It is used to calculate the strains and curvatures of the plate laminate from the vector of imposed external forces and moments:

$$\begin{Bmatrix} N \\ M \end{Bmatrix} = \begin{bmatrix} A & B \\ B & D \end{bmatrix} \begin{Bmatrix} \mathbf{e}^0 \\ \mathbf{k} \end{Bmatrix} \dots\dots\dots (A.9)$$

Where:

$\{N\}$ = force column,

$$\{N\} = \begin{Bmatrix} N_x \\ N_y \\ N_{xy} \end{Bmatrix},$$

N_x = normal force in global x direction (N/mm),

N_y = normal force in global y direction (N/mm),

N_{xy} = shear force in global xy direction (N/mm);

$\{M\}$ = moment column,

$$\{M\} = \begin{Bmatrix} M_x \\ M_y \\ M_{xy} \end{Bmatrix},$$

M_x = moment about the x-axis ($N.mm/mm$),

M_y = moment about the y-axis ($N.mm/mm$),

M_{xy} = moment about the xy diagonal ($N.mm/mm$);

ϵ^0 = global strains. (at 0°),

$$\{\mathbf{e}\} = \begin{Bmatrix} \mathbf{e}_x^0 \\ \mathbf{e}_y^0 \\ \mathbf{g}_{xy}^0 \end{Bmatrix}; \text{ and}$$

$\{\kappa\}$ = global curvatures column,

$$\{\mathbf{k}\} = \begin{Bmatrix} \mathbf{k}_x \\ \mathbf{k}_y \\ \mathbf{k}_{xy} \end{Bmatrix}.$$

Once the global strains and curvatures are calculated, it is possible to calculate the total global strains per ply by:

$$\begin{aligned} (\mathbf{e}_x)_k &= -\mathbf{k}_x h_k + \mathbf{e}_x^0 \\ (\mathbf{e}_y)_k &= -\mathbf{k}_y h_k + \mathbf{e}_y^0 \dots\dots\dots (\text{A.10}) \\ (\mathbf{g}_{xy})_k &= -\mathbf{k}_{xy} h_k + \mathbf{g}_{xy}^0 \end{aligned}$$

Where:

$(\epsilon_x)_k$ = Total global strains on ply k in the x direction;

$(\epsilon_y)_k$ = Total global strains on ply k in the y direction; and

$(\gamma_{xy})_k$ = Total global strains on ply k in the xy direction.

These total global strains can then be transformed to the local axis system for each ply as follows:

$$\begin{Bmatrix} \mathbf{e}_1 \\ \mathbf{e}_2 \\ \mathbf{g}_{12} \end{Bmatrix}_k = [R][T]_k [R^{-1}] \begin{Bmatrix} \mathbf{e}_x \\ \mathbf{e}_y \\ \mathbf{g}_{xy} \end{Bmatrix}_k \dots\dots\dots (A.11)$$

The last step is to calculate the stresses caused by these strains as follows.

$$\{\mathbf{s}\}_k = [Q]_k \{\mathbf{e}\}_k \dots\dots\dots (A.12)$$

Where:

$\{\mathbf{s}\}_k$ = local stress column for ply k (MPa),

$$\{\mathbf{s}\}_k = \begin{Bmatrix} \mathbf{s}_1 \\ \mathbf{s}_2 \\ \mathbf{s}_{12} \end{Bmatrix}; \text{ and}$$

$\{\mathbf{e}\}_k$ = local strain column for ply k (MPa),

$$\{\mathbf{e}\}_k = \begin{Bmatrix} \mathbf{e}_1 \\ \mathbf{e}_2 \\ \mathbf{g}_{12} \end{Bmatrix}.$$

These values of stress can be compared with the failure strength values for the plies.

References

Swanson, S. R. 1997, *Introduction to Design and Analysis with Advanced Composite Materials*, Prentice-Hall Inc., USA.

Appendix B. Production Process

Preparation of unidirectional laminates

The main flange and extra web laminates were made, and allowed to cure at ambient temperature before being cut to size. Typically, reinforcement mats are stacked identically throughout the laminate. The result of such mat arrangement is that it produces laminates with poorly-aligned fibres through the thickness of the laminate as shown on Figure B.1(a). In order to improve fibre orientation within the laminate, alternate mats were inverted as shown on Figure B.1(b). This new technique proved to be advantageous as it reduced excessive waver of the main fibres, and helped keep the laminate compact.

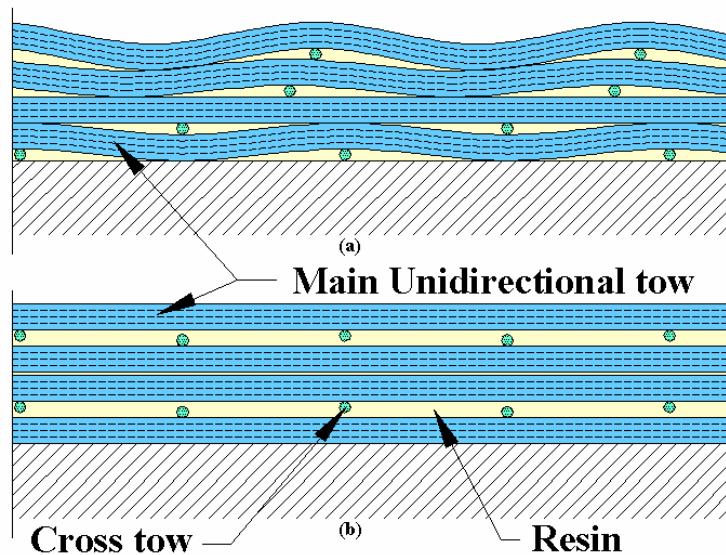


Figure B.1 Unidirectional laminate lay-up sequence

Laying of the inner RHS laminates

The inner RHS laminates were manufactured in a similar way as was described in Section 5.4.2. However, the folding wedge mandrels were made of steel to increase their life-span. The mandrels were cleaned, waxed and buffed prior to assembly. Assembly consisted of sliding the two wedges together while measuring the overall dimension using digital callipers. To avoid adhesion of the laminates to the mandrels, clear plastic sleeves were made and wrapped around them. The inner RHS laminate was then cut and laid (mat infused with resin) over the mandrels in the shape of two overlapping ‘U’s as shown on Figure B.2.

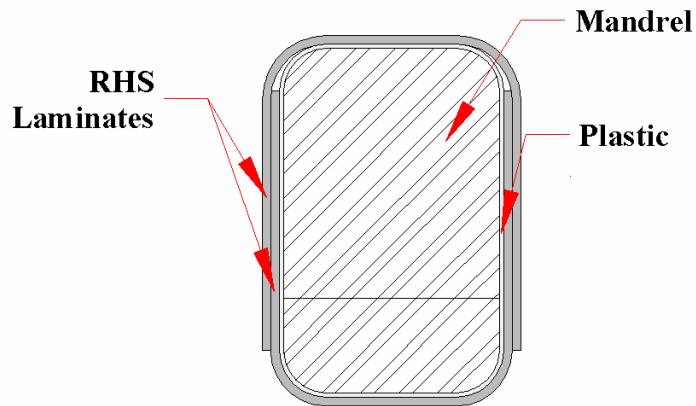


Figure B.2 RHS laminate lay-up

Provision of spacers

During the manufacturing of each set of beams, the PFR mix was proportioned in excess so that a small amount would remain to be used for making spacers for the next series. The excess amount of PFR mix was poured into a container and left to cure. Once cured, the solid block was fixed to a milling machine and cut accurately into slithers for web and flange spacers. Polyurethane foam was also cut for the end flange spacers.

Assembling the mould

Like the mandrels, the steel mould was also cleaned, waxed and buffed, prior to assembly. The mould was manufactured so that the beams were on their side, as this simplified the positioning of the flange and web laminates and increased placement accuracy. The laminates and mandrel were placed in the mould and separated via the use of spacers as shown on Figure B.3. The mould was then closed.



Figure B.3 Mandrels and laminates in mould

To seal the ends of the mould, a mix of very viscous PFR was used as putty. This putty was squeezed in and around the ends of the mould, ensuring a complete seal. The use of a metallic end cover was considered, but such a cover would not have allowed flexibility in mandrel size and placement. The putty in the ends of the mould was left to cure overnight. This method of manufacturing the beams required the inner RHS laminate to cure within the mould overnight, prior to the pumping of the PFR mix the following day. Tests on specimens were conducted and no decrease in bond strength due to this practice was noticed.

Pumping of PFR

The pump used to inject the PFR mix into the moulds had to be designed such that it did not damage the fly-ash micro-spheres within the PFR slurry. Experience at the University of Southern Queensland's Fibre Composite Design and Development Centre has shown that conventional mixing and pumping mechanisms, using helical screw mixers and pumps, caused significant damage to the fly-ash micro-spheres, crushing and grinding them. Subsequent trials using piston pumps showed that these did not cause undue damage to the spheres within the slurry of the PFR. The adopted design, shown on Figure B.4, used compressed air to force a polyurethane foam plunger down the cylinder that was filled with the PFR slurry. A plastic diaphragm was provided at the air inlet side of the pump to act like a balloon to ensure that the air did not mix with and go into saturation with the PFR.

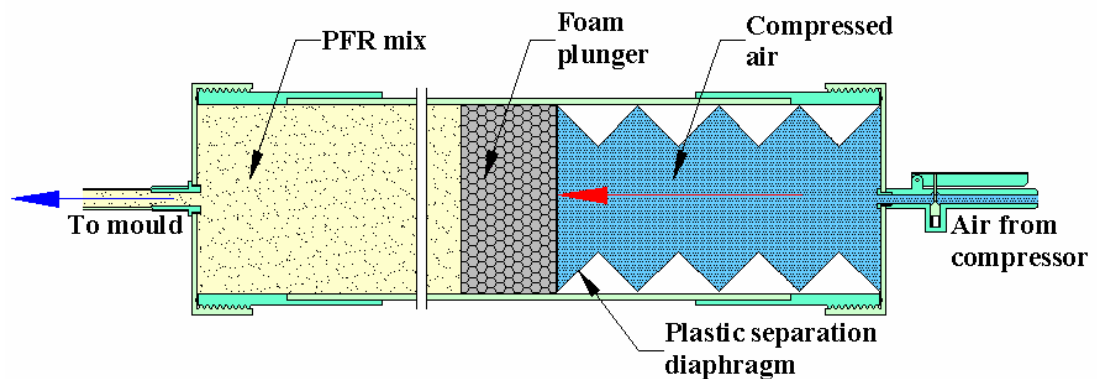


Figure B.4 Pump operation

The PFR slurry was proportioned by weight of resin, hardener and micro-spheres. The constituents were mixed together in a mixing bowl, by hand using a plastic spatula. To ensure that air entrapped in the PFR could be expelled, the pump was filled and left in a vertical position for 15 minutes. The end-cap was then screwed on tightly and the pump was

operated in the vertical position to expel the remaining air from the top of the pump and outlet tube.

The mould had five inlet ports to the bottom steel plate and five outlet ports to the top steel plate, so that each beam was injected independently. The inlet and outlet ports were at opposite ends of each beam. The mould was placed on a slight angle (from horizontal) with the inlet ports to the lower side to ensure that no air was trapped in the mould during pumping. Plastic tubes were attached to the outlet ports to give a visual sign of overflow and to avoid spillage of excess slurry.

The pump was inverted and hung from the ceiling. PFR slurry was injected into each beam until overflow out of the outlet port occurred. Once a beam was complete, the inlet tube was clamped near the inlet port using a G clamp. The tube was then cut and attached to the next inlet port and the procedure repeated until all beams were injected. Figure B.5 shows a photograph of the pumping arrangement.



Figure B.5 Injection moulding

Laying the outer RHS laminates

Once the beams had cured sufficiently they were removed from the mould. They were then lightly sanded and all peel ply material was removed from the web and flange laminates. The exposed surfaces of the beam were cleaned using an acetone-impregnated cloth. The outer RHS laminates were cut and laid over the mandrels in the shape of two overlapping 'U's (orientation similar to that depicted on Figure B.2). The beams were left at ambient temperature to cure for a further 24 hours.

Curing the beams

Figure B.6 depicts the curing cycle recommended by the resin manufacturer to achieve full cure and the best possible mechanical properties. Accordingly, the beams were ambient cured for 24 hours, then oven cured for 8 hours at 80° Celsius with a 2-hour ramp up and down time.

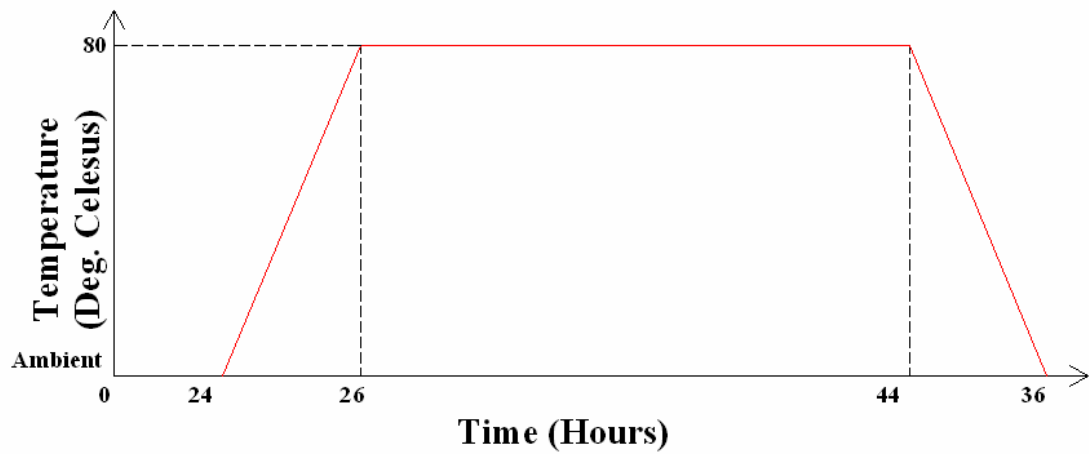


Figure B.6 Curing cycle

Appendix C. Theory

C.1 Transformed section

From experimental data (Section 5.3.3), it had been determined that the modulus of the core material was non-linear and could be modelled by using values of:

$$E_{cc} = 5159 \text{ MPa}$$

and

$$E_{ct} = C_{ta} + C_{tb} \mathbf{e}_t \text{ MPa} \dots\dots\dots (5.1)$$

(the values of the coefficients are given in Section 5.3.3). Once the stiffness of the core is established, the thicknesses of the laminates are calculated as follows:

$$t_i = n_i t_{pi} \dots\dots\dots (C.1)$$

and the widths of the laminates are as follows:

$$w_i = n_i t_{pi} \dots\dots\dots (C.2)$$

Noting the symmetry of the beam:

$$\begin{array}{ll} w_1 = w_{14} & t_1 = t_{14} \\ w_2 = w_{13} & t_2 = t_{13} \\ w_3 = w_{12} & t_3 = t_{12} \\ w_4 = w_{11} & \text{and } t_4 = t_{11} \dots\dots\dots (C.3) \\ w_5 = w_{10} & t_5 = t_{10} \\ w_6 = w_9 & t_6 = t_9 \\ w_7 = w_8 & t_7 = t_8 \end{array}$$

In order to simplify the calculations, the use of a transformed section with a reference modulus of one ($E = 1$) is used. The transformed widths are calculated for laminates in compressive zones as follows:

$$w_{ii} = w_i E_{ci} \dots\dots\dots(C.4)$$

and for laminates in tensile zones as follows:

$$w_{ii} = w_i E_{ti} \dots\dots\dots(C.5)$$

The neutral axis location is then calculated for the cracked section. This is achieved by determining the geometric centroid of the transformed cross-section. The equation is in the following form:

$$A_q c^2 + Bc + C = 0 \dots\dots\dots(C.6)$$

where the parameters are:

$$A_q = w_{t5} + w_{t6} + w_{t7} - w_{t8} - w_{t9} - w_{t10} \dots\dots\dots(C.7)$$

$$B = \sum_{i=1}^4 w_{ti} t_i + \sum_{i=11}^{14} w_{ti} t_i - 2 \left[(w_{t5} + w_{t6})(D - t_1 - t_2 - t_3 - t_4) + Dw_{t7} - (w_{t9} + w_{t10})(t_{11} + t_{12} + t_{13} + t_{14}) \right] \dots\dots\dots(C.8)$$

and

$$C = (w_{t5} + w_{t6})(D - t_1 - t_2 - t_3 - t_4)^2 + w_{t7} D^2 - (w_{t9} + w_{t10}) \left(\sum_{i=11}^{14} t_i \right)^2 + t_1 w_{t1} \left(D - \frac{t_1}{2} \right) + t_2 w_{t2} \left(D - t_1 - \frac{t_2}{2} \right) + t_3 w_{t3} \left(D - t_1 - t_2 - \frac{t_3}{2} \right) + t_4 w_{t4} \left(D - t_1 - t_2 - t_3 - \frac{t_4}{2} \right) + t_{11} w_{t11} \left(t_{14} + t_{13} + t_{12} + \frac{t_{11}}{2} \right) + t_{12} w_{t12} \left(t_{14} + t_{13} + \frac{t_{12}}{2} \right) + t_{13} w_{t13} \left(t_{14} + \frac{t_{13}}{2} \right) + t_{14}^2 w_{t14} / 2 \dots\dots\dots(C.9)$$

Solution is by the following familiar formula:

$$c = \frac{-B \pm \sqrt{B^2 - 4A_q C}}{2A_q} \dots\dots\dots(C.10)$$

Once the neutral axis had been determined, the thicknesses of laminates L_5, L_6, L_7, L_8, L_9 and L_{10} can be calculated as follows:

$$t_5 = t_6 = D - \sum_{i=1}^4 t_i - c \dots\dots\dots(C.11)$$

$$t_7 = D - c \dots\dots\dots(C.12)$$

$$t_8 = c \dots\dots\dots(C.13)$$

$$t_9 = t_{10} = c - \sum_{i=11}^{14} t_i \dots\dots\dots(C.14)$$

so that the second moment of area is calculated as follows:

$$\begin{aligned}
 I = & \frac{\sum_{i=1}^4 w_{ii} t_i^3 + 2 \sum_{i=5}^{10} w_{ii} t_i^3 + \sum_{i=11}^{14} w_{ii} t_i^3}{12} + w_{i1} t_1 \left(dc - \frac{t_1}{2} \right)^2 + w_{i2} t_2 \left(dc - t_1 - \frac{t_2}{2} \right)^2 \\
 & + w_{i3} t_3 \left(dc - t_1 - t_2 - \frac{t_3}{2} \right)^2 + w_{i4} t_4 \left(dc - t_1 - t_2 - t_3 - \frac{t_4}{2} \right)^2 + \frac{\sum_{i=5}^{10} w_{ii} t_i^3}{2} \quad (C.15) \\
 & + w_{i11} t_{11} \left(c - t_{14} - t_{13} - t_{12} - \frac{t_{11}}{2} \right)^2 + w_{i12} t_{12} \left(c - t_{14} - t_{13} - \frac{t_{12}}{2} \right)^2 \\
 & + w_{i13} t_{13} \left(c - t_{14} - \frac{t_{13}}{2} \right)^2 + w_{i14} t_{14} \left(c - \frac{t_{14}}{2} \right)^2
 \end{aligned}$$

Since $E = 1$, therefore $I = EI$.

The calculation of the outer beam strains is then performed as follows:

$$e_t = \frac{Mc}{EI} \dots\dots\dots(C.16)$$

$$e_c = \frac{M(D-c)}{EI} \dots\dots\dots(C.17)$$

and the remaining maximum fibre strains for the laminates are:

$$\begin{aligned}
\mathbf{e}_1 &= \mathbf{e}_c \\
\mathbf{e}_2 &= \mathbf{e}_c (dc - t_1)/dc \\
\mathbf{e}_3 &= \mathbf{e}_c (dc - t_1 - t_2)/dc \\
\mathbf{e}_4 &= \mathbf{e}_c (dc - t_1 - t_3 - t_3)/dc \\
\mathbf{e}_{11} &= \mathbf{e}_t (c - t_{14} - t_{13} - t_{12})/c \dots\dots\dots(\text{C.18}) \\
\mathbf{e}_{12} &= \mathbf{e}_t (c - t_{14} - t_{13})/c \\
\mathbf{e}_{13} &= \mathbf{e}_t (c - t_{14})/c \\
\mathbf{e}_{14} &= \mathbf{e}_t
\end{aligned}$$

The deformation of the beam segment can be determined once the radius and angle of curvature is determined (depicted in Figure C.1). The radius of curvature is calculated as follows:

$$R = \frac{D}{\mathbf{e}_c + \mathbf{e}_t} \dots\dots\dots(\text{C.19})$$

and angle of curvature as:

$$\mathbf{q} = \frac{L}{R} \dots\dots\dots(\text{C.20})$$

so that the deformation of the beam segment is:

$$\Delta_m = R \left(1 - \cos \left(\frac{\mathbf{q}}{2} \right) \right) \dots\dots\dots(\text{C.21})$$

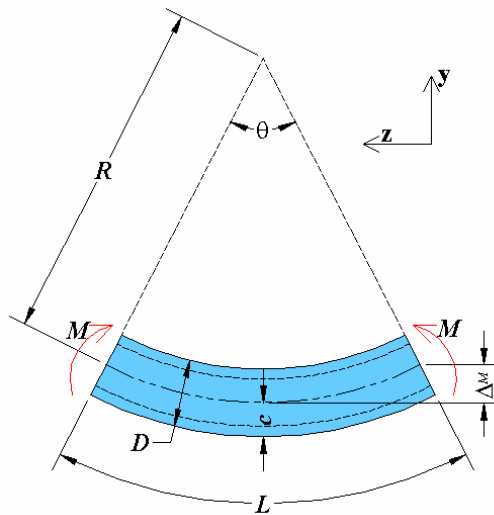


Figure C.1 Curvature of beam undergoing pure moment

C.2 Poisson ratio of the FRP beam web

The longitudinal strain relationship is described by the formulae:

$$\mathbf{n}_x = \frac{\sum_{i=1}^N \mathbf{n}_{xi} z_i E_i}{\sum_{i=1}^N z_i E_i} \dots\dots\dots (C.22)$$

$$\mathbf{n}_z = \frac{\sum_{i=1}^N \mathbf{n}_{zi} z_i}{\sum_{i=1}^N z_i} \dots\dots\dots (C.23)$$

$$\mathbf{e}_{yi} = \left(2 - \frac{\mathbf{n}_x}{\mathbf{n}_{xi}} \right) \mathbf{e}_y \dots\dots\dots (C.24)$$

Where:

Figure C.2 depicts the orientation and;

\mathbf{n}_x = Poisson ratio in the xy direction for entire web;

\mathbf{n}_{xi} = Poisson ratio in the xy direction of laminate i;

\mathbf{n}_z = Poisson ratio in the zy direction for entire web;

\mathbf{n}_{zi} = Poisson ratio in the zy direction of laminate i;

ϵ_y = strain in y direction of entire web;

ϵ_{yi} = strain in y direction of laminate i (taking into account Poisson action);

E_i = Young's modulus of laminate i;

N = total number of laminates;

z_i = thickness of laminate i.

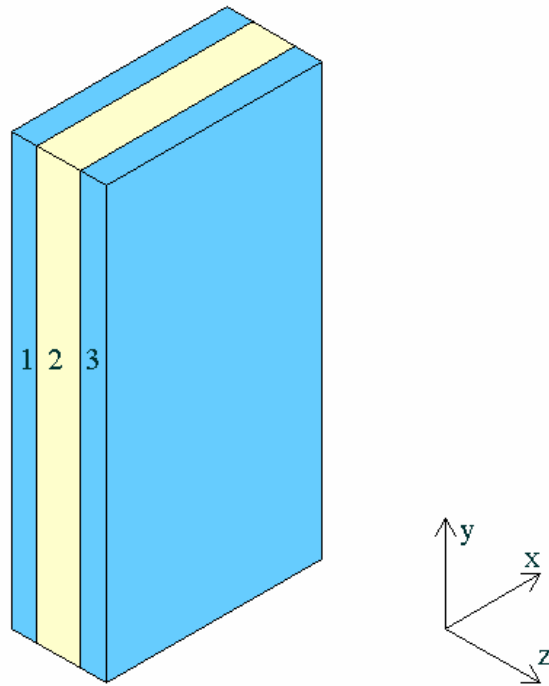


Figure C.2 Laminate orientation

C.3 Derivation of F_w

Figure C.3 is a free body diagram considering the top flange only. A section of that diagram is as in Figure C.4.

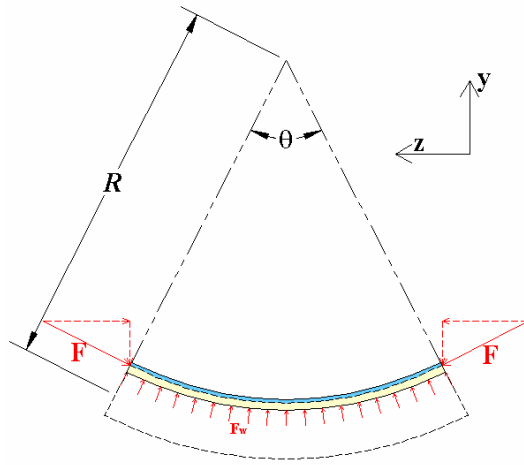


Figure C.3 Curved beam, top flange only

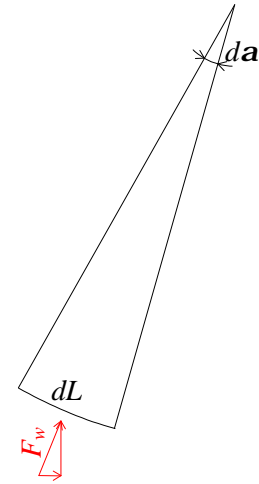


Figure C.4 Section of top laminate

Summation of the forces in the 'y' axis direction results in:

$$\int_0^{\frac{q}{2}} F_w \cos a dL = F \sin\left(\frac{q}{2}\right)$$

where the force in the flange is calculated as follows:

$$F = \sum_{i=1}^4 E_{ci} e_i t_i w_i = E_{t11} e_{11} t_{11} w_{11} + \sum_{i=13}^{14} E_{ii} e_i t_i w_i$$

noting that:

$$da \left(R - (D - c) + \frac{t_f}{2} \right) = dL,$$

therefore:

$$\int_0^{\frac{q}{2}} F_w \cos a \left(R - (D - c) + \frac{t_f}{2} \right) da = F \sin\left(\frac{q}{2}\right)$$

$$\left[F_w \left(R - (D - c) + \frac{t_f}{2} \right) \sin a \right]_0^{\frac{q}{2}} = F \sin\left(\frac{q}{2}\right)$$

$$F_w \left(R - (D - c) + \frac{t_f}{2} \right) \sin \left(\frac{q}{2} \right) = F \sin \left(\frac{q}{2} \right).$$

also noting that

$$R = \frac{EI}{M}$$

results in the following:

$$F_w = \frac{\sum_{i=1}^4 e_i E_{ci} t_i w_i}{\left(\frac{EI}{M} - (D - c) + \frac{t_f}{2} \right)} \dots \dots \dots (C.25)$$

C.4 Flow chart of analytical program for pure bending

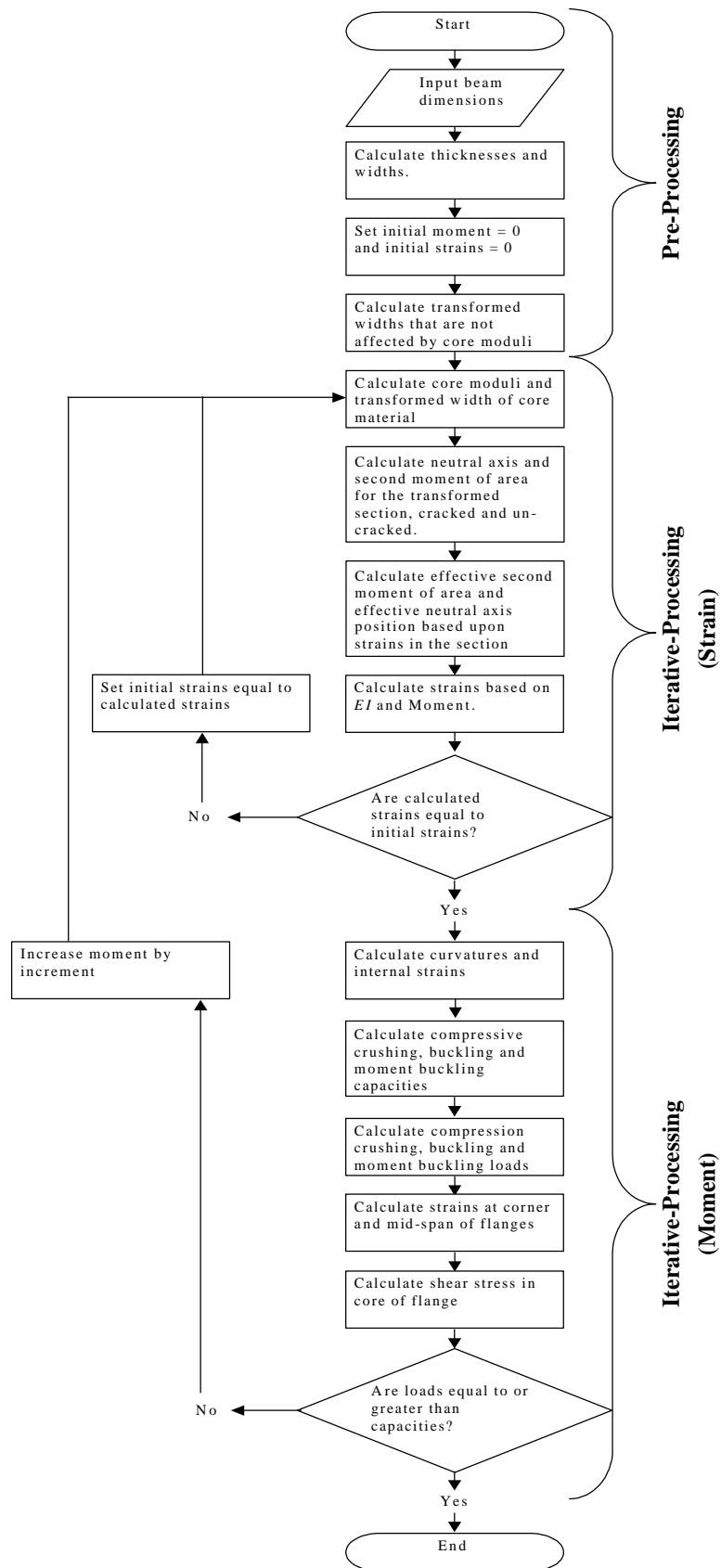


Figure C.5 Flow chart for predicting pure moment behaviour

C.5 Calculation of shear deformation

The equations for shear deformation are derived using the gross section and assuming small deformations theory as follows.

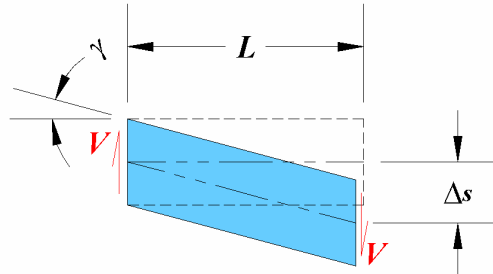


Figure C.6 Shear deformation of a beam segment

From Figure C.6 the shear strain can be estimated by:

$$g \approx \tan g = \frac{dy}{dx} \dots\dots\dots(C.26)$$

where

$$g = \frac{t}{G} \dots\dots\dots(C.27)$$

so that the shear deflection for the segment in Figure C.6 is equal to

$$\Delta_s = gL \dots\dots\dots(C.28)$$

The deflection at mid-span of a simply-supported beam of length L is as follows:

$$\Delta_s = \int_0^{\frac{L}{2}} \left(\frac{t}{G} \right) dx \dots\dots\dots(C.29)$$

An example of a solution is that of a simply-supported beam with uniform distributed load:

$$\Delta_s = \frac{wL^2}{8GA_t} \dots\dots\dots(C.30)$$

The shear modulus (G) was taken as unity in the transformed section.

C.6 Flow chart of analytical program for pure shear

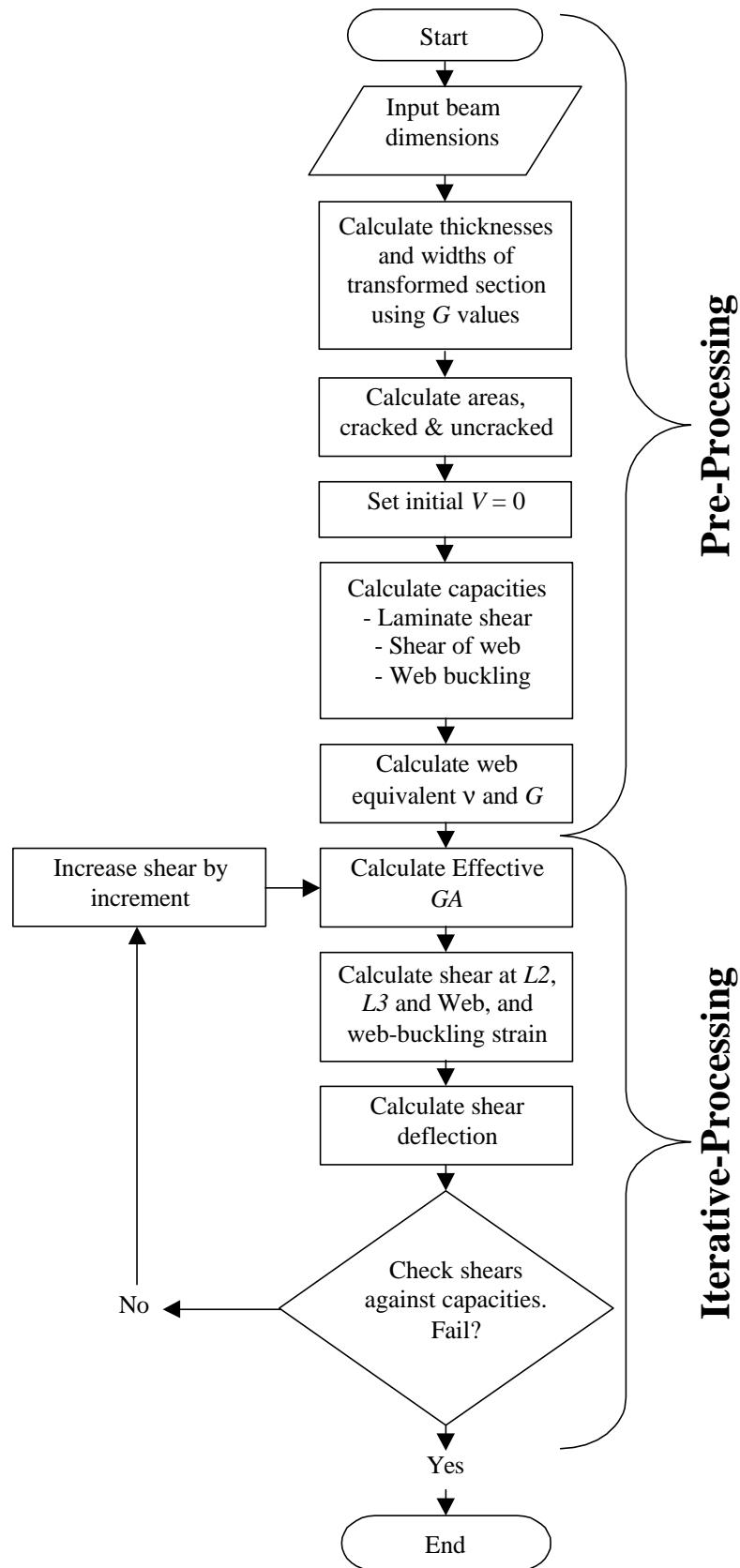


Figure C.7 Analytical flow chart for shear behaviour

C.7 Flow chart of analytical program for combined shear and moment

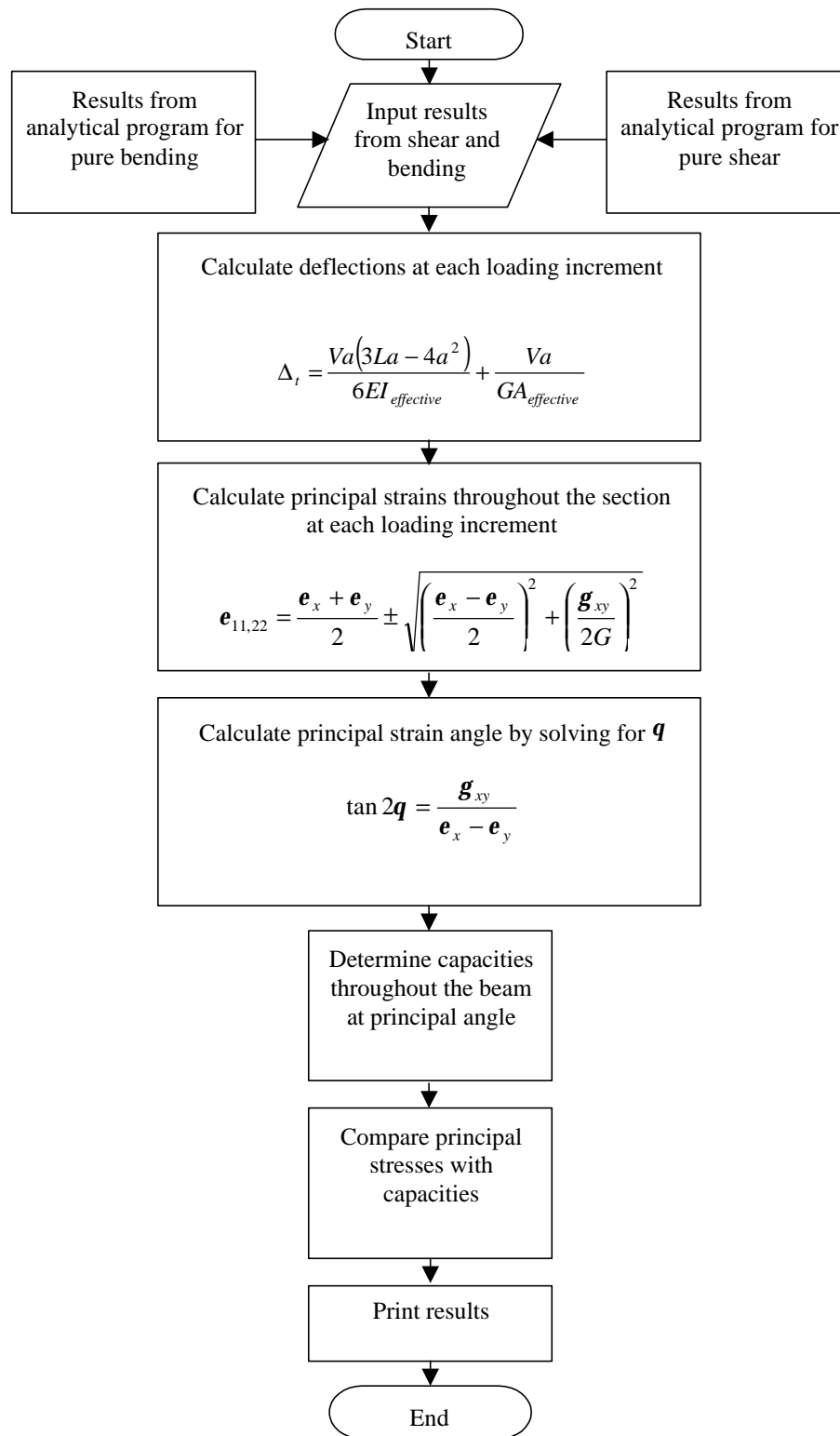


Figure C.8 Analytical flow chart for combined shear and moment behaviour (Mohr's circle)

C.8 Analytical formulation of lateral torsional buckling behaviour

Figure 6.32 depicts the free end of a cantilever beam with an applied load, P

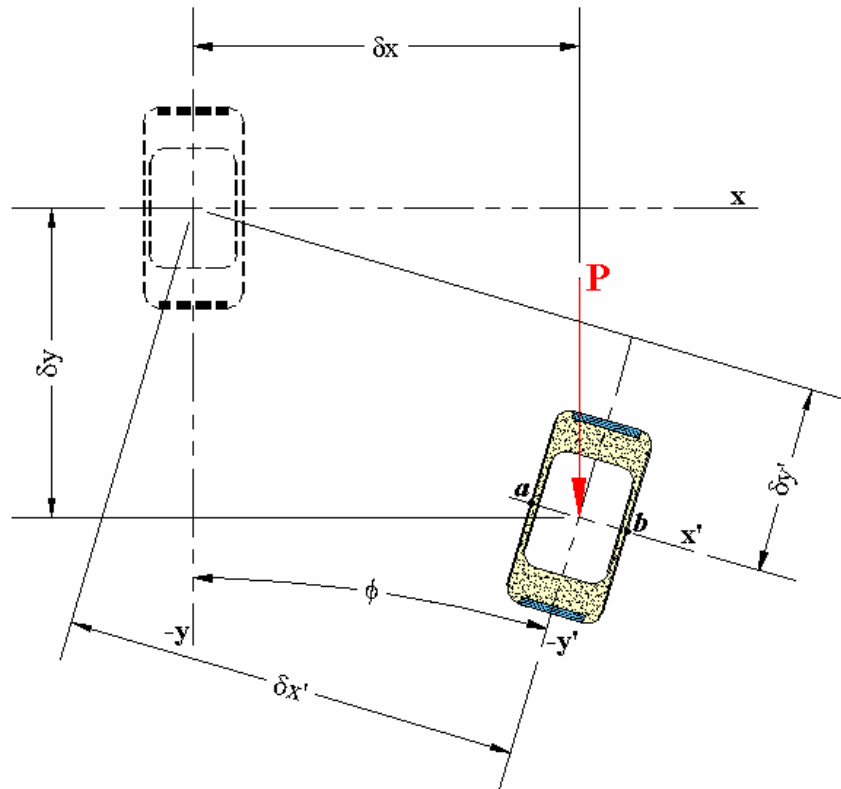


Figure C.9 Deflections of a beam undergoing lateral torsional buckling

The force, P , is resolved into the two component directions x' and y' as shown on Figure C.10.

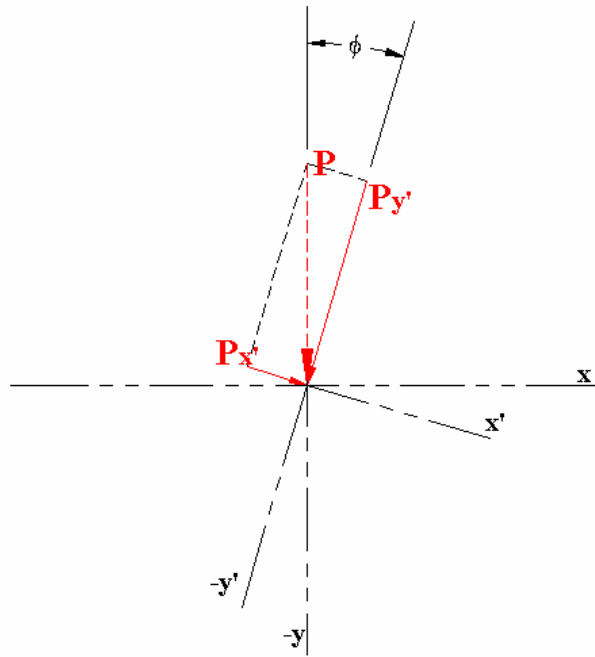


Figure C.10 Force P transformed into the x' and y' component forces

These component forces can be calculated as follows:

$$P_{x'} = P \sin f \dots\dots\dots(C.31)$$

$$P_{y'} = P \cos f \dots\dots\dots(C.32)$$

The deflections caused by these forces, at the end of the beam, relative to the x' and y' axis, are as follows:

$$dx' = \frac{L^3 P_{x'}}{3EI_y} + \frac{P_{x'} L}{GA_s} = P \sin f \left[\frac{L^3}{3EI_y} + \frac{L}{GA_s} \right] \dots\dots\dots(C.33)$$

$$dy' = \frac{L^3 P_{y'}}{3EI_x} + \frac{P_{y'} L}{GA_s} = P \cos f \left[\frac{L^3}{3EI_x} + \frac{L}{GA_s} \right] \dots\dots\dots(C.34)$$

Transposing these deformations, to the original coordinate system, results in:

$$\begin{aligned} dx &= dx' \cos f - dy' \sin f \\ &= \frac{L^3 P \sin f \cos f}{3} \left(\frac{1}{EI_y} - \frac{1}{EI_x} \right) \dots\dots\dots(C.35) \end{aligned}$$

and:

$$\begin{aligned} dy &= dx' \sin f + dy' \cos f \\ &= P \left[\left(\frac{L^3}{3EI_y} + \frac{L}{GA_s} \right) \sin^2 f + \left(\frac{L^3}{3EI_x} + \frac{L}{GA_s} \right) \cos^2 f \right] \dots\dots\dots(C.36) \end{aligned}$$

The average torsion on the deformed beam is obtained by integrating over the length of the beam:

$$T_{average} = \frac{P \int_0^L dx(z) dz}{L} \dots\dots\dots(C.37)$$

and results in:

$$T_{average} = \frac{P}{4} dx \dots\dots\dots(C.38)$$

This torsion is equated to the torsional resistance of the beam as follows:

$$f = \frac{TL}{GJ} = \frac{PdxL}{4GJ} \dots\dots\dots(C.39)$$

Substituting equation (C.39) into equations (C.35) and (C.36) results in:

$$dx = \frac{L^3 P}{3} \sin \left(\frac{PdxL}{4GJ} \right) \cos \left(\frac{PdxL}{4GJ} \right) \left[\frac{1}{EI_y} - \frac{1}{EI_x} \right] \dots\dots\dots(C.40)$$

and:

$$dy = P \left[\left(\frac{L^3}{3EI_y} + \frac{L}{GA_s} \right) \sin^2 \left(\frac{PdxL}{4GJ} \right) + \left(\frac{L^3}{3EI_x} + \frac{L}{GA_s} \right) \cos^2 \left(\frac{PdxL}{4GJ} \right) \right] \dots\dots(C.41)$$

Giving the relationships between load and displacement.

C.9 Flow chart of analytical program for torsion

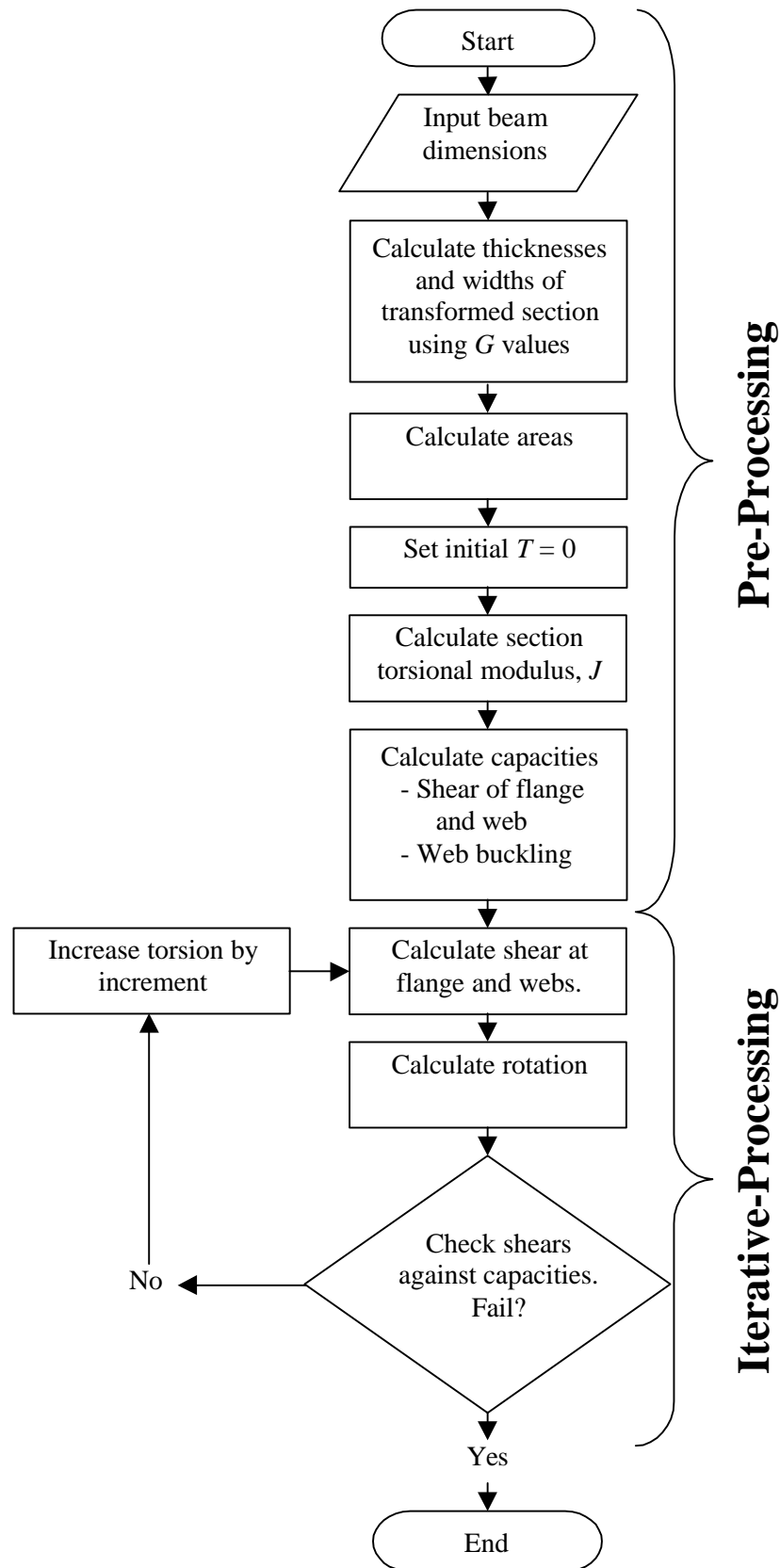


Figure C.11 Flow chart of torsion numerical analysis

C.10 Flow chart of analytical program for lateral torsional buckling

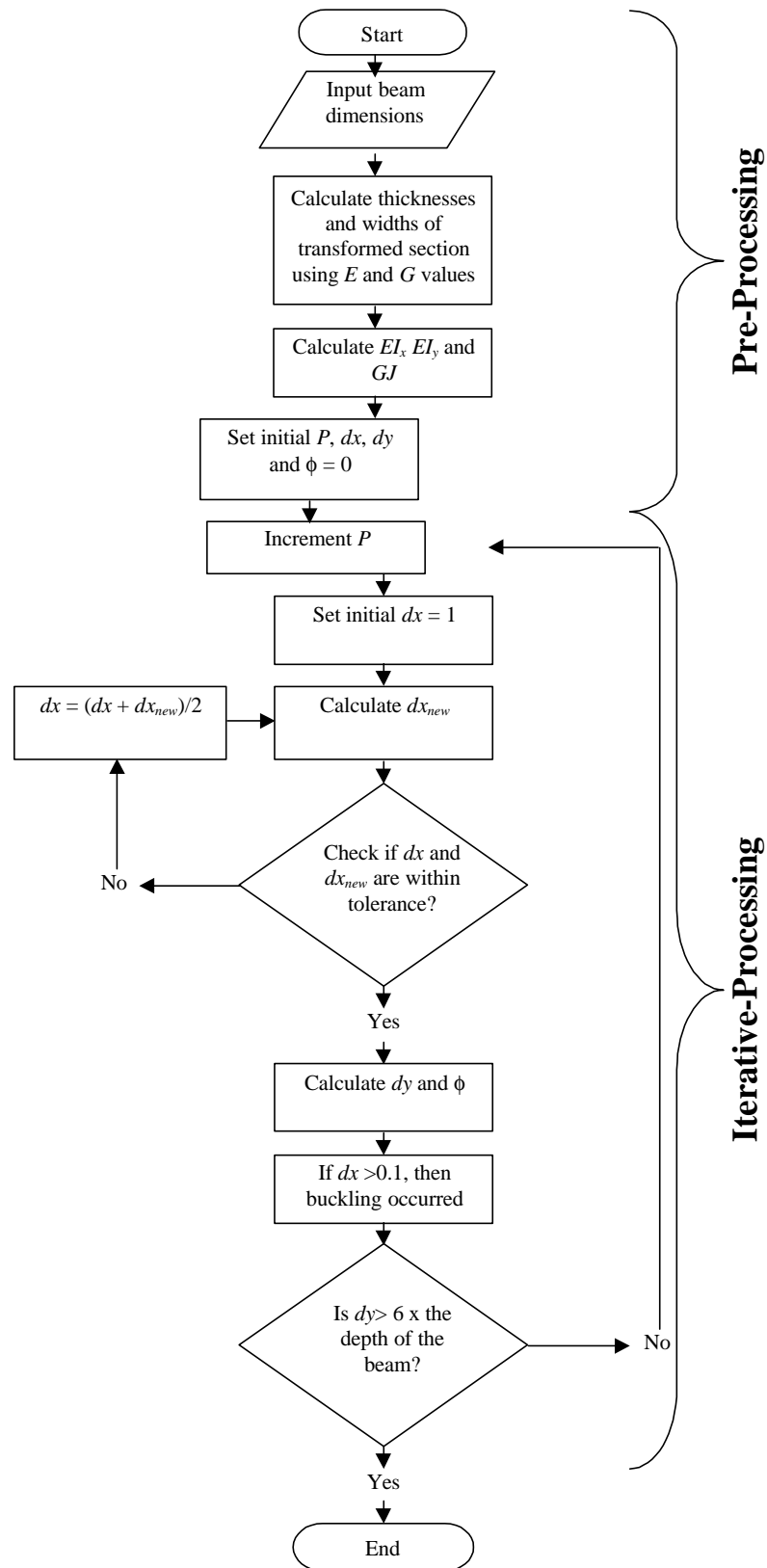


Figure C.12 Flow chart of lateral torsional buckling analysis

Appendix D. Experimentation

D.1 Web buckling

Table D.1 Buckling specimens

<i>Specimen</i>	<i>Width (mm)</i>	<i>Thickness (mm)</i>	<i>Length (mm)</i>
ms07-1-1	25.17	4.54	99.52
ms07-1-2	25.14	4.56	99.48
ms07-1-3	25.11	4.51	99.65
ms07-1-4	25.07	4.56	99.54
ms07-2-1	19.25	3.77	255
ms07-2-2	19.04	3.71	255

Appendix E. Results

E.1 Beams in pure bending

B4 (ms03-b4)

Tests conducted on the 2nd of November 2000. Results are presented in Table E.1.

Table E.1 ms03-b4 results

ms03-b4-1	Maximum load was 22252 <i>N</i> at a moment of 2.503E6 <i>N.mm</i> . Maximum tensile strain 1.685%. First cracking heard at a load of 10280 <i>N</i> . The beam failed prematurely when the tensile reinforcement punched through the core material into the hollow in the beam.
ms03-b4-2	Maximum load was 21436 <i>N</i> at a moment of 2.412E6 <i>N.mm</i> . Maximum tensile strain 1.694%. A faint cracking sound heard at load of 8136 <i>N</i> , loud cracking sound at a load of 10169 <i>N</i> . The beam failed prematurely in the same manner as ms03-b4-1.
ms03-b4-3	Maximum load was 19387 <i>N</i> at a moment of 2.181E6 <i>N.mm</i> . Maximum tensile strain 1.403% Loud cracking sound at a load of 8904 <i>N</i> . The beam failed in a similar manner to ms03-b4-1.

B5 (ms03-b5)

Tests were conducted on the 3rd of November 2000. Results in Table E.2.

Table E.2 ms03-b5 results

ms03-b5-1	Maximum load was 24004 <i>N</i> at a moment of 2.701E6 <i>N.mm</i> . Maximum compressive and tensile strains were 1.222 and 1.793% respectively. First cracking heard at a load of 10840 <i>N</i> . The beam failed via tension reinforcement failure.
ms03-b5-2	Maximum load was 19890 <i>N</i> at a moment of 2.238E6 <i>N.mm</i> . Maximum compressive and tensile strains were 0.734 and 1.579% respectively. A faint cracking sound was heard at load of 4788 <i>N</i> , and a loud cracking sound at load of 9692 <i>N</i> . The beam failed via tension reinforcement failure.
ms03-b5-3	Maximum load was 20755 <i>N</i> at a moment of 2.335E6 <i>N.mm</i> . Maximum compressive and tensile strains were 0.742 and 1.882% respectively. A faint cracking sound heard at load of 7194 <i>N</i> , and loud cracking sound at a load of 12682 <i>N</i> . The beam failed via tension reinforcement failure.

B6 (ms03-b6)

Testing of the beam was conducted on the 2nd of November 2000. Results are in Table E.3.

Table E.3 ms03-b6 results

ms03-b6	Maximum load was 23660 <i>N</i> at a moment of 2.662E6 <i>N.mm</i> . Maximum compressive and tensile strains were 1.048 and 1.8105% respectively. Note that the internal tensile strain gauges broke at first crack. First faint cracking heard at a load of 9582 <i>N</i> . First loud cracks heard at a load of 12352 <i>N</i> . Strain gauges within the tensile area stopped working at first crack. The beam failed via tension reinforcement failure.
----------------	---

B7 (ms03-b7)

Tests were conducted on the 3rd of November 2000. Results are presented in Table E.4.

Table E.4 ms03-b7 results

ms03-b7-1	Maximum load of 21625 <i>N</i> at a moment of 2.433E6 <i>N.mm</i> . Maximum compressive and tensile strains were 0.823 and 1.929% respectively. A faint cracking sound heard at load of 9692 <i>N</i> , loud cracking sound at a load of 12429 <i>N</i> . The beam failed in tension flange due to the failure of the unidirectional reinforcement.
ms03-b7-2	Maximum load of 16359 <i>N</i> at a moment of 1.840E6 <i>N.mm</i> . Maximum compressive and tensile strains were 0.779 and 1.697% respectively. Loud cracking sound at a load of 10611 <i>N</i> . The beam failed in tension flange due to the failure of the unidirectional reinforcement.
ms03-b7-3	Maximum load of 17674 <i>N</i> at a moment of 1.982E6 <i>N.mm</i> . Maximum compressive and tensile strains 0.806 1.468% respectively. Loud cracking sound at a loading of 9067 <i>N</i> . The beam failed in tension flange due to the failure of the unidirectional reinforcement.
ms03-b7-4	Maximum load of 17906 <i>N</i> at a moment of 2.014E6 <i>N.mm</i> . Maximum compressive and tensile strains were 0.6839 and 1.569% respectively. Loud cracking sound at a load of 9681 <i>N</i> . The beam failed in tension flange due to the failure of the unidirectional reinforcement.
ms03-b7-5	Maximum load of 22318 <i>N</i> at a moment of 2.511E6 <i>N.mm</i> . Maximum compressive and tensile strains were 1.175 and 1.892% respectively. Loud cracking sound at a load of 10046 <i>N</i> . The beam failed in tension flange due to the failure of the unidirectional reinforcement.
ms03-b7-6	Maximum load was 26245 <i>N</i> at a moment of 2.488E6 <i>N.mm</i> . Due to a preset software lock, strain readings ceased at 1.6% so maximum tensile strain not known. First cracking heard at a loading of 10809 <i>N</i> . The beam failed prematurely when one of the double bias shear reinforcement plies buckled and delaminated from the rest of the beam due to poor adhesion.
ms03-b7-7	Maximum load achieved was 25708 <i>N</i> at a moment of 2.892E6 <i>N.mm</i> . Software lockout still at 1.6% and an error in the tensile strain gauge was detected, so tensile strain not known. A faint cracking sound heard at load of 7595 <i>N</i> , loud cracking sound at a loading of 15137 <i>N</i> . The beam failed in the tension flange due to the failure of the unidirectional reinforcement.
ms03-b7-8	Maximum load achieved was 21070 <i>N</i> at a moment of 2.370E6 <i>N.mm</i> . Maximum tensile strain 1.496%. Loud cracking sound at a loading of 9860 <i>N</i> . The beam failed in the tension flange due to the failure of the unidirectional reinforcement.
ms03-b7-9	Maximum load achieved was 25845 <i>N</i> at a moment of 2.908E6 <i>N.mm</i> . Software lockout still at 1.6% so maximum tensile strain not known. Loud cracking sound at a load of 12701 <i>N</i> . The beam failed in the tension flange due to the failure of the unidirectional reinforcement.
ms03-b7-10	Maximum load achieved was 22149 <i>N</i> at a moment of 2.492E6 <i>N.mm</i> . Software lockout solved by reducing excitation to 1 Volt. Max tensile strain 1.623% Loud cracking sound at a loading of 10372 <i>N</i> . The beam failed prematurely in a similar way to beam ms03-b3-1.

B8 (ms03-b8)

Tests conducted 3rd of November 2000. Results given in Table E.5.

Table E.5 ms03-b8 results

ms03-b8-1	Maximum load of 19397 <i>N</i> at a moment of 2.182E6 <i>N.mm</i> . Maximum tensile strain 1.6769%. A faint cracking sound heard at load of 8723 <i>N</i> , loud cracking sound at a load of 14189 <i>N</i> . The beam failed in tension flange due to the failure of the unidirectional reinforcement.
ms03-b8-2	Maximum load 18139 <i>N</i> , at a moment of 2.041E6 <i>N.mm</i> . Maximum tensile strain 1.5292%. A faint cracking sound heard at load of 9201 <i>N</i> , loud cracking sound at a load of 11961 <i>N</i> . The beam failed in tension flange due to the failure of the unidirectional reinforcement.

B9 (ms03-b9)

Tests conducted 2nd of November 2000. The results are presented in Table E.6.

Table E.6 ms03-b9 results

ms03-b9-1	Maximum load 17780 <i>N</i> , moment of 2.000E6 <i>N.mm</i> . Maximum tensile strain 1.369% A faint cracking sound heard at load of 11185 <i>N</i> , loud cracking sound at a load of 13283 <i>N</i> . The beam failed prematurely via compressive failure of the flange. The top flange buckled and failed under loading points.
ms03-b9-2	Maximum load 18626 <i>N</i> , moment of 2.095E6 <i>N.mm</i> . Maximum tensile strain 1.4588% A faint cracking sound heard at load of 11574 <i>N</i> , loud cracking sound at a load of 12691 <i>N</i> . The beam failed prematurely via compressive failure of the flange in the same manner as ms03-b9-1.

E.2 Web compression buckling**Table E.7** Web buckling results, series 1

<i>Sample</i>	<i>Length (mm)</i>	<i>Effective length, L_{ef} (mm)</i>	<i>Critical load, P_{cr} (N)</i>
ms07-1-1	99.52	49.76	3970
ms07-1-2	99.48	49.74	3977
ms07-1-3	99.65	49.83	4293
ms07-1-4	99.54	49.77	4355
<i>Average</i>	99.55	49.77	4148.75
<i>95th percentile</i>	99.53	49.77	3971.05
<i>Standard deviation</i>	0.0727	0.0364	203.96

Table E.8 Web buckling results, series 2

<i>Sample</i>	<i>Length (mm)</i>	<i>Effective length, L_{ef} (mm)</i>	<i>Critical load, P_{cr} (N)</i>
ms07-2-1	255	127.5	300
ms07-2-2	255	127.5	332
<i>Average</i>	255	127.5	316
<i>95th percentile</i>	255	127.5	301.6
<i>Standard deviation</i>	0	0	22.627

E.3 Beam crushing

Table E.9 Beam crushing results

<i>ms07-b3 fully loaded compression specimens.</i>			
<i>Beam</i>	<i>Beam length (mm)</i>	<i>Failure load (N)</i>	<i>Failure mode</i>
ms07-b3-1	51.02	15768	Flange core tension fail
ms07-b3-2	50.87	15365	Flange core tension fail
ms07-b3-3	51.14	12752	Flange core tension fail
ms07-b3-4	51.1	16652	Flange core tension fail
ms07-b3-5	50.68	14898	Flange core tension fail

E.4 Web shear capacity

S1 (ms04-1)

These specimens did not have extra tab material near the jaw grips. Specimens tested on the 30th of November 2000. Results are presented in Table E.10.

Table E.10 ms04-1 tab results

ms04-1-1	Failed at a load of 2943 <i>N</i> . The failure was near the support. One side was perpendicular to the load, the other side at 45 degrees to load.
ms04-1-2	Failed at a load of 2627 <i>N</i> . The failure was away from the support. Both sides at 45 degrees to load.
ms04-1-3	Failed at a load of 3549 <i>N</i> . The failure was near the support. Both sides were perpendicular to the load
ms04-1-4	Failed at a load of 3209 <i>N</i> . The failure was near the support. Both sides were perpendicular to the load

S2 (ms04-2)

These specimens had the extra tab material near the jaw grips as shown in Figure 7.23. Tested on the 21st of February 2001. Results are presented in Table E.11.

Table E.11 ms04-2 tab results

ms04-2-1	Failed at a load of 4511 <i>N</i> . First crack at 2599 <i>N</i> . The failure was away from the support and at the location of the first crack. One side was perpendicular to the load, the other side at 45 degrees to load. The initial failure was the fibre failure, this was followed by a twisting of the specimen, delamination of the intact side of the specimen from the core and followed by fibre pull-out of the remaining side.
ms04-2-2	Failed at a load of 4688 <i>N</i> . First crack at 3730 <i>N</i> . The failure was away from the support and at the location of the first crack. One side was perpendicular to the load, the other side at 45 degrees to load. Failure mechanism was similar to ms04-2-1.
ms04-2-3	Failed at a load of 4634 <i>N</i> . First crack at 3900 <i>N</i> . The failure was away from the support and at the location of the first crack. One side was perpendicular to the load for 1/2 the width of the specimen then 45 degrees, the other side at 45 degrees to load. Failure mechanism was similar to ms04-2-1.
ms04-2-4	Failed at a load of 4612 <i>N</i> . No first cracking heard. The failure was away from the support. One side was perpendicular to the load for 1/2 the width of the specimen then 45 degrees, the other side at 45 degrees to load. Failure mechanism was similar to ms04-2-1.

Complete results shown in Table E.12, Table E.13 and Table E.14.

Table E.12 Web shear testing results taking area as total area of specimen

<i>SHEAR TESTS</i>					<i>At 0.1% strain</i>		<i>At 0.5% strain</i>				
<i>Specimen</i>	<i>Average Area (mm²)</i>	<i>Peak Load (N)</i>	<i>Peak Strain (%)</i>	<i>Load at 5% strain</i>	<i>Load (N)</i>	<i>Shear strain (%)</i>	<i>Load (N)</i>	<i>Shear Strain (%)</i>	<i>Shear stress at failure (MPa)</i>	<i>G (MPa)</i>	<i>Failure Mode</i>
ms04-1-1	72.61	2943	1.95	2943	410	0.2	1239	1.08	20.27	648.7	Mixed
ms04-1-2	80.3	2627	1.89	2627	517	0.2	1923	1.00	16.36	1094.3	Mainly shear
ms04-1-3	66.89	3549	2.32	3549	464	0.2	1806	1.00	26.53	1253.9	Fibre fail
ms04-1-4	64.61	3209	6.14	3037	486	0.2	1834	1.00	23.50	1303.9	Fibre fail
<i>Average</i>	71.10	3082	3.08	3039	469	0.2	1701	1.02	21.66	1075.2	
ms04-2-1	102.25	4511	3.08	4511	581	0.1	2329	0.5	22.06	2136.9	Fibre fail
ms04-2-2	103.32	4688	3.31	4688	626	0.1	2456	0.5	22.69	2219.5	Fibre fail
ms04-2-3	102.2	4634	3.61	4634	613	0.1	2386	0.5	22.67	2173.9	Fibre fail
ms04-2-4	101.99	4612	3.62	4612	642	0.1	2438	0.5	22.61	2201.1	Fibre fail
<i>Average</i>	102.44	4611	3.41	4611	616	0.1	2402	0.5	22.51	2182.9	

Table E.13 Web shear results taking only laminate area into account

<i>Taking area as only that of glass fibres</i>					
<i>Specimen</i>	<i>Average Area (mm²)</i>	<i>Peak Load (N)</i>	<i>Peak Strain (%)</i>	<i>Load at 5% strain (N)</i>	<i>Shear stress at failure (Mpa)</i>
ms04-1-1	13.0968	2943	1.95	2943	112.3556
ms04-1-2	13.0628	2627	1.89	2627	100.5527
ms04-1-3	13.0832	3549	2.32	3549	135.6319
ms04-1-4	12.988	3209	6.14	3037	116.9156
ms04-2-1	17.068	4511	3.08	4511	132.1478
ms04-2-2	17.1088	4688	3.31	4688	137.0055
ms04-2-3	17.0748	4634	3.61	4634	135.6970
ms04-2-4	17.1224	4612	3.62	4612	134.6773
<i>Average</i>	15.0756	3847	3.24	3825	125.6229
<i>stnd dev</i>	2.15753	858.0904	1.365640	878.2664	13.81584
<i>95%</i>	13.01418	2738	1.91	2738	104.6837

Table E.14 Web shear specimens including glass stresses

<i>Specimen</i>	<i>Average Area (mm²)</i>	<i>Peak Load (N)</i>	<i>Peak Strain (%)</i>	<i>Load at 5% strain</i>	<i>Shear stress at failure (Mpa)</i>	<i>Glass stress (MPa)</i>
ms04-1-1	13.097	2943	1.95	2943	112	225
ms04-1-2	13.063	2627	1.89	2627	101	201
ms04-1-3	13.083	3549	2.32	3549	136	271
ms04-1-4	12.988	3209	6.14	3037	117	247
ms04-2-1	17.068	4511	3.08	4511	132	264
ms04-2-2	17.109	4688	3.31	4688	137	274
ms04-2-3	17.075	4634	3.61	4634	136	271
ms04-2-4	17.122	4612	3.62	4612	135	269
<i>Average</i>	15.076	3847	3.24	3825	125.6229	266.232
<i>stnd dev</i>	2.1575	858.090	1.366	878.266	13.816	9.930
<i>95%</i>	13.014	2738	1.91	2738	104.684	251.380

E.5 Beams under combined loading of moment and shear

S1 (ms04-b-1)

Figure E.1 depicts the shear strain of the fourth beam. The shear strains within the webs showed a linear response to increases in shear until sudden failure.

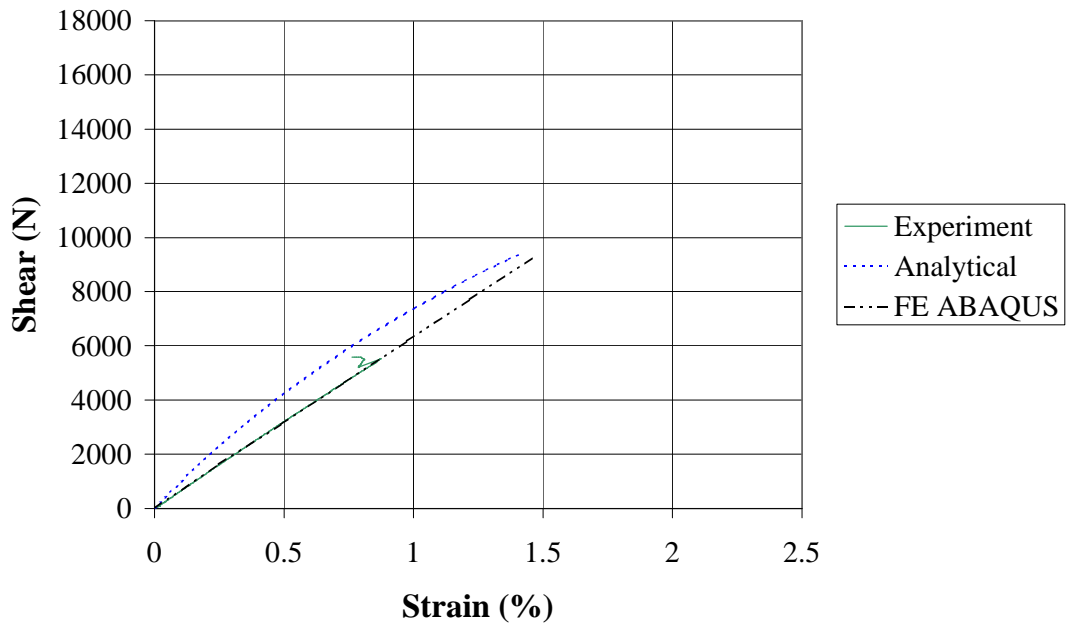


Figure E.1 Experimental shear strains series 1 (Experimental results line up with FE ABAQUS)

Table E.15 ms04-b-1 beam results

ms04-B1-1	First crack occurred at a load of 8820 <i>N</i> . Ultimate failure was of the webs to one side of the beam followed closely by buckling and tearing of the outer RHS laminate. The tearing took place to the tensile side of the beam under the load point. Failed at loading of 19063 <i>N</i> .
ms04-B2-1	First crack at 6550 <i>N</i> . Ultimate failure occurred with buckling of the top RHS laminate and what would appear to be crushing failure of the webs under the loading points. The beam's top laminate failed under the strain gauge. Failed at a loading of 19765 <i>N</i>
ms04-B3-1	First crack at 6250 <i>N</i> . Ultimate failure occurred after warping of RHS laminate and a delamination / longitudinal cracking at web flange interface. This was followed by disintegration of the core web material and a marked increase in shear deformation. Failed at a loading of 19266 <i>N</i>
ms04-B4-1	First cracking at 8300 <i>N</i> . Failure started with a delamination and longitudinal cracking of the RHS laminate at the web flange interface. Ultimate failure (premature) occurred due to a crushing of the web core at the end of the beam. Failed at loading of 11459 <i>N</i>

S2 (ms04-b-2)

The shear strain is shown in Figure E.2.

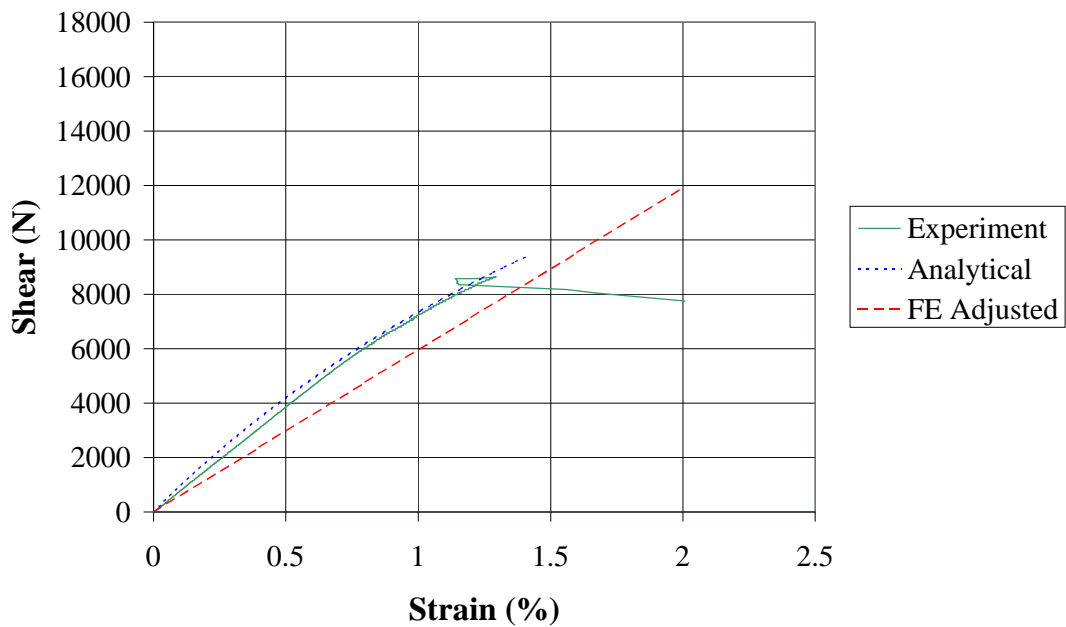


Figure E.2 Experimental shear strains series 2

Table E.16 ms04-b-2 beam results

ms04-B1-2	First cracking occurred at 13100 <i>N</i> . Failure may have been premature under the loading point. Local buckling (or crushing) of webs at web flange interface occurred. As well as web cracking throughout the beam. Ultimate load was 21750 <i>N</i> .
ms04-B2-2	First crack at 9300 <i>N</i> . Failure started with delamination and longitudinal cracking of the RHS laminate at the web flange interface. Ultimate failure appeared to occur simultaneously with tearing of the outer web RHS laminate and crushing of the core at the support. Ultimate load was 21492 <i>N</i> .
ms04-B3-2	First crack at 7450 <i>N</i> . Failure very similar to ms04-b2-2. The end-bearing stopper pushed out causing end-bearing failure to occur. Ultimate failure at 17720 <i>N</i> .
ms04-B4-2	First crack at 10140 <i>N</i> . Failure started with buckling of the webs and the longitudinal delamination of the RHS laminate at the web flange interface. This was followed by web core cracking and ultimate failure that propagated near the support at a load of 17204 <i>N</i>

S3 (ms04-b-3)

The shear strain from beam ms04-b4 followed a linear relationship until shear cracking occurred. The cracking crossed over the strain gauge rosette causing the RHS laminate to delaminate and buckle just prior to ultimate failure (Figure E.3).

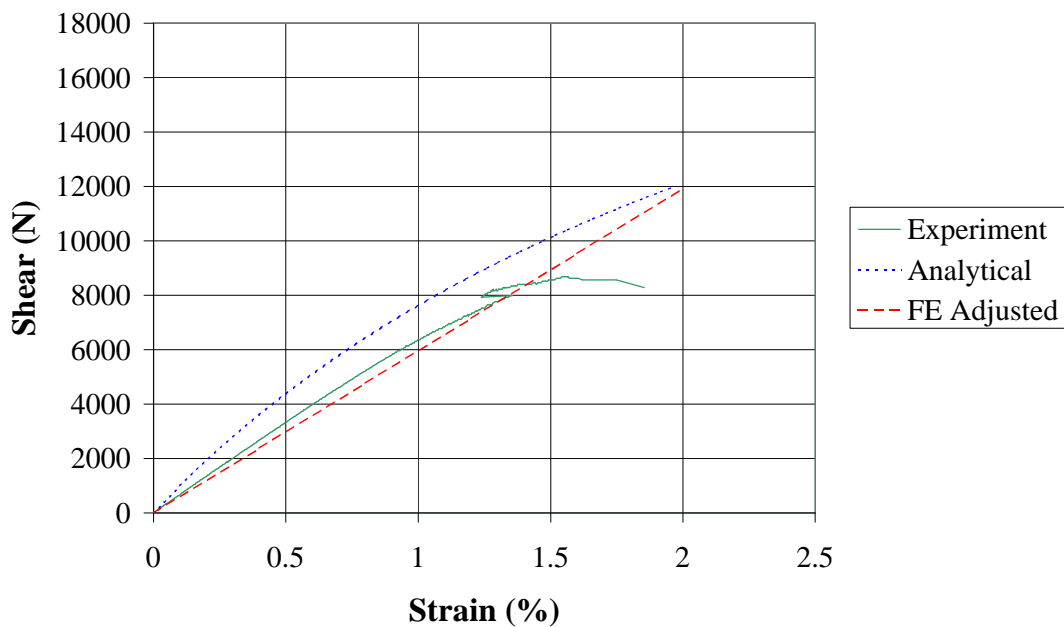


Figure E.3 Experimental shear strains series 3

Table E.17 ms04-b-3 beam results

ms04-B1-3	First crack at 12880 <i>N</i> . Failure was of shear in the webs, shear cracking occurred in centre of webs evident as fine cracks in resin. Not at 45 degrees (sloping closer to vertical showing effect of moment). Outer RHS delaminated along web flange interface. Failure via cracking and tearing of outer laminate after core cracking. Failure load 20342 <i>N</i>
ms04-B2-3	First cracking heard at 14220 <i>N</i> . Failure mechanism very similar to ms04-b1-3. Buckling of outer RHS evident due to web core failure. One side of the beam had a horizontal tear of the outer RHS. Failure at a load of 23518 <i>N</i>
ms04-B3-3	First crack at 9630 <i>N</i> . Failure occurred via buckling of the core webs and the delamination of the RHS laminate along the web flange interface in the shear zone of the beam. Failure load 18346 <i>N</i>
ms04-B4-3	First crack 12150 <i>N</i> The failure started in the shear zone similar to ms04-b3-3. Vertical tearing occurred in the RHS laminate at failure. Failure load was 17366 <i>N</i>

S4 (ms04-b-4)

Shear strain of the webs closely followed the analytical prediction (Figure E.4).

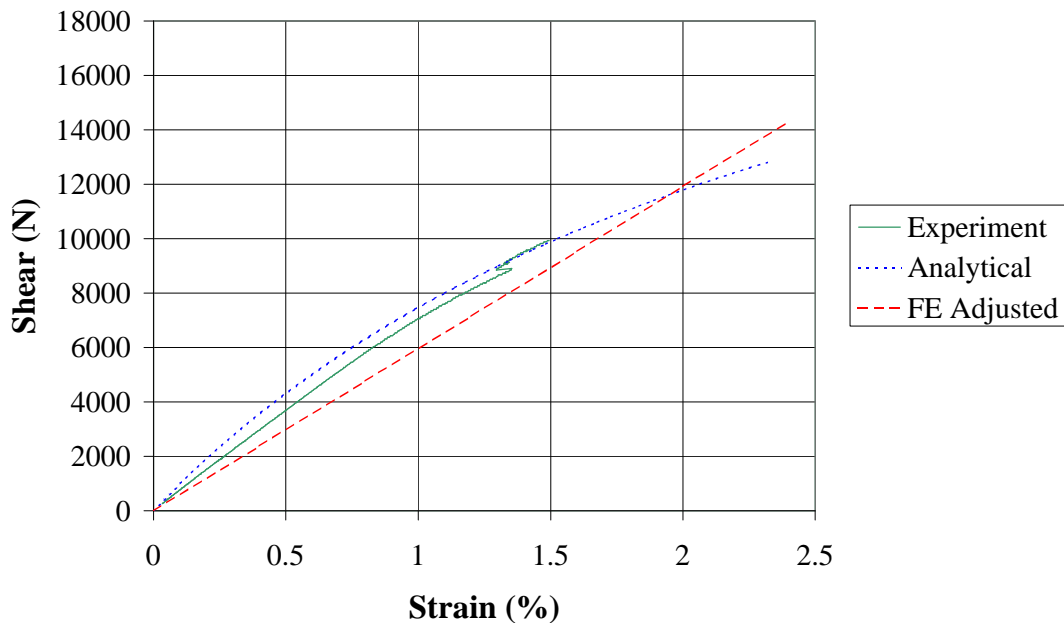


Figure E.4 Experimental shear strains series 4

Table E.18 ms04-b-4 beam results

ms04-B1-4	First cracking occurred at 19100 <i>N</i> . Failure started with fine shear cracks in core and progressive disintegration of the core material. The RHS laminate delaminated in the centre due to the core pushing out and at the web flange interface. Ultimate failure at 21822 <i>N</i> .
ms04-B2-4	First cracking occurred at a load of 14140 <i>N</i> . Failure was from similar causes as ms04-b1-4 however the RHS laminate tore horizontally (at web flange interface) and then vertically up on one web face. Failure load 22878 <i>N</i>
ms04-B3-4	First crack at 14280 <i>N</i> . Failure similar to ms04-b2-4. Failure load 18924 <i>N</i> .
ms04-B4-4	First crack at 16330 <i>N</i> . Failure caused by cracking of core in webs and subsequent buckling, followed by delamination of the RHS laminate at the web flange interface. Tearing of the RHS laminate occurred along one of the core vertical (slightly inclined) cracks at the higher moment end. Failure load 22620 <i>N</i> .

S5 (ms04-b-5)

The shear strains depicted in Figure E.5 were similar to the preceding beams.

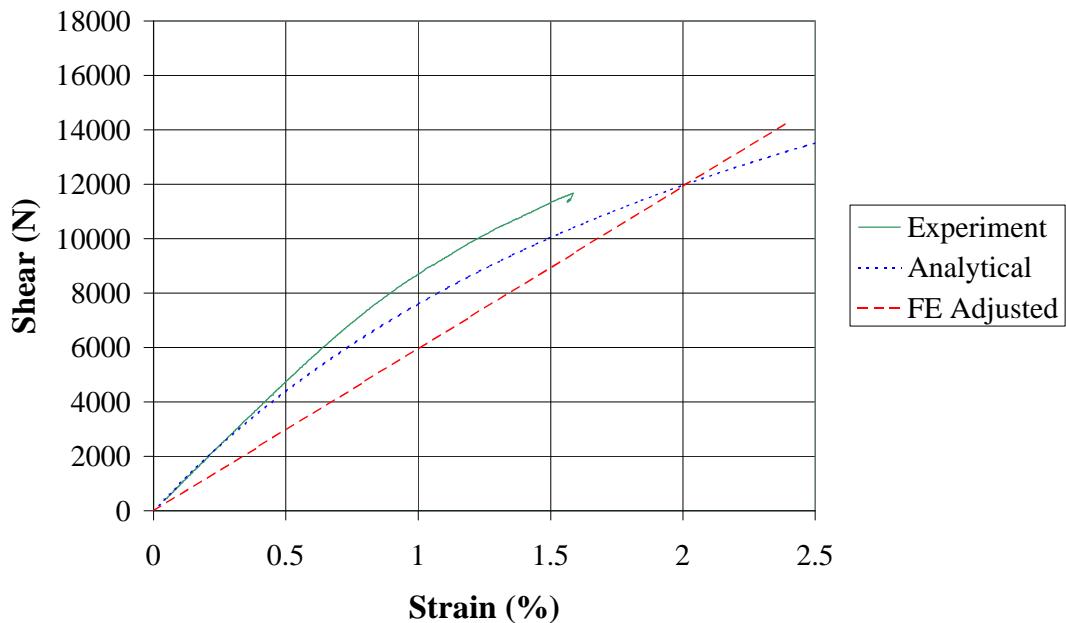


Figure E.5 Experimental shear strains series 5

Table E.19 ms04-b-5 beam results

ms04-B1-5	First crack at 25730 <i>N</i> . This cracking could have been shear not moment related. The core cracked at almost 45 degrees under one load point. Core web disintegration followed and the top flange tore away from the rest of the beam. Ultimate load was 29154 <i>N</i> .
ms04-B2-5	First cracks at 19770 <i>N</i> . Failure was around the flange web interface and appears to have started as web crushing followed by or caused by the web buckling. Ultimate load was 29774 <i>N</i>
ms04-B3-5	First crack at 22192 <i>N</i> . Failure similar to ms04-b1-5. Ultimate load 22192 <i>N</i>
ms04-B4-5	First crack at 19900 <i>N</i> . Failure started with core cracking at 45 degrees to the normal on one web face followed by longitudinal delamination of the RHS laminate at the web flange interface. Failure via buckling of one web due to core breakout. Load at failure 23252 <i>N</i> .

S6 (ms04-b-6)

The shear strains show a curve-linear trend similar to beams ms04-b4-5 (Figure E.6).

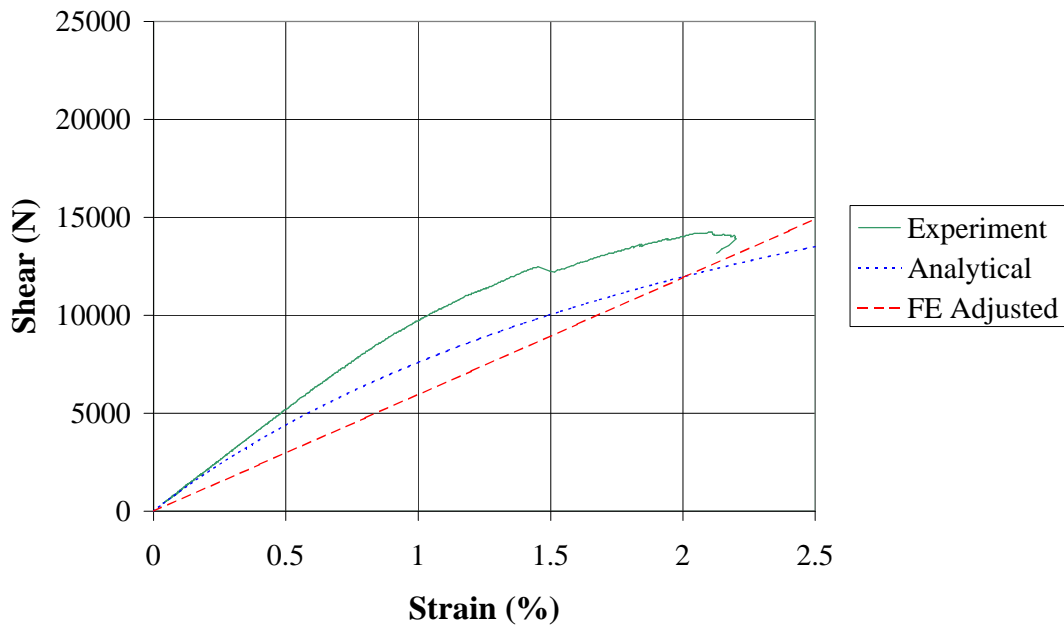


Figure E.6 Experimental shear strains series 6

Table E.20 ms04-b-6 beam results

ms04-B1-6	Crack heard at 17200 <i>N</i> . Failure occurred via end bearing failure. Maximum load 24522 <i>N</i> .
ms04-B2-6	Crack heard at 33010 <i>N</i> . Failure in shear zone starting with core web cracking and causing buckling of the RHS laminate which then delaminated at the web flange interface. Failure at 33422 <i>N</i> .
ms04-B3-6	First crack at 27470 <i>N</i> . Failure occurred after the web core cracked and delamination of the RHS laminate occurred on one web face. The other web face had the RHS laminate tearing at the web flange interface. Ultimate load 27762 <i>N</i> .
ms04-B4-6	First cracking at 9910 <i>N</i> (very faint). Failure occurred after the web core cracked at 45 degrees and caused local delamination of the RHS laminate. The RHS laminate then proceeded to crack at the web flange interface. Ultimate load 28266 <i>N</i>

E.6 Beams under torsion loading

Beams T-b1 and T-b2

ms05-b1-1 to 3 tested on the 16th December 2001, ms05-b1-4 to 6 tested on the 6th of June 2001 and ms05-b2 tested on the 20th of September 2001, Results presented in Table E.21.

Table E.21 Torsion test results

<i>Beam</i>	<i>Result</i>
ms05-b1-1	As the beam was being tested delamination of the outer RHS laminate could be observed at the web-flange interface. Failure occurred when a transverse crack appeared at an angle of 45 degrees to the axis of the beam. Failure was at a torque of 507000 <i>N.mm</i> . Rotation last measured at a torque of 455000 <i>N.mm</i> as 0.142625 radians.
ms05-b1-2	The beam behaved similarly to ms05-b1-1. Failure was precipitated by delamination of the outer RHS laminate at the flange-web interface. No transverse cracking was observed at maximum torque of 529500 <i>N.mm</i> . Rotation last measured at a torque of 520000 <i>N.mm</i> as 0.23775 radians
ms05-b1-3	The beam showed little visual signs of damage to failure. A small crack appeared at the flange-web interface prior to failure. The failure was that of the cable and not the beam. Load reached was 650000 <i>N.mm</i> with a rotation of 0.197945 radians
ms05-b1-4	The beam showed little visual signs of damage to a torque of 520000 when audible cracking sounds were detected. At the failure torque of 85000 <i>N.mm</i> (rotation of 0.244571 radians) a crack at 45 degrees to the beam axis was noted in the web.
ms05-b1-5	The outer RHS laminate started to delaminate from the core at a torque of 370500 <i>N.mm</i> near the flange-web interface. Core cracks in the web progressively appeared at an angle of 45 degrees to the axis of the beam until failure at a torque of 507000 <i>N.mm</i> . Rotation last measured at a torque of 507000 <i>N.mm</i> at 0.241211 radians.
ms05-b1-6	The beam showed little signs of damage to failure. Failure was of the cable not the beam. Rotation last measured at a torque of 585000 <i>N.mm</i> at 0.198628 radians
ms05-b2-1	The beam rotated without loud sounds being heard until a torque of 331500 <i>N.mm</i> was reached. Further, larger audible cracking was heard at 604500 <i>N.mm</i> . Failure was at 604500 <i>N.mm</i> at a rotation of 0.207843 radians.
ms05-b2-2	The beam showed little sign of damage until the first audible cracking at 409500 <i>N.mm</i> Torque. De lamination of the outer RHS laminate near the flange web interface progressed until ultimate failure at 585000 <i>N.mm</i> and 0.242961 radians

E.7 Distribution angle

Table E.22 Bearing distribution results

<i>Beam</i>	<i>Bearing plate (mm)</i>	<i>First crack (N)</i>	<i>Fail load (N)</i>	<i>Fail</i>
ms07-b1-1	125	7600	23860	Shear fail at support
ms07-b1-2	75	20000	26487	Bearing
ms07-b1-3	25	20600	27481	Bearing
ms07-b1-4	0	12500	17942	Bearing
ms07-b2-1	13.7	13500	23033	Crush
ms07-b2-2	28.09	14300	24405	Shear bearing
ms07-b2-3	49.93	19200	37783	Bearing-buckle
ms07-b2-4	62.05	31800	42275	Bearing
ms07-b2-5	32.14	13100	28594	Punching/buckling
ms07-b2-6	38	14600	19377	End bearing
ms07-b2-7	38	20000	25250	Punching/buckling
ms07-b2-8	43.72	37400	41044	Punching/buckling

E.8 Time effects: Short-term failure load and deflection of the beams

B1 (ms03-b1)

The beams in this series were tested on the 21st of July 2000. The beams were made as the control beams for the creep testing. These beams had eight layers of unidirectional mat in the flanges of the beams, unlike the remainder of the beams used in this study. Figure E.7 shows the relationship between the moments and the strains on the top and bottom flanges of the beam. The results are presented in Table E.23.

Bearing length of 65 mm was used.

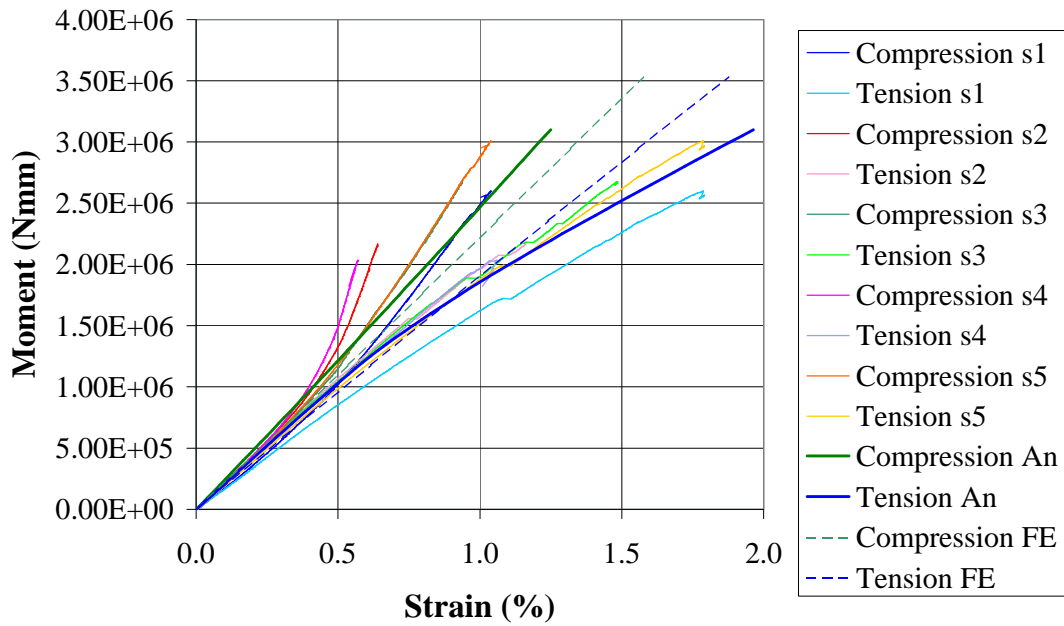


Figure E.7 ms03-b1

Table E.23 ms03-b1 results

ms03-b1-1	Failed in compression beside load point. Moment at failure was 2.57E6 <i>N.mm</i> . The loading plate was not flexing sufficiently thereby causing stress concentrations at either end of the plates. Span was 575 <i>mm</i> and internal span 200 <i>mm</i> .
ms03-b1-2	Beam failed due to end bearing failure. Bearing load was 11548 <i>N</i> . The failure was sudden. First cracking sound at 18837 <i>N</i> load. Span was 575 <i>mm</i> and internal span 200 <i>mm</i> . The compressive strain gauge appeared to buckle during the test.
ms03-b1-3	Beam failed due to end bearing failure. Bearing load was 15083 <i>N</i> . First cracking sound at 18734 <i>N</i> load. Span was 555 <i>mm</i> and internal span 200 <i>mm</i> .
ms03-b1-4	Beam failed due to end bearing failure. Bearing load was 11456 <i>N</i> . First cracking sound at 18713 <i>N</i> load. Span was 555 <i>mm</i> and internal span 200 <i>mm</i> . The compressive strain gauge appeared to buckle similar to beam ms03-b1-2.
ms03-b1-5	Beam failed in compression near loading point. Moment at failure was 3.156E6 <i>N.mm</i> . First cracking sound around 22266 <i>N</i> load. Span 575 <i>mm</i> and internal span 150 <i>mm</i> .

Appendix F. FEA

F.1 Fortran program for damage analysis and material properties used by ABAQUS

```
SUBROUTINE USDFLD(FIELD, STATEV, PNEWDT, DIRECT, T, CELENT,
1 TIME, DTIME, CMNAME, ORNAME, NFIELD, NSTATV, NOEL, NPT, LAYER,
2 KSPT, KSTEP, KINC, NDI, NSHR, COORD, JMAC, JMTYP, MATLAYO, LACCFLA)
C
C   INCLUDE 'ABA_PARAM.INC'
C
C MATERIAL AND STRENGTH PARAMETERS
PARAMETER(YT=37, XC=2000, YC=151, SC=47.2)
PARAMETER(G12U=3009, ALPHA=2.44D-8, SStrainU=1.8D-2)
PARAMETER(FStrainU=1.9649D-2, PFRFail=0.006)
PARAMETER(G12P=1122, SStrainP=1.3D-2, FStrainP=1.475D-2)
C
C   CHARACTER*80 CMNAME, ORNAME
C   CHARACTER*8  FLGRAY(15)
C   DIMENSION FIELD(NFIELD), STATEV(NSTATV), DIRECT(3,3),
1 T(3,3), TIME(2)
C   DIMENSION ARRAY(15), JARRAY(15), JMAC(*), JMTYP(*), COORD(*),
1 PS(3)
C
C
C INITIALIZE FAILURE FLAGS FROM STATEV.
DAMLAM = STATEV(1)
EM      = STATEV(2)
EFS     = STATEV(3)
DAMAGE = STATEV(4)
C
C GET COMMEN VALUES
C
CALL GETVRM('E', ARRAY, JARRAY, FLGRAY, JRCD,
$          JMAC, JMTYP, MATLAYO, LACCFLA)
E11 = ARRAY(1)
E12 = ARRAY(4)
C
C IF PFR WORK OUT PFR FAILURE CRITERIA
C
IF(CMNAME(1:3).EQ.'PFR') THEN
C
C CALCULATE PRINCIPAL STRAINS
C where S=ARRAY, LSTR=2, NDI=3, NSHR=3
CALL SPRINC(ARRAY, PS, 2, 3, 3)
EMAX = PS(1)
DO I = 2, 3
IF (PS(I).GT.EMAX) THEN
EMAX = PS(I)
ENDIF
ENDIF
```

```

        ENDDO
C
C PFR DAMAGE: tensile softening and failure
C
        IF (EMAX.GT.PFRfail) THEN
            DAMLAM_N = 1.D0
        ELSEIF (E11.GT.0.D0) THEN
            DAMLAM_N = 0.8D0*EMAX/PFRFail + 0.1D0
        ELSE
            DAMLAM_N = 0.D0
        ENDIF
C MAKING SURE LAMINATE DOESN'T HEAL
        IF (DAMLAM_N.GT.DAMLAM) THEN
            DAMLAM = DAMLAM_N
        ENDIF
C UPDATE FIELD VARIABLES
C
        FIELD(1) = DAMLAM
        STATEV(1) = FIELD(1)
        ELSE
C
C IF UNI OR PWV WORK OUT UNI FAILURE CRITERIA
C
C GET STRESSES FROM PREVIOUS INCREMENT
C
        CALL GETVRM('S',ARRAY,JARRAY,FLGRAY,JRCD,
$           JMAC, JMTYP, MATLAYO, LACCFLA)
        S11 = ARRAY(1)
        S22 = ARRAY(2)
        S12 = ARRAY(4)
C
C INITIALIZE CAPACITIES
C
        IF (CMNAME(1:3).EQ.'PWV') THEN
            G12 = G12P
            SStrain = SStrainP
            FStrain = FStrainP
        ELSE
            G12 = G12U
            SStrain = SStrainU
            FStrain = FStrainU
        ENDIF
C
C LAMINATE DAMAGE: tensile failure
C
        IF (E11.GT.FStrain) THEN
            DAMLAM_N = 1.D0
        ELSEIF (E11.GT.SStrain) THEN
            DAMLAM_N = 0.9D0*(E11 - SStrain)/(FStrain - SStrain) + 0.1D0
        ELSEIF (E11.GT.0.D0) THEN
            DAMLAM_N = 0.1D0
        ELSE
            DAMLAM_N = 0.D0

```



```

        ENDIF
C MAKING SURE LAMINATE DOSEN'T HEAL
        IF (DAMLAM_N.GT.DAMLAM) THEN
            DAMLAM = DAMLAM_N
        ENDIF
C
C DAMAGE INDEX: = 0 IF NO STRAIN TO PREVENT DIVIDE BY ZERO
C
        IF (E12.NE.0) THEN
            DAMAGE = (3.D0*ALPHA*G12*S12**2 - 2.D0*ALPHA*(S12**3)/E12) /
&            (1.D0 + 3.D0*ALPHA*G12*S12**2)
        ELSE
            DAMAGE = 0.D0
        ENDIF
C
        F1 = S12**2/(2.D0*G12) + 0.75D0*ALPHA*S12**4
        F2 = SC**2 / (2.D0*G12) + 0.75D0*ALPHA*SC**4
C
C MATRIX TENSILE/COMPRESSIVE FAILURE
        IF (EM .LT. 1.D0) THEN
            IF (S22 .LT. 0.D0) THEN
                EM = SQRT((S22/YC)**2 + F1/F2)
            ELSE
                EM = SQRT((S22/YT)**2 + F1/F2)
            ENDIF
            STATEV(1) = EM
        ENDIF
C
C FIBER-MATRIX SHEAR FAILURE
        IF (EFS .LT. 1.D0) THEN
            IF (S11 .LT. 0.D0) THEN
                EFS = SQRT((S11/XC)**2 + F1/F2)
            ELSE
                EFS = 0.D0
            ENDIF
            STATEV(2) = EFS
        ENDIF
C
C UPDATE FIELD VARIABLES
C
        FIELD(2) = 0.D0
        FIELD(3) = 0.D0
        IF (EM .GT. 1.D0) FIELD(2) = 1.D0
        IF (EFS .GT. 1.D0) FIELD(3) = 1.D0
        FIELD(4) = DAMAGE
        STATEV(4) = FIELD(4)
        FIELD(1) = DAMLAM
        STATEV(1) = FIELD(1)
    ENDIF
C
    RETURN
END

```

F.2 Damage and failure of a laminated composite plate

Copied from (Hibbitt, Karlsson & Sorensen Inc. 2003)

“Problem description and material behaviour

The material accumulates damage in shear, leading to a nonlinear stress-strain relation of the form

$$g_{xy} = G_{xy}^{-1} s_{xy} + a s_{xy}^3, \dots \dots \dots (F.1)$$

where G_{xy} is the (initial) ply shear modulus and the nonlinearity is characterized by the factor $a = 2.44 \times 10^{-8} \text{ MPa}^{-3}$.

Failure modes in laminated composites are strongly dependent on geometry, loading direction, and ply orientation. Typically, one distinguishes in-plane failure modes and transverse failure modes (associated with interlaminar shear or peel stress). Since this composite is loaded in-plane, only in-plane failure modes need to be considered, which can be done for each ply individually. For a unidirectional ply as used here, five failure modes can be considered: matrix tensile cracking, matrix compression, fibre breakage, fibre matrix shearing, and fibre buckling. All the mechanisms, with the exception of fibre breakage, can cause compression failure in laminated composites.

The failure strength in laminates also depends on the ply lay-up. The effective failure strength of the lay-up is at a maximum if neighbouring plies are orthogonal to each other. The effective strength decreases as the angle between plies decreases and is at a minimum if plies have the same direction. (This is called a ply cluster.) Chang and Lessard [Chang, 1989 #296] have obtained some empirical formulas for the effective transverse tensile strength; however, in this model we ignore such effects. Instead, we use the strength properties for the laminate.

The strength parameters can be combined into failure criteria for multiaxial loading. Four different failure modes are considered in the model analysed here.

- Matrix tensile cracking can result from a combination of transverse tensile stress, s_y , and shear stress, s_{xy} . The failure index, e_m , can be defined in terms of these stresses and the strength parameters, Y_t and S_c . When the index exceeds 1.0, failure is assumed to occur. Without nonlinear material behaviour, the failure index has the simple form,

$$e_m^2 = \left(\frac{\mathbf{s}_y}{Y_t} \right)^2 + \left(\frac{\mathbf{s}_{xy}}{S_c} \right)^2 \dots\dots\dots (F.2)$$

With nonlinear shear behaviour taken into consideration, the failure index takes the more complex form,

$$e_m^2 = \left(\frac{\mathbf{s}_y}{Y_t} \right)^2 + \frac{2\mathbf{s}_{xy}/G_{xy} + 3\mathbf{a}\mathbf{s}_{xy}^4}{2S_c^2/G_{xy} + 3\mathbf{a}S_c^4} \dots\dots\dots (F.3)$$

- Matrix compressive failure results from a combination of transverse compressive stress and shear stress. The failure criterion has the same form as that for matrix tensile cracking:

$$e_m^2 = \left(\frac{\mathbf{s}_y}{Y_c} \right)^2 + \frac{2\mathbf{s}_{xy}/G_{xy} + 3\mathbf{a}\mathbf{s}_{xy}^4}{2S_c^2/G_{xy} + 3\mathbf{a}S_c^4} \dots\dots\dots (F.4)$$

The same failure index is used since the previous two failure mechanisms cannot occur simultaneously at the same point. After the failure index exceeds 1.0, both the transverse stiffness and Poisson's ratio of the ply drop to zero.

- Matrix-matrix shearing failure results from a combination of fibre compression and matrix shearing. The failure criterion has essentially the same form as the other two criteria:

$$e_{fs}^2 = \left(\frac{\mathbf{s}_x}{X_c} \right)^2 + \frac{2\mathbf{s}_{xy}/G_{xy} + 3\mathbf{a}\mathbf{s}_{xy}^4}{2S_c^2/G_{xy} + 3\mathbf{a}S_c^4} \dots\dots\dots (F.5)$$

This mechanism can occur simultaneously with the other two criteria; hence, a separate failure index is used. Shear stresses are no longer supported after the failure index exceeds 1.0, but direct stresses in the fibre and transverse directions continue to be supported.

- Fibre buckling failure occurs when the maximum compressive stress in the fibre direction ($-\mathbf{s}_x$) exceeds the fibre buckling strength, X_c , independent of the other stress components:

$$e_b = \frac{\mathbf{s}_x}{X_c} \dots\dots\dots (F.6)$$

It is obvious that, unless the shear stress vanishes exactly, matrix-matrix shearing failure occurs prior to fibre buckling. However, fibre buckling may follow subsequent to fibre shearing because only the shear stiffness degrades after matrix-matrix shearing failure. Fibre buckling in a layer is a catastrophic mode of failure. Hence, after this failure index exceeds 1.0, it is assumed that the material at this point can no longer support any loads.

Material model implementation

To simulate the shear nonlinearity and the failure modes (matrix failure in tension or compression and matrix-matrix shear failure), the elastic properties are made linearly dependent on three field variables. The first field variable represents the matrix failure index, the second represents the matrix-matrix shear failure index, and the third represents the shear nonlinearity (damage) prior to failure. The dependence of the elastic material properties on the field variables is shown in **Table 8.1**.

To account for the nonlinearity, the nonlinear stress-strain relation must be expressed in a different form: the stress at the end of the increment must be given as a linear function of the strain. The most obvious way to do this is to linearise the nonlinear term, leading to the relation

$$\mathbf{g}_{xy}^{(i+1)} = \left(G_{xy}^{-1} + a(\mathbf{s}_{xy}^{(i)})^2 \right) \mathbf{s}_{xy}^{(i+1)}, \dots\dots\dots (F.7)$$

where *i* represents the increment number. This relation can be written in inverted form as

$$\mathbf{s}_{xy}^{(i+1)} = \frac{G_{xy}}{1 + aG_{xy}(\mathbf{s}_{xy}^{(i)})^2} \mathbf{g}_{xy}^{(i+1)}, \dots\dots\dots (F.8)$$

thus providing an algorithm to define the effective shear modulus.

However, this algorithm is not very suitable because it is unstable at higher strain levels, which is readily demonstrated by stability analysis. Consider an increment where the strain does not change; i.e., $\mathbf{g}_{xy}^{(i+1)} = \mathbf{g}_{xy}^{(i)} = \mathbf{g}_{xy}$. Let the stress

at increment i have a small perturbation from $\mathbf{s}_{xy}^e^{(i)}$, the exact solution at that increment: $\mathbf{s}_{xy}^{(i)} = \mathbf{s}_{xy}^e^{(i)} + \Delta\mathbf{s}_{xy}^{(i)}$. Similarly, at increment $i+1$, $\mathbf{s}_{xy}^{(i+1)} = \mathbf{s}_{xy}^e^{(i+1)} + \Delta\mathbf{s}_{xy}^{(i+1)}$. For the algorithm to be stable, $\Delta\mathbf{s}_{xy}^{(i+1)}$ should not be larger than $\Delta\mathbf{s}_{xy}^{(i)}$. The perturbation in increment $i+1$ is calculated by substituting $\mathbf{s}_{xy}^{(i)}$ in the effective shear modulus equation and linearising it about $\mathbf{s}_{xy}^e^{(i)}$:

$$\Delta\mathbf{s}_{xy}^{(i+1)} = \frac{-2G_{xy}^2 \mathbf{s}_{xy} \mathbf{g}_{xy}}{(1 + aG_{xy} \mathbf{s}_{xy}^2)^2} \Delta^{(i)}, \dots \dots \dots (F.9)$$

where $\mathbf{s}_{xy} = \mathbf{s}_{xy}^e^{(i)}$. The perturbation in increment $i+1$ is larger than the perturbation in increment i if

$$2aG_{xy}^2 \mathbf{s}_{xy} \mathbf{g}_{xy} > (1 + aG_{xy} \mathbf{s}_{xy}^2)^2, \dots \dots \dots (F.10)$$

which, after elimination of \mathbf{g}_{xy} , reduces to the expression

$$a\mathbf{s}_{xy}^3 > G_{xy}^{-1} \mathbf{s}_{xy}, \dots \dots \dots (F.11)$$

Hence, instability occurs when the "nonlinear" part of the shear strain is larger than the "linear" part of the shear strain.

To obtain a more stable algorithm, we write the nonlinear stress-strain law in the form

$$\mathbf{g}_{xy} + \mathbf{b}\mathbf{s}_{xy}^3 = G_{xy}^{-1} \mathbf{s}_{xy} + (\mathbf{a} + \mathbf{b})\mathbf{s}_{xy}^3, \dots \dots \dots (F.12)$$

where \mathbf{b} is an as yet unknown coefficient. In linearised form this leads to the update algorithm

$$\left(1 + \frac{\mathbf{b}(\mathbf{s}_{xy}^{(i)})^3}{\mathbf{g}_{xy}^{(i)}} \right) \mathbf{g}_{xy}^{(i+1)} = \left(G_{xy}^{-1} + (\mathbf{a} + \mathbf{b})(\mathbf{s}_{xy}^{(i)})^2 \right) \mathbf{s}_{xy}^{(i+1)}, \dots \dots \dots (F.13)$$

or, in inverted form,

$$\mathbf{s}_{xy}^{(i+1)} = \frac{1 + \mathbf{b}(\mathbf{s}_{xy}^{(i)})^3 / \mathbf{g}_{xy}^{(i)}}{1 + (\mathbf{a} + \mathbf{b})G_{xy}(\mathbf{s}_{xy}^{(i)})^2} G_{xy} \mathbf{g}_{xy}^{(i+1)} \dots\dots\dots (F.14)$$

Following the same procedure as that for the original update algorithm, it is readily derived that a small perturbation, $\Delta \mathbf{s}_{xy}^{(i)}$, in increment i reduces to zero in increment $i+1$ if $\mathbf{b} = 2\mathbf{a}$. Hence, the optimal algorithm appears to be

$$\mathbf{s}_{xy}^{(i+1)} = \frac{1 + 2\mathbf{a}(\mathbf{s}_{xy}^{(i)})^3 / \mathbf{g}_{xy}^{(i)}}{1 + 3\mathbf{a}G_{xy}(\mathbf{s}_{xy}^{(i)})^2} G_{xy} \mathbf{g}_{xy}^{(i+1)} \dots\dots\dots (F.15)$$

Finally, this relation is written in terms of the damage parameter d :

$$\mathbf{s}_{xy}^{(i+1)} = (1 - d)G_{xy} \mathbf{g}_{xy}^{(i+1)}, \dots\dots\dots (F.16)$$

where

$$d = \frac{3\mathbf{a}G_{xy}(\mathbf{s}_{xy}^{(i)})^2 - 2\mathbf{a}(\mathbf{s}_{xy}^{(i)})^3 / \mathbf{g}_{xy}^{(i)}}{1 + 3\mathbf{a}G_{xy}(\mathbf{s}_{xy}^{(i)})^2} \dots\dots\dots (F.17)$$

This relation is implemented in user subroutine USDFLD, and the value of the damage parameter is assigned directly to the third field variable used for definition of the elastic properties.

The failure indices are calculated with the expressions (F.3), (F.4), and (F.5) discussed earlier, based on the stresses at the start of the increment:

$$e_m^2 = \left(\frac{\mathbf{s}_y^{(i)}}{Y_t} \right)^2 + \frac{3\mathbf{a}(\mathbf{s}_{xy}^{(i)})^4 + 2(\mathbf{s}_{xy}^{(i)})^2 / G_{xy}}{3\mathbf{a}S_c^4 + 2S_c^2 / G_{xy}} \text{ if } \mathbf{s}_y^{(i)} > 0, \dots\dots\dots (F.18)$$

$$e_m^2 = \left(\frac{\mathbf{s}_y^{(i)}}{Y_c} \right)^2 + \frac{3\mathbf{a}(\mathbf{s}_{xy}^{(i)})^4 + 2(\mathbf{s}_{xy}^{(i)})^2 / G_{xy}}{3\mathbf{a}S_c^4 + 2S_c^2 / G_{xy}} \text{ if } \mathbf{s}_y^{(i)} < 0, \dots\dots\dots (F.19)$$

$$e_{fs}^2 = \left(\frac{\mathbf{s}_x^{(i)}}{X_c} \right)^2 + \frac{3\mathbf{a}(\mathbf{s}_{xy}^{(i)})^4 + 2(\mathbf{s}_{xy}^{(i)})^2 / G_{xy}}{3\mathbf{a}S_c^4 + 2S_c^2 / G_{xy}} \dots\dots\dots (F.20)$$

The values of the failure indices are not assigned directly to the field variables: instead, they are stored as solution-dependent state variables. Only if the value of a failure index exceeds 1.0 is the corresponding user-defined field variable set equal to 1.0. After the failure index has exceeded 1.0, the associated user-defined field variable continues to have the value 1.0 even though the stresses may reduce significantly, which ensures that the material does not "heal" after it has become damaged."

References

Hibbitt, Karlsson & Sorensen Inc. 2003, 'Damage and failure of a laminated composite plate', in *ABAQUS Example Problems Manual*, vol. 1, ed. Hibbitt Karlsson & Sorensen Inc., pp. 1.1.13-1 - 1.1.13-12.